Chiral Analysis Using Molecular Rotational Resonance Spectroscopy

by

Fan Xie

A thesis submitted in partial fulfillment of the requirements for the degree of

Doctor of Philosophy

Department of Chemistry
University of Alberta

Abstract

The chirality controlled structural panoramas of several prototypic chiral molecular systems were studied in a conformational specific manner using molecular rotational resonance spectroscopy. Comprehensive conformational ensemble spaces were explored theoretically to aid the interpretation of rotational spectra observed experimentally. The binding topologies of these chiral aggregates, including binary and ternary complexes were determined, revealing interesting chirality controlled structural preferences. Comprehensive conformational abundance analyses of the chiral molecular systems were carried out. The experimental conformational abundances showed a complex competition between thermodynamically and kinetically controlled formation processes of chiral molecular aggregates under supersonic jet expansion conditions. Furthermore, analytically oriented experiments, including impurity identification and enantiomeric excess measurements were performed using a chirped pulse Fourier transform microwave spectrometer.

Perillyl alcohol, a chiral alcohol with multiple conformational degrees of freedom, has a complicated potential energy surface landscape. Its structural diversity was investigated systematically using a joint experimental rotational spectroscopic and theoretical approach. Comprehensive theoretical searches produced 54 minimum structures. Twelve of them were expected to be observable under supersonic jet expansion conditions after consideration of conformational cooling. Experimentally, the first eight most stable conformers were detected in the chirped pulse rotational spectrum obtained. This study points out the importance of a comprehensive conformational search in molecular rotational resonance studies. A similar study was done on a prototype chiral carboxylic acid, namely tetrahydro-2-furoic acid. Experimentally, three conformers were observed, including different ring puckering configurations and *trans-/cis*-COOH configurations. Unlike many common carboxylic acids, the acid strongly favors the *trans*-COOH configuration because of an intramolecular H-bond.

Subsequently, chirality recognition in the tetrahydro-2-furoic acid···propylene oxide complex and in the tetrahydro-2-furoic acid dimer was investigated in a conformer-specific manner. The kinetically and thermodynamically controlled complex formation processes predicted drastically different binary products. To identify the conformers responsible for the extremely dense rotational spectra observed, several hundred homo/heterochiral conformers were located theoretically, and equally importantly, the energetic connections among the minima were evaluated. The experimental outcomes pointed to a complicated competition between these two processes and interesting conformational panoramas caused by the competition between intra- and intermolecular H-bond interactions. These studies further reveal interesting chirality dependent structure–energy ordering relationships. Using a recently proposed chiral-tag approach, enantiomeric excess (ee) determination experiments and detailed statics error analyses were performed for both chiral binary complexes.

Several structures of the homo- and heterochiral ternary propylene oxide clusters were decoded experimentally. This study represents a challenging case in spectroscopic investigations of molecular structures: extensive theoretical conformational searches failed to provide a suitable candidate for the set of rotational transitions assigned to the heterochiral propylene oxide trimer. By improving instrument sensitivity and optimizing sample conditions, rotational spectra of eighteen ^{13}C isotopologues of both homo- and heterochiral propylene oxide timers were observed in their natural abundances. A Python script was written to aid the extraction of the trimer structures from the experimental isotopic data. This study points out some current deficiencies in the theoretical conformational search approach and the potential in using chirped pulsed Fourier transform microwave spectroscopy in decoding structural diversity of even larger (chiral) molecular clusters and uncovering the associated chirality controlled structural preferences.

Preface

This thesis is a partial collection of my research done at the University of Alberta during my Ph.D. program from September 2016 to December 2020. The contributions of co-authors are described below.

The study in Chapter 3 was published as Fan Xie, Nathan Seifert, Matthias Heger, Javix Thomas, Wolfgang Jäger, and Yunjie Xu, “The rich conformational landscape of perillyl alcohol revealed by broadband rotational spectroscopy and theoretical modeling," *Phys. Chem. Chem. Phys*. 2019, 21, 15408-15416.” I was responsible for the theoretical search, spectral assignment, abundance analysis, and manuscript writing. Dr. Nathan Seifert instructed me on how to perform spectrum collection, spectral assignment, and interpretation. Dr. Matthias Heger did the two-dimensional scan calculation. Dr. Javix Thomas made an early experimental attempt at the system. Prof. Yunjie Xu was the supervisory author who guided me through paper writing, concept establishment. Prof. Wolfgang Jäger provided constructive discussions.

The study in Chapter 4 was published as Fan Xie, Xiaoqian Ng, Nathan A. Seifert, Javix Thomas, Wolfgang Jäger, and Yunjie Xu, “Rotational spectroscopy of chiral tetrahydro-2-furoic acid: conformational landscape, conversion, and abundances”, *J. Chem. Phys.* 2018, 149, 224306. I was responsible for automating conformational search procedure, spectral assignment, abundance analysis, and manuscript writing. Xiao Qian joined this project as a summer undergraduate student. She did a manual conformational search and wrote the initial draft of the introduction. Dr. Nathan Seifert supervised me with experiments. Dr. Javix Thomas made an early experimental search attempt. Prof. Yunjie Xu was the supervisory author who guided me through paper writing, concept establishment, and elaboration. Prof. Wolfgang Jäger provided constructive discussions.

The manuscript about the research result in Chapter 5 will be submitted shortly to Chemistry-A European Journal. I was responsible for writing several programming scripts, theoretical calculations, spectrum collection and assignment, abundance, and enantiomer excess analyses. Dr. Nathan Seifert worked together with me with the early experimental data collection. Prof. Yunjie Xu was the supervisory author who guided me through paper writing, concept establishment, and elaboration. Prof. Wolfgang Jäger provided constructive discussions.

The study in Chapter 6 was published as Fan Xie, Nathan A. Seifert, Wolfgang Jäger, and Yunjie Xu, "Conformational panorama and chirality controlled structure-energy relationship in a chiral carboxylic acid dimer," *Angew. Chem. Int. Ed.* 2020, 59, 15703-15710. I was responsible for writing several programming scripts, theoretical calculations, spectrum collection and assignment, abundance, and enantiomer excess analyses. Dr. Nathan Seifert worked together with me with the early experimental data collection. Prof. Yunjie Xu was the supervisory author who guided me through paper writing, concept establishment, and elaboration. Prof. Wolfgang Jäger provided constructive discussions.

The study in Chapter 7 was published as Fan Xie, Marco Fusè, Arsh S. Hazrah, Wolfgang Jäger, Vincenzo Barone, and Yunjie Xu, "Discovering the elusive global minimum in a ternary chiral cluster: rotational spectra of propylene oxide trimer," *Angew. Chem. Int. Ed.,* 2020, 59, 22427-22430. I was responsible for writing several programming scripts, theoretical calculations, spectrum collection and assignment, and abundance analysis. Dr. Macro Fusè and Prof. Vincenzo Barone are the collaborators of this study who were responsible for the high level anharmonic calculations. Arsh Hazrah participated in the experiments and discussions. Prof. Yunjie Xu was the supervisory author who guided us through paper writing, concept establishment, and elaboration. Prof. Wolfgang Jäger provided constructive discussions.

Acknowledgments

"The art of teaching is the art of assisting discovery." (Mark Van Doren)

Here, I express my deep gratitude to all the most excellent teachers I encountered in my Ph.D. career. They are my friends, partners, and advisers who bestowed me with unlimited vitality and passion in science.

Firstly, I would like to thank my supervisor Prof. Yunjie Xu who patiently provides me step-by-step guidance raising me from an academic infant to an adult. Her wisdom, inspiration, and conscientiousness always stimulate me. From my first microwave experiment to paper writing training, she has always been there offering supports with countless meetings and nearly four thousand emails throughout the day and night of my Ph.D. career. I am also thankful to Prof. Wolfgang Jäger for providing me thoughtful and constructive suggestions and criticisms that help my scientific understanding and horn my experimental skills. I am grateful to Prof. Alex Brown, Prof. Gabriel Hanna, and Prof. Li Liang for providing supervision and supports during my Ph.D. program. I am also thankful to my teaching assistant coordinators Dr. Norman Gee, Dr. Yoram Apelblat, and Dr. Reza Poopari for their supportive guidance. Learning to teach is also a great experience. A special note of thanks to Dr. Nathan Seifert and Dr. Matthias Heger; they are my postdoctoral advisers who walked me through many essential techniques, calculations, and programming. I also express my gratitude to all my friends: Arsh, Bowei, Haolu, Qian, Mohammad, Mutasem, Raiden, Tao, Guojie, and Yanqing for their friendship and scientific discussions.

Funding from the University of Alberta, Natural Sciences and Engineering Research Council of Canada, Compute/Calcul Canada, and an H. E. Gunning Research Fellowship are acknowledged.

Table of Contents

List of Tables

List of Figures

List of Symbols

A, B, C	Rotational constants
$\mu_{a,b,c}$	Electric dipole moment components
ΔD_e	Relative raw dissociation energies
ΔD_0	Corrected dissociation energies
D_J , D_{JK} , D_K , d_1, d_2	Quartic distortion constants
H_{rot}	Rigid rotor Hamiltonian
$P_{a,b,c}$	Angular momentum on principal axes
$I_{a,b,c}$	Moments of inertia along the *a*-, *b*-, and *c*-axes
J	Rotational quantum number
K	Projection of J onto the principal axis
$K_{a,c}$	Quantum number at oblate and prolate limit
H_0	Hamiltonian of the two-level system
μ_{ab}	Transition dipole moment
E	Strength of external electric filed
$\Phi(t)$	Time dependant wavefunction
$\hbar$	Reduced Planck constant
Ω	Driving vector
Θ	Bloch vector

List of Abbreviations

MRR	Molecular rotational resonance
CP-FTMW	Broadband chirped pulse Fourier transfer microwave
ee	Enantiomeric excess
PA	Perillyl alcohol
THFA	Tetrahydro-2-furoic acid
PO	Propylene oxide
RWA	Rotating wave approximation
FID	Free induction decay
AWG	Arbitrary waveform generator
TWT	Traveling-wave tube amplifier
OSC	Oscilloscope
SPST	The single-pull single-throw switch
CREST	Conformer-Rotamer Ensemble Sampling Tool
xTB	A tight bonding semiempirical quantum chemical method
HF	Hartree-Fock
MP	Møller–Plesset perturbation theory
D3BJ	Grimme's dispersion correction with Becke Johnson damping
DFT	Density Functional Theory
B3LYP	Becke, 3-parameter, Lee–Yang–Parr, Hybrid functional
MD	Molecular Dynamics

Chapter 1

Introduction

"Most natural organic products, the essential products of life, are asymmetric and possess such asymmetry that they are not superimposable on their image. This establishes perhaps the only well-marked line of demarcation that can at present be drawn between the chemistry of dead matter and the chemistry of living matter." — LOUIS PASTEUR[1]

1.1 Chirality and chirality recognition

The word *Chirality* comes from Greek χειρ meaning "hand", an intuitive chiral object. A chiral object is defined as a structure that cannot be superimposed onto its mirror image. A chiral molecule and its mirror image are called an enantiomeric pair. In 1848, Louis Pasteur discovered two mirror-imaged crystal forms of sodium ammonium tartrate that cannot be superimposed onto each other[2]. Later, he found that tartaric acid derived from living organisms rotates the plane of linearly polarized light while the synthetic one causes no such effect[3]. These observations led him to think that artificial tartaric acid is a mixture of two mirror-imaged molecules that are 'dissymmetric', a historical name of today's 'chiral'. Since the discovery of the mysterious property of tartaric acid by Louis Pasteur, more and more chiral molecules with biological origin have been revealed, such as L-amino acids, D-sugars, nucleic acids. These remarkable discoveries ultimately lead to uncovering the homochirality in life[4-6]. Because of the asymmetry nature of chiral molecules, they often produce different biological outcomes. For example, S-limonene usually tastes like lemon, whereas R-limonene has a taste closer to orange. Such different responses to a pair of enantiomers are of significant importance in the pharmacy industry. Today, more than half

of drugs on the market have at least one chiral center, and more than a quarter of them need to be used in a single-enantiomer form[7]. Severe consequences may follow if such chiral metabolism selectivity was not well understood and tested. For instance, racemic thalidomide was put on the market as a treatment for nausea in pregnant women. However, only R-thalidomide is therapeutic active, and S-thalidomide causes defects in newborns. It was later discovered that the two enantiomeric forms can interconvert in the human body[8]. From a fundamental point of view, these enantioselectivities are made possible through chiral recognition, i.e., how a chiral molecule differentiates another object's chirality. The concept of chirality recognition plays an important role in life science[9-13], biochemistry[14-17], asymmetric synthesis[18,19] analytical and separation science[20-23]. For example, one of the most successfully commercialized chiral columns used in chromatography is made of chiral polysaccharide derivatives. It serves as a non-isotropic environment that interacts with analytes via intermolecular interactions, i.e., hydrogen bonding, halogen bonding, dipole-dipole, and dispersions interactions. Enantiomers move at different speeds as a racemic analyte passing through the chiral column. Such dynamics lead to the separation of the sample.

Nevertheless, the exact binding topologies of chiral recognitions existing in these macroscopic systems mentioned above remain unknown. My thesis investigates the structure energy relationship in clusters of prototype chiral molecules in a conformational specific manner. The research presented fundamental understandings of small chiral molecules' kinetic and thermodynamic behavior and possible inspiring insights to larger systems.

1.2 Studies of chiral molecular systems using molecular rotational resonance (MRR) spectroscopy

1.2.1 MRR spectroscopy for structural and energetic properties

To understand the mechanism of chiral recognition at the molecular level, one needs to examine a chiral molecule's structural flexibility and how non-covalent interactions with another molecule, especially another chiral molecule, modify its structural preference. Molecular structure determination is a procedure to acquire the three-dimensional nuclear coordinates of molecules and clusters. Often, such information can be extracted from various spectroscopic techniques[24-31]. For example, in X-ray crystallography, diffracted X-ray light contains information about the crystalline structure. In UV-visible spectroscopy, light interacts with the ground and excited electronic states, and the corresponding spectral signatures may reveal structural details of the chromophore. In infrared vibrational spectroscopy, infrared light excitation offers the opportunity to probe vibrational energy levels and transitions associated with functional groups in a molecule, especially in the fingerprint region. Microwave radiation can drive a macroscopic polarization between rotational states and provide a rotational spectrum. The rotational constants determined experimentally can be linked to molecular mass distribution in space, i.e., the molecule's geometry. Radiofrequency (RF) radiation can interact with the nuclei spin states, split by a strong static magnetic field. The observed RF signal's relative positions reveal the electronic environment surrounding a specific nucleus, which can be further linked to molecular structure and symmetry.

While all these spectroscopic techniques offer some structural information, MRR spectroscopy is the chosen technique for this thesis for several reasons outlined below. In solution phase spectroscopic studies, the transitions are often broadened by many effects, i.e., short lifetime, pressure, and Doppler broadening. Moreover, the overall spectra are often complicated with a variety of high energy structures. It is difficult to interpret the

over-packed spectral patterns in a conformational specific manner. As stated with details in Chapter 2.2, a MRR spectrometer is often couple with molecular beam techniques. Analytes are vaporized into the gas phase, then introduced into a vacuum chamber via the supersonic jet expansion. The rotational and conformational degrees of freedom of molecular systems are cooled, forming a molecular beam that contains low energy conformers of monomers and clusters. The resulting rotational spectra contain rich and interpretable spectral features. With the aid of high-level ab initio calculations, molecular structures are identified by matching experimental rotational constants and dipole moment components to the theoretical ones of a species, i.e., a structure. Each type of rotational transition intensity is proportional to the square of the specific dipole moment component. A simple example to demonstrate the resolving power of MRR spectroscopy is the THFA monomer study included in Chapter 4 of this thesis. Two sets of rotational spectra that belong to tetrahydro-2-furoic acid (THFA) conformer I and III are shown in Figure.1.1, where their structures differ by the location of proton. Hence, their spectroscopic constants, including rotational constants and dipole moment components are different, resulting in two distinctive spectral patterns that can be easily resolved by MRR spectroscopy. Unsurprisingly, the binding specificity in chiral complexes can be identified as well. Examples can be found in Chapter 5, 6, and 7. Both homochiral and heterochiral conformers of the THFA dimer, the THFA Propylene oxide (PO) dimer, and the PO trimer are observed and discussed in detail.

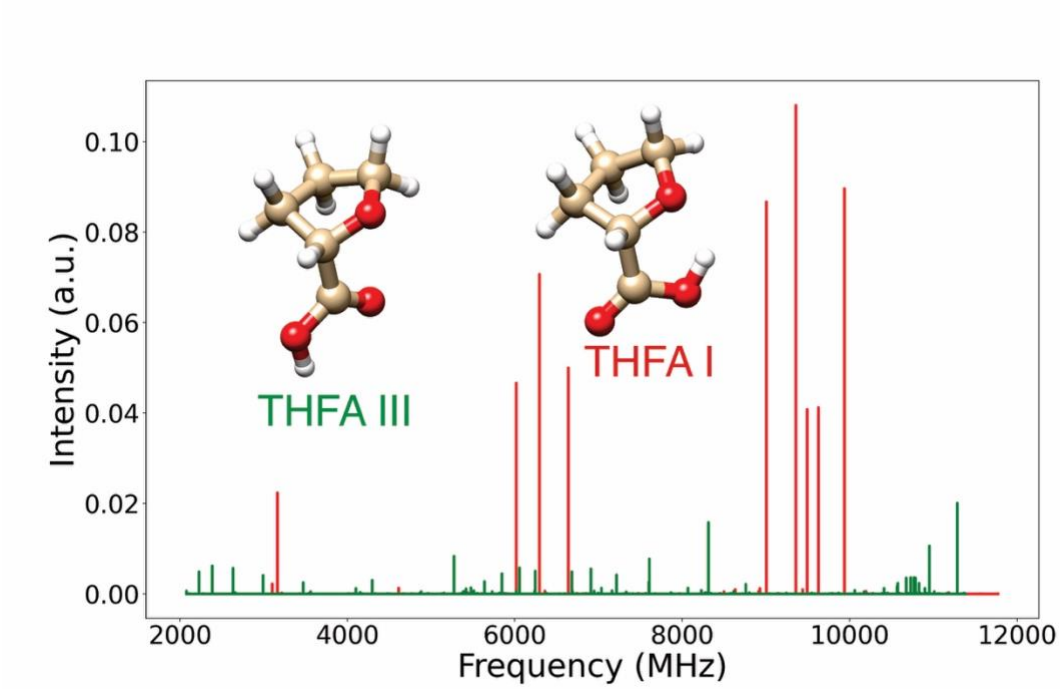

Figure 1.1. The simulated rotational spectra of THFA conformer I and III using experimental fitted rotational constants and calculated dipole moment components.

1.2.2 Broadband chirped pulse Fourier transform microwave spectroscopy (CP-FTMW)

The primary MRR spectroscopic instrument used in this thesis is the broadband CP-FTMW. In 2006, Pate and co-workers developed the first broadband MRR spectrometer. It significantly reduced the level of difficulties in spectra searches and assignments compared to narrowband instruments, i.e., cavity based Fourier transform microwave spectrometer. Benefitting from modern telecommunication and radar technologies, chirped pulsed microwave radiation is discretely generated and collected by electronic devices and coherently locked via an atomic clock (see Chapter 2.3 for details). Such a configuration enables highly precise and sensitive measurements of frequencies. For instance, a typical CP-FTMW instrument offers a resolution of 25 kHz (~10^{-6} cm^{-1}) and an excitation bandwidth of several GHz.[32] When coupled to a supersonic jet expansion, it can offer a line width of ~130 kHz (full width at half height). The maximum resolving capability is

expected to be more than seven thousand transitions per GHz. With such high resolution power, any subtle changes in spectroscopic constants can alter the rotational spectrum patterns enough for detection.

Furthermore, the phase coherence of MRR time domain signal ensures that the noise level decreases with respect to the number of experiments. Thereby, low population species could be resolved in the spectrum with deep acquisitions, typically a few million experimental cycles. By counting and comparing the abundance of observed conformers, we could investigate not only cluster binding specificity but also the dynamics of interested molecular systems under pulse jet expansion conditions.[33,34] All the above capabilities make the CP-FTMW technique very well suited to study molecules and clusters in a conformational specific manner.

1.2.3 Foreseeable applications

Other than being utilized in fundamental studies of chirality recognition mechanisms, there are emerging applications of MRR spectroscopy, such as online monitoring of stereoisomers and impurities.[35-37] Chiral stereoisomers differ from each other by inverting one or more stereogenic centers. Determining the abundant ratios of them is a challenging analytical problem. Thanks to the extremely high sensitivity and resolving power of the CP-FTMW technique, these stereoisomers' rotational spectra can be easily differentiated from one another. The transition intensities can be used directly to derive individual isomers' abundances in the (gas phase) sample.

Enantiomeric excess (ee) measurement is an essential analytical procedure in various applications, including crude natural product separations, asymmetric syntheses, and drug developments. There are many tools available commercially and some utilized in research, and each has its pros and cons. One of the most commonly used methods is chiral chromatography, where the sample is passing through a chiral column, enantiomers move

at different speeds, leading to two separated peaks at the end of the column. The value of ee can be obtained by evaluating the areas under each peak. For more volatile chiral molecules, such column separation may be difficult. With MRR spectroscopy, a chiral tag is used to form homo- and heterochiral diastereomers with the enantiomeric pair via intermolecular bonding, resulting in drastically different spectral patterns, i.e., rotational transitions for the enantiomeric pair. One can then use these diastereomeric transitions' experimental intensities to calculate the ee value (as elaborated in Chapter 2, 5, 6). Compared to other analytical tools like chiral chromatography[38], NMR[39], and fluorescence[40] spectroscopies, the significant advantages of the MRR ee method are: first, there is no need to perform tedious and /or difficult syntheses, and second there are typically thousands of transition pairs available for calculating ee. Thus, one can obtain an averaged ee measurement with a statistically meaningful error bar. Moreover, crucial mixtures including unreacted reactants, desired and undesired products from the production line can be analyzed directly without further separation and purification.[35]

1.3 Organization of the thesis

This thesis is divided into eight chapters. Chapter 1 provides the general introduction to my thesis work. In Chapter 2, I briefly present the principles of the CP-FTMW instrument, MRR spectroscopy, theoretical conformational search procedures, ee excess calculations from MRR spectra, and several python scripts I wrote to facilitate automatic data processing in spectral assignments, rotational temperature, abundance estimation, and enantiomeric excess calculations. Chapter 3 describes the MRR spectroscopic study of perillyl alcohol (PA). PA is a chiral dietary monoterpene with multiple flexible dihedral angles, leading to an extremely complicated conformational landscape with 54 conformers identified theoretically. Under pulse jet expansion condition, conformers with low interconversion barriers are expected to be cooled, i.e., converted to the lower energy conformers. Twelve among the 54 conformers were identified as the observable candidates

according to the associated potential energy surface scans. Experimentally, the first eight most stable candidate conformers were observed, demonstrating the cooling dynamics under pulse jet expansion conditions. A clear preference for the equatorial conformations over axial ones was identified. This study points out the importance of comprehensive conformational search in MRR studies and a systematic methodology of using the MRR spectrum to benchmark theoretical stabilities. Chapter 4 reports the diverse structures of tetrahydro-2-furoic acid (THFA), chiral carboxylic acid. Unlike common carboxylic acids, THFA monomers tend to form intramolecular H-bond by adopting *trans*-COOH configuration. In this study, the THFA monomers observed are mainly existing in the *trans*-COOH configuration over the *cis*-COOH one. Chapter 5 discusses the complexation between THFA and propylene oxide (PO). PO is a simple, iconic chiral molecule with only one conformation but multiple binding sites. Hence, the binary THFA-PO complex is an interesting system to study the competition of THFA *trans* versus *cis* configuration and intramolecular versus intermolecular H-bond interactions and how they influence chirality-controlled structural preference. While *cis*-THFA is much less populated than *trans*-THFA, the *cis*-THFA-PO diastereomer is much more stable than *trans*-THFA-PO. Such a 'conflict' leads to a fascinating conformational panorama. The *cis*-THFA versus *trans*-THFA population in the binary THFA-PO chiral complex is about two times more than the ratio in the THFA monomer from the experiments. In Chapter 6, the conformational landscape of the THFA dimer was explored. The dimerization mechanism in a jet expansion is explored comprehensively using a combined experimental and theoretical approach. Two drastically different scenarios were proposed for the experimental outcome: a kinetically controlled dimer bound by weak interactions between heavily populated *trans*-THFA or a thermodynamically favored dimer with a classic double H-bonded ring structure formed by two *cis*-THFA subunits. Interestingly, both types of dimers were observed. Strong chirality controlled conformational preference was revealed, demonstrating an exciting chirality dependent structure-energy relationship. Furthermore, a method for ee determination of THFA was presented using a recently proposed chiral self-tag approach.[35] Chapter 7 extends MRR spectroscopy capabilities to a new level by decoding

the structures of chiral ternary PO clusters based on the experimental data. The theoretical conformational search procedures failed to identify the observed heterochiral PO trimer. Therefore, I put considerable efforts into improving the MRR instrument sensitivity and sample conditions to acquire rotational spectra of eighteen ^{13}C isotopologues of both homo- and heterochiral PO timers in their natural abundances. A Python script was written to aid the extraction of the PO trimer structures from the experimental isotopic data. This study shows some current deficiencies in the theoretical conformational search approach, which failed to produce a suitable candidate for the heterochiral PO trimer detected. The study demonstrates the potential to further exploit the sensitivity and resolution of CP-FTMW spectroscopy to decode large (chiral) molecular clusters' structures. Finally, Chapter 8 summarizes the thesis's main discoveries and offers some future directions to further explore chirality recognition in chiral clusters.

References

[1] L. C. R. Pasteur, *Acad. Sci.* **1858**, *46*, 615-818.

[2] L. Pasteur, *Ann. Chim. Phys.* **1848**, *28*, 56-99.

[3] L. Pasteur, *Compt. Rend. Acad. Sci.* **1853**, *36*, 19-26.

[4] D. G. Blackmond, *Cold Spring Harbor perspectives in biology* **2010**, *2*, a002147.

[5] G. Tranter, *J. Theor. Biol.* **1986**, *119*, 467-479.

[6] N. Fujii, T. Saito, *The Chemical Record* **2004**, *4*, 267-278.

[7] J. Gal, in *Chirality in Drug Research*, **2006**, pp. 1-26.

[8] W. Lenz, in *Problems of Birth Defects*, Springer, **1962**, pp. 199-199.

[9] A. Berthod, *Analytical Chemistry* **2006**, *78*, 2093-2099.

[10] J. Cronin, J. Reisse, in *Lectures in Astrobiology, Vol. 1*, **2005**, p. 473.

[11] W. A. Bonner, *Origins of Life and Evolution of the Biosphere* **1995**, *25*, 175-190.

[12] K. Michaeli, N. Kantor-Uriel, R. Naaman, D. H. Waldeck, *Chem. Soc. Rev.* **2016**, *45*, 6478-6487.

[13] L. Caglioti, K. Micskei, G. Pályi, *Chirality* **2011**, *23*, 65-68.

[14] T. H. Webb, C. S. Wilcox, *Chem. Soc. Rev.* **1993**, *22*, 383-395.

[15] S. C. Stinson, *Chem. Eng. News* **2001**, *79*, 45-57.

[16] T. Hirao, *J. Organomet. Chem.* **2009**, *694*, 806-811.

[17] B. Zheng, Y. Liu, J. Liu, S. Yin, J. Xu, *Int. J. Mech. Sci.* **2019**, *161-162*, 105025.

[18] M. Tsukamoto, H. B. Kagan, *Advanced Synthesis & Catalysis* **2002**, *344*, 453-463.

[19] A. Voituriez, A. Panossian, N. Fleury-Brégeot, P. Retailleau, A. Marinetti, *J. Am. Chem. Soc.* **2008**, *130*, 14030-14031.

[20] G. K. E. Scriba, *J. Chromatogr. A* **2016**, *1467*, 56-78.

[21] J. R. Sanchez-Valencia, T. Dienel, O. Gröning, I. Shorubalko, A. Mueller, M. Jansen, K. Amsharov, P. Ruffieux, R. Fasel, *Nature* **2014**, *512*, 61-64.

[22] B. L. Feringa, R. A. van Delden, *Angew. Chem. Int. Ed.* **1999**, *38*, 3418-3438.

[23] O. Riant, O. Samuel, H. B. Kagan, *J. Am. Chem. Soc.* **1993**, *115*, 5835-5836.

[24] G. J. Palenik, W. P. Jensen, I.-H. Suh, *J. Chem. Educ.* **2003**, *80*, 753.

[25] K. C. Engman, P. Sandin, S. Osborne, T. Brown, M. Billeter, P. Lincoln, B. Nordén, B. Albinsson, L. M. Wilhelmsson, *Nucleic Acids Research* **2004**, *32*, 5087-5095.

[26] M. T. Zanni, N.-H. Ge, Y. S. Kim, R. M. Hochstrasser, *Proceedings of the National Academy of Sciences* **2001**, *98*, 11265.

[27] D. Van Hemelrijk, L. Van den Enden, H. J. Geise, H. L. Sellers, L. Schaefer, *J. Am. Chem. Soc.* **1980**, *102*, 2189-2195.

[28] J. M. Steed, T. A. Dixon, W. Klemperer, *J. Chem. Phys.* **1979**, *70*, 4095-4100.

[29] K. Wuthrich, *Science* **1989**, *243*, 45.

[30] S. J. Opella, F. M. Marassi, *Chem. Rev.* **2004**, *104*, 3587-3606.

[31] S. Woutersen, P. Hamm, *J. Phys. Chem. B* **2000**, *104*, 11316-11320.

[32] G. B. Park, R. W. Field, *J. Chem. Phys.* **2016**, *144*, 200901.

[33] C. Abeysekera, L. N. Zack, G. B. Park, B. Joalland, J. M. Oldham, K. Prozument, N. M. Ariyasingha, I. R. Sims, R. W. Field, A. G. Suits, *J. Chem. Phys.* **2014**, *141*, 214203.

[34] S. M. Fritz, P. Mishra, J. Wullenkord, P. G. Fugazzi, K. Kohse-Höinghaus, T. S. Zwier, N. Hansen, *Proceedings of the Combustion Institute* **2020**.

[35] B. H. Pate, L. Evangelisti, W. Caminati, Y. Xu, J. Thomas, D. Patterson, C. Perez, M. Schnell, in *Chiral Analysis (Second Edition)* (Ed.: P. L. Polavarapu), Elsevier, **2018**, pp. 679-729.

[36] J. L. Neill, A. V. Mikhonin, T. Chen, R. E. Sonstrom, B. H. Pate, *J. Pharm. Biomed. Anal.* **2020**, *189*, 113474.

[37] L. A. Joyce, Danielle M. Schultz, E. C. Sherer, J. L. Neill, R. E. Sonstrom, B. H. Pate, *Chem. Sci.* **2020**, *11*, 6332-6338.

[38] M. Lämmerhofer, *J. Chromatogr. A* **2010**, *1217*, 814-856.

[39] T. R. Hoye, C. S. Jeffrey, F. Shao, *Nat. Protoc.* **2007**, *2*, 2451-2458.

[40] M. Hu, Y.-X. Yuan, W. Wang, D.-M. Li, H.-C. Zhang, B.-X. Wu, M. Liu, Y.-S. Zheng, *Nat. Commun.* **2020**, *11*, 161.

Chapter 2

Experimental, Theoretical and Data Analysis Approaches of MRR Spectroscopy

2.1. Introduction

This chapter will briefly describe the principles of molecular rotational resonance spectroscopy, methodologies, and program scripts I have written during my graduate study. In section 2.2, the theoretical treatment of rotational spectroscopy is introduced. Section 2.3 presents the chirped pulse instrument principles. Sections 2.4 to 2.6 present the conformational ensemble space exploration techniques combined with ab initio calculations. Section 2.7 discusses the application of enantiomer excess measurement. In section 2.8, the spectral fitting programs I used are summarized.

2.2 Rotational spectra

The theoretical principles of rotational spectroscopy are well established. There are excellent and widely cited references[1-4]. Here, I only briefly discuss the minimum theoretical knowledge needed to interpret spectral observations. Microwave radiation interacts with molecular rotational energy levels. The rotational eigenstates of a freely rotating, rigid molecule can be obtained by solving the time-independent Schrödinger equation with the rigid rotor Hamiltonian shown below:

$$H_{rot} = AP_a^2 + BP_b^2 + CP_c^2 \quad (2.1)$$

A, B, C are the rotational constants, and $P_{a,b,c}$ represent the projection of total angular momentum on the *a*-, *b*-, and *c*-principal axes. The H_{rot} operator is associated with only the kinetic energy of molecular rotation since there is no potential energy involved for a freely rotating molecule in space. Rotational constants are related to the principal moments of inertia with the following equations:

$$A = h/(8\pi^2 I_a),\ B = h/(8\pi^2 I_b),\ C = h/(8\pi^2 I_c) \quad (2.2)$$

where h is the Planck's constant, and $I_{a,b,c}$ are the principal moments of inertia along the *a*-, *b*-, and *c*-axis, respectively.

$$I_x = \Sigma_{i=1}^{n} m_i r_i^2 \text{ with } x=a, b, c \quad (2.3)$$

In the above formula, n is the total number of atoms in the molecule, and m_i is the mass of atom i, r_i is the distance between the atom i and the x principal axis. I_x represents a sum of each atom's mass distribution in the principal axis system. The convention used is that $I_c \geq I_b \geq I_a$, therefore $A \geq B \geq C$. In simple words, rotational constants represent the overall shape of a molecule. For example: $A = B = C$ represents a spherical top. $A > B = C$ and $A = B > C$ are prolate and oblate tops respectively. Most molecules, including many chiral molecules, are asymmetric tops with $A > B > C$.

For a symmetric top, the free rigid rotor Schrödinger equation's eigenvalues are indexed by two quantum numbers J and K. They correspond to P and P_a, respectively. Since P_a is a projection of total angular momentum P, the value of K can take on -J, -J+1, to J-1 and J values, leading to a (2J+1) degeneracy for each J level. In the case of asymmetric molecules, one first evaluates the matrix elements of rotational Hamiltonian operators using, for example, symmetric top wavefunctions as the basis set, and then diagonalize the matrix to obtain the rotational eigenvalues. Each rotational level is labeled by three quantum numbers J, K_a, and K_c. The rotational transitions we observe correspond to the energy difference between rotational energy levels, following the rotational selection rules. The

selection rules require a non-zero permanent dipole moment component along a principal axis to excitation a specific transition type. For example, *a*-type transitions need to have a non-zero permanent dipole moment component along the *a*-principal axis, i.e., $\mu_a \neq 0$. The additional selection rules for *a*-type transitions are ΔJ=0, +/-1 and ΔK_a = even and ΔK_c = odd. Similarly, *b*-type transitions have ΔK_a = odd and ΔK_c = odd, and *c*-type transitions have ΔK_a = odd and ΔK_c = even.

Rotational transitions are typically measured in the microwave region from a few to a few hundred GHz nowadays. With a typical transition frequency accuracy of a few kHz and a resolution capability of a few tens of kHz, subtle changes in molecular structure and mass distributions can be easily detected. The intensity of a rotational transition is proportional to the square of its corresponding permanent dipole moment component. Therefore, we can extract the relative magnitude of each permanent dipole moment components from the rotational spectrum of a molecular target. Compared to the theoretical predictions, this experimental information can identify the spectrum's carrier, as illustrated in Chapters 3,4,5,6 and 7.

2.3 Pulsed Fourier transform microwave measurements

2.3.1. Theoretical background

Below I consider a typical microwave pulse excitation experiment using a simplified model: a two-level system interacting with a classic electromagnetic wave via electric dipole interaction. Detailed treatments can be found in textbooks and other literature.[5,6] The time-dependent Hamiltonian can be expressed as:

$$H = H_0 - \mu_{ab} E \cos(\omega t) \qquad (2.4)$$

H_0 is the Hamiltonian of the two-level system with $\hbar\omega_a$ and $\hbar\omega_b$ as the lower and upper states' eigenvalues. μ_{ab} is the transition dipole moment. E is the strength of external electric

field. A near and/or exact resonance radiation is used to drive the population transfer between the energy levels. The solution of the above model under the rotating wave approximation (RWA) is:

$$\mathbf{\Phi}(t) = a(t)\,\Phi(t)_a + b(t)\,\Phi(t)_b \tag{2.5}$$

$$n_a(t) = a(t)a(t)^* = (\Delta/\Omega)^2 + [(\mathbf{K}\,E / \Omega]^2 \cos^2(\Omega t/2) \tag{2.6}$$

$$n_b(t) = b(t)b(t)^* = [(\mathbf{K}\,E / \Omega]^2 \sin^2(\Omega t/2) \tag{2.7}$$

with

$$\mathbf{K} = \mu_{ab} / \hbar, \tag{2.8}$$

$$\Delta = \omega - \omega_0, \tag{2.9}$$

$$\Omega = [\Delta^2 + (\mu_{ab}\,E/\hbar)^2]^{1/2} \tag{2.10}$$

$\mathbf{\Phi}(t)$ is the time-dependent wavefunction that describes the system, and a(t) and b(t) are the time-dependent coefficients. $n_a(t)$ and $n_b(t)$ are the products of these coefficients with their complex conjugate. They represent the probability of finding one particle at the upper or lower state at a particular time. Under the exact resonance condition where the frequency of external field is the same as the transition frequency between the two states, $\Omega = \mu_{ab}\,E/\hbar$. The preceding probability terms are simplified below:

$$n_a(t) = \cos^2(E\mu_{ab}t/2\hbar) \tag{2.11}$$

$$n_b(t) = \sin^2(E\mu_{ab}t/2\hbar) \tag{2.12}$$

As one can see, the population is oscillating between the ground and excited states. At t = 0, $n_a(t) = 1$ and $n_b(t) = 0$. All particles are in the ground state. When $E\mu_{ab}t/\hbar = \pi$, $n_a(t) = 0$ and $n_b(t) = 1$. The population is inversed. When $E\mu_{ab}t/\hbar = 2\pi$, the initial distribution is restored. Hence, we call this quantity, $E\mu_{ab}t/\hbar$, the Rabi frequency. Intuitively, it describes the interaction strength between the molecule and the external radiation and the population cycle between the lower and upper states under external radiation.

One can use a Bloch vector diagram to gain a more graphic description and insightful understanding of the coherent optical process described above. In the rotating frame representation, there are three components *u*, *v* and *w* in Bloch vector **Θ**:

$$u = \cos(\omega t)\, r_1 + \sin(\omega t)\, r_2 \tag{2.13}$$

$$v = -\sin(\omega t)\, r_1 + \cos(\omega t)\, r_2 \tag{2.14}$$

$$w = r_3 \tag{2.15}$$

with

$$r_1 = a(t)^* b(t) + a(t) b(t)^*, \tag{2.16}$$

$$r_2 = a(t)^* b(t) - a(t) b(t)^*, \tag{2.17}$$

$$r_3 = b(t) b(t)^* - a(t) a(t)^* = n_b(t) - n_a(t) \tag{2.18}$$

Recall that a(t) and b(t) are the time-dependent coefficients of the ground and the excited state, respectively. Therefore, *w* and r_3 represent the population difference between these two states at a given time. The Bloch vector's projection on *v,w* plane is proportional to the magnitude of coherent polarization of the molecular ensemble, which corresponds to the detected signal, i.e., Free Induction Decay (FID), in MW experiments. The driving vector **Ω** creates a torque on the Bloch vector **Θ** as following:

$$\frac{d\boldsymbol{\Theta}}{dt} = \boldsymbol{\Omega} \times \boldsymbol{\Theta} \tag{2.19}$$

$$\text{With } \boldsymbol{\Omega} = (-E\mu_{ab}t/\hbar,\ 0,\ \Delta) \tag{2.20}$$

The Bloch vector will precess around the driving vector at the rate of $[\Delta^2 + (\mu_{ab} E/\hbar)^2]^{1/2}$, which is the off-resonance Rabi frequency.

Figure 2.1 is taken from references[7,8], providing a vivid visualization of this precession motion. a) and b) illustrate the situation in a cavity-FTMW experiment, where the mirror distance is adjusted to amplify a specific transition frequency with a typical bandwidth of 1 MHz. Under the exact and/or near-resonant condition, a narrow bandwidth pulse

excitation is applied to the system. Here the driving vector **Ω** can be viewed as ($-E\mu_{ab}t/\hbar$, 0, 0), along *u* axis. It applies a torque to rotate the Bloch vector **Θ** in the *v,w* plane. The population periodically oscillates between the ground and excited states with a Rabi frequency. c), d), and e) depict the scenario in a chirped pulse FTMW experiments where a weak field, chirped pulse serves as the external radiation. At t = 0, the driving vector **Ω** = ($-E\mu_{ab}t/\hbar$, 0, Δ) is far from the resonance axis *u*. The Bloch vector precesses rapidly around the driving vector. As the radiation swept through resonance, the driving vector is close to ($-E\mu_{ab}t/\hbar$, 0, 0), where the quantity of Et term is tiny compared to the case of a cavity-FTMW experiment. The Bloch vector starts rotating slightly in the *vw* plane. After the radiation passes the resonance axis, the driving vector **Ω** tilts away from the *u*-axis, and the Bloch vector **Θ** will precess around the driving vector again. The system's population distribution remains nearly unchanged, while the polarization is also created accordingly throughout the chirped pulse interaction process. Since the swept bandwidth is not restricted to near resonance, it can excite the polarization of a wide range transitions, typically on the order of a few GHz.

Figure 2.1. The schematic representation of Bloch vector precesses under an external MW radiation (Ref 7 and 8). A narrow band strong pulse: (a) and (b). A broadband chirped pulse: (c) to (d). See text for details.

We have not considered the relaxation effects in the above Schrodinger solution and the optical Bloch picture to this point of discussion. In reality, there are relaxation processes, including the population relaxation towards the equilibrium distribution and polarization decoherence. We use T_1 and T_2 to represent the decay times of these two processes. The final expressions of the *optical Bloch equations* are as following:

$$\frac{du}{dt} = -\Delta v - u/T_2 \tag{2.21}$$

$$\frac{dv}{dt} = +\Delta u - v/T_2 + E\mu_{ab}w/\hbar \tag{2.22}$$

$$\frac{dw}{dt} = -(w-w^{eq})/T_1 - E\mu_{ab}v/\hbar \quad (2.23)$$

In a thermodynamic equilibrium environment, such as a waveguide MW experiment with static gas samples, the polarization coherence is quickly destroyed by collisions. As a result, the lifetime of "the excited states" is shortened, leading to a broader linewidth. To achieve a longer lifetime for FID observation in modern microwave experiments, a molecular ensemble is commonly prepared in a pulsed jet expansion. The molecules of interest are seeded in a carrier gas (Helium, Neon, or Argon), and the mixture is then expanded into a vacuum chamber through an orifice. The orifice dimension is typically much bigger than the mean free path of carrier gases. Thus, many collisions occur as the gas mixture passes through the orifice. During this nearly adiabatic process, the molecular ensemble's internal energy is mostly transferred to the highly directional mass flow forming a supersonic molecular jet. The relative translation between molecules is nearly zero, resulting in a nearly collision-free environment. As a result, the macroscopic polarization induced by the pulse excitation is nearly undisturbed from collisions. Furthermore, the low internal energy in the rotational and often conformational degrees of freedom leads to extremely low temperatures for these motions. Which is commonly known as the "cooling" effect.

2.3.2 Chirped pulse Fourier transform instruments

Walter Gordy first reviewed microwave spectroscopy in 1948.[9] After nearly a century of development, modern microwave spectroscopy has reached remarkable performances in sensitivity, resolution, and excitation bandwidth. The broadband chirped pulse Fourier transform microwave (CP-FTMW) technique was developed by Pate and co-workers in 2006 at the University of Virginia.[10] It has transformed the field of microwave spectroscopic research, increasing the detection efficiency by at least 1000-fold compared to cavity FTMW spectroscopy.[7] The CP-FTMW technique has provided the opportunity to investigate many interesting species that would otherwise be extremely difficult to study using cavity FTMW spectroscopy. This technique can routinely provide spectral resolution

of a few to 10s of kHz and a broadband capability of a few GHz, for example, from 2-8 or 8-16 GHz.[10] With cavity FTMW spectroscopy, it is difficult to obtain reliable intensity information related to a molecular species. Because the observed intensity is strongly influenced by the cavity mode intensity and the reproducibility of nozzle pulse-to-pulse operation, the molecular signal may fluctuate significantly from one mode to the next, as one scans from one frequency to the next. The missing intensity information makes it extremely challenging to assign an observed spectrum, a major hurdle in a MW spectroscopic investigation. CP-FTMW spectroscopy revolutionizes the neck-breaking spectral assignment procedure, especially when combining theoretical calculations and automatic spectral assignment aids[11]. This revolution allows researchers to study more interesting and increasingly complex molecular systems and untangle various factors that influence their structural diversities.

Analyses of experimentally observed rotational spectra can generally provide experimental rotational constants and dipole moment components that are directly linked to a molecular structure. With measurements of several isotopologues, experimental molecular structures can be determined with accuracy better than 0.01 Å in coordinates. Under a molecular beam pulsed jet expansion condition, often multiple conformations of a molecular system can be detected. Such information obtained has been used to test high level ab initio calculations in terms of structures predicted and relative stabilities predicted, for example, for different conformers.

MW spectroscopy application has gone beyond providing precise structural and energetic information of molecules and their clusters. For example, experimental transition frequencies have been used to aid astrophysical detections of interstellar molecules[12]. CP-FTMW measurements have been used to do online monitoring of impurity species or to extract enantiomeric excess (ee) of a chiral sample in recent developments[13,14]. The latter is a topic of interest in my thesis research.

The schematic diagram of the CP-FTMW instrument developed at the University of Alberta is presented in Figure 2.2. A broadband chirped pulse from 2 to 6 GHz is generated by an arbitrary waveform generator (AWG) with a sample rate of 12 Gs/s. The chirped pulse, transmitted through SMA cables, is amplified by a traveling-wave tube amplifier (TWT). The amplified chirped pulse is then broadcast into a vacuum chamber through a horn antenna. Meanwhile, the molecular jet expansion from a pulsed nozzle is introduced into the vacuum chamber and intercepts the MW chirped pulse perpendicularly. The interaction between molecules in the jet and MW radiation leads to the molecular ensemble's coherence polarization. As a result, the molecular ensemble starts to emit radiation associated with the molecular rotational transitions. The molecular radiation is collected by a receiving horn antenna as FID and transmitted to a digital oscilloscope (OSC), where the time domain signal is digitized, and Fourier transformed into the frequency domain signal. A few other devices are used between the receiving horn antenna and the OSC to improve the signal-to-noise ratio. For example, the single-pull single-throw (SPST) switch blocks the high-power chirped pulse from entering the detection circuitry during the excitation phase. The SPST switch only connects to the detection circuit once the chirped pulse has died down substantially, allowing the FID to be collected. A power limiter is inserted before the SPST switch as additional protection for the switch. A low noise signal amplifier downstream is used to amplify the incoming FID before digitization.

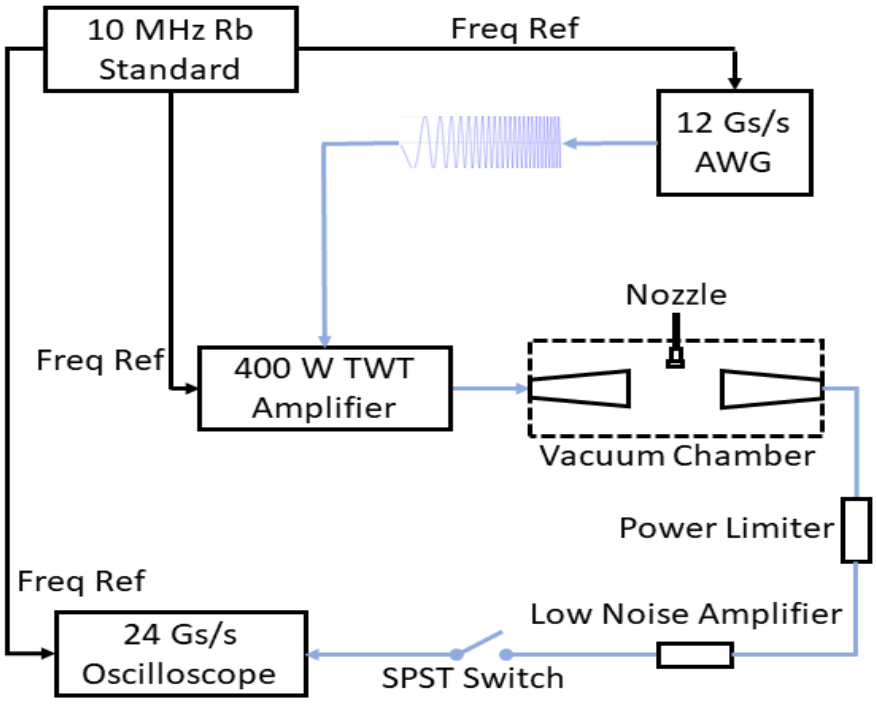

Figure 2.2. The schematic diagram of the 2-6 GHz CP-FTMW spectrometer developed at the University of Alberta.

Below, I will focus on the time sequence control of the CP-FTMW spectrometer. The key to a successful spectrum acquisition is to maintain the phase coherence of the time domain signal. This is essential to ensure the signal to noise ratio of MW transitions keeps increasing with deep averaging. To do so, we use the rubidium atomic clock shown in Figure 2.2 to provide the phase and frequency reference at 10 MHz to the master pulse generator illustrated in Figure 2.3. The master pulse generator provides two trigger pulses, AB and CD, fed to the nozzle driver and the AWG, respectively. The AWG is triggered about 900 us later than the nozzle driver to allow the pulsed molecular jet to travel to the detection zone center. The delay time is optimized for different carrier gases, i.e., helium, neon, and argon. Then, the AWG generates two triggers, maker1(MK1) and maker2(MK2).

MK1 triggers the slave pulse generator that controls the circuit connection of both excitation and detection. The slave pulse generator connects the switch built in the TWT amplifier with the S1 trigger, while the generated chirped pulse is fed to the TWT amplifier. Once the molecular jet is polarized, the slave pulse generator gives a second trigger S2 to the SPST switch before the OSC, allowing the FID to be received by the detection circuits. MK2 serves as the trigger of OSC. In a typical experiment, the chirped pulse width is set to 1 or 4 us, and the FID is collected for 20 or 40 us, depending on the property of the molecular system and the desired resolution. The processes indicated in the dashed line box in Figure 2.3 are repeated 6 or 12 times within one molecular pulse. It enables us to deep average the signal within a reasonable time frame. The nozzle repetition rate controlled by the master pulse generator is typically operated at 2 Hz. In summary, about two million FIDs can be collected per day with the 2 Hz, 12 frames set up.

I wrote a series of python scripts to control the waveform and time sequence used in the AWG. It enables a variety of experiments, including chirped up, chirped down, and fast acquisition. Besides the chirped pulse experiments, I have also carried out other experiments such as multiple state excitation, frequency comb, and phase coherence tests. These experiments are not included in this thesis. The details of these scripts can be found at https://github.com/FanXie001/MW-spectroscopy/tree/master/AWG

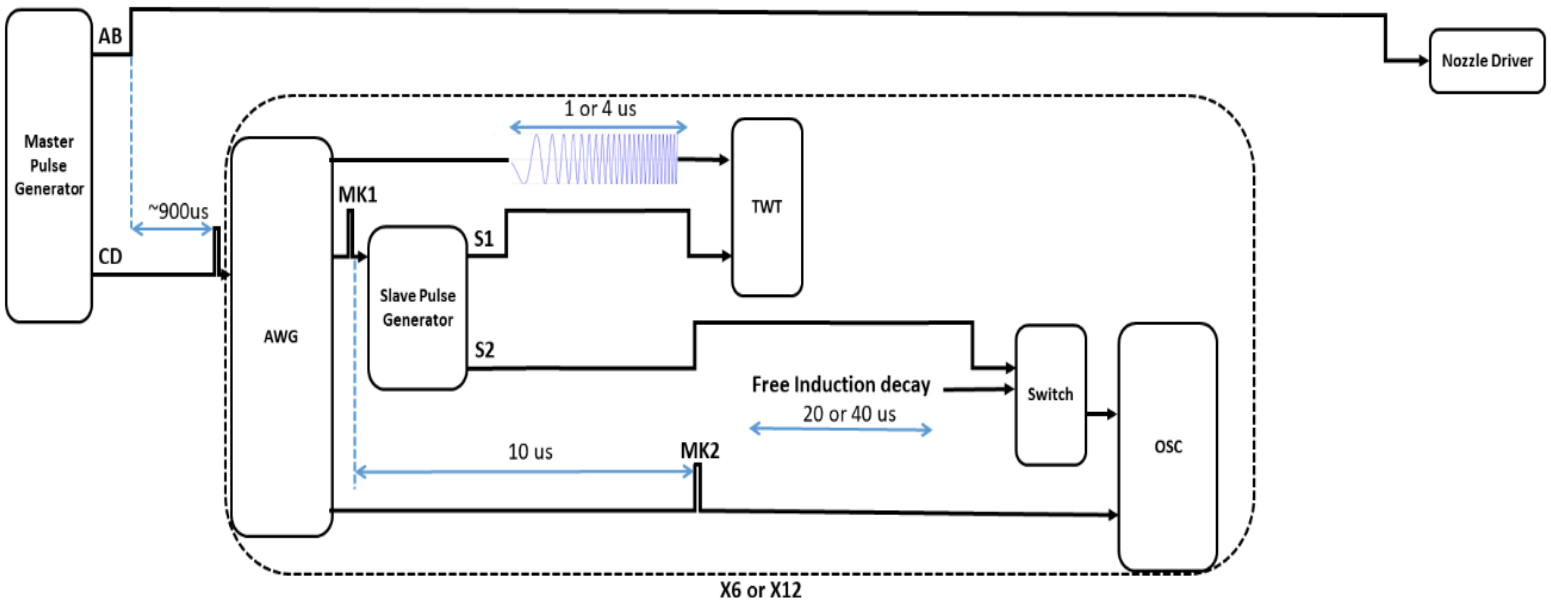

Figure 2.3. The schematic diagram of the time sequences of the CP-FTMW Spectrometer

2.4. Conformational ensemble search

Generally, all species with a permanent electric dipole moment are detectable in a single broadband experiment in the jet expansion discussed above. Therefore, the spectrum obtained often contains thousands to millions of transitions that span a wide intensity scale. To identify a species, one needs to assign a group of rotational transitions belonging to the species in the very dense spectrum. Theoretical calculations can greatly aid this procedure. The conformational diversity of molecules can be vast if there are many flexible angles and dihedral angles. In this thesis research, one main interest is placed on binary and ternary chiral molecular clusters. As one can imagine, the conformational ensemble space and the degrees of freedom can be huge.

One recently developed conformer sampling tool called CREST (Conformer-Rotamer Ensemble Sampling Tool)[15] has been used in this research. In CREST, a computationally cheap but with a decent accuracy level of theory called xTB[16]: a tight bonding semiempirical quantum chemical method is used to calculate structures, vibrations, and noncovalent interactions. In the earlier versions of CREST, users need to compose multiple runs with simulated annealing as part of the search workflow. Such a strategy was utilized in the early studies of this thesis. In the latest CREST version, users no longer need to do these multiple runs manually. Instead, these runs are constructed automatically, aiming to map out a comprehensive ensemble space, especially all the low-lying, thermally accessible conformers that commonly show up in the rotational spectra observed. These procedures are described as the MF-MD-GC algorithm[17], the major conformational search method used in this research, embedded in CREST, version 2.6.

2.5. Ab initio calculations

The term "*ab initio*" means from the first principle. The inputs in ab initio calculations are physical constants and rules, whereas empirical chemistry notions are excluded. The core of ab initio calculations is to solve the electronic Schrodinger equation with the known nuclear coordinates and the number of electrons. The Hartree-Fock (HF) method[18] solves the many-electron Schrödinger equation under the Born-Oppenheimer approximation without considering electron correlation. To properly account for intermolecular interactions, one primary interest of my research is the contribution from dispersion interactions. The Møller–Plesset (MP) perturbation theory[19] is one of the post Hartree-Fock methods that include electron correlation effects. Given the computational cost, we typically use the second-order perturbation, namely MP2. An alternative, cheaper method is Density Functional Theory (DFT)[20]. To better address the exchange and correlation terms, we typically use the hybrid functional B3LYP with empirical dispersion corrections D3BJ.[21-23]

2.6. The workflow of theoretical calculations

The usage of a pulse jet expansion dramatically enhances the sensitivity and resolution of microwave spectroscopic measurements and provides an opportunity to investigate many interesting species that are not stable under chronic conditions, such as non-covalently bonded species. Flexible molecules and their associated non-covalently bonded species tend to have many possible conformers that may be responsible for the transitions detected. For this reason, it is essential to identify all possible low energy stable structures of a species. The strategic workflow on the way to interpret experimental observations is presented in Figure 2.4. Firstly, an input structure plotted using chemical intuition is pre-optimized with a cheap forced field method. Then we apply CREST to perform Molecular Dynamics (MD) based conformational ensemble sampling. Possible molecular structures generated on the trajectory of MDs are saved and optimized with xTB. Repeating and unrealistic structures are then filtered out. The remaining conformers are ranked by their

xTB energies, included in the CREST conformer ensemble. Second, the preliminary structures identified by CREST are used as input structures for the subsequent ab initio calculations. The new ensemble is again filtered to remove repeated structures, and the resulting structures are re-ranked based on their ab initio energies. Finally, the spectroscopic constants predicted for the global minimum and other low energy conformers are used to simulate their rotational spectra and aid the experimental spectrum assignment.

Once assigned, the experimental spectroscopic constants are compared to the predicted ones to identify the carrier, i.e., a particular conformer, of a group of rotational transitions observed. There are a variety of spectroscopic constants that are used together to conclude. For example, rotational constants, relative magnitudes of the three electric dipole moment components, various hyperfine structures such as tunneling splittings and nuclear quadrupole hyperfine structures, and the related constants can all be used to verify the identity of a carrier. Often, carriers of strong transitions are identified first in a typical experiment. These usually belong to the most stable structures.

If no identification can be made, other CREST search and/or a higher level of ab initio theory are needed until the carriers of the assigned transitions are identified. However, there are cases where the current structure search flow fails to produce a suitable structure that can be used to account for the transitions assigned. In these challenging scenarios, one may use extensive isotopic data to map out an experimental molecular topology and apply this to generate a suitable structure for further theoretical calculations to predict the associated spectroscopic constants. These cases highlight some deficiencies in the current theoretical modeling and provide valuable data to improve the conformational search and other theoretical calculations. The study in Chapter 7 is one such example. Because a large number of theoretical calculations were needed, I wrote a series of python and Linux scripts to deal with CREST and Gaussian outputs. The goal is to automatically couple these two software programs for a large scale of calculations performed on supercomputers. These scripts can be found at my Github website:

https://github.com/FanXie001/MWspectroscopy/tree/master/conformational%20search

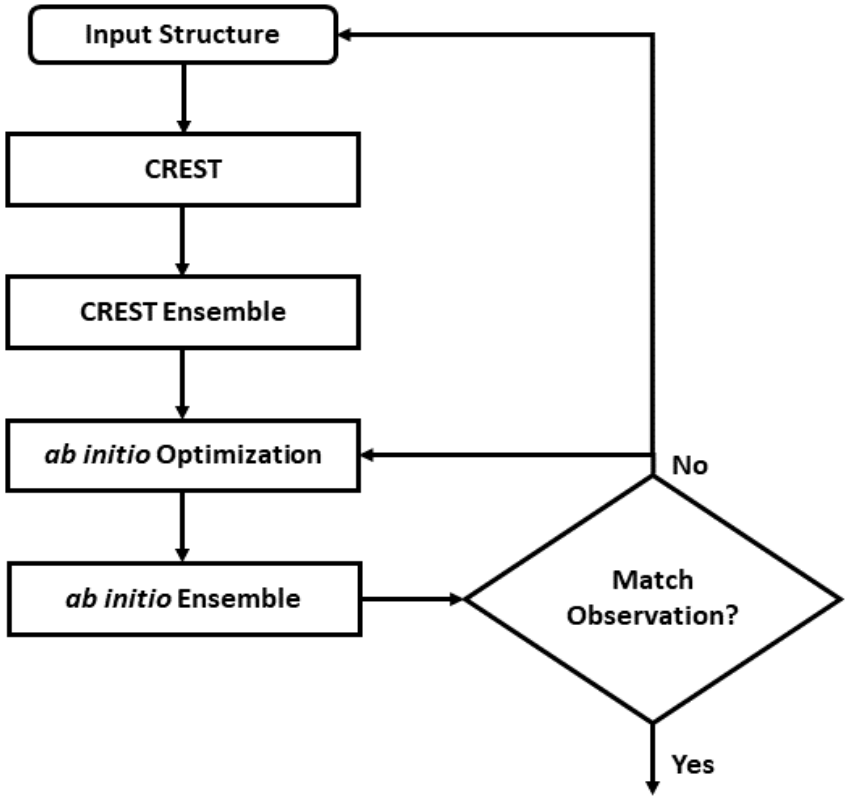

Figure 2.4. The workflow for theoretical conformational ensemble space exploration. The conformational sampling tool, CREST, is combined with the related *ab initio* calculations in the workflow.

2.7. Enantiomeric excess measurements

In many real-life applications, it is necessary to know the enantiomer excess (ee) of a chiral sample. This can be done with chiral tag CP-FTMW spectroscopy[13]. With broadband CP-FTMW spectra, there are typically dozens or even hundreds of MW transitions in one

spectrum that can be used to extract the ee value, providing a statistically averaged ee value. The procedure used is as follows.

1. A mixture containing a small amount of the targeted chiral sample and the racemic chiral tag in rare gas is prepared. A broadband MW spectrum of the mixture is measured, and the rotational spectroscopic assignments of the homochiral and heterochiral binary complexes between the sample and the tag are achieved.

2. Select, for example, 50 and 60 transitions of the homochiral and heterochiral dimers, respectively. Extract the experimental intensity ratio (r_0) for each pair. In this example, we have 50 * 60 = 3000 possible pairs.

3. Repeat steps 1 and 2 with the enantiopure (or high known ee) chiral tag. Do the measurement under the same experimental conditions as the racemic tag. Obtain the experimental intensity ratio (r_1) for the same pairs identified in Step 2.

4. For each transition pair, ee of the unknown sample is calculated using the following equations[14]:

$$R = r\_1 / r\_0 \qquad (2.24)$$

$$(1-R) / (1+R) = ee\_tag * ee\_sample \qquad (2.25)$$

The ee_tag is 1 for the enantiopure chiral tag. By considering all transition pairs, a statistically averaged ee_sample can be derived.

Similar procedures can also be applied on chiral self-tag ee measurements, where the chiral tag and the chiral sample are the same molecule. In the first step, a racemic sample is measured. In the second step, a non-racemic sample is measured. For each transition pair, ee_sample can be derived from the corresponding equations:

$$R = r\_1 / r\_0 \qquad (2.25)$$

$$(1-R) / (1+R) = (ee\_sample)^2 \quad (2.26)$$

I wrote a python script to automatically calculate ee from broadband spectra, which is at https://github.com/FanXie001/MW-spectroscopy/tree/master/ee_cal

2.8. Spectral assignment aids and fitting software

There are several publicly distributed programs available for assisting the assignments and fitting of rotational spectra, for example, AUTOFIT[11], PGOPHER[24], and JB95[25]. AUTOFIT serves as an initial transition pattern search tool if a spectrum is overwhelmed with dense transitions. In this thesis's studies, the final assignments are fit to an asymmetric top, non-rigid rotor Hamiltonian[26,27] built-in PGOPHER. XIAM[28] was used in analyzing the internal rotation of the methyl group in Chapter 3.

References

[1] A. Bauder, *Handbook of High-resolution Spectroscopy* **2011**.

[2] J. M. Brown, J. M. Brown, A. Carrington, *Rotational spectroscopy of diatomic molecules*, Cambridge University Press, **2003**.

[3] W. Gordy, R. L. Cook, *Microwave molecular spectra*, Wiley, **1984**.

[4] C. H. Townes, A. L. Schawlow, *Microwave spectroscopy*, Courier Corporation, **2013**.

[5] W. Tait, *Phys. Rev. B* **1972**, *5*, 648.

[6] J. Weiner, P.-T. Ho, *Light-matter interaction: fundamentals and applications, Vol. 1*, John Wiley & Sons, **2008**.

[7] G. B. Park, R. W. Field, *J. Chem. Phys.* **2016**, *144*, 200901.

[8] D. Schmitz, V. Alvin Shubert, T. Betz, M. Schnell, *J. Mol. Spectrosc.* **2012**, *280*, 77-84.

[9] W. Gordy, *Rev. Mod. Phys.* **1948**, *20*, 668.

[10] G. G. Brown, B. C. Dian, K. O. Douglass, S. M. Geyer, S. T. Shipman, B. H. Pate, *Rev. Sci. Instrum.* **2008**, *79*, 053103.

[11] N. A. Seifert, I. A. Finneran, C. Perez, D. P. Zaleski, J. L. Neill, A. L. Steber, R. D. Suenram, A. Lesarri, S. T. Shipman, B. H. Pate, *J. Mol. Spectrosc.* **2015**, *312*, 13-21.

[12] B. A. McGuire, P. B. Carroll, R. A. Loomis, I. A. Finneran, P. R. Jewell, A. J. Remijan, G. A. Blake, *Science* **2016**, *352*, 1449-1452.

[13] S. R. Domingos, C. Pérez, M. D. Marshall, H. O. Leung, M. Schnell, *Chem. Sci.* **2020**.

[14] B. H. Pate, L. Evangelisti, W. Caminati, Y. Xu, J. Thomas, D. Patterson, C. Perez, M. Schnell, in *Chiral Analysis (Second Edition)* (Ed.: P. L. Polavarapu), Elsevier, **2018**, pp. 679-729.

[15] P. Pracht, F. Bohle, S. Grimme, *Phys. Chem. Chem. Phys.* **2020**, *22*, 7169-7192.

[16] C. Bannwarth, S. Ehlert, S. Grimme, *J. Chem. Theory Comput.* **2019**, *15*, 1652-1671.

[17] S. Grimme, *J. Chem. Theory Comput.* **2019**, *15*, 2847-2862.

[18] C. F. Fischer, **1977**.

[19] in *Ideas of Quantum Chemistry* (Ed.: L. Piela), Elsevier, Amsterdam, **2007**, pp. 498-566.

[20] in *Ideas of Quantum Chemistry* (Ed.: L. Piela), Elsevier, Amsterdam, **2007**, pp. 567-614.

[21] S. Grimme, J. Antony, S. Ehrlich, H. Krieg, *J. Chem. Phys.* **2010**, *132*, 154104.

[22] S. Grimme, R. Huenerbein, S. Ehrlich, *ChemPhysChem* **2011**, *12*, 1258-1261.

[23] S. Grimme, S. Ehrlich, L. Goerigk, *J. Comput. Chem* **2011**, *32*, 1456-1465.

[24] C. M. Western, *J. Quant. Spectrosc. Radiat. Transf.* **2017**, *186*, 221-242.

[25] D. F. Plusquellic, R. D. Suenram, B. Maté, J. O. Jensen, A. C. Samuels, *J. Chem. Phys.* **2001**, *115*, 3057-3067.

[26] J. K. G. Watson, *J. Chem. Phys.* **1967**, *46*, 1935-1949.

[27] J. K. G. Watson, *Mol. Phys.* **1968**, *15*, 479-490.

[28] H. Hartwig, H. Dreizler, *Zeitschrift für Naturforschung A* **1996**, *51*, 923-932.

Chapter 3

The Rich Conformational Landscape of Perillyl Alcohol Revealed by Broadband Rotational Spectroscopy and Theoretical Modelling [a]

[a] This study has been published. Fan Xie, Nathan Seifert, Matthias Heger, Javix Thomas, Wolfgang Jäger and Yunjie Xu. The rich conformational landscape of perillyl alcohol revealed by broadband rotational spectroscopy and theoretical modelling. *Phys. Chem. Chem. Phys.* **2019**, 21, 15408-15416

3.1. Introduction

Perillyl alcohol (PA) is a naturally occurring, chiral, dietary monoterpene that can be extracted from various plants, such as lavender, peppermint and cherries. PA has been shown to act as a chemo-preventive and chemotherapeutic agent in multiple animal studies and its application to human cancer treatment has been explored.[1] Generally, it is believed that PA inhibits tumor development and growth by taking part in various cellular metabolic pathways, such as interactions with Na/K-ATPase protein, phosphatidyl and Ras-related proteins, although the detailed role played by PA is still an active research topic.[2,3] The structural formula of PA is shown in Figure 3.1. The PA molecule contains a cyclohexene ring and three units, i.e. –OH, –CH_2OH, and –$C(CH_2)CH_3$, which can rotate fairly freely about the O2-C4, C4-C5, and C10-C11 bonds, respectively. The three dihedral angles associated with these rotational motions are indicated in Figure 3.1. These relatively free rotation motions, in addition to the ring puckering motion of the cyclohexane ring generate a complex conformational landscape for PA. A comprehensive, detailed study of the conformational distribution of PA may facilitate our understanding of the structural properties of PA.

Rotational spectroscopy coupled with a molecular jet expansion has been used extensively to extract structural and energetic information about conformers of organic molecules and their complexes in the gas phase.[4,5,6] Although Fraser and co-workers carried out pioneering work in identifying conformationally rich molecules, such as 1-octene,[7] already in the early 2000s using a cavity-based Fourier transform microwave (FTMW) spectrometer, very few reports in this area with the cavity-based technique have appeared in the last twenty years or so. The advent of the chirped pulse Fourier transform microwave (CP-FTMW)[8] technique has made it possible to record a broadband spectrum (with typical frequency coverage of several GHz) in one molecular jet pulse. As a result, one can obtain a survey broadband

spectrum with much more consistent relative intensities using a CP-FTMW spectrometer than using a cavity-based FTMW instrument, although the latter usually offers better resolution. This important advantage has significantly advanced the capability to explore complicated conformational landscapes. For example, Seifert et al. applied CP-FTMW spectroscopy to investigate the conformational space of 1-hexanal and reported experimental detection of 12 out of 38 possible conformers of 1-hexanal.[9] Schnell and co-workers identified 15 conformers of citronellal, an acyclic monoterpene, experimentally out of the 17 conformers predicted within a 6 kJ mol^{-1} energetic span.[10] The citronellal conformations were generated by scanning five different heavy-atom dihedral angles, where the conformational interconversion barriers are generally high enough to avoid efficient conformational cooling in a jet expansion. More recently, Loru et al. reported conformational flexibility of limonene oxide,[11] a molecule which shares some structural similarity to PA, and identified five conformers experimentally. PA is of significant interest in this respect since it is anticipated to have a rich conformational landscape associated with not only the heavy-atom dihedral angles, but also the cyclohexene ring puckering motions and *cis*- or *trans*-COOH configurations.

In the current study, we employed both cavity-based and CP-FTMW spectrometers to record rotational spectra of PA. Extensive theoretical searches were conducted to identify all possible PA conformers within an energetic span of up to 20 kJ mol^{-1}. To aid the spectroscopic assignments of the PA conformers, their relative stabilities and interconversion barriers were also explored using ab initio calculations. There are two reasons to keep this energetic window wider than the usual few kJ mol^{-1}. First, with the high sensitivity achieved with CP-FTMW spectroscopy, it is increasingly possible to detect higher energy conformers as demonstrated in the recent studies of tetrahydro-2-furoic acid[12] and citronellal.[10] Second, it has been reported recently that high energy conformers may become dominant players in larger molecular aggregates[13,14,15] or in hydrated clusters. For example, in the 2-

fluoroethanol (FE) tetramer,[13] one conformer consisting of four highest energy FE subunits was predicted to have similar energy as the most stable one consisting only of the most stable FE subunits. In the case of hexafluoroisopropanol, the chiral trimer made of three less stable chiral subunits was detected experimentally, despite a cumulative energy penalty of 15 kJ mol^{-1} and a strong preference for the achiral subunit in isolated or dimerized form in a jet expansion.[15] It is of great interest to follow the change in conformational preferences as one moves from an isolated molecule to increasingly large aggregates or hydrated clusters, in order to gain insight into their links to properties of condensed phases. Finally, detection of a larger number of higher energy conformers would open up the opportunity to comprehensively assess the influence of conformational cooling on the experimental conformational abundances. As one may expect, different cooling paths and efficiencies in a jet expansion may alter the experimental conformational abundances, in comparison to their Boltzmann factors based on the relative energies. This issue is of current interest for benchmarking theoretical energy calculations using experimental abundances.[16]

3.2. Results and discussion

3.2.1. Conformational searches

To identify possible conformers, we utilized two different approaches. In the first one, we considered all possible structural factors which contribute to the conformational structural diversity of PA. We scanned the three dihedral angles: Φ_1 / H3-C4-O2-H1, Φ_2 / C6-C5-C4-O2 and Φ_3 / C12-C11-C10-C7 shown in Figure 3.1, separately. The 1D potential energy surface (PES) scans along Φ_1, Φ_2, and Φ_3 (vide infra) identify three low energy minima at ~180°, +60° and -60° in each scan, which are labeled as T, G+ and G- (see Figure 3.1), respectively. We label each conformer with three letters in the order of $\Phi_1\Phi_2\Phi_3$, for example, G^+TG^+. Further conformational flexibility comes from the $-C(CH_2)CH_3$ group which may take on an equatorial (Eq) or axial (Ax) configuration. As such, we have $3^3 \times 2 = 54$ possible minima. While cyclohexane has a strong preference for the chair conformation because each bond of its ring can adopt a staggered conformation, the cyclohexene ring has a double bond and adopts an eclipsed conformation at that bond. We therefore also consider the two known configurations of the cyclohexene ring: half-chair and boat,[17] and this results in a total of 108 possible minima.

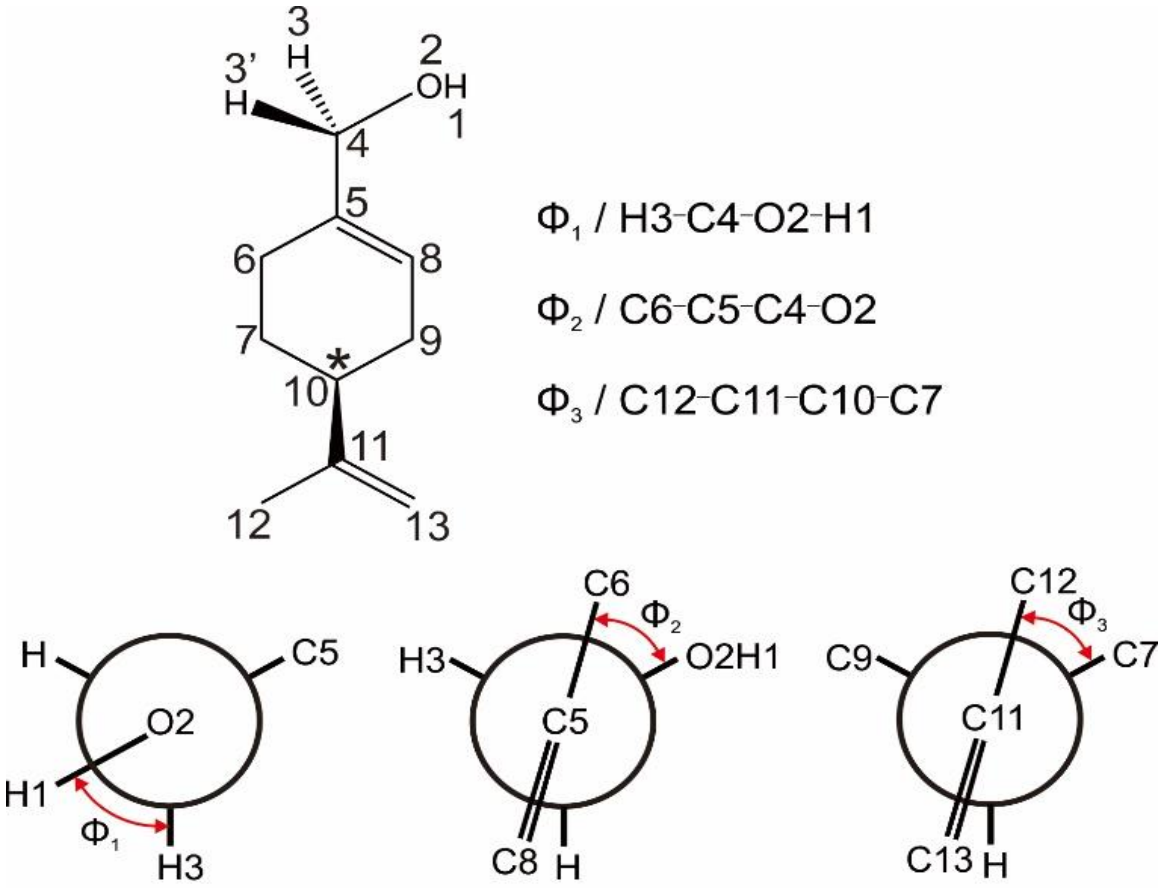

Figure 3.1. Top: structural formula of (S)-PA and the three flexible dihedral angles, Φ_1 / H3-C4-O2-H1, Φ_2 / C6-C5-C4-O2 and Φ_3 / C12-C11-C10-C7 used in the conformational searches. "*" indicates the stereogenic center. Bottom: the Newman projections of the three flexible dihedral angles, Φ_1, Φ_2, Φ_3. When Φ_i (i = 1-3) = 60°, -60°, and 180° are labelled as G+, G-, and T, respectively.

For the 54 conformers associated with the half-chair cyclohexene ring configuration, all structures were further optimized at the DFT level and confirmed to be true minima. Their relative raw and zero-point energy (*ZPE*) corrected energies, rotational constants, and electric dipole moment components at the B3LYP-D3(BJ)/def2-TZVP and LMP2/aug-cc-pVQZ levels of theory are compared in Table 3.1 for the first 25 conformers, while a complete list for all 54 conformers is given

in Table 3.S1, Supporting Information (SI). The relative free energies at 350 K at the B3LYP-D3(BJ)/def2-TZVP level are also provided in Table 3.S1.

Table 3.1. The theoretical raw ΔD_e and *ZPE* corrected ΔD_0 relative dissociation energies (in kJ mol^{-1}), rotational constants (in MHz) and electric dipole moment components (in Debye) of the first 25 half-chair conformers calculated at the B3LYP-D3(BJ)/def2-TZVP and LMP2/Aug-cc-pVQZ levels of theory

B3LYP-D3(BJ)/def2-TZVP										LMP2/aug-cc-pVQZ									
Conformer[a]	ΔD_e	ΔD_0	*A*	*B*	*C*	$\lvert\mu_a\rvert$	$\lvert\mu_b\rvert$	$\lvert\mu_c\rvert$	$\lvert\mu\rvert$	Conformer[a]	ΔD_e	ΔD_0[b]	*A*	*B*	*C*	$\lvert\mu_a\rvert$	$\lvert\mu_b\rvert$	$\lvert\mu_c\rvert$	$\lvert\mu\rvert$
Eq-TG-G+	0.0	0.0	2790	520	502	1.1	0.7	0.8	1.5	**Eq-TG-G+**	0.0	0.0	2800	524	505	1.2	0.8	0.7	1.6
Eq-TG-T	1.1	1.0	2829	531	481	1.2	1.2	0.3	1.7	**Ax-G+G+G-**	0.1	0.6	2039	669	643	1.3	0.8	1.0	1.8
Eq-G+G+G+	1.2	1.1	2722	519	507	1.2	1.0	0.3	1.6	**Eq-TG-T**	0.7	0.7	2836	535	484	1.3	1.2	0.2	1.8
Eq-TG-G-	2.2	2.0	2794	529	483	1.2	0.6	0.3	1.4	**Eq-G+G+G+**	1.2	1.1	2716	523	512	1.3	1.0	0.4	1.7
Eq-TTG+	2.7	2.2	2774	519	491	1.0	0.6	0.6	1.3	**Ax-TG-G-**	0.7	1.4	1687	758	714	1.5	1.2	0.3	1.9
Eq-G+G+T	2.4	2.3	2702	531	490	1.2	1.3	0.1	1.8	**Eq-G+G+T**	2.0	1.9	2696	535	494	1.3	1.2	0.2	1.8
Ax-G+G+G-	1.9	2.4	2122	644	620	1.3	0.6	1.2	1.9	Eq-TG-G-	2.2	2.1	2803	534	485	1.2	0.7	0.3	1.4
Eq-G+G+G-	3.3	3.2	2642	539	489	1.1	0.6	0.5	1.3	**Eq-TTG+**	3.3	2.8	2777	523	494	1.1	0.7	0.7	1.5
Eq-TTT	3.8	3.2	2729	534	474	1.1	0.0	1.3	1.7	Eq-G+G+G-	3.3	3.2	2631	545	492	1.2	0.3	0.7	1.4
Ax-TG-G-	2.6	3.2	1741	725	687	1.5	1.2	0.3	1.9	**Ax-G+TG-**	3.4	3.4	1961	680	658	1.9	0.5	0.4	2.0
Eq-G+TG+	3.8	3.3	2784	518	490	0.9	0.8	1.3	1.8	**Eq-TTT**	4.0	3.5	2731	538	477	1.1	0.1	1.2	1.6
Eq-G+TT	4.7	4.1	2744	531	473	0.9	0.6	0.5	1.2	Eq-G-G-G+	4.5	3.5	2822	525	504	0.8	0.6	0.7	1.2
Eq-TTG-	5.1	4.5	2794	528	475	1.2	1.1	1.0	1.9	Eq-G+TG+	4.4	3.9	2788	522	494	1.0	0.9	1.3	1.9
Ax-G+TG-	4.6	4.6	2037	655	632	1.9	0.5	0.3	2.0	Ax-G-G+G-	4.6	4.2	2011	676	648	0.0	0.1	1.0	1.0
Eq-G-G-G+	5.6	4.6	2814	521	500	1.0	0.4	0.7	1.3	Eq-G-G+G+	5.3	4.3	2738	525	511	0.9	0.4	1.5	1.8
Eq-G+TG-	6.0	5.4	2822	527	472	1.0	0.8	0.9	1.6	Ax-TTG-	4.3	4.3	2023	668	649	1.1	1.5	1.0	2.1
Ax-TTG-	5.4	5.5	2109	643	624	1.1	1.5	1.2	2.2	Eq-G-G-T	5.4	4.4	2862	536	483	0.7	1.1	1.2	1.8
Eq-G-G+G+	6.6	5.6	2747	520	506	0.9	0.3	1.6	1.9	Eq-G+TT	4.9	4.4	2746	536	477	1.0	0.7	0.6	1.4
Eq-G-G-T	6.9	5.9	2856	531	480	0.8	1.0	1.3	1.8	Eq-G-TG+	6.5	5.0	2786	525	496	1.0	1.5	0.2	1.8
Eq-G+G-G+	7.1	6.0	2817	516	496	0.8	0.7	0.9	1.4	Eq-G-G+T	5.9	5.0	2724	537	494	0.9	0.3	1.0	1.4
Eq-TG+G+	6.8	6.1	2746	518	502	1.0	0.8	1.5	2.0	Eq-TTG-	5.6	5.0	2791	533	477	1.3	1.1	0.9	1.9
Eq-G-TG+	7.8	6.2	2785	521	492	1.1	1.5	0.4	1.9	Eq-G-TT	7.1	5.6	2740	541	479	1.0	1.1	0.5	1.6

Eq-G-G+T	7.5	6.6	2732	531	489	1.0	0.2	0.9	1.4	Ax-G-TG-	6.5	5.6	2004	676	655	0.2	1.5	0.9	1.8
Eq-G-G-G-	8.0	6.9	2808	530	482	0.8	0.4	1.5	1.7	Eq-G-G-G-	6.8	5.4	2815	535	485	0.7	0.2	1.5	1.7
Eq-TG+T	7.7	7.0	2730	528	486	0.9	0.8	0.5	1.3	Ax-G-G-G-	6.3	5.7	1733	744	701	0.9	0.8	0.9	1.5

[a] The ordering is based on ΔD_0. The bolded conformers are the ones which survive the conformational conversion in a jet expansion. Those in red are the ones observed experimentally. See the main text for discussions.

[b] The *ZPE* corrections were taken from the B3LYP-D3(BJ) calculations.

It is immediately apparent that the relative stability orderings obtained at the DFT and LMP2 levels differ from each other. While the DFT calculations suggest that the first six low energy conformers are all equatorial, the LMP2 calculations show a more even presence of both axial and equatorial configurations. The discrepancy in the predicted energy ordering for the axial versus equatorial conformers by the MP2 and DFT methods was reported before, for example, in limonene oxide.[11] In addition, some predicted rotational constants of the same axial conformer also differ noticeably between the DFT and LMP2 calculations. We cannot judge a priori which conformers will be observed experimentally; this can only be resolved through experiment. This situation highlights the importance of using experimental data to benchmark theoretical calculations.

In the second approach, we utilized the GFN-xTB program.[42,43] With any particular starting point, we were able to recover about 80% of the 54 structures identified in the manual scans using the "Crest" program provided with the latest version of the GFN-xTB package.[43] Our tests show that one would still need to try with various input parameters in order to recover all structures since these molecular dynamics runs may not generate exactly the same outcome even with identical input parameters. We recognized in further DFT calculations and GFN-xTB searches that the conformers with the boat ring configuration are substantially higher in energy (~30 kJ mol^{-1}) and many of them are not true minima. For conciseness, this group

of structures was not further considered in the current study. Nine optimized Eq-XXG+ conformational geometries, where the $-C(CH_2)CH_3$ group adopts the G+ configuration, are presented in Figure 3.2. The other two labels, XX, indicate the configurations of -OH and $-CH_2OH$, which can be T, G+ and G-. The remaining 18 equatorial structures which adopt the T or G- arrangements in Φ_3 are given in Figure 3.S1. Similarly, there are 27 axial geometries, analogous to the equatorial ones. The nine conformers of Ax-XXG+ are depicted in Figure 3.3, while the others, Ax-XXT and Ax-XXG-, are given in Figure 3.S2.

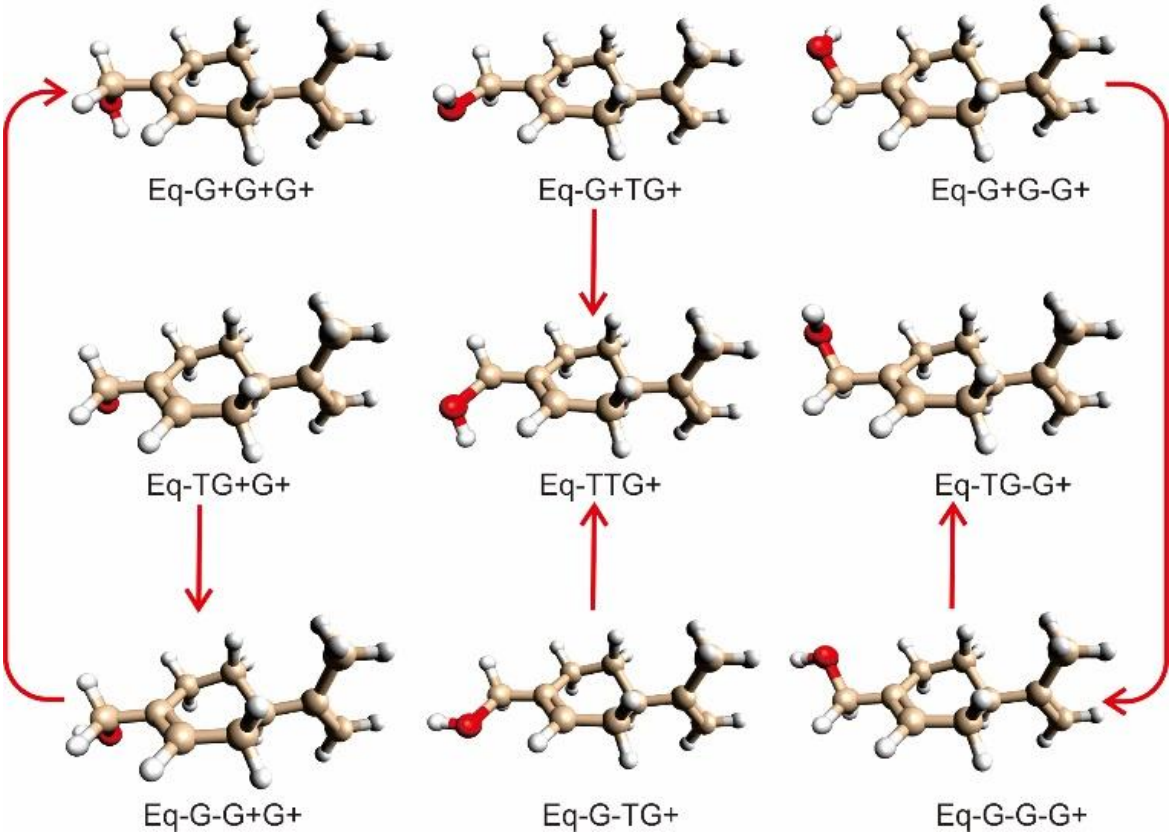

Figure 3.2. Optimized geometries of the nine Eq-XXG+ conformers where X can take on G+, T, and G-. The red arrows indicate that the corresponding conformational barriers are low enough to allow nearly complete conformational cooling of the higher energy conformers in a jet expansion. See the main text for discussion.

A closer examination of these structures indicates that the motions associated with the –OH direction (Φ_1) and the rotation of the $–CH_2OH$ group (Φ_2) appear to be highly cooperative. The rotation of the $–CH_2OH$ group brings the –OH group in close contact with the cyclohexene ring. Consequently, the –OH group must modify its direction to minimize the steric repulsion between itself and the ring. The situation is illustrated in Figure 3.S3, where the results from NCI analyses show that the Eq-TG+G+ and Eq-G-TG+ conformers are less stable than Eq-G+G+G+, primarily due to the more severe steric repulsion mentioned above. On the other hand, the preferred equatorial orientation of $–C(CH_2)CH_3$ appears to be more or less independent from the $–CH_2OH$ and –OH orientation since they are sufficiently far away (~5.9 Å). For example, in Eq-XXG+, the three most stable conformers, in order of decreasing relative stability, are XX=G+G+, TT, and TG-. This ordering remains the same for the Eq-XXT and Eq-XXG-, Ax-XXG+, and Ax-XXT series, whereas for the Ax-XXG- series, the stability ordering is G+G+, G+T, and TG-, where X can take on G+, T, and G-. The red arrows indicate that the corresponding conformational barriers are low enough to allow nearly complete conformational cooling of the higher energy conformers in a jet expansion. See the main text for discussion.

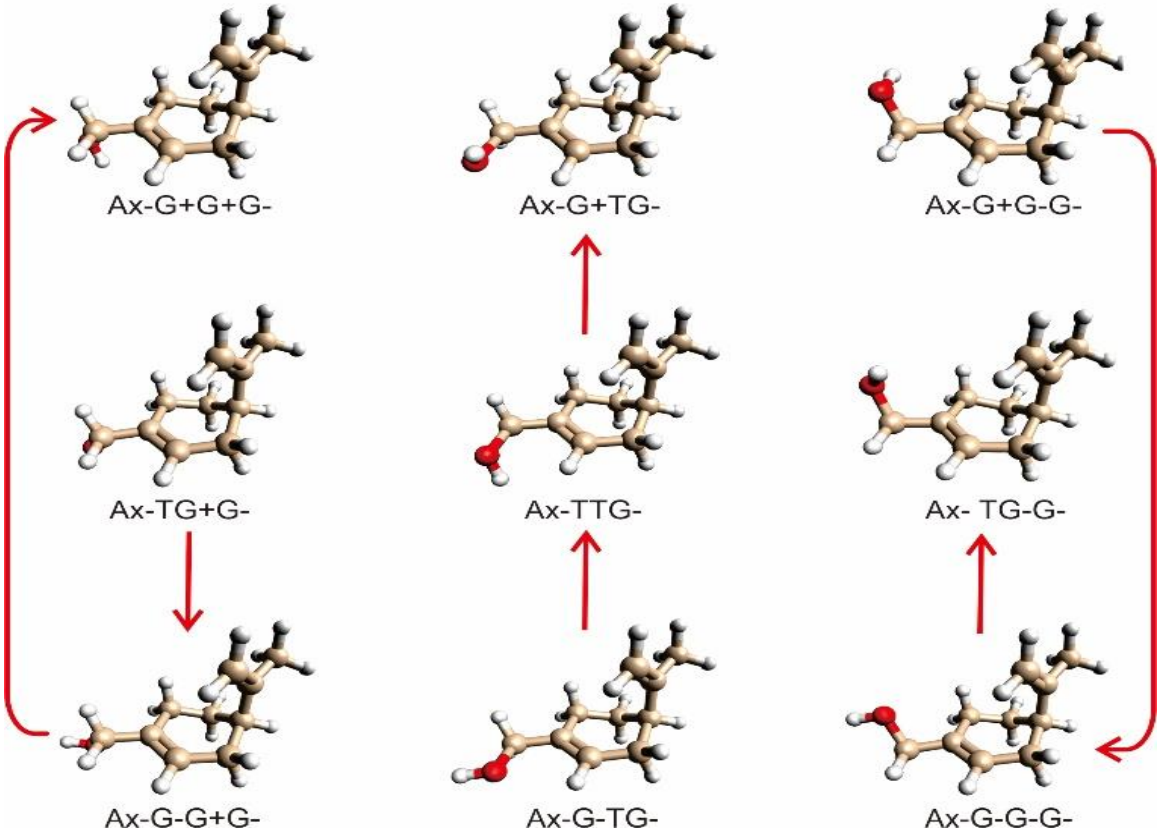

Figure 3.3. Optimized geometries of the nine Ax-XXG+ conformers

3.2.2. Conformational conversion barriers

Our initial attempt to assign the fairly dense microwave spectrum was only partially successful because of the large number of possible conformers within a 10 kJ mol^{-1} energy window (see Table 3.1) and the uncertainty in their stability ordering. It became obvious that further theoretical studies to estimate the conformational interconversion barriers and whether the *ZPE* levels are above or below the respective barriers would be crucial to achieve experimental spectral assignments.

Starting from Eq-G+G+G+, we performed 1D PES scans along the three dihedral angles shown in Figure 3.1, i.e. Φ_1, Φ_2, and Φ_3. The resulting PES scans and the *ZPE* corrected barriers are depicted in Figure 3.4(a), (b) and (c). The existence of these transition states was confirmed with intrinsic reaction coordinate (IRC) calculations.[18] As can be seen in

Figure 3.4(a), conformers Eq-TG+G+ and Eq-G-G+G+ are in fairly shallow potential wells where the conversion barriers to a nearby lower energy conformer are only 0.5 and 2.4 kJ mol^{-1}, respectively. On the other hand, conformer Eq-G+G+G+ is trapped in a relatively deeper potential well with a 7.1 kJ mol^{-1} conversion barrier. In a free jet expansion, the Ne carrier gas may collide with the target molecule and cool it into a lower energy conformation. One main deciding factor for the efficiency of such a cooling process is the conversion barrier. Earlier studies suggest an empirical upper limit of ~4.8 kJ mol^{-1} for an efficient conformational cooling.[19] Along the –OH rotation coordinate, Φ_1, we expect therefore only to observe Eq-G+G+G+, since Eq-G-G+G+ and Eq-TG+G+ have efficient cooling paths into this minimum. In Figure 3.4(b), the three Eq-G+G+G+, Eq-G+TG+ and Eq-G+G-G+ conformers are shown in deeper wells with conformational conversion barriers of 12.5, 10.1 and 6.5 kJ mol^{-1}, respectively. One can anticipate that all three of them are detectable in a jet expansion.

As discussed before, the preferred –OH direction is dependent on the orientation of the $–CH_2OH$ group. To verify and to better visualize this claim, a 2D PES scan along Φ_1 and Φ_2 coordinates was also computed and the result is depicted in Figure 3.5. It is clear from Figure 3.5 that the conversion barriers associated with Φ_1, the –OH rotation, are generally low, whereas such barriers are higher along Φ_2, the $–CH_2OH$ rotation, consistent with the conclusions drawn from the analysis of the 1D-PES scans. Possible efficient cooling paths are summarized with arrows in Figure 3.2 and 3 for the Eq-XXG+ and Ax-XXG+ series of conformers, respectively. One main consequence of the above analyses is that the number of detectable conformers in a jet now decreases to 54/3 = 18.

In Figure 3.4(c), the 1D PES scan along Φ_3, the $–CCH_2CH_3$ rotation, with Eq-G+G+G+ as the starting point, is presented. The conversion barrier from the higher energy conformer Eq-G+G+G- to the lower one, Eq-G+G+T, is 2.0 kJ mol^{-1}. Therefore, only two (Eq-G+G+G+ and Eq-G+G+T) out of three conformers are expected to be detectable in a jet. For the corresponding axial conformers, a similar

1D PES scan along Φ_3 is shown in Figure 3.4(d). Again, only two (Ax-G+G+G- and Ax-G+G+G+) out of three conformers are expected to be detectable in a jet. With all the above considerations, the number of conformers which may be detected further decreases to 18×(2/3) = 12. This includes six equatorial and six axial conformers which are bolded in Table 3.S1 and nine of them are listed in Table 3.1.

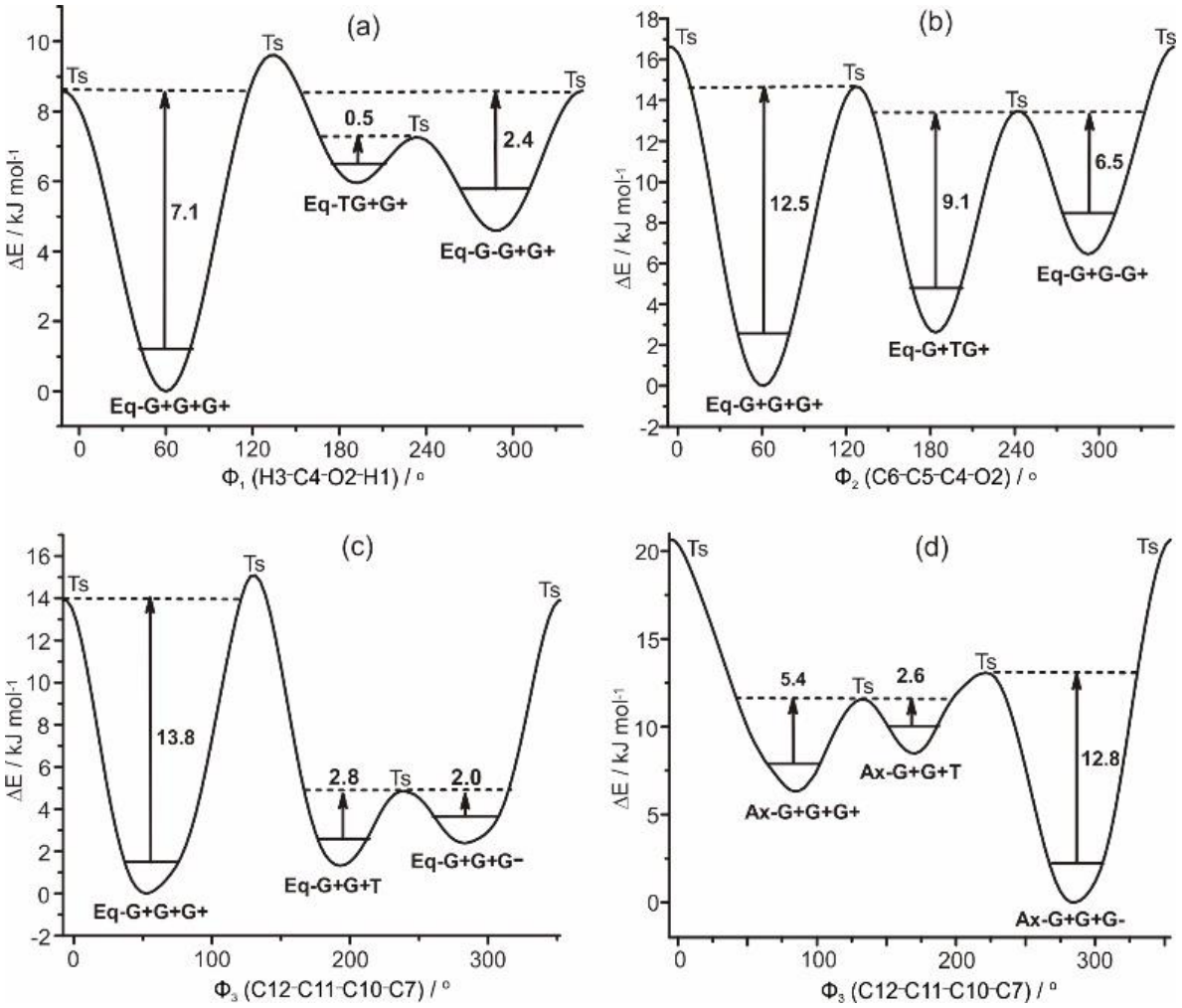

Figure 3.4. 1D potential energy scans and *ZPE* corrected barriers calculated at the B3LYP-D3(BJ)/6-311++G(2d,p) level of theory, along (a) Φ_1, the –OH group rotation coordinate, (b) Φ_2, the $-CH_2OH$ group rotation coordinate, and Φ_3, the $-C(CH_2)CH_3$ group rotation coordinate for the equatorial (c) and the axial (d) geometries. For each scan, 100 relaxed single point energy calculations distributed evenly along each rotation coordinate were performed.

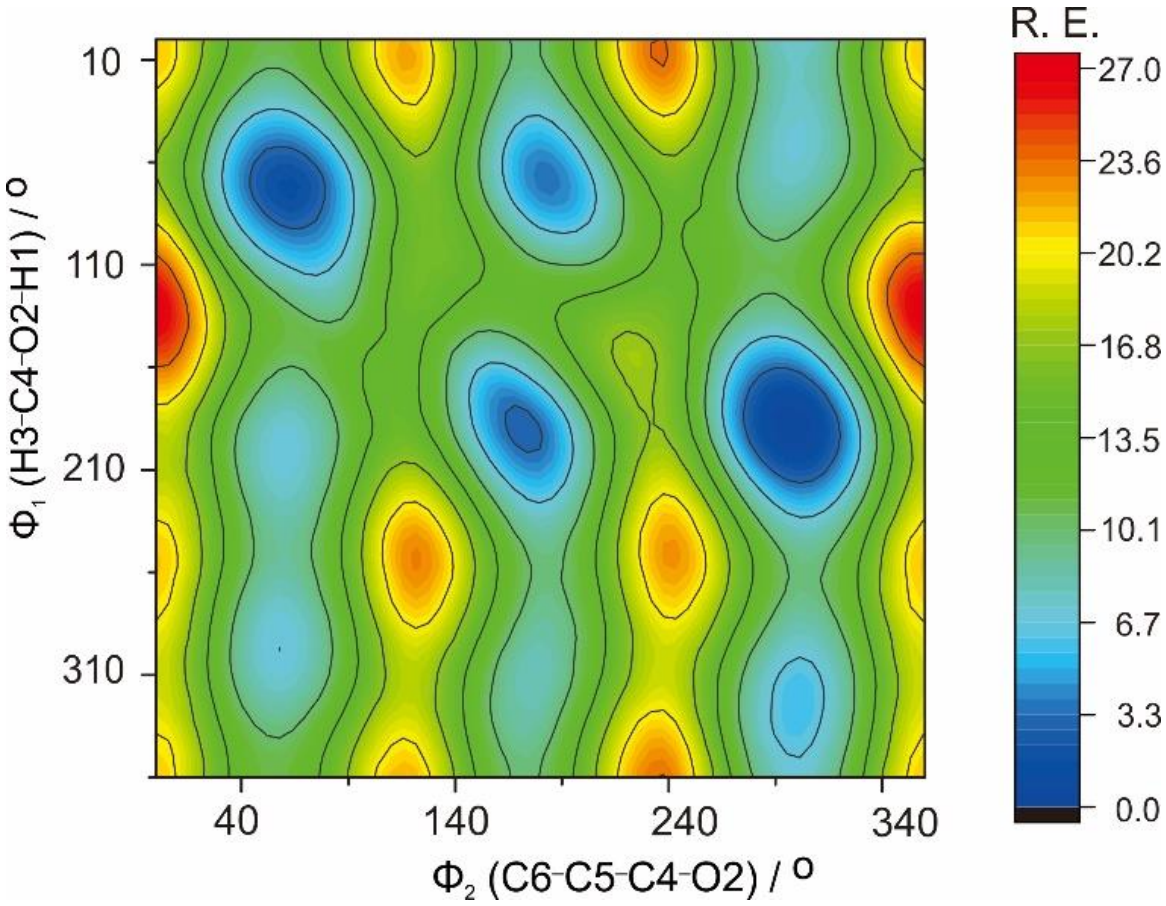

Figure 3.5. A 2D PES contour map along Φ_1 and Φ_2, calculated at the B3LYP-D3/def2-TZVP level of theory using the MOLPRO package. 12 single point energy

calculations were performed for each dihedral angle scan. In total, 144 energy points are included to construct the map. 'R.E.' stands for relative energy in kJ mol^{-1} with respect to the global minimum conformer, Eq-TG-G+. The nine minima (blue wells) can be easily identified in the 0-360° square.

3.2.3. Spectroscopic analyses and conformational assignments

With the greatly reduced number of detectable conformers, it was easier to sort out the spectroscopic assignments in the CP-FTMW spectrum. The 12 possible PA candidates can be roughly divided into two groups according to their relative energies. Based on both DFT and LMP2 calculations, the first 8 (6 equatorial + 2 axial) conformers have relative energies lower than 4 kJ mol^{-1}, whereas the next 4 (all axial) conformers have relative energies in the range of ~5-12 kJ mol^{-1} (see Table 3.S1). The rotational transition patterns were predicted using the *ab initio* rotational constants and permanent electric dipole moment components using the Pgopher program[20] and were used to guide the assignments.

The axial and equatorial conformers have very different rotational constants. Six sets of rotational transitions observed have their *A*, *B* and *C* values matching generally those of equatorial conformers, while two sets match those of axial conformers. Further assignment to individual conformers was achieved by comparing the values of experimental rotational constants and the relative magnitude of dipole moment components (see Table 3.2), with those predicted theoretically. Overall, the best matches are with those predicted in the first group of

8 conformers, whereas the next 4 were not observed, most likely because of their low abundances, a subject which will be further discussed in the next section.

Table 3.2. Experimental spectroscopic parameters of the eight observed conformers of PA

Conformers	Eq-TG-G+	Eq-TG-T	Eq-G+G+G+	Eq-G+G+T
A /MHz	2780.2190(60)[a]	2816.2320(33)	2699.13515(77)	2680.1160(84)
B /MHz	518.39067(79)	529.03099(82)	518.52042(76)	529.91347(49)
C /MHz	500.04762(88)	479.67698(64)	506.19067(74)	489.63439(48)
Δ*J* /kHz	-0.026(23)	-0.020(13)	-[b]	-
Δ*K* /kHz	36(12)	-1.22(65)	-	-
δ*j* /kHz	-0.025(21)	0.016(10)	0.035(16)	-
δ*k* /kHz	-	-	-	-
V_3[c] /kJ mol^{-1}	7.08(73)	7.03(21)	7.24(48)	7.45(22)
ε[c] /rad	2.42(36)	1.8(12)	2.3(12)	2.2(12)
δ[c] /rad	1.79(14)	1.09(9)	1.13(19)	2.14(12)
N[d]	52	32	36	30
σ[e] /kHz	4.7	4.7	4.9	3.6
Obs. dipoles[f]	$u_a > u_b \geq u_c$	$u_a \approx u_b > u_c$	$u_a > u_b \geq u_c$	$u_a \geq u_b$ no u_c
Conformers[g]	Eq-TTG+	Ax-G+G+G-	Eq-TTT	Ax-TG-G-
A /MHz	2754.7232(38)	2055.0424(13)	2709.4534(27)	1703.7443(43)
B /MHz	518.09447(73)	653.45314(40)	532.94813(44)	735.4097(15)
C /MHz	489.99590(61)	628.52250(39)	473.09342(21)	694.8213(14)
N	18	25	17	16

σ /kHz	8.1	8.3	6.1	12.1
Obs. dipoles[f]	$u_a > u_b \approx u_c$	$u_a \geq u_c > u_b$	$u_c \geq u_a$ no u_b	$u_a > u_b$ no u_c

In addition to the eight sets of rotational transitions discussed above, we identified two additional sets of rotational transitions in the assignment process. These lines are of similar intensity as some of the less stable PA conformers detected. Although the fitted *B* and *C* rotational constants are somewhat similar to those of the equatorial PA conformers, the *A* rotational constants are noticeably larger and the relative magnitudes of *a*-, *b*-, and *c*-type transitions do not agree well with any of the possible PA candidates. These two additional sets of transitions were later identified as belonging to the two equatorial conformers of perillaldehyde, which have been reported before.[21] Perillaldehyde is likely a residual impurity in PA since it is readily converted to PA and may have been used as a precursor in the production process.

Further measurements were carried out in the 8.0-16.0 GHz region using a cavity-based FTMW instrument. In particular, we were able to measure some higher K transitions of the 4 stronger conformers: Eq-TG-G+, Eq-G+G+G+, Eq-TG-T and Eq-G+G+T. Interestingly, additional splittings were detected in these higher K transitions. The patterns detected appear to be consistent with a methyl group internal rotation. In order to analyze the splittings in detail, theoretical scans were done to obtain predictions of these three-fold methyl internal rotation barriers and the XIAM internal rotation program was used to predict the splitting patterns and to fit the observed transitions of these 4 stronger conformers.[22,23] For the four weaker conformers, these higher K transitions could not be detected due to low intensity. Since very few transitions observed for these four weaker conformers in the low frequency region show such splitting, we applied the Pgopher program to fit the observed transitions to Watson A-reduction semi-rigid rotor Hamiltonian.[24] The measured transition frequencies, together with the quantum number assignments,

are listed in Tables 3.S2-S9, SI. All fitted spectroscopic parameters obtained from the XIAM internal rotation fits and the Pgopher semi-rigid rotor fits, are summarized in Table 3.2. The methyl internal rotation barriers obtained are all about 7 kJ mol^{-1}, similar to the predicted values.

For the eight observed conformers, the predicted permanent electric dipole moment components are very consistent between the B3LYP-D3(BJ) and LMP2 calculations, and in general with the experiment (Table 3.2). The percentage differences between the experimental and theoretical (both DFT and LMP2) rotational constants of the eight observed conformers are compared in Table 3.S10. For the equatorial conformers, the percentage differences are about 0.4% and 0.9% at the B3LYP-D3(BJ) and the LMP2 levels, respectively, whereas the corresponding values are 1.8% and 2.0% for the axial conformers. Very similar percentage errors of 0.9% and 3% were previously reported for the equatorial and axial conformers of limonene oxide, respectively, at the MP2/6-311++G(d,p) level.[11] Overall, the rotational constants and therefore the geometries of the equatorial conformers are better predicted than those of the axial conformers at both levels of theory, similar to the case of limonene oxide where several DFT functionals and the MP2 method were used with the 6-311++G(d,p) and aug-cc-pVTZ basis sets.[11] Since the orientation of the $–C(CH_2)CH_3$ group in the axial conformers is very sensitive to its long-range interactions with the six-membered ring, whereas in the equatorial conformers these two functional groups are far apart, the noticeably poorer theoretical performance for the axial versus equatorial conformers highlights the challenge in capturing such long-range NCI accurately.

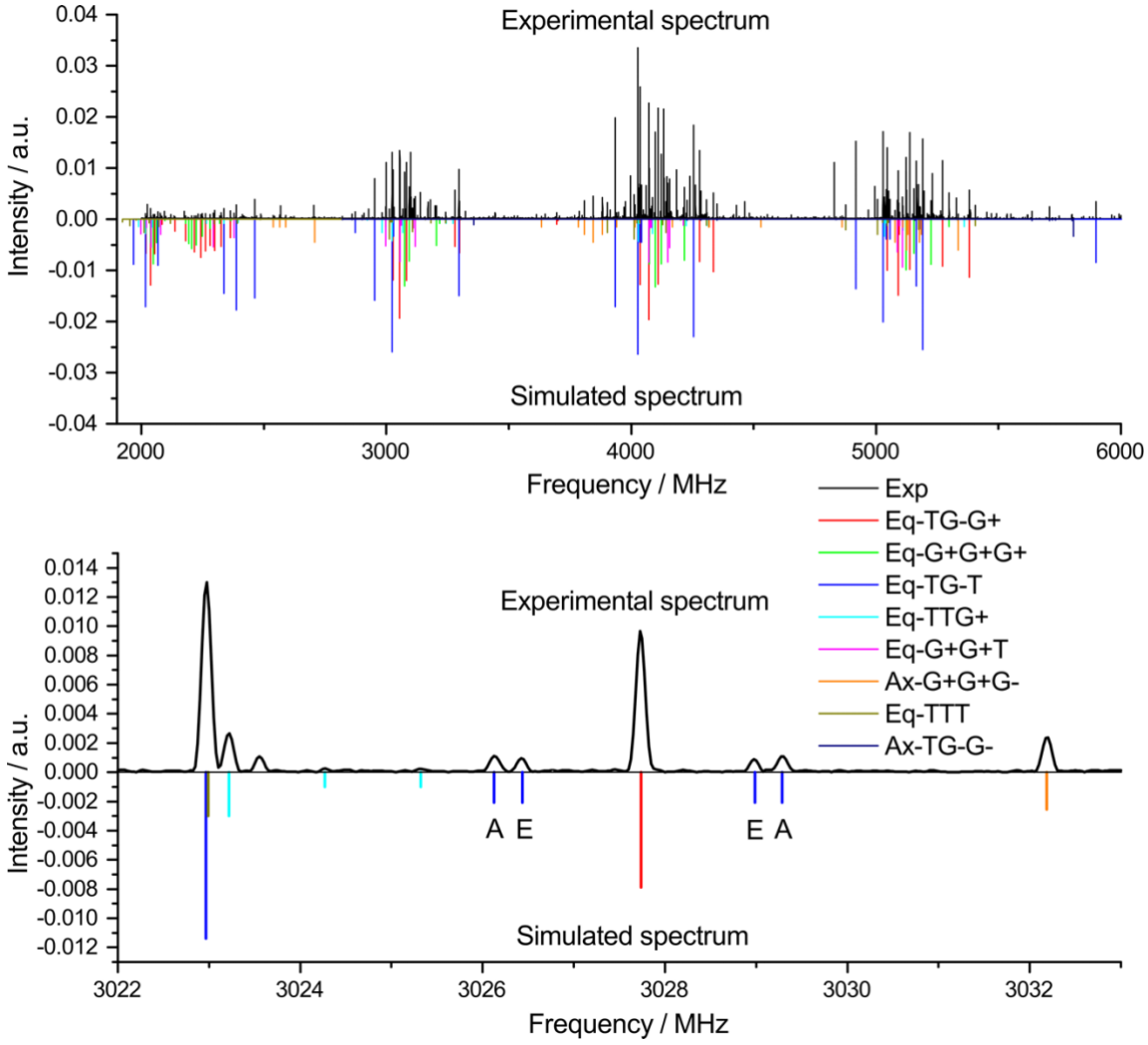

Figure 3.6. a) An chirped pulse overview spectrum (in black) in the 2.0 to 6.0 GHz range and the simulated rotational spectra of the eight PA conformers. The lower intensities at both frequency ends are due to the experimental setup. In the simulations, the experimental spectroscopic constants, the permanent electric dipole

moment components calculated at the B3LYP-D3(BJ)/def2-TZVP level, an estimated rotational temperature of 0.5 K, and estimated relative abundances of Eq-TG-G+: Eq-TG-T: Eq-G+G+G+: Eq-TTG+: Eq-G+G+T: Eq-TTT: Ax-G+G+G-: Ax-TG-G- = 27: 23: 20: 6: 9: 6: 6: 3 were used. Please see the text for discussion on the conformational cooling and abundances; b) A zoomed-in section of the rotational spectrum showing the methyl internal rotation splittings of the 3_{22}-2_{21} and 3_{21}-2_{20} transitions of Eq-TG-T, and other transitions belonging to the Eq-TG-T, Eq-TTT, Eq-TTG+, Eq-TG-G+ and Ax-G+G+G conformers.

3.2.4. Conformational conversion and experimental abundances

An overview of the experimental chirped pulse spectrum is shown in Figure 3.6 (top), together with a zoomed-in section (bottom) which shows methyl internal rotation splittings and rotational transitions belonging to several PA conformers. One can see that the line intensities in the 2.0 to 2.7 GHz and 5.5 to 6.0 GHz regions are noticeably weaker than in the central region; the reasons are due to instrumental effects (see the experimental section). Nevertheless, by comparing the observed line intensities in the 2.7 to 5.5 GHz region to the prediction, one can extract the relative abundances of the different conformers observed, using the theoretical electric dipole moment values. The experimentally determined percentage conformational abundances are summarized in Table 3.3. Initially, it was somewhat surprising that the strongest experimental lines come from the second most stable conformer Eq-TG-T rather than the most stable Eq-TG-G+ identified at all levels of calculations. This observation can in part be attributed to the respective permanent dipole moment components of these two conformers. The other contributing factor is the conformational cooling in a jet expansion, which is analyzed below.

In our analysis, we first consider the axial and equatorial conformers separately for several reasons: a) the conversion barrier between them is sufficiently high and little conversion is expected in a pulsed jet expansion; b) the DFT and LMP2 relative

energies show obvious discrepancies for the axial conformers, a point we will address later on. We note that the DFT relative free energies (Table 3.S1) provide a mostly similar relative stability ordering as the DFT *ZPE* corrected energies. To avoid unnecessarily tedious analyses, we will focus only on ΔD_0 in the discussion below. We consider three scenarios with different degrees of conformational cooling during the supersonic expansion.

(1) *No conformational cooling.* Taking the sample source temperature of ~350 K as the conformational temperature, theoretical Boltzmann population factors were calculated based on the relative energy values obtained at the B3LYP-D3(BJ) and LMP2 levels of theory. These values are summarized for all 54 conformers in Table 3.S11. The experimental percentage abundances for the first three (two) most stable equatorial (axial) conformers agree roughly with the theoretical predictions at both levels of theory, although the exact relative percentages are off. The agreement deteriorates for the higher energy conformers. In particular, some conformers with observable abundances are missing. For example, Eq-TG-G+, which has a higher theoretical abundance (7.2%) than Eq-TTT (2.8%), was not detected experimentally, whereas the latter was.

(2) *Complete conformational cooling for low barriers.* Based on Figure 3.2 and the assumption that complete conformational conversion occurs for the low barrier cases (<~2 to 3 kJ mol^{-1}) in a jet expansion, we obtained the Boltzmann factors after including such conversion (Table 3.S10). Basically, the above consideration reduces the number of observable conformers in a jet from 54 to 12 as already discussed before. Furthermore, it alters the percentage distribution of the observed conformers. For example, the population of Eq-TG-T in the jet can be regarded as coming from its original abundance and from conformational cooling of five other conformers, whereas the population of the most stable Eq-TG-G+ comes from two other conformers and itself. While these new numbers explain the aforementioned missing conformers, the experimental abundance trend is no longer reproduced for the first few most stable conformers. For example, Eq-TG-G+, the

most abundant one experimentally, is now predicted to be less abundant than Eq-TG-T at both levels of theory.

(3) *Some degree of conformational cooling for all barriers*. We consider that there is some degree of cooling of all conformers, without or with additional complete conformational transfer for very low barriers. Such general cooling had been reported and discussed before, for example in the CP-FTMW study of 1-hexanal where a conformational temperature of 135 (11) K was reported.[9] The corresponding Boltzmann factors at 150 K without and with the complete conformational low-barrier conversion are also included in Table 3.S11, for comparison. At both levels of theory, it appears that a conformational temperature of 150 K plus the aforementioned 100% low-barrier conformational conversion is in good agreement with the experiment, if axial and equatorial conformers are considered separately.

For completeness, we now consider axial and equatorial conformers together. The same analyses as before were carried out for all 54 conformers. A complete list is provided in Table 3.S12, while a concise summary for the first 20 conformers is given in Table 3.3. Clearly, the B3LYP-D3(BJ) energies provide a fairly good agreement with the experimental data, whereas the LMP2 calculations overestimate the abundances of the axial conformers and are in poor agreement with experiment. Similarly, in the previous case of limonene oxide, the MP2 method predicted the axial conformers to have considerably lower energies with one of the axial forms being the global minimum, in disagreement with the experiment.[11] It is also worth pointing out that in the cases of 1-hexanal, a much better performance of B3LYP-D3/aug-cc-pVTZ and B3LYP-D3/6-311++g(d,p) versus MP2/6-311++g(d,p) in terms of conformational abundances was also reported.[9] Overall, while both levels of calculations can reproduce the experimental relative stabilities qualitatively within the axial and equatorial series of conformers separately, it appears that the LMP2 (and MP2) calculations overestimate the stabilities of the axial conformations with respect to the equatorial ones based on the current study and others

Table 3.3. Comparison of the experimental and theoretical conformational abundances[a]

Conformer[b]	Exp[c] %	150K %	C_150K[d] %	ΔD_0 kJ mol^{-1}	150K %	C_150K[d] %	ΔD_0 kJ mol^{-1}
Eq-TG-G+	**27**	**33**	**34**	**0.0**	**25**	**26**	**0.0**
Eq-TG-T	**23**	**15**	**22**	**1.0**	**14**	**20**	**0.7**
Eq-G+G+G+	**20**	**14**	**14**	**1.1**	**10**	**11**	**1.1**
Eq-TG-G-	0	7	0	2.0	5	0	2.1
Eq-TTG+	**6**	**6**	**8**	**2.2**	**3**	**4**	**2.8**
Eq-G+G+T	**9**	**5**	**8**	**2.3**	**5**	**8**	**1.9**
Ax-G+G+G-	**6**	**5**	**5**	**2.4**	**15**	**16**	**0.6**
Ax-TG-G-	**3**	**3**	**3**	**3.2**	**8**	**8**	**1.4**
Eq-G+G+G-	0	3	0	3.2	2	0	3.2
Eq-TTT	**6**	**3**	**5**	**3.2**	**1**	**3**	**3.5**
Eq-G+TG+	0	2	0	3.3	1	0	3.9
Eq-G+TT	0	1	0	4.1	1	0	4.4
Eq-TTG-	0	1	0	4.5	0	0	5.0
Ax-G+TG-	**0**	**1**	**1**	**4.6**	**2**	**3**	**3.4**
Eq-G-G-G+	0	1	0	4.6	1	0	3.5
Eq-G+TG-	0	0	0	5.4	0	0	8.8
Ax-TTG-	0	0	0	5.5	1	0	4.3
Eq-G-G+G+	0	0	0	5.6	1	0	4.3
Eq-G-G-T	0	0	0	5.9	1	0	4.4
Eq-G+G-G+	0	0	0	6.0	0	0	5.9
Sum	100	100	100	N/A	96	100	N/A

3.3. Conclusions

In summary, the combined rotational spectroscopic and theoretical study of PA reveals its rich conformational landscape in great detail. Aided by theoretical modelling, we were able to narrow down the number of observable conformers from 54 to 12 and detected 8 out of the 12 conformers experimentally. These observed conformers show a clear preference for the equatorial conformations over the axial ones. While the B3LYP-D3(BJ) calculations provide a stability ordering in general agreement with experiment, the LMP2 calculations appear to overestimate the stability of the axial conformers. A main message from this study is that detailed knowledge about the overall conformational landscape and theoretical abundances of *all* relevant conformers is crucial in order to relate experimental conformational abundances to relative stabilities and use them subsequently to benchmark theoretical methods. The study showcases the power of CP-FTMW spectroscopy in distinguishing many conformers with only minor structural differences and the importance of identifying these conformers in detail in order to properly benchmark theoretical relative stabilities with the experimental ones.

3.4. Experimental and computational details

The broadband rotational spectrum of PA was recorded with a recently constructed CP-FTMW spectrometer,[25] operating in the 2-6 GHz range, with a similar design to that of the 2-8 GHz CP-FTMW instrument first reported by Perez et al. [26] The use of 2-6 GHz instead of the usual 2-8 GHz band was due to cost considerations when the instrument was developed. A brief documentation of the specific parameters used is summarized below. MW chirped-pulses were directly generated with a 12 Gs/s arbitrary waveform generator, and amplified using a 400 W, 2.5 to 7.5 GHz traveling wave tube amplifier. The amplified pulse was then broadcasted through a horn antenna situated inside the vacuum chamber, intercepting the pulsed jet expansion perpendicularly. After excitation, the coherent molecular emission was

digitized using a 25 Gs/s oscilloscope. About 0.7 million free induction decays were accumulated and the averaged time domain data was Fourier transformed to obtain the frequency spectrum. The rotational transition frequencies in the 6 to 16 GHz region were obtained through the use of a Balle-Flygare-type[27,32,33] cavity FTMW spectrometer which has been described in detail before.[28, 29]

The sample of PA was obtained from Sigma-Aldrich (96% purity) and was used without further purification. For both instruments, the sample was prepared by placing a small amount of solid PA sample inside a pulsed nozzle cap (Parker Series 9 pulse valve) which was heated to ca. 75 °C, while the backing pressure of the neon carrier gas was set at 3 bars.

All geometry optimizations and harmonic frequency calculations were completed with the Gaussian 16 program package[30] and the MOLPRO (version 2015.1) program.[31] We used (S)-PA in all calculations and utilized dispersion corrected[32] density functional theory, B3LYP-D3[33] with Becke-Johnson damping,[34] with the def2-TZVP basis set.[35,36] We also used the aug-cc-pVQZ basis set, together with local electron correlation (indicated by an "L" prefix)[37] second-order Møller–Plesset perturbation (LMP2)[38] theory which affords a drastic speed-up of the computations. The good performance of LMP2 with respect to conformational energies has been reported before.[39] Several one- or two-dimensional (2D) dihedral angle scans were performed at the B3LYP-D3(BJ) level of theory using the algorithm by Schlegel and co-workers,[40,41] in order to identify possible transition states, conformers, and the associated conformational conversion barriers. For conformational searches, we also used GFN-xTB,[42,43] a semiempirical tight-binding (TB) quantum chemistry code, designed for prediction of equilibrium structural properties, such as geometries, vibrational frequencies, and non-covalent interactions (NCIs). NCI analyses[44] were used to visualize the intramolecular interactions.

References

[1] T. C. Chen, C. O. Da Fonseca, A. H. Schönthal, *Am. J. Cancer. Res.*, 2015, **5**, 1580-1593.

[2] P. J. M. Boon, D. van der Boon, and G. J. Mulder, *Toxicol. Appl. Pharmacol.*, 2000, **167**, 55-62.

[3] T. C. Chen, C. O. Da Fonseca, A. H. Schönthal, *Int. J. Mol. Sci.*, 2018, **19**, 3905/1-21.

[4] J. G. Hill, A. C. Legon, D. P. Tew and N. R. Walker, *Top. Curr. Chem.*, 2015, **358**, 43-78.

[5] M. Becucci and S. Melandri, *Chem. Rev.*, 2016, **116**, 5014-5037.

[6] C. B. Park and R. W. Field, *J. Chem. Phys.*, 2016, **144**, 200901.

[7] G. T. Fraser, R. D. Suenram, and C. L. Lugez, *J. Phys. Chem. A*, 2001, **105**, 9859-9864.

[8] G. G. Brown, B. C. Dian, K. O. Douglass, S. M. Geyer, S. T. Shipman, B. H. Pate, *Rev. Sci. Instrum.*, 2008, **79**, 053103.

[9] N. A. Seifert, I. A. Finneran, C. Perez, D. P. Zaleski, J. L. Neill, A. L. Steber, R. D. Suenram, A. Lesarri, S. T. Shipman, B. H. Pate, *J. Mol. Spectrosc*., 2015, **312**, 13-21.

[10] S. R. Domingos, C. Pérez, C. Medcraft, P. Pinacho, M. Schnell, *Phys. Chem. Chem. Phys.* 2016, **18**, 16682-16689.

[11] D. Loru, M. M. Quesada-Moreno, J. R. Avilés-Moreno, N. Jarman, T. R. Huet, J. J. López-González, M. E. Sanz, *ChemPhysChem,* 2017, **18**, 274-280.

[12] F. Xie, X. Ng, N. A. Seifert, J. Thomas, W. Jäger, Y. Xu, *J. Chem. Phys*., 2018, **149**, 224306/1-10.

[13] N. A. Seifert, J. Thomas, W. Jäger, Y. Xu, *Phys. Chem. Chem. Phys.,* 2018, **20**, 27630-27637.

[14] J. Thomas, N. A. Seifert, W. Jager, Y. Xu, *Angew. Chem. Int. Ed.,* 2017, **56**, 6289-6293.

[15] S. Oswald, N. A. Seifert, F. Bohle, M. Gawrilow, S. Grimme, W. Jäger, Y. Xu and M. A. Suhm, *Angew. Chem. Int. Ed.,* 2019, **58**, 5080-5084.

[16] A. Poblotzki, H. C. Gottschalk and M. A. Suhm, *J. Phys. Chem. Lett.*, 2017, **8**, 5656-5665.

[17] F. R. Jensen and C. H. Bushweller, *J. Am. Chem. Soc.*, 1969, **91**, 5774–5782.

[18] K. Fukui, *Acc. Chem. Res.,* 1981, **14**, 363-368.

[19] R. S. Ruoff, T. D. Klots, T. Emilsson and H. S. Gutowsky, *J. Chem. Phys*., 1990, **93**, 3142-3150.

[20] C. M. Western, *J. Quant. Spectrosc. Radiat. Transfer*, 2017, **186**, 221-242.

[21] J. R. A. Moreno, F. P. Ureña, J. J. L. González and T. R. Huet, C*hem. Phys. Lett.*, 2009, **473**, 17-20.

[22] H. Hartwig and H. Dreizler, *Z. Naturforsch. A* 1996, **51**, 923-932.

[23] N. Hansen, H. Mäder and T. Bruhn, *Mol. Phys.*, 1999, **97**, 587-595.

[24] J. K. G. Watson, in Vibrational Spectra and Structure, ed. J. R. Durig, Elsevier, New York, 1977, vol. 6, p. 1.

[25] C. D. Carlson, N. A. Seifert, M. Heger, F. Xie, J. Thomas and Y. Xu, *J. Mol. Spec.,* 2018, **351**, 62-67.

[26] C. Pérez, S. Lobsiger, N. A. Seifert, D. P. Zaleski, B. Temelso, G. C. Shields, Z. Kisiel and B. H. Pate, *Chem. Phys. Lett.*, 2013, **571**, 1-15.

[27] T. J. Balle and W. H. Flygare, *Rev. Sci. Instrum.*, 1981, **52**, 33-45.

[28] Y. Xu, J. Van Wijngaarden and W. Jäger, *Int. Rev. Phys. Chem.*, 2005, **24**, 301-338.

[29] Y. Xu and W. Jäger, *J. Chem. Phys.*, 1997, **106**, 7968–7980.

[30] Gaussian 16, Revision B.01, M. J. Frisch, G. W. Trucks, H. B. Schlegel, G. E. Scuseria, M. A. Robb, J. R. Cheeseman, G. Scalmani, V. Barone, G. A. Petersson, H. Nakatsuji, X.; Li, M. Caricato, A. V. Marenich, J. Bloino, B. G. Janesko, R.

Gomperts, B. Mennucci, H. P.. Hratchian, J. V. Ortiz, A. F. Izmaylov, J. L. Sonnenberg, D. Williams-Young, F. Ding, F. Lipparini, F. Egidi, J. Goings, B. Peng, A. Petrone, T. Henderson, D. Ranasinghe, V. G. Zakrzewski, J. Gao, N. Rega, G. Zheng, W. Liang, M. Hada, M. Ehara, K. Toyota, R. Fukuda, J. Hasegawa, M. Ishida, T. Nakajima, Y. Honda, O. Kitao, H. Nakai, T. Vreven, K. Throssell, J. A. Montgomery Jr., J. E. Peralta, F. Ogliaro, M. J. Bearpark, J. J. Heyd, E. N. Brothers, K. N. Kudin, V. N. Staroverov, T. A. Keith, R. Kobayashi, J. Normand, K. Raghavachari, A. P. Rendell, J. C. Burant, S. S. Iyengar, J. Tomasi, M. Cossi, J. M. Millam, M. Klene, C. Adamo, R. Cammi, J. W. Ochterski, R. L. Martin, K. Morokuma, O. Farkas, J. B. Foresman, D. J. Fox, Gaussian, Inc., Wallingford CT, 2016.

[31] MOLPRO, version 2015.1, a package of ab initio programs, H.-J. Werner, P. J. Knowles, G. Knizia, F. R. Manby, M. Schütz, P. Celani, W. Györffy, D. Kats, T. Korona, R. Lindh, A. Mitrushenkov, G. Rauhut, K. R. Shamasundar, T. B. Adler, R. D. Amos, A. Bernhardsson, A. Berning, D. L. Cooper, M. J. O. Deegan, A. J. Dobbyn, F. Eckert, E. Goll, C. Hampel, A. Hesselmann, G. Hetzer, T. Hrenar, G. Jansen, C. Köppl, Y. Liu, A. W. Lloyd, R. A. Mata, A. J. May, S. J. McNicholas, W. Meyer, M. E. Mura, A. Nicklass, D. P. O'Neill, P. Palmieri, D. Peng, K. Pflüger, R. Pitzer, M. Reiher, T. Shiozaki, H. Stoll, A. J. Stone, R. Tarroni, T. Thorsteinsson, and M. Wang. see http://www.molpro.net.

[32] S. Grimme, S. Ehrlich and L. Goerigk, *J. Comput. Chem.*, 2011, **32**, 1456–1465.

[33] S. Grimme, J. Antony, S. Ehrlich and H. Krieg, *J. Chem. Phys.*, 2010, **132**, 154104.

[34] A. D. Becke and E. R. Johnson, *J. Chem. Phys.,* 2005, **123**, 154101.

[35] F. Weigend and R. Ahlrichs, *Phys. Chem. Chem. Phys.*, 2005, **7**, 3297-3305.

[36] A. Schäfer, C. Huber and R. Ahlrichs, *J. Chem. Phys.*, 1994, **100**, 5829–5835.

[37] T. Korona, D. Kats, M. Schütz, T. B. Adler, Y. Liu and H.-J. Werner, in *Linear-Scaling Techniques in Computational Chemistry and Physics* (Springer Netherlands, 2011), pp. 345–407.

[38] M. J. Frisch, M. Head-Gordon and J. A. Pople, *Chem. Phys. Lett.*, 1990, **166**, 275-280.

[39] J. Kaminsky, R. A. Mata, H.-J. Werner and F. Jensen, *Mol. Phys.*, 2008, **106**, 1899-1906.

[40] C. Peng and H. B. Schlegel, *Isr. J. Chem.*, 1993, **33**, 449-454.

[41] X. Li and M. J. Frisch, *J. Chem. Theory Comp.*, 2006, **2**, 835-839.

[42] S. Grimme, C. Bannwarth and P. Shushkov, *J. Chem. Theory Comput.*, 2017, **13**, 1989-2009.

[43] S. Grimme, *J. Chem. Theory Comput.*, 2019, **15**, 2847-2862. Article ASAP DOI: 10.1021/acs.jctc.9b00143.

[44] E. R. Johnson, S. Keinan, P. Mori-Snchez, J. Contreras-García, A. J. Cohen and W. Yang, *J. Am. Chem. Soc.*, 2010, **132**, 6498–6506.

Chapter 4

Rotational Spectroscopy of Chiral Tetrahydro-2-Furoic Acid: Conformational Landscape, Conversion, and Abundances [a]

[a] This study has been published. Fan Xie, Xiaoqian Ng, Nathan A. Seifert, Javix Thomas, Wolfgang Jäger, Yunjie Xu, "Rotational spectroscopy of chiral tetrahydro-2-furoic acid: conformational landscape, conversion, and abundances", *J. Chem. Phys.* **2018**,149, 224306.

4.1. Introduction

Tetrahydro-2-furoic acid (THFA), a chiral carboxylic acid, is one of the smallest tetrahydrofuran derivatives with an amphiphilic structure. THFA exhibits a complex conformational landscape with a number of conformational flexibilities related to the relative orientations of the carboxyl group and its proton, and the ring puckering motions in the molecule. The ring configurations and ring puckering motions associated with the tetrahydrofuran (THF) ring have been the subject of a considerable number of research papers.[1,,,,,6] We adopt the previous naming scheme for THF where the C atoms neighboring the O atom are labelled as α and α' and the other two as β and β'. Engerholm et al. reported the first rotational spectroscopic study of THF in 1969[1] and proposed a potential energy surface (PES) which supports four equivalent minima, $E^{\alpha}/E^{\alpha'}$ and $E_{\alpha}/E_{\alpha'}$ (*E* denotes the *envelope* configuration), separated by two pairs of non-equivalent maxima ${}^{\beta}T_{\beta'}/{}^{\beta'}T_{\beta}$ (*T* denotes the *twist* configuration) and E^{O}/E_{O} (See Figure 2(a) in Ref. 2). In 1999, Meyer et al.[3] applied a flexible model to analyze the observed splittings in rotational transitions and proposed a very similar PES as Engerholm's.[1] Later, Mamleev et al.[4] and Melnik et al.[5] proposed two similar new PESs where the minima and maxima were *reversed* in relation to Meyer's PES. In these PESs, the two equivalent global minima take on *twist* configurations, ${}^{\beta}T_{\beta'}$ and ${}^{\beta'}T_{\beta}$, and the two equivalent secondary minima are E^{O} and E_{O}, whereas $E^{\alpha}/E^{\alpha'}$ and $E_{\alpha}/E_{\alpha'}$ are four equivalent maxima. The PES of THF was again modified in 2005 when Rayón and Sordo carried out high-level *ab initio* calculations at the CCSD(T) level. While the four equivalent maxima remain, the two equivalent most stable minima are E^{O} and E_{O}, whereas ${}^{\beta}T_{\beta'}$ and ${}^{\beta'}T_{\beta}$ are the two equivalent second most stable minima.[2] Considering all the twists and turns in the high resolution spectroscopic and theoretical studies of the THF ring configurations, it is of interest to study the conformation of the THF ring in THFA to appreciate how the carboxylic acid group alters the ring puckering motions and the resultant preferred ring configuration, as well as to test the accuracy of the corresponding theoretical predictions.

In addition, THFA is often used as precursor in syntheses of pharmaceuticals, such as Alfuzosin, a drug for the treatment of benign prostatic hyperplasia.[7] THFA has also been successfully used as a proline hydrogenase inhibitor which is used against metastasizing cancer cells.[8] Its applications as drug precursors and enzyme inhibitors are indicative of its unique structural configuration, for example its similarity to the proline substrate.[9] One may imagine the specific conformation adopted by THFA would have significant influence over its intermolecular interactions with other biomolecules. Therefore, an in-depth understanding of its conformational landscape is desirable.

In this paper, we report the first rotational spectroscopic investigation of the conformational landscape of THFA, aided by extensive semiempirical-molecular dynamics conformational searches and DFT and *ab initio* calculations. We also searched for possible conformers generated by combinations of unique configurations and orientations of the carboxyl functional group and the THF ring puckering coordinate using DFT. We applied both broadband chirped-pulse and cavity-based Fourier transform microwave (FTMW) spectroscopies to identify the preferred conformations experimentally. Furthermore, we examined possible conformational conversion paths and barriers and used them to explain the differences between the calculated and experimental abundances of the detected conformers.

4.2. Results and discussion

4.2.1. Conformational searches

The GFN-xTB program package[38,40] was used for an extensive search of the conformational landscape of THFA. To prevent the trapping of structures into local minima

separated by high barriers and to ensure that all relevant conformational space was searched, several starting geometries were placed in equilibrium with two heat baths of 300 K and 3000 K separately. The temperatures of the baths were then lowered in stages, trapping structures in local minima during annealing; the trapped geometries were then optimized with the GFN-xTB program. The 3000 K bath simulation resulted in nine minima, including the four produced by the 300 K bath. Evidently, a high bath temperature if necessary to access regions of the potential energy surface that are separated by relatively high barriers. These GFN-xTB minima were then re-optimized at the B3LYP-D3(BJ)/def2-TZVP, B3LYP-D3(BJ)/6-311++G(2d,p), and MP2/6-311++G(2d,p) levels of theory, resulting in a total of nine minimum energy geometries.

We also carried out systematic conformer searches manually in a stepwise fashion to verify the completeness of the conformational search by GFN-xTB. The COOH functional group may adopt either a "*Z*-COOH" or "*E*-COOH" configuration[10] (see Figure 4.S1, Supporting Information for a pictorial presentation) where C=O and OH are on the same or opposite sides of the C3O2 bond (see Figure 4.1 for atom labelling), respectively. The THF ring may take on *envelope* and *twist* ring conformations. We then scanned the O2-C3-C5-O6 dihedral angle from 0° to 360°, in steps of 3.6°, with four different starting geometries: a) *envelope* ring and *Z*-COOH; b) *twist* ring and *Z*-COOH; c) *envelope* ring and *E*-COOH; d) *twist* ring and *E*-COOH. The relaxed O2-C3-C5-O6 dihedral angle scans are summarized in Figure 4.2. Altogether, these four scans produced nine minima where the carbonyl O4 and ester O6 atom are in the *syn* or *anti* relation labelled by letters "*s*" or "*a*", respectively. The four possible rotameric configurations are labelled as *aE*-COOH, *aZ*-COOH, *sE*-COOH, and *sZ*-COOH, while those related to the ring configurations are discussed below.

Since THFA is a chiral derivative of THF, it has lower symmetry and may possess additional *envelope* and *twist* ring configurations. To make sure that our conformational search is as complete as possible, we decided to generate all possible ring starting configurations, i.e. ten *envelope* ones where each atom in the THF ring can be up or down

and ten *twist* ones where any two adjacent ring atoms can be an up/down pair. These twenty possible ring configurations were combined with the four rotameric configurations to produce a whole new set of starting geometries which were optimized at the B3LYP-D3(BJ)/def2-TZVP level of theory. It is worth noting that this exhaustive exercise produced exactly the same nine minima that were identified with the GFN-xTB CRE program.[38,40] As a note of caution, we also carried out a similar search for the THF monomer with the GFN-xTB program. The program identified two equivalent minima, namely ${}^{\beta}T_{\beta'}$ and ${}^{\beta'}T_{\beta}$ which are secondary minima at the CCSD(T) level, and missed the CCSD(T) global minima E^{O} and E_{O}. This is not surprising since E^{O} and E_{O} are transition structures at the lower levels of theory and only become minima at the MP2/aug-cc-pVTZ level. Similar issues associated small ring molecules, such as cyclobutene, were discussed in the GFN-xTB article.[38] We note that the energy difference is only about 50 cm^{-1} between the *envelope* and *twist* THF forms mentioned above. For such small energy differences, further checking, such as the one carried out in this work, should be performed to ensure completeness of the conformational search. We speculate that the GFN-xTB program works well for THFA because of the much larger conformational energy differences, which are a consequence of the carboxyl group substituent.

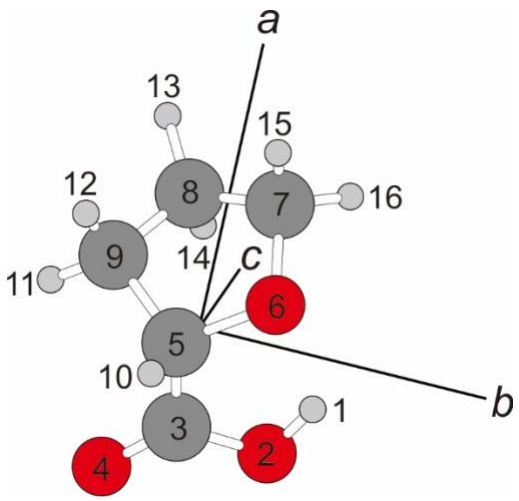

Figure 4.1. The most stable THFA conformer **I**, E_8 *aE-COOH*, in its principal inertial axis system with atom numbering.

These nine minima identified in the conformational searches are labelled as **I-IX** in Figure 4.2. The harmonic zero-point energy (*ZPE*) corrected barriers were calculated from the *ZPE* corrected energy difference between the minima and the associated transition states. The *ZPE*-corrected ground state vibrational energy levels are shown in Figure 4.2 with a solid line if they are below the two nearest barriers or as a dashed line if they are above one of the two barriers, indicating whether the respective well supports a corresponding conformer or not, respectively. Considering these *ZPE* corrections, one can see that **IX** does not exist as a separate conformer.

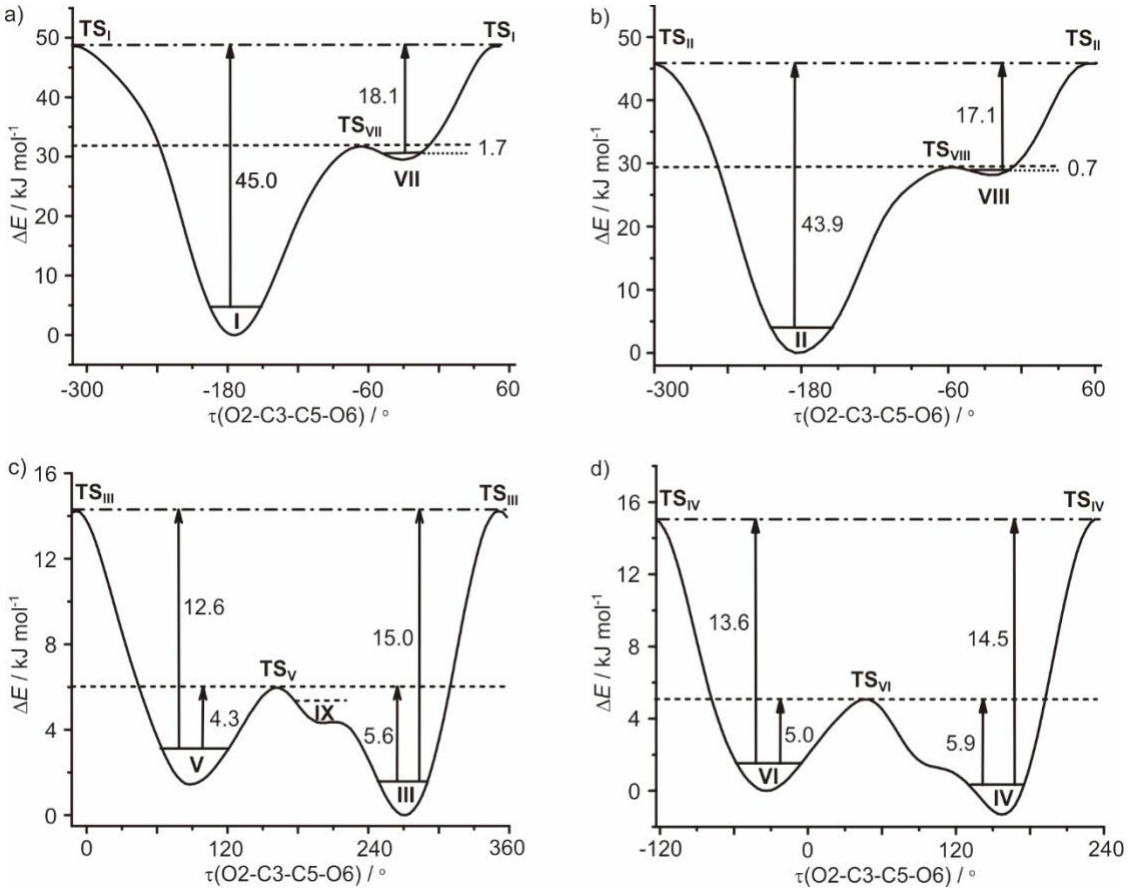

Figure 4.2. The potential energy along the four relaxed O2-C3-C5-O6 dihedral angle scans with four different starting geometries: a) *envelope* ring and *Z*-COOH; b) *twist* ring and *Z*-

COOH; c) *envelope* ring and *E*-COOH; d) *twist* ring and *E*-COOH. The *ZPE* levels for **I-IX** are also indicated with solid or dashed lines. See the text for a more detailed description.

The relative electronic energies and the spectroscopic constants of the eight relevant conformers calculated at the B3LYP-D3(BJ)/def2-TZVP level of theory are provided in Table 4.1, while those obtained at the other two levels are shown in Tables 4.S1 and 4.S2, Supporting Information. The Roman numbers **I-IX** indicate the descending stability ordering of the THFA conformers with **I** being the most stable, based on the DFT *ZPE*-corrected relative electronic energies. Overall, the spectroscopic properties predicted at the three levels of theory are quite consistent with each other.

Table 4.1. Calculated relative raw energies ΔE_e, *ZPE* corrected energies ΔE_0 (in kJ mol^{-1}), rotational constants *A*, *B*, and *C* (in MHz), and electric dipole moment components $|\mu_a|$, $|\mu_b|$, and $|\mu_c|$ (in Debye) of the eight THFA conformers at the B3LYP-D3(BJ)/def2-TZVP level of theory.

Conformers	ΔE_e	ΔE_0	*A*	*B*	*C*	$\|\mu_a\|$	$\|\mu_b\|$	$\|\mu_c\|$
I	0.0	0.0	3733	1724	1414	4.73	0.22	0.26
II	2.1	1.8	4173	1587	1267	5.06	0.37	0.10
III	7.4	6.1	3801	1642	1508	0.22	2.34	0.71
IV	8.5	7.5	4057	1574	1360	0.60	2.43	0.58
V	9.3	8.1	3755	1670	1515	1.81	0.11	1.67
VI	9.4	8.4	4141	1547	1369	2.00	0.11	1.77
VII	28.9	26.9	3775	1648	1512	1.71	3.92	1.00
VIII	30.3	28.6	4010	1584	1363	2.38	3.89	1.00

The optimized geometries of the eight THFA conformers are shown in Figure 4.3. We label each conformer with its specific ring configuration and the four rotameric configurations. The *E* (*envelope*) ring configuration is characterised by 4 adjacent coplanar atoms, and the

5^{th} atom numbering in superscript or subscript denotes that the atom is above or below the 4 atom-plane, respectively, as shown in the figure.[11] The *T* (*twist*) ring conformations involve 3 adjacent coplanar atoms, with the remaining 2 atoms being above/below the plane. Here, the atom numbers are placed in superscript or subscript to indicate that the atom is above or below the 3 atom-plane, respectively. The additional labels, which follow the ring configuration label, indicate the *syn* or *anti* relationship between the oxygen atoms of the carbonyl and ether groups, and the *Z*/*E*-COOH configuration.

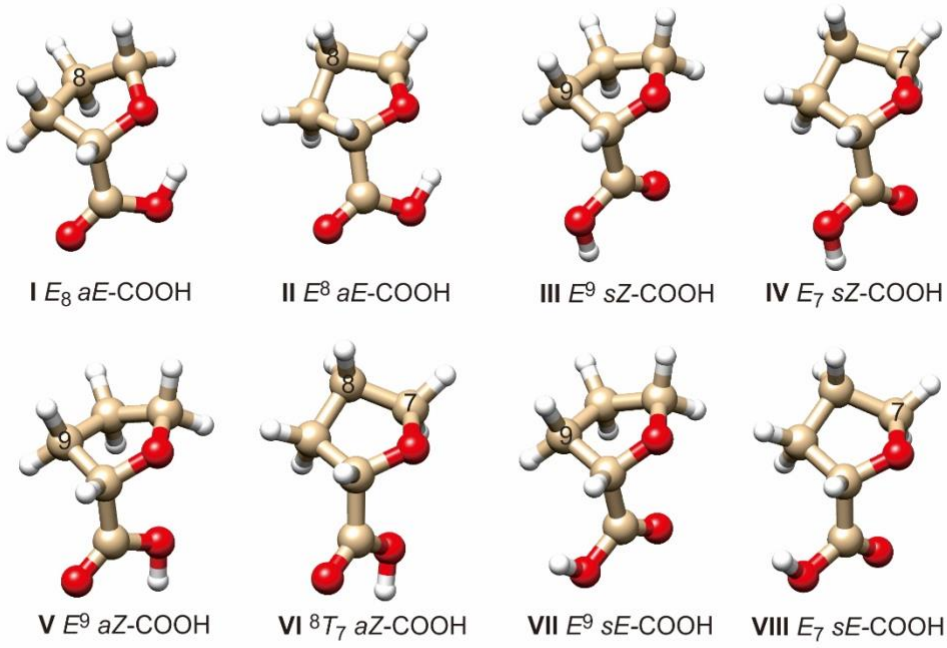

Figure 4.3. The optimized equilibrium geometries of the eight THFA conformers. The atom numbering is the same as in Figure 4.1 but only the relevant ones are indicated. See the text for a more detailed naming description.

4.2.3. Spectral searches and assignments

The preliminary search for rotational transitions of the THFA conformers was initially carried out using the 8-18 GHz chirped pulse FTMW spectrometer. It was straightforward to recognize the strong *a*-type transition pattern of conformer **I** in the chirped pulse spectrum, by comparing to the simulated spectrum generated with the Pgopher program[12] using the theoretical spectroscopic constants. Subsequently, several rotational transitions of the five ^{13}C mono-substituted isotopologues of **I** were detected in their natural abundances using the cavity FTMW spectrometer and analysed.

Although **II** is only 1.8 kJ mol^{-1} less stable in **I**, it was uncertain at the outset of the spectral search whether we would be able to detected experimentally or not. An immediate observation is that **I** and **II** look quite similar to each other, with only a slight difference in their ring configurations. Since the ring puckering barriers are very low (< 70 cm^{-1}) in THF, one may speculate a similarly low conversion barrier from **II** to **I** which would allow efficient cooling of **II** to **I** in a supersonic jet expansion. In addition, the 8-18 GHz chirped pulse scan did not reveal any other strong lines besides those belonging to **I**. On the other hand, for completeness sake, we decided to turn to 'deep averaging' in the 2-6 GHz region in order to search for higher energy THFA conformers since the 2-6 GHz chirped pulse spectrometer offers better sensitivity. Surprisingly, we were able to assign two new sets of rotational transitions which are consistent with other THFA conformers. One of them contains very strong *a*-type and weak *b*-type transitions and no *c*-type transitions, whereas the other one has of strong *b*-type transitions and weak *c*-type transition and no *a*-type

transitions. These observations and the respective rotational constants obtained (vide infra) allow us to confidently assign their carriers to THFA conformers **II** and **III**.

The measured transition frequencies of the individual conformers and of the ^{13}C isotopologues were fitted using Watson's *S*-reduction[13] Hamiltonian in its I^r representation using the Pgopher program.[28] The experimental spectroscopic constants obtained for the normal isotopologues of THFA **I**, **II**, and **III** are provided in Table 4.2, while those of the five ^{13}C isotopologues of **I** are listed in Table 4.3. The measured transition frequencies of THFA **I**, **II**, and **III** are listed in Tables 4.S3-5, while those of the five ^{13}C isotopologues of **I** are summarized in Tables 4.S6-S10, Supporting Information. The percent deviations between rotational constants *A*, *B,* and *C* calculated at the three different levels of theory and the experimental ones are given in Table 4.4. Overall, the MP2 calculation seems to provide the best agreement with the experimental rotational constants.

Table 4.2. Experimental spectroscopic parameters[a] of THFA **I**, **II** and **III**

	I	**II**	**III**
A / MHz	3698.2873(19)[a]	4164.14571(60)	3748.82700(74)
B / MHz	1738.31206(36)	1587.32045(10)	1670.56155(47)
C / MHz	1426.40961(30)	1267.76397(10)	1521.80295(49)
D_K / kHz	3.46(45)	0.0 (fixed)	4.76(8)
D_{JK} / kHz	2.20(3)	-1.41(2)	-2.32(1)
D_J / kHz	0.661(7)	0.366(1)	0.64(2)
d_1 / kHz	0.35(3)	0.90(32)	3.02(4)
d_2 / kHz	0.079(2)	0.071(1)	0.121(1)
N[b]	49	19	21
σ[c] / kHz	4.0	6.5	3.5

[a] Errors are in parenthesis and are expressed in the units of the least significant digit.

[b] *N* is the number of rotational transitions included in the fit.

[c] σ is the standard deviation of the fit.

Table 4.3. Experimental spectroscopic constants of the five ^{13}C isotopologues of **I**

Parameters[a]	^{13}C3	^{13}C5	^{13}C7	^{13}C8	^{13}C9
A /MHz	3698.717(46)[b]	3681.269(92)	3686.719(98)	3668.967(51)	3647.473(51)
B /MHz	1727.71023(37)	1734.95143(48)	1715.0751(23)	1717.92971(20)	1734.4473(12)
C /MHz	1419.26961(37)	1426.41026(48)	1409.1530(23)	1413.67672(11)	1416.6569 (9)
N[c]	9	4	6	6	7
σ[d] / kHz	3.1	0.6	4.4	4.7	3.0

[a] The quartic centrifugal distortion constants are fixed at those of the parent ^{12}C isotopologue of **I**.

[b] Errors in parenthesis are expressed in the units of the least significant digit.

[c] *N* is the number of rotational transitions included in the fit.

[d] σ is the standard deviation of the fit.

Table 4.4. Comparison of the rotational constants (in MHz) calculated at the three levels of theory with the experimental ones.

Conformers	*A*	*B*	*C*	*Dev. / %*[a]
		B3LYP-D3(BJ)/def2-TZVP		
I	3733	1724	1414	0.87
II	4173	1587	1267	0.10
III	3801	1642	1508	1.33
		B3LYP-D3(BJ)/6-311++G(2d,p)		
I	3721	1724	1414	0.77
II	4160	1587	1267	0.06
III	3787	1643	1511	1.13
		MP2/6-311++G(2d,p)		
I	3686	1753	1441	0.73
II	4179	1588	1273	0.27
III	3727	1680	1546	0.91

[a] Percentage deviation with respect to the experimental rotational constants in Table 4.2.

A 2.0-7.0 GHz experimental chirped pulse spectrum is depicted in Figure 4.4 a), while Figure 4.4 b) provides a zoom-in section of the spectrum, showing the 2_{11}-1_{10} transitions of the five ^{13}C isotopologues of conformer **I**. Stick spectra simulated using the experimental spectroscopic constants obtained for **I**, **II**, and **III** and their respective theoretical electric dipole moment components are also provided. The rotational temperature was fixed at 0.5 K, which is our empirical best-fit temperature for the 2.5-5.5 GHz data where the instrument behaves roughly in the linear intensity regime. By intensity-matching the predicted spectra to the experimental data, we can ascertain abundance ratios for each conformer. The relative abundances of **I** : **II** : **III** in the jet expansion were determined to 10 : 1 : 1. Interestingly, it appears that a rotational temperature of 1.5 K works best for **I**, whereas 0.5 K works better for **II** and **III**. A simulated spectrum with a rotational

temperature of 1.5 K is compared to the experimental spectrum in Figure 4.S2, Supporting Information, with an estimated abundance ratio of 10 : 1 : 1.6 for **I** : **II** : **III**. Since these minor changes do not alter the subsequent discussions, we will use the results estimated at 0.5 K for clarity and conciseness.

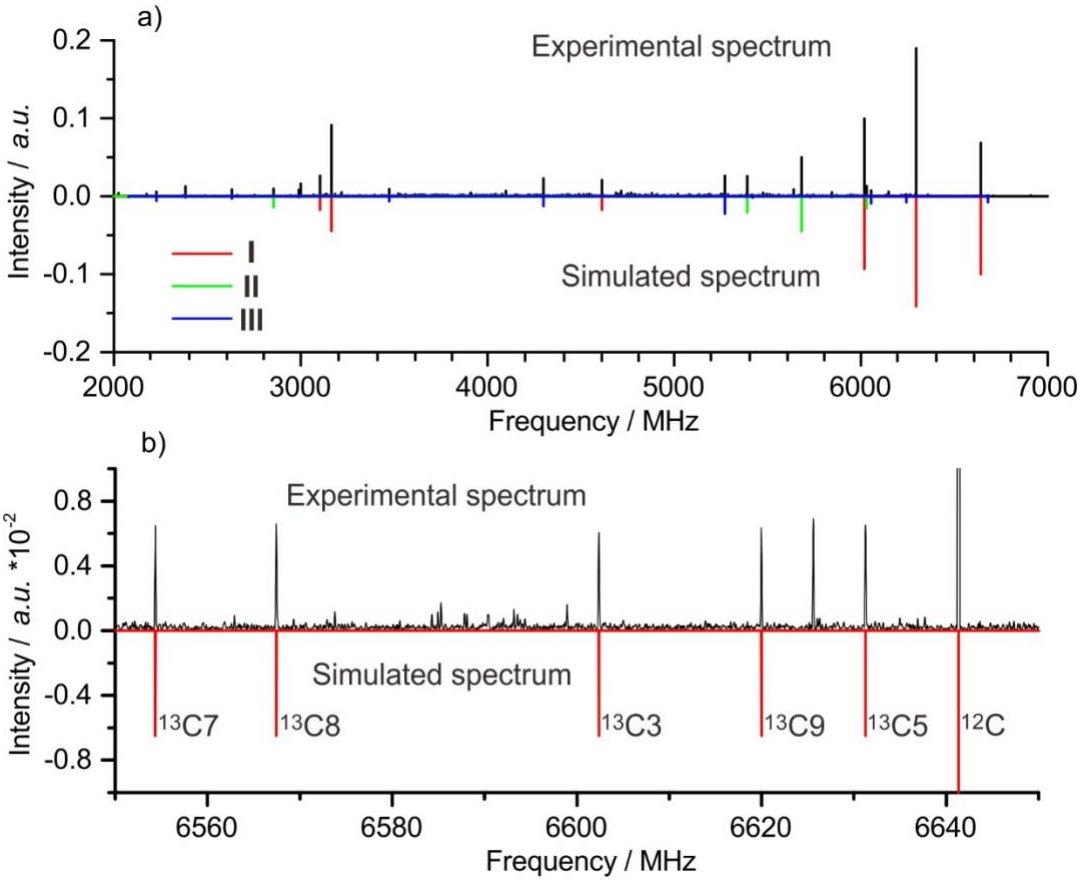

Figure 4.4. a) A 2.0-7.0 GHz experimental chirped pulse spectrum and the simulated rotational spectra of **I**, **II**, and **III** using the experimental spectroscopic constants, the permanent electric dipole moment components calculated at the B3LYP-D3(BJ)/def2-TZVP level, an estimated rotational temperature of 0.5 K, and the estimated relative abundances of **I** : **II** : **III** = 10 : 1 : 1. Please note that the simulated spectrum is already scaled with the estimated abundances. Without the scaling factors, the line intensities of **I** would be only 1/10 of what is plotted; b) A zoom-in section of the rotational spectrum

showing the 2_{11}-1_{10} transition of the five ^{13}C isotopologues and of the ^{12}C parent molecule of **I**. See the text for further discussion about the estimated rotational temperature.

4.2.4. Conformational conversion and collisional cooling

At the source temperature of ~353 K, the percentage abundance of conformers **I**-**VIII** are 53.6%, 29.0%, 6.7%, 4.2%, 3.4%, 3.1%, 0.0%, and 0.0%, respectively. As mentioned previously, the experimental abundances are **I** : **II** : **III** = 10 : 1 : 1, at odds with the prediction of 8 : 4.3 : 1. In addition, since all five ^{13}C isotopologues of **I** were observed in the 2.0-7.0 GHz chirped pulse spectrum, one may expect to detect conformers **I**-**VI** based on the abundances predicted above. For rotational spectra, one also needs to consider the permanent electric dipole moment components of each conformer. For example, the largest dipole moment components of **II**, **IV**, **V**, and **VI** are less than half in magnitude than that of **I**. Taking all these factors into account, it may be challenging to detect conformers **V** and **VI** since their line intensities would be smaller than that of the ^{13}C isotopologues of **I**, close to the detection limit of the current experiment.

To explain the noticeable depletion of **II** and the failure to detect **IV** in the supersonic jet expansion, we turn to examine the complex conformational landscape of THFA, focusing on the possible conformation conversion paths and the associated barriers. For example, for a weak to medium strength hydrogen-bonded complex, a conformational temperature of 100 K can commonly be assumed for a neon expansion and a bit higher in a helium expansion.[14] Earlier studies by Ruoff *et al.* suggest that the conformational ratio of a monomer at the source temperature is essentially maintained in a jet expansion if the conversion barrier is greater than ~4.8 kJ mol^{-1}, regardless of the carriers (i.e. He, Ne, Ar, Kr).[15] In a more recent study, Suhm and co-workers found that the facile O-H torsional motion in trifluoropropanol is cooled much more efficiently than the heavy C-O backbone torsion in a helium expansion.[16] Below, we discuss possible cooling mechanisms based on

three relevant motions: the rotation of the whole carboxyl group, the carboxyl OH torsional motion, and the ring puckering motions.

First, we consider all barriers which are much lower than the empirical cut-off value of 4.8 kJ mol^{-1} and assume that such low barriers would allow for a nearly complete population transfer from a high energy conformer to a low one in the jet expansion. Based on Figure 4.2, we expect that the very low initial populations of **VII** and **VIII** at the source temperature of 335 K would relax efficiently to **I** and **II** in the jet expansion because of the very low conformational conversion barriers of 1.7 and 0.7 kJ mol^{-1}, respectively. Similarly, if **IX** were a stable minimum, it would be expected to completely relax to **III**. In other words, these low conversion barriers do not affect the relative abundances of the conformers significantly. The ring puckering barriers for **IV→III**, and **VI→V** are 1.5 and 3.3 kJ mol^{-1}, respectively, as shown in Figure 4.5. One may anticipate a complete population transfer from **IV** to **III** and from **VI** to **V**, therefore raising the population of **III** to 10.9% and **V** to 6.5%, above the detection sensitivity of the instrument, while nearly no **IV** or **VI** population remains.

Second, we considered the **V→I** conversion which may proceed via two different transition states where the carboxyl OH group points either to the front or to the back (See Figure 4.3) and the corresponding the barriers are 40.6 and 42.9 kJ/mol (*ZPE* corrected), respectively. Similarly, the **VII→II** conversion may also proceed via two different transition states where the barriers are 38.9 and 44.5 kJ/mol (*ZPE* corrected). These very high conversion barriers are not expected to allow any population transfer.

Finally, we consider possible conformational conversion through barriers which are near the cut-off value of ~4.8 kJ mol^{-1}.[15] The ring puckering barrier for **II→I** is at 5.0 kJ mol^{-1} (Figure 4.5), whereas the other two corresponding barriers are 4.3 and 5.0 kJ mol^{-1} for **V→III** and **VI→IV**, respectively. We do not need to be concerned about **VI→IV** since the population of **VI** was already transferred to **V** as discussed above. Such a medium barrier may result in a partial population transfer in the jet expansion. For example, a

conformational temperature of 150 K would correspond to a noticeable population transfer from **II** to **I** and from **V** to **III**. In summary, the above discussion explains the mismatch between experimental conformer abundances and those expected assuming a Boltzmann distribution at the source temperature. In particular, the missing **V** conformer and the noticeable higher experimental abundance of conformer **I** versus **II** is now rationalized.

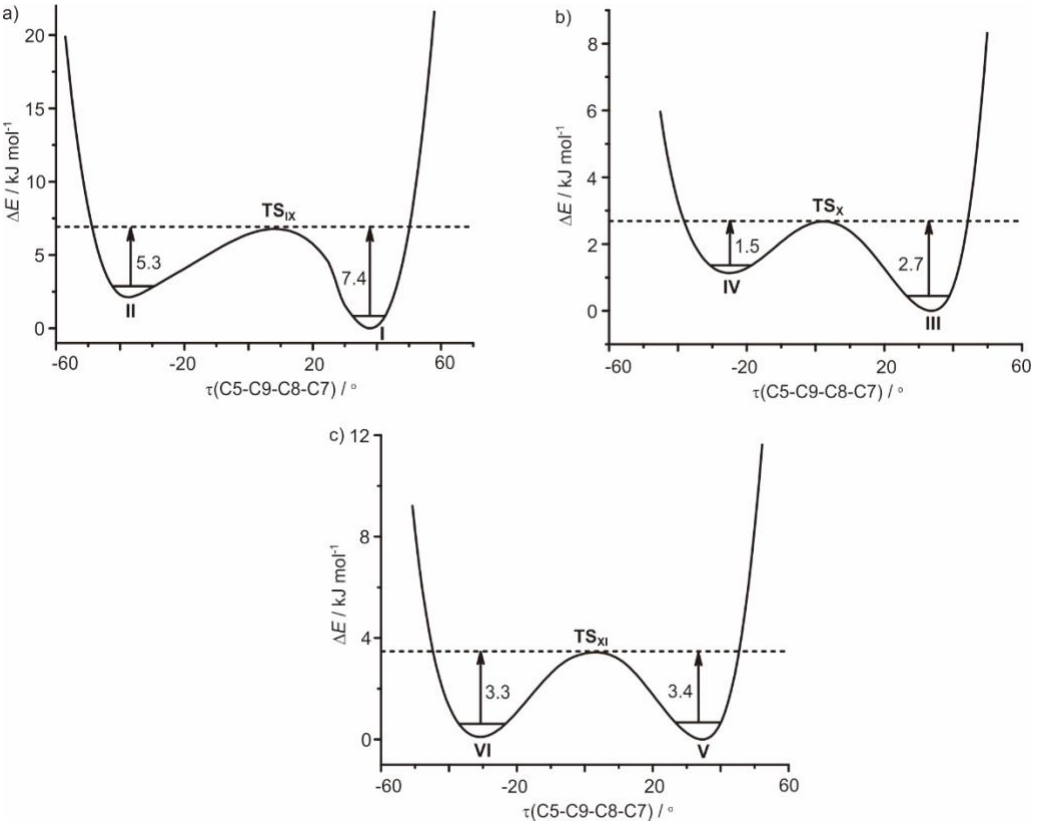

Figure 4.5. Three relaxed scans along the dihedral angle, τ(C5-C9-C8-C7), with three different starting geometries: a) conformer **I**; b) conformer **III**; and c) conformer **V**. The *ZPE* levels of these conformers are indicated with solid lines and the conversion barrier values shown are *ZPE* corrected. See the text for details.

We also carried out chirped pulse experiments using a helium expansion instead of neon and observed essentially the same conformational abundances as in neon. This is consistent with the report by Ruoff *et al.* that different rare gas carrier gases exhibit little differences in cooling of monomers.[15] In light of the discussion above, such insensitivity to the choice of carrier gas may simply be due to the particular conformational conversion barriers present in the system studied and the conclusion may have no general validity. Some beautiful conformational studies using FTMW spectroscopy have been reported before, such as the work on L-threonine[17] and on citronellal, where 15 conformers were identified experimentally.[18] In these studies, conversion barrier heights and effective conformational cooling in a jet expansion were used to explain the absence of some conformers, although not to the actual relative conformational abundances observed. Conformations generated by an OH rotation may warrant some special attention. In some situations where the conversion barrier is high, conformational cooling can still happen efficiently because of the small mass of the H-atom through so-called "incoherent tunneling" in a cold rare gas matrix[19] or in a jet expansion, such as in the case of N-methyl-4-piperidinol.[20]The current study demonstrates that significant insights into conformational landscapes can be achieved with more reliable intensity measurements using chirped pulse FTMW instruments and with extensive conformational modelling at a high level of theory. The study also emphasizes the importance of comprehensive conformational searches. One might draw erroneous conclusions from the difference between the experimental and theoretical relative abundances, without detailed consideration of conformational cooling.

4.2.5. H-bonding interactions and substitution structural analysis

To estimate the strength of the possible H-bonds in the three THFA conformers observed, we used the QTAIM program approach.[42, 21] We also applied the NCI program[43] to visualize non-covalent attractive and repulsive interaction regions. The results of QTAIM and NCI analyses are shown in Figure 4.6. The NCI analysis indicates strong attractive

interactions for the OH···O_{ester} close contacts in **I** and **II**. Similarly, bond critical points (BCPs) and bond paths are identified by the QTAIM analysis for these two close contacts as well. Interestingly, both NCI and QTAIM analyses show no specific non-covalent interaction between the OH group and the carboxylic O atom in the COOH group of **III**. Not surprisingly, a weak repulsive interaction is identified between the $O_{carboxylic}$ and O_{ester} atoms in **III**. The H-bond energies in **I** and **II** can be estimated using $E_{HB} \approx E_{BCP} = 0.5a_0^3V(r)$, where $V(r)$ is the electronic potential energy density at the corresponding BCP and a_0 is the Bohr radius.[22] The energies for the H-bonds identified in **I** and **II** are 40.6 and 38.1 kJ mol^{-1}, respectively. These medium strength H-bonds are certainly one major factor for the preference of **I** and **II** over other conformers.

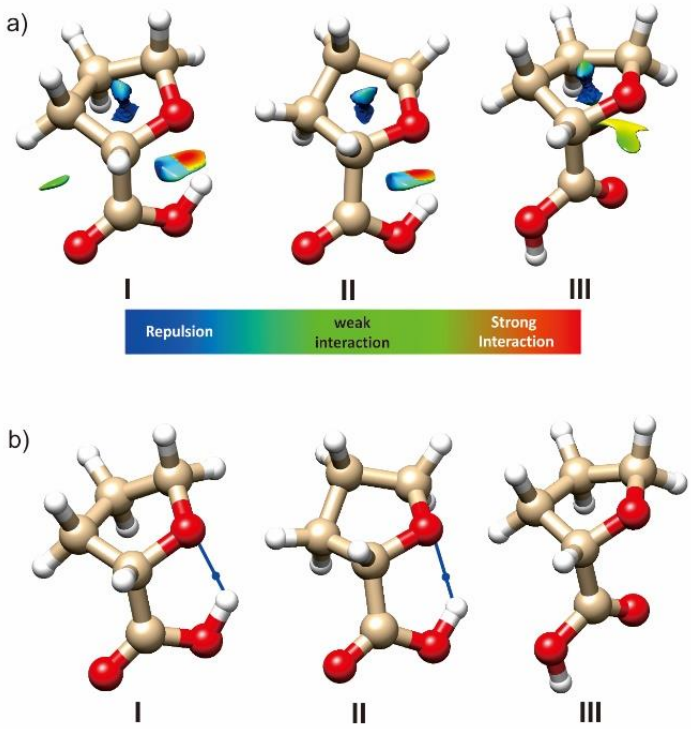

Figure 4.6. a) NCI analyses results of the non-covalent interactions present in the three observed THFA conformers **I**, **II**, and **III**. The NCI iso-surfaces (s = 0.60) of **I**, **II**, and **III** conformer structures calculated at the B3LYP-D3(BJ)/def2-TZVP level of theory are

shown. b) QTAIM analyses of **I**, **II**, and **III**. The BCPs and bond paths identified are indicated by the blue dots and lines, respectively.

The Kraitchman[23] coordinates of the five carbon atoms were calculated by using the ^{12}C isotopologue as the parent species. The substitution coordinates with the associated Costain errors[24] and the related structural parameters obtained are summarized in Table 4.5, alongside the corresponding theoretical values of the B3LYP-D3(BJ)/def2-TZVP and MP2/6-311++G(2d,p) structures. Since only the absolute coordinates are obtained by the substitution procedure, the signs of the substitution coordinates are assigned so that the atomic distances are physical. A subset of coordinates for the C3 and C5 atoms are near zero, resulting in imaginary values, a well-known issue associated with the Kraitchman's substitution procedure.[24] Generally, the agreement between the experimental and theoretical bond lengths is good, although somewhat worse compared to a recently studied system, 1-phenyl-2,2,2-trifluoroethanol,[28a] perhaps reflecting the difficulty in accurately predicting the THF ring structural parameters. The experimental and theoretical angles and dihedral angles are in good agreement with each other. Overall, based on the similarity of the experimental and theoretical structural parameters, we are confident that conformer **I** takes on the *envelope* ring configuration, as predicted.

Table 4.5. Comparison of the Kraitchman coordinates, bond lengths, angles, and dihedral angles with the theoretical predictions at the B3LYP-D3(BJ)/def2-TZVP and MP2/6-311++G(2d,p) levels of theory.

	Exp. Kraitchman's Coord. / Å		
Atom	*a*	*b*	*c*
C3	-1.3419(12)[a]	0.0[b]	0.0[b]
C5	0.0[b]	0.1846(94)	0.7752(22)
C7	1.98352(89)	-0.6534(27)	-0.122(15)
C8	1.66514(95)	0.6497(24)	-0.8318(19)
C9	0.7664(21)	1.3648(12)	0.2415(66)

Structural Parameter	Kraitchman	B3LYP-D3(BJ)
r(C3-C5) / Å	1.561(12)	1.5337
r(C9-C5) / Å	1.5051(92)	1.5312
r(C9-C8) / Å	1.5719(50)	1.5312
r(C7-C8) / Å	1.5176(76)	1.5527
A(C3-C5-C9) / °	110.76(75)	112.41
A(C5-C9-C8) / °	100.17(31)	102.10
A(C9-C8-C7) / °	101.03(47)	101.87
τ(C3-C5-C9-C8) / °	92.24 (76)	93.27
τ(C5-C9-C8-C7) / °	37.53(43)	36.33

[a] Costain errors in units of the least significant digits are given in brackets.

[b] Non-physical values are set to 0.0.

Based on the in general good agreement between the experimental and theoretical rotational constants, we conclude that **I**, **II**, and **III** all take on the *envelope* ring configuration as predicted. THFA exhibits thus the same preference for the *envelope* ring configuration as the THF monomer. On the other hand, the most stable minimum is no longer E^O or E_O as in THF.[2] In fact, E^O or E_O are not minima in the case of THFA. While ${}^{\beta}T_{\beta'}$ and ${}^{\beta'}T_{\beta}$ are the two equivalent second most stable minima which are fairly close in the energy as E^O and E_O in THF, the *twist* ring configuration, i.e. **VI**, appears only as a much higher energy conformer in THFA. All this highlights the effect of the COOH substitution on the preferred ring configuration in THFA.

4.3. Conclusions

Rotational spectra of THFA were recorded using two broadband CP-FTMW spectrometers and one cavity-based FTMW spectrometer. Exhaustive conformational searches were carried out using the semiempirical GFN-xTB-CRE program and manually in a step wise fashion. Both searches arrived at the same eight conformers identified at the MP2 and B3LYP-D3(BJ) levels of theory with two different basis sets, i.e. 6-311++G(2d,p) and def2-TZVP. The three most stable conformers predicted, i.e. **I**, **II**, and **III**, were observed experimentally and conclusively assigned, although the experimental relative abundances differ drastically from the theoretically predicted abundances. Further extensive theoretical searches were done to identify the conformation conversion paths and the associated barriers. These details of the THFA conformational landscape were used successfully to explain the experimental conformational abundances in terms of some very low conformational conversion barriers and the near total population transfer of several higher energy conformers, as well as the medium conformational conversion barrier and

collisional cooling of **II** to **I** in a jet expansion. The current combined experimental and theoretical investigation thus provides a great deal of new insights into the very complex conformational landscape of THFA.

4.4. Experimental and computational details

Rotational spectra of THFA in the 2-6 GHz and 8-18 GHz regions were measured using two chirped pulse FTMW spectrometers and in the 8-18 GHz region also with a Balle-Flygare type [25] cavity-based FTMW spectrometer, [26] coupled with a supersonic jet expansion. The 2-6 GHz and 8-18 GHz chirped pulse FTMW spectrometers were built based on the pioneering work of Pate and others[27] and have been described before.[28,29] In the 2-6 GHz set up, a 1 μs long chirped (2-6 GHz) excitation pulse is produced with a 12 GS/s arbitrary waveform generator (AWG) and amplified by a 400 W, 2.5-7.5 GHz, travelling wave tube (TWT) amplifier. The mismatch in the frequency cut-off of the TWT and chirp is a result of cost considerations, although the TWT still provides sufficient gain in the 2.0-2.5 GHz region. Interestingly, we were also able to detect transitions above 6 GHz, i.e. up to 7.0 GHz. We assume that non-linearities either in the AWG or the TWT generate a frequency-doubled chirp from 4.0 to 12.0 GHz, which provides sufficient power into the 7.5 GHz range. However, the sensitivity responses at both extrema of the band are somewhat lower than in the middle, due to instrumental effects. A pair of identical 62 cm high gain microwave horn antennas, situated perpendicular to the pulsed molecular beam, are used to broadcast the chirped pulse into the sample region of the spectrometer and to receive the resulting molecular free induction decay (FID) signal which is then amplified and detected for over a time of 20 μs. For each gas pulse, six excitation/detection sequences are performed. A 25 GS/s mixed signal digital oscilloscope is used to record and average the FID signals. After zero padding and application of a Kaiser-Bessel window function, the final averaged FID is Fourier transformed to give the frequency spectrum. In the current

study, initial survey scans were taken in the 8-18 GHz region and final frequency measurements in this region were done with the cavity FTMW instrument. In the low frequency region, ca. 800,000 FIDs were averaged over 18 hours. The spectral resolution and accuracy of the broadband instruments are 25 and ca. 12 kHz, respectively. The frequency uncertainty is 2 kHz and the full line width at half height is 10 kHz in case of the cavity FTMW instrument.

For the 8-18 GHz chirped and cavity experiments, THFA liquid was placed in a stainless-steel reservoir right behind a General Valve nozzle and neon gas at backing pressures of 2-4 bar was flowed over the sample to bring a trace amount of THFA into the sample cavity. For the 2-6 GHz chirped pulse experiments, THFA liquid was placed directly inside a modified General Valve nozzle cap and 2-4 bar of helium or neon was used as carrier gas. The sample was heated to 70-90 °C in all experiments.

High level *ab initio* calculations were performed with the Gaussian 16 suite of programs[30] using wavefunction calculations at the level of second-order Møller-Plesset perturbation theory (MP2)[31] and also DFT calculations, using the B3LYP functional[32] with D3 dispersion corrections[33] and Becke-Johnson damping,[34] i.e. B3LYP-D3(BJ). The basis sets used were 6-311++G(2d,p)[35] and def2-TZVP developed by the group of Ahlrichs.[36] Several one-dimensional relaxed dihedral angle scans were performed at the B3LYP-D3(BJ) level of theory, utilizing the algorithm developed by Schlegel and co-workers,[37] in order to identify possible low energy THFA conformers.

For conformational searches, we used GFN-xTB,[38] a semiempirical tight-binding (TB) quantum chemistry code, designed for prediction of equilibrium structural properties, such as Geometries, vibrational Frequencies, and Non-covalent interactions. “x” in the name refers to the eXtended special purpose TB variant[39] which uses an augmented atomic orbital (AO) basis set, in contrast to the minimal AO basis sets typically employed by most semiempirical methods. GFN-xTB is parameterized to cover all *spd*-block elements and

the lanthanides up to Z=86. In particular, we utilized the recently implemented "CRE" (an abbreviation for Conformer/Rotamer Ensemble) method in GFN-xTB[40] to search for conformers. The CRE generation utilizes a composite algorithm which consists of normal mode following, genetic structure crossing, and long molecular dynamics (about 1-2 ns) based on simulated annealing.[41]

Quantum theory of atoms-in-molecules (QTAIM)[42] and non-covalent interactions (NCI)[43] analyses were performed to visualise the weak interactions involved in the observed THFA conformers and also to estimate the strengths of the intramolecular hydrogen (H)-bonds. The QTAIM analysis was visualized with both Avogadro[44] and MultiWFN[45], while the NCI analysis was visualized with Chimera.[46] For consistency, the *S*-THFA enantiomer is used for the presentation of the results through the paper.

References

[1] G. G. Engerholm, A. C. Luntz, W. D. Gwinn, and D. O. Harris, *J. Chem. Phys.* **50**, 2446 (1969).

[2] V. M. Rayón and J. A. Sordo, *J. Chem. Phys.* **122**, 204303 (2005).

[3] R. Meyer, J. C. López, J. L. Alonso, S. Melandri, P. G. Favero, and W. Caminati, *J. Chem. Phys.* **111**, 7871 (1999).

[4] A. H. Mamleev, L. N. Gunderova, and R. V. Gallev, *J. Struct. Chem.* **42**, 365 (2001).

[5] D. G. Melnik, S. Gopalakrishnan, T. A. Miller, and F. C. De Lucia, *J. Chem. Phys.* **118**, 3589 (2003).

[6] A. Wu, D. Cremer, *Int. J. Mol. Sci.* **4**, 158-192 (2003).

[7] G. Vallancien, M. Emberton, A. Alcaraz, H. Matzkin, R. J. A. van Moorselaar, R. Hartung, N. Harving, M. Elhilali, *BJU Int.* **101**, 847–852 (2008).

[8] I. Elia, D. Broekaert, S. Christen, R. Boon, E. Radaelli, M. F. Orth, C. Verfaillie, T. G. P. Grünewald, S.-M. Fendt, *Nat. Commun.* **8**, 15267 doi: 10.1038/ncomms15267 (2017).

[9] M. Zhang, T. A. White, J. P. Schuermann, B. A. Baban, D. F. Becker, J. J. Tanner, *Biochem.* **43**, 12539–12548 (2004).

[10] J. Bellet, A. Deldalle, C. Samson, G. Steenbeckeliers, R. Wertheimer, J. Mol. Struct. **9**, 65 (1971).

[11] F. W. Lichtenthaler, In *Ullmann's Encyclopedia of Industrial Chemistry*; Wiley-VCH Verlag GmbH & Co. KGaA: Weinheim, Germany, 2003.

[12] C. M. Western, B. E. Billinghurst, *Phys. Chem. Chem. Phys.* **19**, 10222–10226 (2017).

[13] J. K. G. Watson, in *Vibrational Spectra and Structure*, Vol. 6 (Ed.: J. R. Durig), Elsevier, New York, pp. 1- 89, (1977).

[14] a) N. Borho, Y. Xu, *Phys. Chem. Chem. Phys.* **9**, 4514–4520 (2007); b) N. Borho, Y. Xu, *Angew. Chem. Int. Ed.* **46**, 2276–2279 (2007); *Angew. Chem.* **119**, 2326–2329 (2007).

[15] R. S. Ruoff, T. D. Klots, T. Emilsson, H. S. Gutowsky, *J. Chem. Phys*. **93**, 3142-3150 (1990).

[16] M. Heger, K. E. Otto, R. A. Mata, M. A. Suhm, *Phys. Chem. Chem. Phys.* **17**, 9899-9909 (2015).

[17] J. L. Alonso, C. Pérez, M. E. Sanz, J. C. López, S. Blanco, *Phys. Chem. Chem. Phys.* **11**, 617-627 (2009).

[18] S. R. Domingos, C. Pérez, C. Medcraft, P. Pinacho, M. Schnell *Phys. Chem. Chem. Phys.* **18**, 16682-16689 (2016).

[19] P. R. Schreiner, H. P. Reisenauer, F. C. Pickard IV, A. C. Simmonett, W. D. Allen, E. Mátyus, and A. G. Császár, Nature **453**, 906 (2008).

[20] J. Thomas, E. Mariona, Y. Xu, *J. Chem. Phys.* **146**, 104303 (2017).

[21] a) M. Petković and M. Etinski, *RSC Adv*. **4**, 38517-38526 (2014); b) O. O. Brovarets, R. O. Zhurakivsky and D. M. Hovorun, *J. Comput. Chem*. **35**, 451-466 (2014).

[22] a) E. Espinosa, E. Molins, C. Lecomte, *Chem. Phys. Lett*. **285**, 170-173 (1998); b) I. Mata, I. Alkorta, E. Espinosa, E. Molins, *Chem. Phys. Lett*. **507**, 185-189 (2011).

[23] J. Kraitchman, *Am. J. Phys.* **21**, 17−24 (1953).

[24] C. C. Costain, *J. Chem. Phys.* **29**, 864−874 (1958).

[25] T. J. Balle, E. J. Campbell, M. R. Keenan, W. H. Flygare, *J. Chem. Phys.* **72**, 922–932 (1980).

[26] Y. Xu, W. Jäger, *J. Chem. Phys.* **106**, 7968-7980 (1997).

[27] a) G. G. Brown, B. C. Dian, K. O. Douglass, S. M. Geyer and B. H. Pate, *J. Mol. Spectrosc.* **238**, 200-212 (2006); b) G. S. Grubbs II, C. T. Dewberry, K. C. Etchison, K. E. Kerr and S. A. Cooke, *Rev. Sci. Instrum.* **78**, 096106/1-3 (2007); c)

C. Pérez, S. Lobsiger, N. A. Seifert, D. P. Zaleski, B. Temelso, G. C. Shields, Z. Kisiel, B. H. Pate, *Chem. Phys. Lett.* **571**, 1–15 (2013).

[28] a) C. D. Carlson, N. A. Seifert, M. Heger, F. Xie, J. Thomas and Y. Xu, *J. Mol. Spectrosc.* **351**, 62–67 (2018); b) N. A. Seifert, J. Thomas, W. Jäger and Y. Xu, *Phys. Chem. Chem. Phys.* (submitted).

[29] a) S. Dempster, O. Sukhrukov, Q. Y. Lei and W. Jäger, *J. Chem. Phys.* **137**, 174303/1-8 (2012); b) J. Thomas, J. Yiu, J. Rebling, W. Jäger and Y. Xu, *J. Phys. Chem. A*. **117**, 13249-13254 (2013).

[30] Gaussian 16, Revision B.01, M. J. Frisch, G. W. Trucks, H. B. Schlegel, G. E. Scuseria, M. A. Robb, J. R. Cheeseman, G. Scalmani, V. Barone, G. A. Petersson, H. Nakatsuji, X.; Li, M. Caricato, A. V. Marenich, J. Bloino, B. G. Janesko, R. Gomperts, B. Mennucci, H. P.. Hratchian, J. V. Ortiz, A. F. Izmaylov, J. L. Sonnenberg, D. Williams-Young, F. Ding, F. Lipparini, F. Egidi, J. Goings, B. Peng, A. Petrone, T. Henderson, D. Ranasinghe, V. G. Zakrzewski, J. Gao, N. Rega, G. Zheng, W. Liang, M. Hada, M. Ehara, K. Toyota, R. Fukuda, J. Hasegawa, M. Ishida, T. Nakajima, Y. Honda, O. Kitao, H. Nakai, T. Vreven, K. Throssell, J. A. Montgomery Jr., J. E. Peralta, F. Ogliaro, M. J. Bearpark, J. J. Heyd, E. N. Brothers, K. N. Kudin, V. N. Staroverov, T. A. Keith, R. Kobayashi, J. Normand, K. Raghavachari, A. P. Rendell, J. C. Burant, S. S. Iyengar, J. Tomasi, M. Cossi, J. M. Millam, M. Klene, C. Adamo, R. Cammi, J. W. Ochterski, R. L. Martin, K. Morokuma, O. Farkas, J. B. Foresman, D. J. Fox, Gaussian, Inc., Wallingford CT, 2016.

[31] J. S. Binkley and J. A. Pople, *Int. J. Quantum Chem.* **9**, 229-236 (1975).

[32] S. Grimme, S. Ehrlich and L. Goerigk, *J. Comp. Chem.* **32**, 1456-1465 (2011).

[33] S. Grimme, S. Ehrlich and L. Goerigk, *J. Comput. Chem.* **32**, 1456–1465 (2011).

[34] A. D. Becke and E. R. Johnson, *J. Chem. Phys.* **123**, 154101 (2005).

[35] R. Krishnan, J. S. Binkley, R. Seeger, and J. A. Pople, *J. Chem. Phys.* **72**, 650-654 (1980).

[36] a) F. Weigend and R. Ahlrichs, *Phys. Chem. Chem. Phys.* **7**, 3297 (2005); b) A.

Schäfer, H. Horn and R. Ahlrichs, *J. Chem. Phys.* **97**, 2571–5648 (1992); c) A. Schäfer, C. Huber and R. Ahlrichs, *J. Chem. Phys.* **100**, 5829–5835 (1994).

[37] a) H. B. Schlegel, *J. Comp. Chem.* **3**, 214-218 (1982); b) C. Peng and H. B. Schlegel, *Isr. J. Chem.* **33**, 449-454 (1993); c) C. Peng and H. B. Schlegel, *Isr. J. Chem.* **33**, 449-454 (1993); d) X. Li and M. J. Frisch, *J. Chem. Theory Comp.* **2**, 835-839 (2006).

[38] S. Grimme, C. Bannwarth, and P. Shushkov, *J. Chem. Theory Comput.* **13**, 1989-2009 (2017).

[39] S. Grimme and C. Bannwarth, *J. Chem. Phys.* **145**, 054103 (2016).

[40] S. Grimme, C. Bannwarth, S. Dohm, A. Hansen, J. Pisarek, P. Pracht, J. Seibert, and F. Neese, *Angew Chem. Int. Ed.* **56**, 14763-14769 (2017); *Angew. Chem.* **129**, 14958-14964 (2017).

[41] S. Kirkpatrick, C. D. Gelatt, Jr., and M. P. Vecchi. *Science* **220**, 671-680 (1983).

[42] R. F. W. Bader, *Chem. Rev.* **91**, 893-928 (1991).

[43] E. R. Johnson, S. Keinan, P. Mori-Sánchez, J. Contreras-García, A. J. Cohen, W. Yang, J. Am. Chem. Soc. **132**, 6498-6506 (2010).

[44] M. D. Hanwell, D. E. Curtis, D. C. Lonie, T. Vandermeersh, E. Zurek, G. R. Hutchinson, J. Cheminformatics, **4**, 1-17 (2012). Version 4.8.6.

[45] T. Lu, F. Chen, J. Comp. Chem. **33**, 580-592 (2012).

[46] E. F. Pettersen, T. D. Goddard, C. C. Huang, G. S. Couch, D. M. Greenblatt, E. C. Meng, T. E. Ferrin, J. Comp. Chem. **25**, 1605-1612 (2004). Version 1.12.

Chapter 5

Conformational Landscape, Chirality Recognition and Chiral Analyses: Broadband Rotational Spectra of the Tetrahydro-2-Furoic Acid···Propylene Oxide Conformers

5.1. Introduction

Rotational spectroscopic studies of chiral molecular contact pairs, which are bound by non-covalent intermolecular forces and produced and stabilized in a supersonic jet expansion, have been provided considerable insight into the chirality-controlled structural preference.[1-5] The advent of the chirped pulse-Fourier transform microwave (CP-FTMW) technique[6], together with these fundamental spectroscopic investigations, has led to the development of chiral-tag rotational spectroscopy for determination of chirality and enantiomeric excess (ee),[7-9] a method which may potentially see wide industrial application. In this paper, we investigate a chiral contact pair consisting two prototype chiral molecules, namely tetrahydro-2-furoic acid (THFA) and propylene oxide (PO) using CP-FTMW spectroscopy and theoretical modelling.

Carboxylic acids occur widely in nature, for example in amino acids and fatty acids, and play an important role in chemistry and biology. A carboxylic acid contains a carboxyl group and can act both as a H-bond acceptor and a donor, leading to rich non-covalent binding topologies in various chemical and biological molecular systems. Of particular interest in the present study is THFA, a chiral carboxylic acid. THFA exhibit a strong preference for the *trans*-COOH over *cis*-COOH configuration, different from the more common situations where the latter is favoured over the former one.[10] Further CP-FTMW study of its dimers reveals very complex conformational landscapes and fascinating chirality-controlled structural preference, enriching our knowledge of *cis*- versus *trans*-COOH and intra- versus intermolecular H-bonding competitions.[7] A detailed knowledge of these competitions is crucial when dealing much more complicated molecular systems. Propylene oxide (PO), is a simple chiral molecule with a fair rigid geometry except for its methyl group internal rotation, and exists in only one conformation. This simplicity is one main reason that PO has been widely used as a model chiral molecule in the development of theoretical treatments of chiroptical spectroscopies, such as vibrational circular dichroism, including its anharmonic treatment,[11-13] and in understanding solvent

effects.[14-16] Not surprisingly, PO is one of the earliest chiral molecules investigated using rotational spectroscopy[17,18] and the first chiral molecule detected in space based on its rotational transitions.[19] PO is known to bind to other molecules utilizing its ester oxygen atom, whereas its methyl group may serve as additional binding site or as steric hinderance. For example, in rare gas-PO[20-23] and CO_2-PO[24], rare gas atom and CO_2 prefer to stay at the *anti*-position, i.e. opposite from the CH_3 group, whereas in the mono- and dihydrate of PO, water prefers to stay in the *syn*-position.[25,26] In addition, rotational spectra of several PO containing homo-/heterochiral dimers[20,27-31] and even PO trimer[32] were analyzed, uncovering the complex conformational panorama and rich structural diversity associated with these binary and ternary chiral clusters.

In the current study, we focus on conformational landscape and effects of chirality recognition in the THFA···PO contact pair. In particular, it would be of considerable interest to uncover the structure-energy relationship introduced by the *cis* versus *trans*-COOH competition in the THFA···PO conformers. Furthermore, we apply chiral-tag strategy to analyze ee of several ad hoc mixtures to evaluate consistency of chiral-tag experimental results.

5.2. Results and Discussion

5.2.1. Conformational searches

The THFA monomer exists dominantly as three conformers in a neon or helium pulse jet expansion: THFA **I**, THFA **II** (both in the *trans*-COOH configuration) and THFA **III** in the *cis*-COOH configuration.[7,10] Even though PO has only one conformer, a rich diversity of structures is still expected with consideration of the *cis/trans* preference of THFA and the *syn/anti* binding topologies of PO. To systematically search for the possible conformers, a powerful conformational exploration program named CREST (conformer-rotamer ensemble sampling tool) was used. This conformational search tool has been utilized in a number of recent rotational spectroscopic studies successfully to sample complicated conformational landscape of organic molecules and the related non-covalently bonded clusters.[33-35] About a few hundred initial conformers generated by CREST[36-38], a conformer-rotamer ensemble sampling tool by Grimme and co-workers, were reoptimized at the B3LYP-D3(BJ)/def2-TZVP level of theory with dispersion corrections and Becke-Johnson damping[39]. Further corresponding harmonic frequency calculations were performed to verify the true minimum nature of these geometries and provide zero-point-energy (ZPE) corrections.

The above comprehensive conformational searches generated about two hundred structures with an energy window of up to 40 kJ mol^{-1}, including both homochiral and heterochiral THFA···PO conformers. To facilitate the spectral analyses, we classify these conformers into three types based on their intermolecular interaction topologies. The ranges of the binding energies and relative stabilities of the three types of structures are provided in Figure 5.1, following a similar pattern observed for the THFA dimers.[7]

In **Type 1**, the H atom of *cis*-COOH is hydrogen-bonded to the ether oxygen atom, while the carbonyl oxygen atom interacts with two CHs of PO. In Type 2, the H atom of *trans*-COOH is hydrogen-bonded to the ether oxygen atom of PO, leading to some degree of

opening of its intramolecular hydrogen-bonded ring. In addition, two H atoms of the methyl group of PO from attractive contacts with the two oxygen atoms of THFA. In Type 3, the proton of COOH is absent from the intermolecular interactions with PO, i.e. the intramolecular hydrogen-bonded ring is essential untouched. This is the major difference compare to the other two types. The main attractive interactions in Type 3 are from the weak CH···O interactions. We name the THFA···PO conformers using the conformation of the THFA subunit and the corresponding intermolecular interactions. For example, **III**(v_a) contains a THFA subunit, **III**, and has "a" van der Waals interaction. Based on the previous study of the THFA monomer[10], there are two *trans*-COOH and four *cis*-COOH THFA conformers possible. If we consider both homo- and heterochiral combinations and one or two van der Waals contacts, we would have 16 **Type 1**, 8 **Type 2** and 4 **Type 3** conformers. In total, there are 28 THFA···PO candidate structures. The calculated spectroscopic constants and relative energies of these 28 structures are listed in Table S5.1, Supporting Information.

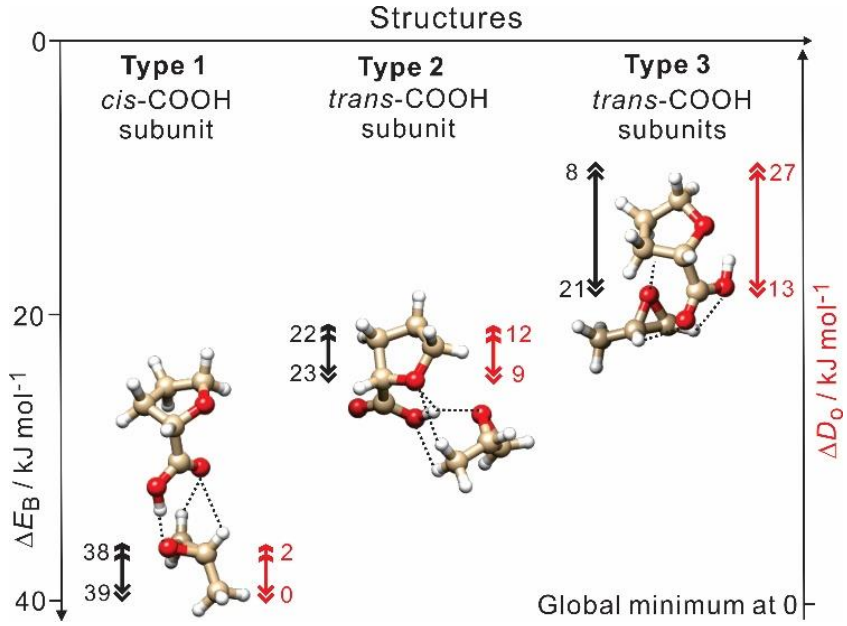

Figure 5.1. Three types of THFA···PO with their characteristic binding topologies and the THFA subunit used in each type. The range of the ΔE_B (in black) and ΔD_o (in red) values for each type are also indicated given. ΔE_B, defined as the difference between the dimer and its subunits, is corrected for *ZPE* and basis set superposition errors (*BSSE*s), calculated using the counterpoise procedure. Close contacts between THFA and PO are indicated with dashed lines.

We further classified each type of structures into several subcategories based on their different binding geometries. In Figure 5.2, the most stable structures of each subcategory are depicted. It was discovered experimentally and verified by potential energy scans and transition state calculations that the *trans*-COOH conformers all cool to THFA **I** with minor **II** residual, while for the *cis*-COOH conformers, only **III** survives in a jet expansion. Such cooling becomes even more efficient with hydrogen-bonding interactions with another THFA molecule and only **I** and **III** survive in the THFA dimers in a jet expansion. A similar outcome is expected here, leading to the ten THFA···PO conformers depicted in Figure 5.2. The calculated relative raw dissociation energies, ZPE corrected relative energies and spectroscopic constants of the eight conformers are list in Table 5.1.

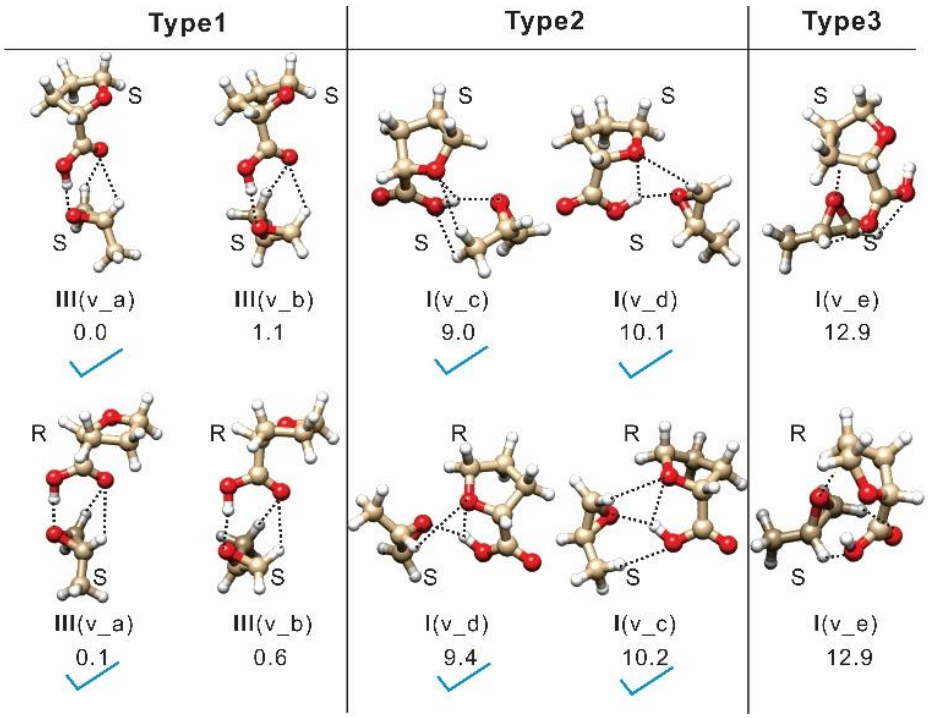

Figure 5.2. Representative homochiral (first row) and heterochiral (second row) geometries of the three types of THFA···PO geometries. Blue checkmarks indicate the conformers observed. The ΔD_0 values with respective to the global minimum are also given in unit of kJ mol^{-1}.

Table 5.1. Relative raw (ΔD_e) and ZPE corrected (ΔD_0) energies (in kJ mol^{-1}), rotational constants (in MHz), and electric dipole moment components (in Debye) of homochiral and heterochiral THFA···PO conformers, calculated at the B3LYP-D3(BJ)/def2-TZVP level of theory.

Conformer	ΔD_e	ΔD_0	A	B	C	$\lvert\mu_a\rvert$	$\lvert\mu_b\rvert$	$\lvert\mu_c\rvert$
SS-**III**(v_a)[a]	0	0	2286	373	366	1.2	0	1.8
SS-**III**(v_b)	1.5	1.1	1934	430	415	1.5	2.5	0.8
SS-**I**(v_c)	8.7	9	1329	607	505	2.8	4.1	0.7
SS-**I**(v_d)	9.5	10.1	1469	529	432	2.4	4.4	0.9
SS-**I**(v_e)	12.8	12.9	1373	594	512	0.7	2.9	0.5
Conformer	ΔD_e	ΔD_0	A	B	C	$\lvert\mu_a\rvert$	$\lvert\mu_b\rvert$	$\lvert\mu_c\rvert$
SR-**III**(v_a)	0.2	0.1	2071	384	375	1.5	1.8	1
SR-**III**(v_b)	1.1	0.6	2087	408	398	1.3	0.7	1.1
SR-**I**(v_d)	8.9	9.4	1367	589	467	3.5	3.9	0.4
SR-**I**(v_c)	9.6	10.2	1368	600	460	2.2	4.5	0.9
SR-**I**(v_e)	12.8	12.9	1378	580	525	0.9	2.8	0.2

[a] Red color indicates the conformers detected experimentally.

5.2.2. Spectral assignment and analysis

Broadband spectra of THFA···PO recorded in the 2-6 GHz range show extremely dense transitions. It turned out that THFA and PO both give rise to a huge number of transitions on their own in a jet expansion. This poses a challenge to identify transitions related to THFA···PO. After some consideration, this problem was solved by a brute force approach. Separate spectra were recorded under similar experimental conditions with a sample of racemic THFA and of racemic PO alone. After that, all transitions with s/n >5 in these two spectra were subtracted from the spectrum obtained with a sample of THFA+PO. Among the transitions subtracted, many of them belong to the known transitions of Ne···PO[20], PO···$H_2O_{1,2}$[25,26], $(PO)_{2,3}$,[23,32] $THFA_{1,2}$[7,10] and THFA···H_2O, in addition to some so far unassigned transitions. The after-cutting spectrum of THFA···PO reveals clear *b*-type R-

brunch patterns (Figure 5.3). Four sets of such *b*-type transitions were assigned. Their carriers can be identified as **Type 2** conformers, SS-**I**(v_c), SS-**I**(v_d), SR-**I**(v_c) and SR-**I**(v_d), based on the comparison of the experimental and predicted rotational constants, as well as the relative electric dipole moment components. Later on, two sets of weak transitions, showing characteristics of near prolate *a*-type patterns, were assigned to **Type 1** conformers SS-**III**(v_a) and SR-**III**(v_a). In summary, totally six THFA···PO conformers were identified and their rotational transitions were fitted using Watson's *S*-reduction Hamiltonian[40] in its I^r representation with the Pgopher program.[41] The resulting experimental spectroscopic constants are list in Table.5.2, while the related six sets of experimental transitions are given in Table S5.2-S5.7, Supporting Information.

Table 5.2. Experimental spectroscopic constants[a] of the six THFA···PO conformers observed.

	SS-**III**(v_a)	SS-**I**(v_c)	SS-**I**(v_d)
A / MHz	2278.954(4)	1345.9723(2)	1479.6033(3)
B / MHz	374.276(5)	592.75389(8)	521.8846(1)
C / MHz	367.312(5)	497.74598(9)	431.2069(1)
D_K / kHz	5.1(9)	0.079(10)	0.35(2)
D_{JK} / kHz	-0.25(5)	0.256(2)	0.296(3)
D_J / kHz	0.017(3)	0.141(1)	0.092(1)
d_1 / kHz	-4.5(2.4)	-0.006(3)	0.130(5)
d_2 / kHz	0.002(1)	0.0258(2)	0.0178(2)
Dipole comp.[b]	$\mu_c > \mu_a$ no μ_b	$\mu_b > \mu_a$ no μ_c	$\mu_b > \mu_a$ no μ_c
N	36	103	117
σ / kHz	4.8	2.4	3.9
	SR-**III**(v_a)	SR-**I**(v_d)	SR-**I**(v_c)
A / MHz	2062.414(3)	1385.2740(2)	1380.8259(2)
B / MHz	385.198(2)	578.63539(9)	586.11421(8)
C / MHz	376.271(2)	462.92997(9)	455.52390(8)

D_K / kHz	2.7(5)	-0.008(1)	0.33(1)
D_{JK} / kHz	-0.65(2)	0.362(2)	0.085(2)
D_J / kHz	0.053(2)	0.157(1)	0.1425(7)
d_1 / kHz	1.3(1.1)	0.433(3)	0.322(3)
d_2 / kHz	-0.0014(3)	0.0230(2)	0.0431(2)
Dipole comp.[b]	$\mu_b > \mu_a$ *no* μ_c	$\mu_b \approx \mu_a$ no μ_c	$\mu_b > \mu_a$ no μ_c
N	37	115	115
σ / kHz	3.2	3.0	3.0

[a] A, B, C = rotational constants, μ = dipole components in Debye and ***only*** the types observed are indicated with their estimated relative magnitudes, N = number of transitions in the fit, and σ = standard deviation in kHz.

[b] The relative magnitude of the permanent dipole moment components, estimated from the experimental transition intensities.

An overview of the experimental spectrum and the fitted spectra of the six THFA···PO conformers assigned are shown in Figure 5.3. To estimate the rotational temperature, a Python routine reported before[7] was used to compare experimental intensities with the simulated ones obtained from Pgopher using the experimental spectroscopic constants, the theoretical dipole moment components, a rotational temperature which steps from 0.5 K to 1.5 K with an 0.1 K increment. The rotational temperature was estimated to 1 K, by comparing the intensities of the simulated one where it gives the smallest averaged error. The experimental relative abundances of the conformers obtained are: SR-**III**(v_a) : SR-**I**(v_c) : SR-**I**(v_d) : SS-**III**(v_a) : SS-**I**(v_c) : SS-**I**(v_d) = 12% : 12% : 25% : 15% : 21% : 15%. These relative abundances were applied to the simulated spectra to match the experimental intensities.

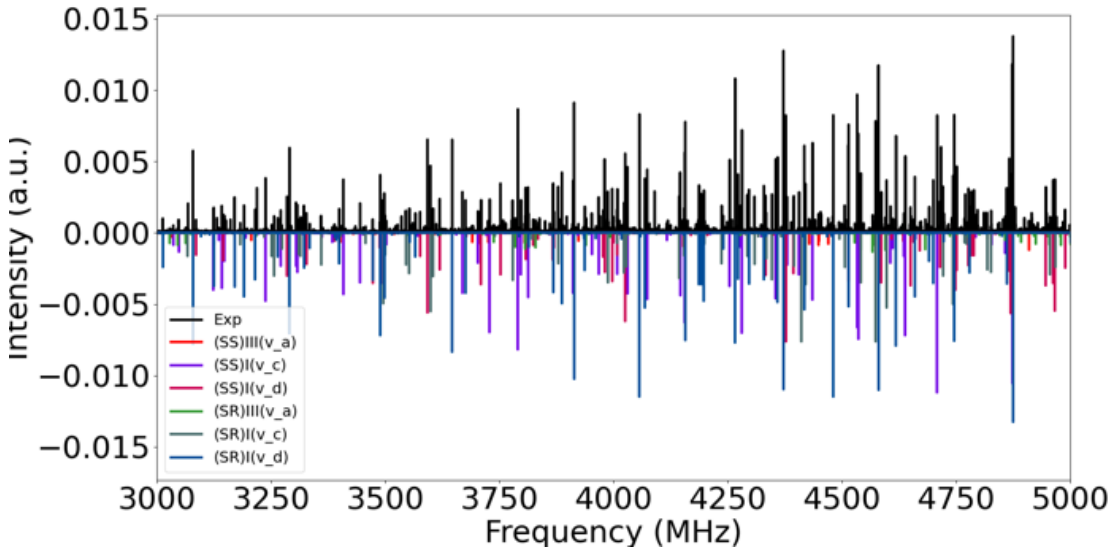

Figure 5.3. An overview of the experimental broadband spectrum recorded with a racemic THFA and racemic PO sample. The strong transitions present in the spectra obtained using only THFA and only PO are removed, as described in the main text. The simulated spectrum was produced with the experimental spectroscopic constants, an estimated rotational temperature of 1 K, and the theoretical dipole moment components, as well as the relative experimental abundances of the conformers. See the main text for detail.

5.2.3. Conformational cooling and chirality-controlled structural preference

It is known that the THFA monomer exists dominantly in *trans*-COOH configuration, i.e. 91% (*trans*): 9% (*cis*) in a jet expansion, whereas its hydrogen-bonding intermolecular interaction with others strongly favors *cis*-COOH. This creates a situation where strong *trans* versus *cis* or intramolecular versus intermolecular hydrogen bonding competitions are anticipated for complexes containing THFA. The experimental abundances of the THFA ···PO conformers obtained in the current study show 73% (*trans*) : 27% (*cis*), considerably higher than the corresponding ratio in the THFA monomer. As shown in Figure 5.1, the intermolecular binding energy of *cis*-THFA···PO is about 16 kJ mol^{-1} higher than that of *trans*-THFA···PO, greatly favoring the formation of *cis*-THFA···PO. One

would have essentially only *cis*-THFA···PO in a jet expansion if the formation process is purely thermodynamically controlled. On the other hand, the *trans*-THFA monomer is much more abundant than *cis*-THFA and the interconversion between from the *trans* to the *cis*-THFA monomer was demonstrated to be unlikely to happen even with the addition of argon to helium jet expansion.[7] This kinetically controlled character is the major factor that *trans* configuration dominates in the binary THFA···PO complex. In summary, the observed phenomenon can be rationalized as a result of both thermodynamic and kinetic controlled complexation process. A similar observation was reported for the THFA dimer. In the THFA dimer, *cis*-THFA serves as a subunit in the *cis*-*trans* dimer and also in the *cis*-*cis* double H-bonded structure which has a very strong energetic preference. As a result, the observed percentage of the *cis*-THFA configuration is about 70% among homochiral conformers and about 60% among the heterochiral conformers. It should be further pointed out that the observed percentage of the *cis*-THFA configuration in the heterochiral THFA dimer is likely to be much higher than 60% stated above because the most stable heterochiral *cis*-*cis* THFA dimer could not be detected due to its zero permanent dipole moment. Overall, the percentage of *cis*-THFA configuration in the THFA dimer is much higher than that in the THFA monomer and in the THFA···PO complex. The above discussion underscores the complexity of the cluster formation process in a jet expansion.

Below we have a closer look at the structure-energy relationship in the THFA···PO conformers, based on the experimental abundances and theoretical relative energies. For **Type 1** conformers, the main intermolecular interactions responsible for the binding energy are the interactions between the *anti* face of PO with the COOH group of THFA, as shown in Figure 5.1. Taking a mirror image of THFA with respect to the COOH plane does not affect the aforementioned intermolecular interactions in Figure 5.1. Consequently, each **Type1** homochiral and heterochiral THFA···PO pair are very close in their stability or energy. For example, SS-**III**(v_a) is only 0.1 kJ mol^{-1} more stable than SR-**III**(v_a), within the energy uncertainty of theoretical calculations. This is consistent with experimental abundances of ~15% and 12% for SS-**III**(v_a) and SR-**III**(v_a), respectively. In **Type 2** structures, the situation is different as illustrated in Figure 5.4. Here, the primary non-

covalent interactions can be pictured as the ester oxygen atom of PO joins the existing intramolecular hydrogen-bond in *trans*-THFA. Depending on the arrangement of the methyl group of PO, there are four binding topologies, leading to four different conformers, i.e. SS- **I**(v_c), SR-**I**(v_d), SR-**I**(v_c) and SS-**I**(v_d). Interestingly, both experimental abundances and calculated relative energies suggest that the structures with the PO methyl group extending to the same side as the THFA ring, i.e. the "upper side" in Figure 5.4, are more stable than when they are to the opposite side. For the homochiral structures, **I**(v_c) is about 1 kJ mol^{-1} more stable than **I**(v_d), corresponding to ~10% higher experimental abundance. In the related heterochiral structures, **I**(v_c) is about 1 kJ mol^{-1} less stable than **I**(v_d), with ~9% lower experimental abundance. Such interesting chirality-controlled structural preference was also reported for the homochiral and heterochiral THFA dimers, where the related less stable THFA conformers are actually unstable structures after ZPE corrections.[7]

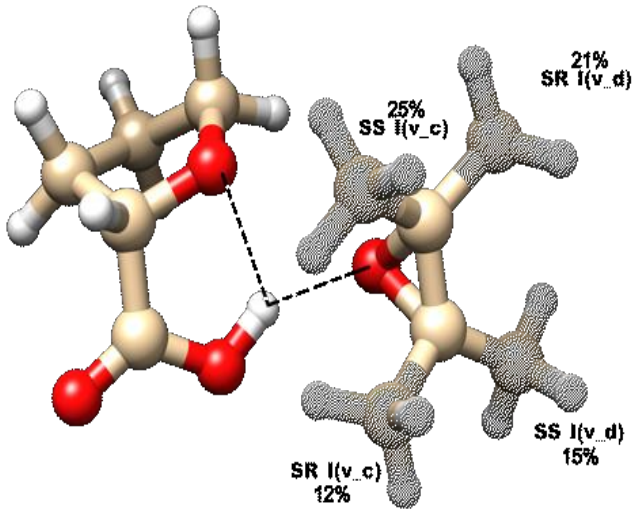

Figure 5.4. The illustration of **Type 2** THFA···PO topologies. The percentages indicate the estimated experimental abundances of the respective conformers.

5.2.4. Chiral-tag experiments and experimental ee determination

Chiral-tag CP-FTMW spectroscopy is an emerging technology for determination of absolute configuration and ee of a chiral sample.[5,7-9] The strategy is to convert a pair of enantiomers to diastereomers in a jet expansion by utilizing non-covalent interactions between the analyte and the chiral tag. Assuming that the intensity of a rotational transition of the diastereomer is linearly proportional to the concentration of each chiral subunit, one can derive the equation to calculate the ee of the analyte, $ee_{analyte}$: $(ee_{analyte})(ee_{tag}) = (1-R)/(1+R)$. Here R is the intensity ratio of a pair of selected homochiral and heterochiral transitions measured with a high enantiopure tag sample. Furthermore, to account for all other factors which can influence intensity of a rotational transition, such as intrinsic transition strength, conformer abundances, frequency-dependent instrument performance, we introduce a normalization factor which can be obtained by the intensity ratio of the same pair of transitions measured using a racemic tag sample. Essentially, if the analyte has zero ee, one expects that R=1 with a high enantiopure tag, after the normalization procedure described above. If the analyte has a non-zero ee, then the R value will deviate from 1 as dictated by $ee_{analyte}$ and ee_{tag}. Since ee_{tag} is known, one can calculate $ee_{analyte}$ accordingly.

We applied this methodology to measure the ee values of four THFA mixtures using PO as the chiral tag. We used a simple syringe to measure the volumes of R-THFA and racemic THFA samples and mixed them to produce four ad hoc samples with ee values of roughly 0%, 30%, 50% and 67% if the high enantiopure THFA sample is taken as 100%. Their broadband spectra were measured with nearly enantiopure S-PO tag and the normalization factors were obtained with the racemic PO tag. Here we selected the transition pairs from the most abundant homo/heterochiral diastereomers, i.e. homochiral **I**(v_c) and heterochiral **I**(v_d). The ee_{tag} of PO value is taken as 99.8% as previously reported.[42,43] The results are demonstrated in Figure 5.5 in the form of histogram. The vertical axis represents the number of transition pairs and the horizontal axis is the ee of sample. The

weight averaged ee of the four THFA samples are 1.5, 29.8, 46.5 and 61.4%. The standard derivation of transition pairs decreases as the enantiomeric purity increases. Similar trend has been reported by Pate and co-workers.[42-46]

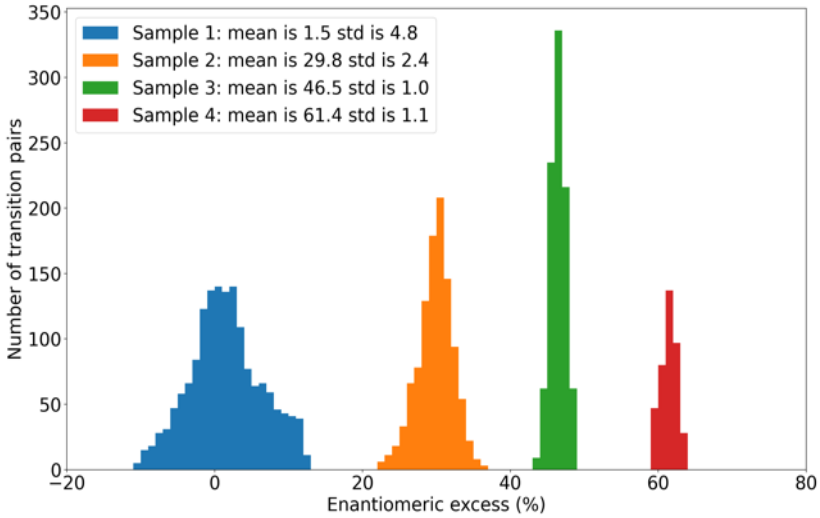

Figure 5.5. The histograms of the four chiral analyses done on four ad hoc THFA samples. See the main text for details.

There are several distinctive advantages of chiral-tag CP-FTMW spectroscopy in comparison to some other commonly used chiral analysis tools such as NMR chiral shift agent approach[47,48]: 1. It does not require a sample analyte of known ee as a reference mark. One can use any suitable tag sample with known ee. 2. There is no need to develop pre-separation procedures for impurities. 3. There is no need for tedious organic synthase of diastereomers. One can use non-covalently bonded diastereomers in a jet expansion directly. 4. There are a large number of homo/heterochiral transition pairs to verify the ee values and provide statistical analyses.

5.3. Conclusion

The conformational landscape of chiral binary complex THFA…PO was investigated in detail using CP-FTMW spectroscopy with the aid of comprehensive theoretical conformational sampling. Six conformers including homochiral and heterochiral diastereomers were observed in the broadband rotational spectra. The formation of binary complex THFA…PO in the pulsed jet expansion is demonstrated to be both kinetically and thermodynamically controlled similar to previously reported THFA related complexes. In addition, *ee* measurements were performed using a recently proposed chiral tagging strategy.

5.4. Experimental details

Broadband spectra of THFA_PO were recorded using a 2-6 GHz CP-FTMW spectrometer.[49,50] It was built based on the pioneering work of Pate and co-workers.[6] Both racemic THFA and PO are purchased from Sigma-Aldrich and used without further purification. THFA was directly placed in a homemade nozzle cap, heated to 105 ˚C and with a 30 mm long and 1 mm diameter collision channel. A trace amount PO was vaporized into a evacuated tank to prepare a 0.1% mixture with ~40 psi of neon. Six sample FIDs were recorded within one nozzle pulse. The nozzle ran at 2 Hz. Thus, the speed of data acquisition was about 1 million per day. In this study, each FID was recorded for 20 us and FFT was applied on 1.25 million FIDs with X1 zero padding. This procedure provides a digitization resolution of 25 kHz.

References

[1] A. K. King, B. J. Howard, *Chem. Phys. Lett* **2001**, *348*, 343-349.

[2] A. Maris, B. M. Giuliano, D. Bonazzi, W. Caminati, *J. Am. Chem. Soc.* **2008**, *130*, 13860-13861.

[3] J. Thomas, F. X. Sunahori, N. Borho, Y. Xu, *Chem. Eur. J.* **2011**, *17*, 4582-4587.

[4] S. R. Domingos, C. Pérez, M. Schnell, AIP Publishing LLC, **2016**.

[5] L. Evangelisti, W. Caminati, D. Patterson, J. Thomas, Y. Xu, C. West, B. Pate, *ISMS* **2017**, RG03.

[6] G. G. Brown, B. C. Dian, K. O. Douglass, S. M. Geyer, S. T. Shipman, B. H. Pate, *Rev. Sci. Instrum.* **2008**, *79*, 053103.

[7] F. Xie, N. A. Seifert, W. Jäger, Y. Xu, *Angew. Chem. Int. Ed.* **2020**, *59*, 15703-15710.

[8] B. H. Pate, L. Evangelisti, W. Caminati, Y. Xu, J. Thomas, D. Patterson, C. Perez, M. Schnell, in *Chiral Analysis*, Elsevier, **2018**, pp. 679-729.

[9] S. R. Domingos, C. Pérez, M. Marshall, H. Leung, M. Schnell, *Chem. Sci.* **2020**.

[10] F. Xie, X. Ng, N. A. Seifert, J. Thomas, W. Jäger, Y. Xu, *J. Chem. Phys.* **2018**, *149*, 224306.

[11] J. R. Cheeseman, M. J. Frisch, F. J. Devlin, P. J. Stephens, *J. Phys. Chem. A* **2000**, *104*, 1039-1046.

[12] R. K. Kondru, P. Wipf, D. N. Beratan, *Science* **1998**, *282*, 2247-2250.

[13] M. A. Lowe, J. S. Alper, *J. Phys. Chem.* **1988**, *92*, 4035-4040.

[14] P. Mukhopadhyay, G. Zuber, M.-R. Goldsmith, P. Wipf, D. N. Beratan, *ChemPhysChem* **2006**, *7*, 2483-2486.

[15] M. Losada, P. Nguyen, Y. Xu, *J. Phys. Chem. A* **2008**, *112*, 5621-5627.

[16] Z. Su, Y. Xu, *Angew. Chem. Int. Ed.* **2007**, *46*, 6163-6166.

[17] J. D. Swalen, D. R. Herschbach, *J. Chem. Phys.* **1957**, *27*, 100-108.

[18] D. R. Herschbach, J. D. Swalen, *J. Chem. Phys.* **1958**, *29*, 761-776.

[19] B. A. McGuire, P. B. Carroll, R. A. Loomis, I. A. Finneran, P. R. Jewell, A. J. Remijan, G. A. Blake, *Science* **2016**, *352*, 1449-1452.

[20] S. Blanco, A. Maris, S. Melandri, W. Caminati, *Mol. Phys.* **2002**, *100*, 3245-3249.

[21] S. Blanco, A. Maris, A. Millemaggi, W. Caminati, *J. Mol. Struct.* **2002**, *612*, 309-313.

[22] S. Blanco, S. Melandri, A. Maris, W. Caminati, B. Velino, Z. Kisiel, *Phys. Chem. Chem. Phys.* **2003**, *5*, 1359-1364.

[23] Z. Su, N. Borho, Y. Xu, *J. Am. Chem. Soc.* **2006**, *128*, 17126-17131.

[24] Y. Orita, Y. Kawashima, E. Hirota, *J. Mol. Spectrosc.* **2011**, *268*, 78-84.

[25] Z. Su, Q. Wen, Y. Xu, *J. Am. Chem. Soc.* **2006**, *128*, 6755-6760.

[26] Z. Su, Y. Xu, *Angew. Chem.* **2007**, *119*, 6275-6278.

[27] S. Blanco, A. Maris, A. Millemaggi, W. Caminati, *J. Mol. Struct.* **2002**, *612*, 309-313.

[28] Z. Su, N. Borho, Y. Xu, *J. Am. Chem. Soc.* **2006**, *128*, 17126-17131.

[29] N. Borho, Y. Xu, *J. Am. Chem. Soc.* **2008**, *130*, 5916-5921.

[30] N. Borho, Y. Xu, *Angew. Chem. Int. Ed.* **2007**, *46*, 2276-2279.

[31] F. X. Sunahori, Z. Su, C. Kang, Y. Xu, *Chem. Phys. Lett.* **2010**, *494*, 14-20.

[32] F. Xie, M. Fusè, A. S. Hazrah, W. Jaeger, V. Barone, Y. Xu, *Angew. Chem. Int. Ed.* **2020**.

[33] D. Bernhard, M. Fatima, A. Poblotzki, A. Steber, C. Pérez, M. Suhm, M. Schnell, M. Gerhards, *Phys. Chem. Chem. Phys.* **2019**, *21*, 16032-16046.

[34] F. Xie, N. A. Seifert, M. Heger, J. Thomas, W. Jäger, Y. Xu, *Phys. Chem. Chem. Phys.* **2019**, *21*, 15408-15416.

[35] S. Oswald, N. A. Seifert, F. Bohle, M. Gawrilow, S. Grimme, W. Jäger, Y. Xu, M. A. Suhm, *Angew. Chem. Int. Ed.* **2019**, *58*, 5080-5084.

[36] C. Bannwarth, S. Ehlert, S. Grimme, *J. Chem. Theory Comput.* **2019**, *15*, 1652-1671.

[37] S. Grimme, *J. Chem. Theory Comput.* **2019**, *15*, 2847-2862.

[38] P. Pracht, F. Bohle, S. Grimme, *Phys. Chem. Chem. Phys.* **2020**, *22*, 7169-7192.

[39] A. D. Becke, E. R. Johnson, *J. Chem. Phys.* **2005**, *123*, 154101.

[40] J. K. G. Watson, *Mol. Phys.* **1968**, *15*, 479-490.

[41] C. M. Western, *J. Quant. Spectrosc. Radiat. Transf.* **2017**, *186*, 221-242.

[42] K. J. Mayer, C. Embly, B. Pate, L. Evangelisti, *ISMS* **2018**, TC06.

[43] K. J. Mayer, B. Pate, C. West, R. E. Sonstrom, M. S. Holdren, T. Smart, L. Evangelisti, *ISMS* **2019**.

[44] R. E. Sonstrom, K. J. Mayer, C. West, B. Pate, L. Evangelisti, *ISMS* **2019**.

[45] C. West, L. Evangelisti, R. E. Sonstrom, B. Pate, *ISMS* **2019**.

[46] R. E. Sonstrom, K. J. Mayer, C. West, B. Pate, *ISMS* **2019**.

[47] J. A. Dale, H. S. Mosher, *J. Am. Chem. Soc.* **1973**, *95*, 512-519.

[48] T. R. Hoye, C. S. Jeffrey, F. Shao, *Nat. Protoc.* **2007**, *2*, 2451-2458.

[49] C. D. Carlson, N. A. Seifert, M. Heger, F. Xie, J. Thomas, Y. Xu, *J. Mol. Spectrosc.* **2018**, *351*, 62-67.

[50] N. A. Seifert, J. Thomas, W. Jäger, Y. Xu, *Phys. Chem. Chem. Phys.* **2018**, *20*, 27630-27637.

Chapter 6

Conformational Panorama and Chirality Controlled Structure-Energy Relationship in a Chiral Carboxylic Acid Dimer [a]

[a] This study has been published. Fan Xie, Nathan A. Seifert, Wolfgang Jäger, Yunjie Xu. Conformational panorama and chirality controlled structure-energy relationship in a chiral carboxylic acid dimer. *Angew. Chem. Int. Ed.,* **2020**, 59, 15703-15710.

6.1. Introduction

Tetrahydro-2-furoic acid (THFA), a colorless oil, is a chiral acid consisting of a tetrahydrofuran and a carboxylic acid group. Enantiopure THFA is typically produced by hydrogenation of furoic acid.[1] Because of its structural similarity to proline, THFA has been used successfully as a proline hydrogenase inhibitor against metastasizing cancer cells.[2] It also serves as an important precursor for pharmaceuticals such as Terazosin, a drug for treatment of prostate enlargement.[3] The conformational distribution of an isolated THFA molecule was recently investigated and THFA was found to exist in three different conformations, I, II and III experimentally.[4] While III adopts the most common *cis*-COOH configuration where OH and C=O are at the same side of the C-C bond, I and II take on *trans*-COOH as a result of an intramolecular hydrogen (H)-bond between the OH group and the ring ether O atom and differ slightly in their ring configurations. The H-bonding interactions among carboxylic acids have long fascinated organic and physical chemists alike.[5] Rotational spectroscopy, especially in combination with the chirped pulse Fourier transform microwave (CP-FMW) technique,[6] offers a window to examine these non-covalently bonded complexes in unprecedented detail in terms of their conformational landscapes. Rotational spectroscopic studies of dimers of carboxylic acids have focused mainly on proton tunneling and conformational diversity.[7] In all but one rotational spectroscopic report, the dimers adopt a cyclic double H-bonded structure which consists of two *cis*-COOH subunits. Only very recently, an acid dimer contain a *trans*-COOH subunit was detected experimentally, showing an unusual intermolecular H-bonding topology.[7h] Although the list of the acid dimers studied by rotational spectroscopy is long, no study of chiral acid dimers has ever been reported despite several prior attempts, hinting at significant experimental challenges.

In this study, we explore the complex conformational panorama of the THFA dimer afforded by the unusual monomeric conformational distribution and chirality controlled conformational preferences. The co-existence of I and II (*trans*-COOH) and III (*cis*-COOH) provides a unique window to examine the competition between intra- and intermolecular H-bonding interactions occurring in the THFA dimer. Two drastically different scenarios can be envisioned for the *detectable* THFA dimer in a jet expansion: a III-III dimer which features an eight-membered, double H-bonded ring whose *binding energy* is expected to be more than 30 kJ mol^{-1} larger than that of I-I, or a weakly bound I-I dimer, without canonical carboxylic dimer linkages. The abundance of I-I would be many times that of III-III, based on a kinetically controlled formation process. Utilizing broadband CP-FTMW spectroscopy and theoretical modeling, we further investigate the role of chirality in these intermolecular interactions by identifying experimentally the homo/heterochiral THFA dimers. We emphasize that these kinds of systems are at a level of complexity where one cannot interpret molecules initially localized in a minimum as its own isolated entity any longer – one has to understand its energetic connectivity to all other minima. The results reported are of great importance for current developments in chiral-tag rotational spectroscopy for chirality determination and enantiomeric excess (ee) monitoring[8,9] of enantioselective reactions in general, and for chiral hydrogenation processes of furoic acid in particular.

6.2. Results and Discussion

6.2.1. Computational conformational search results

Only three THFA monomers, namely I, II and III, were observed experimentally in a helium or neon jet expansion, out of six potential conformations (I to VI) with appreciable population at a nozzle temperature of 90 °C.[4] On the other hand, non-covalent interactions (NCIs) with another THFA molecule may alter the monomeric conformational distribution within the observed dimers significantly. Indeed, some previous studies show that the monomeric conformational abundances alter noticeably upon interactions with another binding partner. For example, in trimers of trifluoroethanol and 1,1,1,3,3,3-hexafluoro-propan-2-ol the unstable or much less favourable isolated subunits become prominent constituents.[10] Based on the previously known carboxylic acid binding motifs[5c] and the known THFA conformations,[4] it was clear early on that there were many possible $(THFA)_2$ structures, making it difficult to capture them manually. We sought the aid of Grimme's newly released computer code named CREST which stands for conformer-rotamer ensemble sampling tool.[11,12] This method has been successfully used by our and other groups for sampling conformal landscapes of organic molecules and their clusters.[10c,13]

Several hundreds of initial geometries identified by CREST were used as input geometries for subsequent geometry optimization and harmonic frequency calculations using the Gaussian 16 suite of programs[14] at the B3LYP-D3(BJ)/def2-TZVP level of theory with dispersion corrections[15] and Becke-Johnson damping.[16] Since the mirror-image pairs RR and SS of homochiral dimers and RS and SR of heterochiral dimers have exactly the same rotational spectra, we will use only RR and RS for homochiral and heterochiral dimers, respectively, in the remainder of the paper for conciseness. In total, about 300 $(THFA)_2$ geometries were identified to be true minima within a relative energy window of ~60 kJ mol^{-1} after zero-point energy (*ZPE*) correction. We divide the conformers into three types based on their binding topologies, as shown in Figure 6.1.

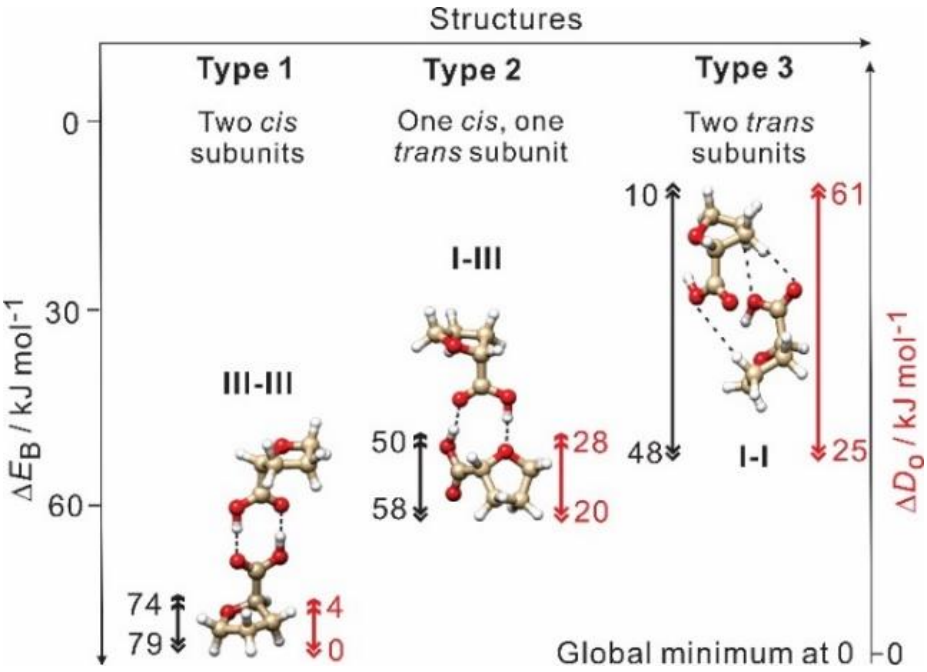

Figure 6.1. Three types of $(THFA)_2$ with their characteristic binding topologies and the subunits. ΔE_B and ΔD_o for each type are also given. ΔE_B, defined as the difference between the dimer and its subunits, is corrected for *ZPE* and basis set superposition errors (*BSSE*s), calculated using the counterpoise procedure.[17]

Type 1 structures which feature a common double H-bonded ring formed by two *cis* THFA subunits are the most stable ones. **Type 1** consists of 10 homochiral and 10 heterochiral $(THFA)_2$ within an energy span of about 4 kJ mol^{-1}. This result is expected since there exist four *cis*-COOH THFA monomers, **III**, **IV**, **V** and **VI** and choosing all possible combinations of two gives C(4,2) = 6 mixed and 4 same subunit dimers, which results in 10 homo- and 10 heterochiral $(THFA)_2$, consistent with the CREST/DFT results. Their relative raw and *ZPE* corrected energies are listed in Tables 6.S1, Supporting Information (SI), together with their spectroscopic constants. The global minimum is **Type 1** heterochiral, RS **III**(Oc)-**III**(Oc) whose geometry is depicted in Figure 6.2, together with its homochiral counterpart.

The **Type 2** structures contain a *trans* THFA subunit, i.e. **I** or **II**, and a higher energy *cis* THFA subunit, i.e. **III** to **VI**. These **Type 2** structures are 20 to 28 kJ mol^{-1} less stable than the **Type 1** global minimum. Based on their NCI characteristics, we separate the **Type 2** structures into four subcategories. Representative **Type 2** RR and RS $(THFA)_2$ geometries in each of the four subcategories are also shown in Figure 6.2. Statistically, one expects (2x4) x 4 = 32 homochiral and 32 heterochiral **Type 2** structures since one chooses one THFA subunit from **I** or **II** and the second subunit from **III**, **IV**, **V** or **VI**, generating 8 different conformers in each category. In the final DFT geometry optimizations, homochiral **II**(Oe)-**III**(Oc) and **II**(Oe)-**IV**(Oc) converged to homochiral **I**(Oe)-**III**(Oc) and **I**(Oe)-**IV**(Oc), respectively (see below for naming). The relevant energies and spectroscopic constants of the 30 homochiral and 32 heterochiral structures are listed in Tables 6.S2 and 6.S3, SI, respectively.

We name each structure based on the THFA subunits (**I** to **VI**) and its H-bond (or NCI) acceptor sites. For example, the **Type 1** RR and RS structure pairs in Figure 6.2 are named **III**(Oc)-**III**(Oe) where 'Oc' and 'Oe' represent the carbonyl and ether oxygen as the H-bond acceptors, respectively. 'va' and 'vb' indicate two different kinds of van der Waals interactions between the Oc atom and the tetrahydrofuran-ring H atom (See Figure 6.2). In some cases, an additional label '+' is used, for example in **I+**, indicating that the OH group is twisted much further away from the monomeric **I** structure.[4]

The remainder of the ~200 structures (**Type 3**) feature much weaker NCIs between the two *trans* THFA subunits and have binding energies ΔE_B at least 30 kJ mol^{-1} less than the most stable dimer. The two most stable **Type 3** dimers are also shown in Figure 6.2. If the dimer formation is purely kinetically controlled, it is likely that only these would be detectable. For conciseness, we do not include other much higher energy **Type 3** structures in the further discussion.

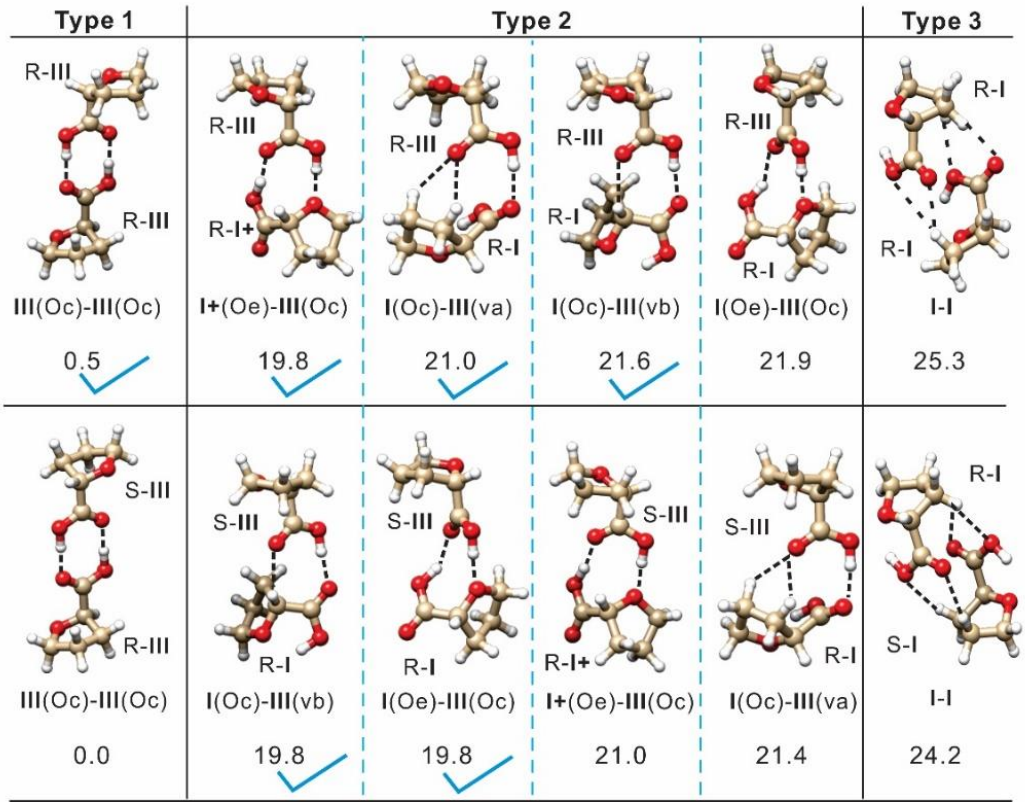

Figure 6.2. Representative homo- (top) and heterochiral (bottom) geometries of three types of $(THFA)_2$. Blue checkmarks indicate the conformers observed. The ΔD_0 values with respective to the global minimum are also given in unit of kJ mol^{-1}.

6.2.2. Experimental detection, assignments, and abundances of the homo- and heterochiral dimers

Broadband spectra of $(THFA)_2$ were recorded with a 2-6 GHz CP-FTMW spectrometer,[18] which is based on the pioneering work of Pate and co-workers.[6a,6b] Both racemic (97% purity) THFA and nearly enantiopure R-THFA (99.9% purity; no data on ee) samples were purchased from Sigma-Aldrich and used without further purification. The THFA liquid was placed directly inside a modified General Valve nozzle cap (details in Figure 6.S1, SI) and heated to 90 °C. The carrier gas was ~3 bar neon. The MW field used was ¼ of the

maximum possible in our set up and no rapid adiabatic passage phenomena[6c,19] were observed under this condition. For every gas pulse, six free induction (FID) decays were recorded and a total of ~ 1 million FIDs were averaged. The measured line widths and accuracy of the broadband instrument are ~125 kHz (FWHH) and ~5 kHz, respectively.

Based on the ΔE_B and ΔD_0 values given in Figure 6.1, one would expect the dense experimental spectra to be dominated by transitions of several low energy **Type 1** conformers. However, only transitions of the *most stable* RR **III**(Oc)-**III**(Oc) could be assigned. Next, we turned to identify **Type 2** structures in the spectra. This was a daunting task initially because there are many lower energy (within 3 kJ mol^{-1}) RR/RS conformers predicted. Exhaustive *ab initio* scans of possible conformational conversion paths within the **Type 2** structures, detailed in the next section, leads to the conclusion that the number of potentially observable conformers is reduced to the four RR and four RS **Type 2** dimers, i.e. the most stable ones in each category shown in Figure 6.2. Three of the four aforementioned RR **Type 2** $(THFA)_2$ were assigned first in the R-THFA spectrum. The corresponding transitions of all assigned RR $(THFA)_2$, as well as those of the three assigned THFA monomers and their minor isotopologues,[4] were then removed from the racemic spectrum. New spectral patterns belonging to the RS species emerged in the subtracted spectrum and two RS THFA dimers could be assigned.

In total, six sets of rotational transitions of $(THFA)_2$ were assigned and fitted using Watson's *S*-reduction[20] Hamiltonian in its I^r representation with the Pgopher program.[21] The resulting experimental spectroscopic constants are compared with the theoretical ones in Table 6.1, while the full sets of spectroscopic constants and the measured transition frequencies are listed in Tables 6.S5-S11.

Figure 6.3 shows the broadband spectrum recorded with the racemic sample and simulated spectra of the six assigned THFA dimers. All main experimental features are reproduced by the simulated spectra. Some of the $(THFA)_2$ conformers exhibit distinctive spectral

patterns. For example, RR **III**(Oc)-**III**(Oc) has a strong *c*-type K_a=2←1 Q branch pattern at 3.4 to 3.8 GHz and RS **I**(Oc)-**III**(vb) and **I**(Oe)-**III**(Oc) have characteristic, dense *b*-type Q branch patterns around 5.72 and 5.62 GHz, respectively, greatly easing assignment of the spectra.

To estimate the experimental relative abundances of the conformers observed, we utilized the experimental intensities of all rotational transitions with signal-to-noise better than 5 in the 3.0 to 5.5 GHz region where the experimental intensities are deemed reliable for our setup.[18] A Python routine was written to compare experimental intensities with the simulated ones obtained from Pgopher using the experimental spectroscopic constants, the theoretical dipole moment components, a rotational temperature which steps from 0.5 K to 1.5 K with an 0.1 K increment. The best agreement was achieved for ~1 K for all conformers. The experimental relative abundances of the conformers obtained are: homochiral **III**(Oc)-**III**(Oc) : **I**+(Oe)-**III**(Oc) : **I**(Oc)-**III**(va) : **I**(Oc)-**III**(vb) : heterochiral **I**(Oc)-**III**(vb) : **I**(Oe)-**III**(Oc) = 23% : 6% : 26% : 7% : 27% : 11% in the racemic sample. In the nearly enantiopure THFA sample, homochiral **III**(Oc)-**III**(Oc) : **I**+(Oe)-**III**(Oc) : **I**(Oc)-**III**(va) : **I**(Oc)-**III**(vb) = 39% : 10% : 42% : 9%. While we consider the general trend of the relative abundances to be reliable, the standard deviation of intensity is in the range of 20~40%, similar to that reported previously using CP-FTMW spectroscopy.[6a,6c,22]

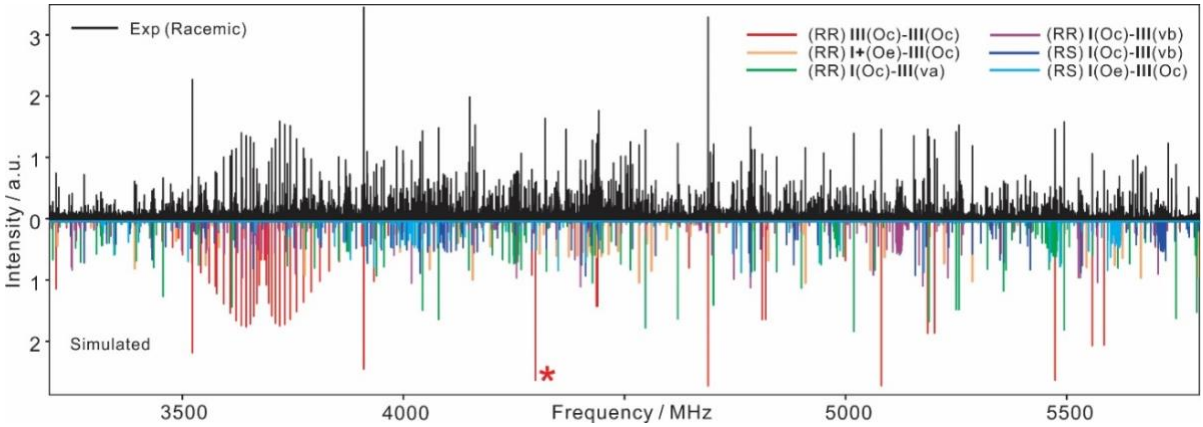

Figure 6.3. An overview of the broadband spectrum recorded with a racemic THFA sample. Lines due to the THFA monomers are removed for clarity. * indicates that this $(THFA)_2$ transition overlaps with a THFA monomer transition. The simulated spectrum was produced with the experimental spectroscopic constants, a rotational temperature of 1 K, and the theoretical dipole moment components, as well as the relative experimental abundances of the conformers. See the text for detail.

Table 6.1. Experimental and theoretical spectroscopic constants[a] of the six $(THFA)_2$ conformers observed.

	RR **III**(Oc)-**III**(Oc)		RR **I+**(Oe)-**III**(Oc)		RR **I**(Oc)-**III**(va)		RR **I**(Oc)-**III**(vb)		RS **I**(Oc)-**III**(vb)		RS **I**(Oe)-**III**(Oc)	
	Exp.	Theo.	Exp.	Theo.	Exp.	Theo.	Exp.	Theo.	Exp.	Theo.	Exp.	Theo.
A	1416.19705(26)	1437	1113.38900(31)	1115	884.99358(25)	882	965.91323(35)	956	1039.13124(43)	1035	1048.04605(41)	1040
B	190.25994(15)	189	241.82418(14)	242	291.83986(17)	292	247.13957(19)	250	231.63946(19)	233	256.09287(26)	259
C	187.57456(18)	186	217.36260(12)	217	260.04140(17)	260	218.96286(18)	221	211.85513(16)	213	233.46374(19)	236
$\|\mu\|$	μ_c	0,0,3.7	$\mu_b > \mu_a$	1.0,4.7,0.3	$\mu_b > \mu_a \sim \mu_c$	1.7,2.9,1.5	$\mu_b >> \mu_c > \mu_a$	1.7,4.6,2.2	$\mu_b > \mu_a$	1.4,2.3,0	$\mu_b >> \mu_c$	0.3,3.4,1.1
N, σ	92, 2.8	-	89, 4.4	-	177, 6.3	-	64, 4	-	102, 5.4	-	52, 4.1	-

[a] A, B, C = rotational constants in MHz, μ = dipole components in Debye and ***only*** the types observed are indicated with their estimated relative magnitudes, N = number of transitions in the fit, and σ = standard deviation in kHz.

6.2.3. Conformational cooling of THFA and $(THFA)_2$ in the jet

What to expect in terms of abundances of $(THFA)_2$ conformers has been an enigma throughout this work, making initial identification of carriers of experimental spectral patterns extremely difficult. Unlike many CP-FTMW studies reported before, identification of all low energy $(THFA)_2$ minima is far from sufficient to assign the very dense experimental spectra. It is clear that neither kinetically nor thermodynamically controlled processes alone can explain the outcome. Detailed knowledge of conformational conversion paths including the related transition states is critical to make sense of the experimental abundances. In addition, the pre-expansion conditions may also play a role in the abundances of different types of $(THFA)_2$, as reported in a recent Raman study.[23] Below, we discuss first a series of experiments to examine the influence of different carrier gases and nozzle temperatures on the formation of $(THFA)_2$, and then the related theoretical conversion pathways.

Different carrier gases and source temperatures: These experiments were carried out with three different carrier gasses, i.e. helium, neon, and a mixture of 10% argon with helium at 3 bar, and at four different nozzle temperatures: 26 °C, 56 °C, 86 °C, and 116 °C in neon at 3 bar (experimental details in Point S1, SI). In Figure 6.4a, one can see clearly that the intensity of **II** drops significantly in the He+Ar mixture compared to helium, whereas **III** remains more or less constant. The observation is consistent with the result of previous theoretical modeling,[4] summarized in Figure 6.4b. For $(THFA)_2$, as shown in Figure 6.5a, the obvious spectral pattern of **Type 1** RR **III**(Oc)-**III**(Oc) disappears upon addition of argon. In fact, transitions of all $(THFA)_2$ observed are no longer visible in the entire spectral range. The new strong transitions appearing were assigned to Ar-THFA.[24] The implication of this observation will be discussed latter.

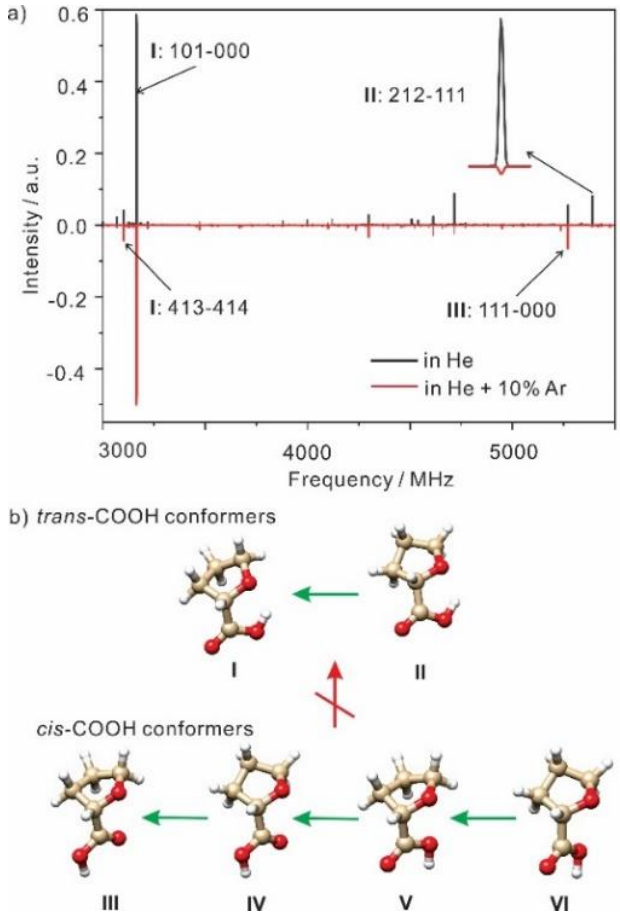

Figure 6.4. a) Comparison of the experimental THFA spectra recorded using helium and helium+10% argon as carrier gases. b) The six most stable THFA conformers. The conversion within the *trans* and *cis* subgroups is expected because of the low barriers (< ~5 kJ mol^{-1}), while that between them is unlikely because of the high barriers (~40 kJ mol^{-1}).[4]

With the nozzle temperature rising from 26 °C to 116 °C, the intensity of **I**, **II**, and **III** increases noticeably (Figure 6.5b). This is mainly because the vapor pressure of THFA in the pre-expansion nozzle increases considerably at higher temperatures. For the $(THFA)_2$ conformers, no transitions could be detected at 26 °C and 56 °C and the dimer signals appear at 86 °C and remain about the same at 116 °C. In a previous solution study of 0.42 M THFA in $CDCl_3$ at room temperature, the authors established experimentally the molar

factions of **I** + **II** (*trans*-COOH), **III** + **IV** + **V** + **VI** (*cis*-COOH), **III-III** (**Type 1** dimer) as 0.40, 0.25, and 0.35, respectively.[25] The equilibrium is expected to be shifted further to the dimers in the THFA liquid sample. *No* dimers of any type, however, were detected at low nozzle temperatures in the jet. In addition, even though no **Type 2** dimers were reported in the solution study,[25] they were detected with higher total population than that of **Type 1** in the jet expansion. Furthermore, if **III-III** was present in significant quantities pre-expansion, it would be unlikely that addition of 10% Ar can essentially wipe it out in favor of Ar-THFA since the latter is formed in the jet expansion and is much less stable. All these evidences support the hypothesis that the THFA dimers are *mostly* formed in the jet expansion and that the acid dimers are not present in noticeable amounts pre-expansion.

Interestingly, the above observations differ from what was reported in a recent Raman study where intensities of the formic acid and acetic acid dimers dropped drastically as the nozzle temperature increased from room temperature to 110 °C.[23] The difference may be related to: 1) much higher partial vapor pressures and dominant *cis* conformers of formic acid and acetic acid, favouring formation of **Type 1** dimers under pre-expansion conditions; 2) the very different slit nozzle set up used in the Raman study in contrast to the current circular nozzle assembly; 3) much different THFA monomer conformational distributions where *trans* dominates. One may appreciate the last point by looking at an "in-between" case, i.e. the o-anisic acid···formic acid heterodimer.[7h] In this example, o-anisic acid exists in three conformations T1 (*trans*-COOH), C1 and C2 (*cis*-COOH) in decreasing abundance. While the mixed dimer containing T1 remains the strongest, *noticeable* deviation from a statistical distribution was reported.

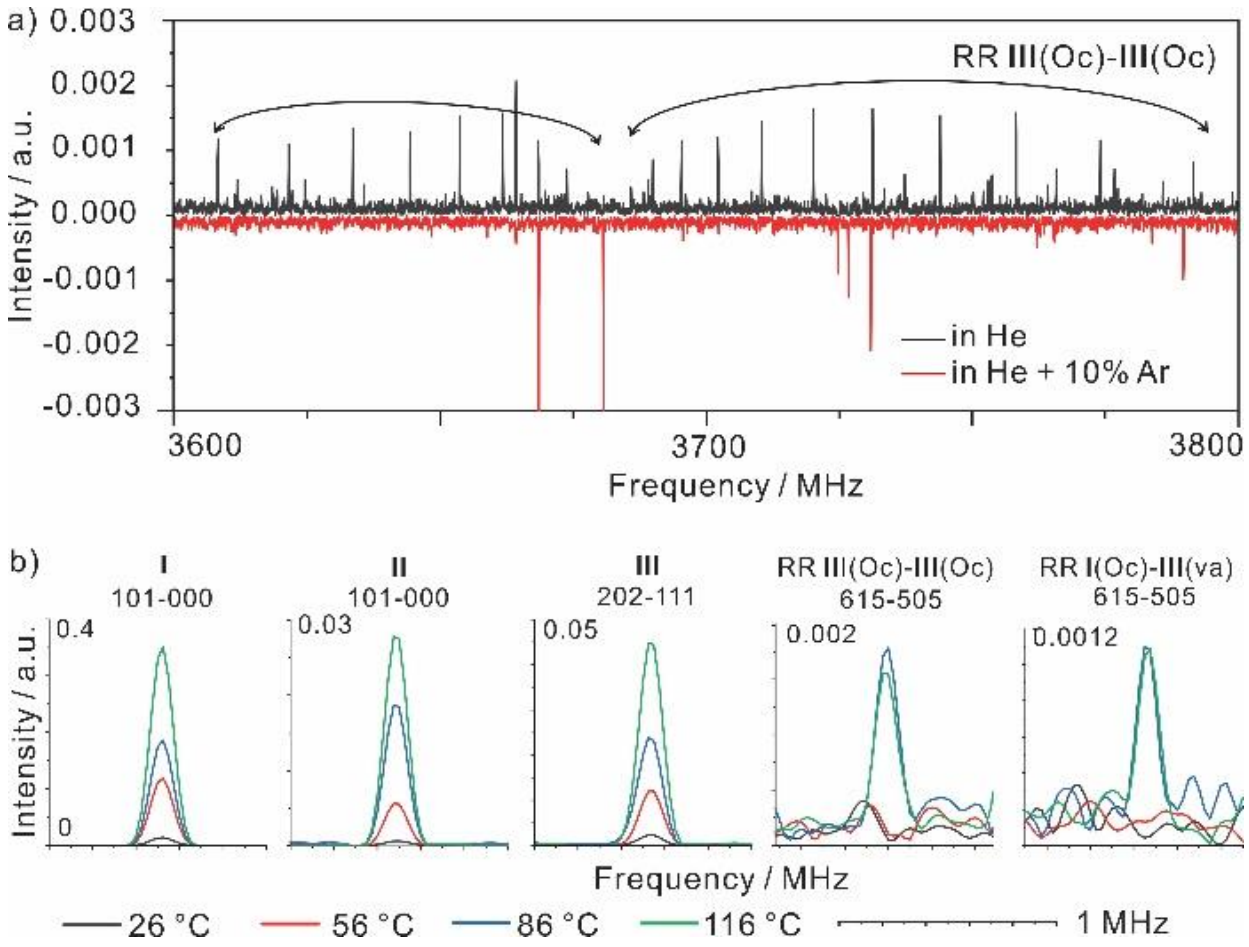

Figure 6.5. a) The effect of argon addition on the intensity of RR **III**(Oc)-**III**(Oc). These are zoom-in sections of the same spectra shown in Figure 6.4a. b) The effect of nozzle temperatures on the intensities of several example rotational transitions of THFA and $(THFA)_2$.

Relaxation pathways and barriers: Below we discuss the calculations of relaxation pathways and barriers within **Type 1**, **2**, and **3** geometries and between types. These systematic potential energy scans were performed at the B3LYP-D3(BJ)/def2-TZVP level of theory along a number of conformational conversion coordinates. In addition, the transition state calculations were carried out at the same level of theory using the Synchronous Transit-Guided Quasi-Newton (STQN) method.[26] Since the RR and RS dimers cannot convert from one to the other unless a dimer falls apart and its subunits participate in subsequent formation of another dimer, we consider their relaxation pathways within each type separately below.

Among **Type 1** geometries, only RR **III**(Oc)-**III**(Oc) was detected. All other 19 homo/heterochiral candidates within an energy span of ~4 kJ mol^{-1} could not be detected despite repeated attempts. Possible conformational cooling paths among the **Type 1** RR and RS dimers were searched for. Similar to the *cis*-COOH monomers, dimers with **IV**, **V**, and **VI** monomers will readily relax to those with **III**. Some representative relaxed one-dimensional minimum energy scans are given in Figure 6.S2, SI. For example, **IV**(Oc)-**III**(Oc) and **V**(Oc)-**III**(Oc) can convert to **III**(Oc)-**III**(Oc) through relatively low barriers of ~2 to 6 kJ mol^{-1}. Empirically, efficient conformational cooling with a circular nozzle jet expansion was reported for a conversion barrier of ~4.8 kJ mol^{-1} or less,[27] similar to the experience with our nozzle assembly.[4,28] All **Type 1** RR $(THFA)_2$ conformers would therefore be expected to convert (at least partially) to the most stable RR **III**(Oc)-**III**(Oc). A similar outcome is predicted for the **Type 1** RS dimers with RS **III**(Oc)-**III**(Oc) as the only reasonably abundant conformer in a jet expansion. Since RS **III**(Oc)-**III**(Oc) has a zero permanent electric dipole moment, pure rotational transitions of any **Type 1** RS species are therefore not observed. Overall, the effective conformational cooling from **IV**, **V**, and **VI** to **III** observed in the THFA monomer[4] appears to be not much affected by H-bonding to a second THFA.

For **Type 2** RR and RS dimers, cooling pathways for the 62 structures were calculated by considering the four subcategories separately. The thermodynamic relationships among these 62 low energy conformations also echo those of the THFA monomers: *only* dimers made of **I** and **III** subunits survive the conformational cooling. Some example scans along the conformational conversion pathways are given in Figure 6.S3, SI. The cooling from **II** to **I** appears to be even more efficient in dimers than in monomers. As a result, the number of potentially observable conformers reduces to the four RR and four RS dimers shown in Figure 6.2, i.e. only the most stable binary adducts in each the four subcategories are expected to be observed.

We also performed some transition state calculations along possible relaxation pathways between **Type 1** and **Type 2** conformers. Results of some example calculations are given in Figure 6.S4, SI. Overall, conformational conversion from **Type 2** to **Type 1** conformers is not expected because of the high barriers ($\geq$ ~40 kJ mol^{-1}).

Finally, we discuss **Type 3** RR and RS **I-I** in Figure 6.2. These two conformers were in fact the focus of our initial experimental efforts, based on the study of *o*-anisic acid···formic acid.[7h] However, no transitions associated with **I-I** could be identified experimentally. A possible explanation is that fewer **I-I** conformers are formed in a jet expansion than **I-III** because of the lower binding energies of **I-I** conformers compared to **I-III** (Figure 6.1). Second, the largest dipole moment component of the **I-I** conformers is ~1/3 of that of **III-III** or **I-III**, further reducing their transition intensities to below the detection limit. The conversion barriers from the most stable **Type 3 I-I** to a **Type 2** structure are estimated to be ~40 kJ mol^{-1} based on the *trans* to *cis* barrier in the THFA monomer (summarized in the caption of Figure 6.S4).

Here we summarize our rationales on why the six particular conformers were detected based on the experimental and theoretical evidence: 1) **Type 1**, **Type 2** and **Type 3** $(THFA)_2$ conformers are cooled separately because of high conversion barriers between

types; 2) In **Type 1**, RR and RS $(THFA)_2$ conformers are cooled to their respective most stable conformer. Therefore, only RR **III**(Oc)-**III**(Oc) was detected since RS **III**(Oc)-**III**(Oc) has zero electric dipole moment; 3) In **Type 2**, $(THFA)_2$ conformers in each category are cooled to the four RR and four RS structures given in Figure 6.2; 4) Of the three **Type 2** structures *not* observed (see Figure 6.2), RR **I**(Oe)-**III**(Oc) and RS **I**+(Oe)-**III**(Oc) do not exist as real conformers and RS **I**(Oc)-**III**(va) is (partially) cooled to RS **I**(Oc)-**III**(vb). The reasons are presented in the next section on role of chirality; 5) **Type 3** structures are not detected because of their low binding energies and much smaller dipole moment components.

6.2.4. Role of chirality in conformational preference

Chirality plays a decisive role in the spectral abundance of some **Type 1** and **Type 2** RR versus RS structures. The most stable **Type 1** RR **III**(Oc)-**III**(Oc) and RS **III**(Oc)-**III**(Oc) structures share similar H-bonding topologies (Figure 6.2), whereas chirality dictates the tetrahydrofuran ring of one **III** subunit to orient quite differently in RR compared to in RS. This chirality influence renders the former with a large *c*-type dipole moment while the latter has a zero permanent dipole moment and is invisible to rotational spectroscopy.

For **Type 2** structures, the effect is demonstrated in Figure 6.6 by comparing the transition state calculation along the conversion coordinate between RR **I**(Oe)-**III**(Oc) and RR **I**+(Oe)-**III**(Oc) to that of RS **I**+(Oe)-**III**(Oc) and RS **I**(Oe)-III(Oc). While all four dimers are minima on the potential energy surface (see Tables 6.S2 and S3), the *ZPE* corrected energy of RR **I**(Oe)-**III**(Oc) is 0.2 $kJmol^{-1}$ higher than the transition state, indicating that this structure is not a real conformer (or only supported by an extremely shallow well given uncertainties in the theoretical energies) and only the twisted form, **I**+(Oe)-**III**(Oc), survives. For the RS pair, in contrast, the untwisted form, **I**(Oe)-III(Oc), survives. A similar transition state calculation along a possible relaxation pathway from RR **I**(Oc)-**III**(vb) to RR **I**(Oc)-**III**(va) is compared to the corresponding one from RS **I**(Oc)-**III**(va) to RS **I**(Oc)-**III**(vb) in Figure 6.S5, SI. Here, RR **I**(Oc)-**III**(vb) is slightly more stable than RR **I**(Oc)-**III**(va) and they may convert back and forth through the barriers of ~5 $kJmol^{-1}$, consistent with the fact that both were detected experimentally. In the RS dimers on the other hand, RS **I**(Oc)-**III**(vb) is noticeably more stable than RS **I**(Oc)-**III**(va) and one may expect (partial) cooling from RS **I**(Oc)-**III**(va) to RS **I**(Oc)-**III**(vb), causing the former to be too weak to be detected. Such chirality related structural selectivity may offer insights into their functionality as pharmaceutical candidates or precursors. For example, (S)-Terazosin, which shares the same stereogenic carbon center as its precursor THFA, has been found to be more potent than its (R) enantiomer.[29]

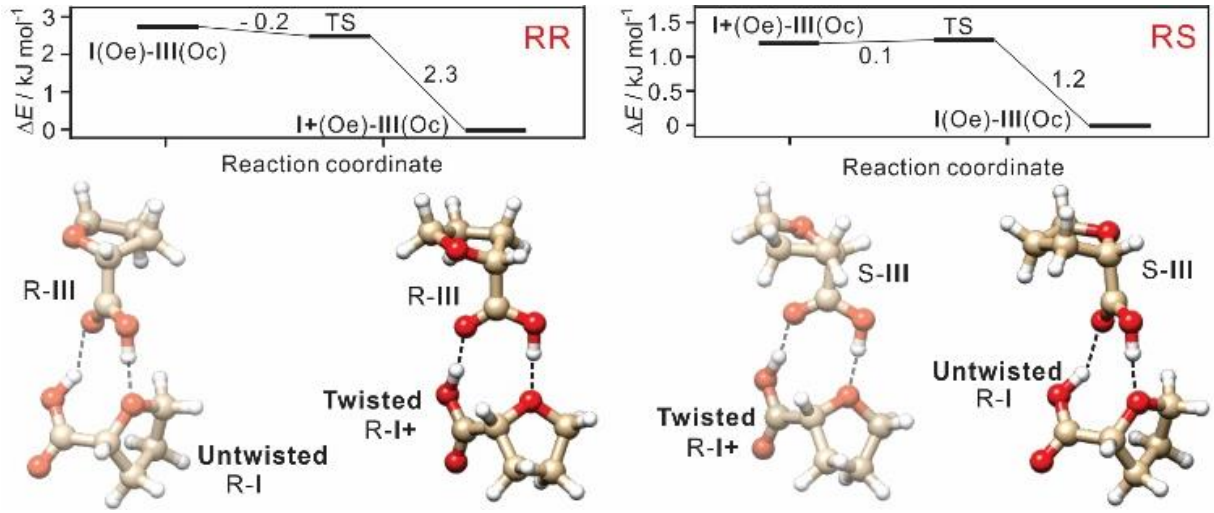

Figure 6.6. Geometry preference controlled by chirality. The faded geometries are not expected to exist as stable conformers.

6.2.5. Chiral analysis using chiral tag rotational spectroscopy

A novel practical application of rotational spectroscopy to chiral analysis is chiral tag rotational spectroscopy for determination of absolute configuration and ee of a chiral sample.[8] The basic principle is to convert a pair of sample enantiomers to two diastereomers, utilizing NCIs between a chiral sample and a chiral tag. The strategy used is similar to the NMR chiral shift agent approach,[30] with the bonus that it does not require tedious synthetic steps as in NMR. A further significant advantage is the exceptionally high spectral resolution available which can distinguish rotational transitions of different diastereomers readily, far exceeding what is possible by NMR or even chiral chromatography.

In the current study, since the chiral target and tag are the same, we term this "chiral self-tag". [31] Assuming that the intensity of a rotational transition of the diastereomer is linearly proportional to the concentration of each chiral subunit, it was derived that $ee_{sample} = ee_{tag} = [(1-R)/(1+R)]^{1/2}$.[8] A zoomed-in section of the broadband experimental spectra of $(THFA)_2$ is given in Figure 6.7. When using a racemic tag, one may expect R to be 1 based on statistics. This, however, is clearly *not* the case in reality. It is important to recognize that R is determined not only by the ee value(s) but also by other factors such as line strength, conformational abundance, rotational temperature, and frequency-dependent sensitivity variations in the instrument. It is essential to normalize for these additional factors before extracting the ee value from R. This is done by measuring the same pair of transitions using a racemic tag, i.e. racemic THFA and normalizing their intensity ratio.

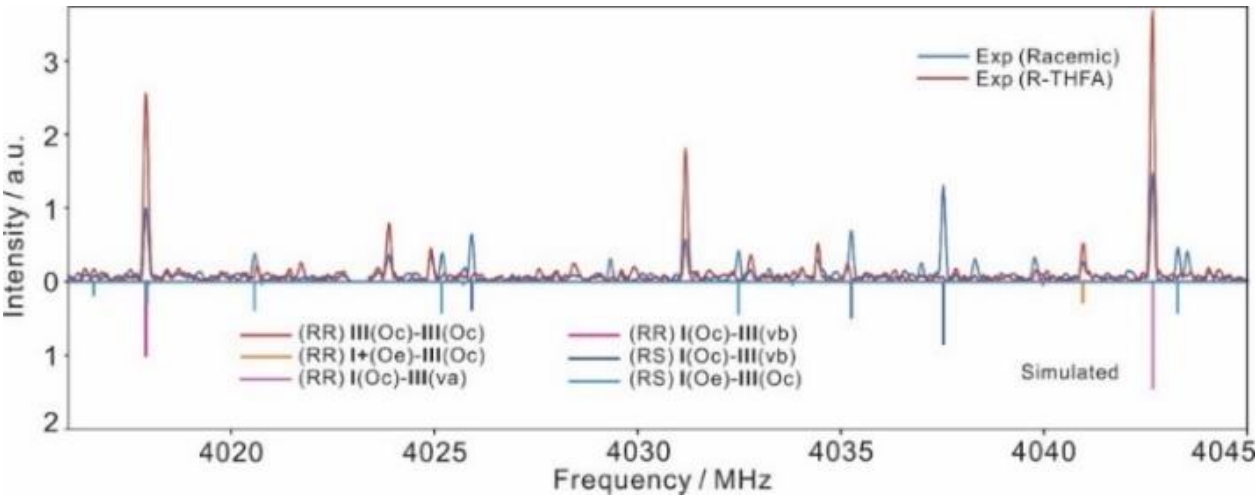

Figure 6.7. Top traces: a section of broadband experimental spectra of $(THFA)_2$ recorded with nearly enantiopure R-THFA (in red) and racemic THFA (in blue) samples. Bottom traces: simulated stick spectra of six assigned conformers produced with the relative experimental abundances of the conformers in the racemic sample.

Because of the complicated $(THFA)_2$ conformational distribution, it is not clear a priori if the assumption of a linear dependence of dimer intensity on its constituent concentrations would hold. We ran two ee analyses using two RR dimers **III**(Oc)-**III**(Oc) and **I**(Oc)-**III**(va) separately, with all experimental lines with s/n ratio larger than 5 and the strongest transition of RS **I**(Oc)-**III**(vb). Consistent ee results of ≥ 97.29(21)% and ≥ 97.31(24)% were obtained for the nearly enantiopure THFA sample. The ee analysis details are summarized in Point S2, SI. It is satisfying that even with the complicated conformational cooling paths discovered here and even though the global minimum structure, the heterochiral **III**(Oc)-**III**(Oc), is invisible to rotational spectroscopy, the intensity normalization step in the ee analysis still effectively removes any related intensity anomalies. The results suggest that the chiral self-tag procedure is a viable method to determine accurate ee values of these carboxylic acids.

6.3. Conclusions

The complex conformational panorama of a chiral carboxylic acid dimer, $(THFA)_2$, was investigated in detail using CP-FTMW spectroscopy and extensive CREST and DFT calculations. Applying the recently proposed chiral self-tag approach, the ee of a nearly enantiopure THFA sample was determined accurately. The current study also reveals strong chirality controlled conformational preference in the dimers. The experimental conformational abundances cannot be explained by kinetically nor thermodynamically controlled processes alone because of the unique THFA monomeric configurations. Generally, the abundance of a specific $(THFA)_2$ conformer depends not only on its own Boltzmann abundance but also sensitively on other less stable conformers which may convert to it, making a reliable theoretical prediction of the final outcome so much more daunting. High resolution, conformer-specific studies such as this are therefore important for current research activities in benchmarking theoretical energetic predictions and in exploring practical applications of chiral tag spectroscopy.

References

[1] M. Maris, W.-R. Huck, T. Mallat, A. Baiker, *J. Catal.* **2003**, *219*, 52-58.

[2] I. Elia, D. Broekaert, S. Christen, R. Boon, E. Radaelli, M. F. Orth, C. Verfaillie, T. G. P. Grünewald, S.-M. Fendt, *Nat. Commun.* **2017**, *8*,15267/1-11.

[3] J. Fischer, C. R. Ganellin, Analogue-based Drug Discovery. John Wiley & Sons. **2006**, p. 455.

[4] F. Xie, X. Ng, N. A. Seifert, J. Thomas, W. Jäger, Y. Xu, *J. Chem. Phys.* **2018**, *149*, 224306/1-10.

[5] a) F. Madeja, M. Havenith, K. Nauta, R. E. Miller, J. Chocholoušová, P. Hobza, *J. Chem. Phys.* **2004**, *22*, 10544-10560; b) M. Losada, H. Tran, Y. Xu, *J. Chem. Phys.* **2008**, *128*, 014508/1-11; c) M. Albrecht, V. A. Soloshonok, L. Schrader, M. Yasumoto, M. A. Suhm, J. Fluo. Chem. **2010**, *131*, 495-504; d) M. Shome, N. Mishra, *Indian J. Adv. Chem. Sci.* **2016**, *4*, 56-67; e) A. S. Perera, J. Cheramy, M. R. Poopari, Y. Xu, *Phys. Chem. Chem. Phys.* **2019**, *21*, 3574-3584; f) G. Giubertoni, O. O. Sofronov, H. J. Bakker, *J. Phys. Chem. Lett.* **2019**, *10*, 3217-3222.

[6] a) G. G. Brown, B. C. Dian, K. O. Douglass, S. M. Geyer, B. H. Pate, *Rev. Sci. Instrum.* **2008**, *79*, 053103/1-13; b) C. Pérez, S. Lobsiger, N. A. Seifert, D. P. Zaleski, B. Temelso, G. C. Shields, Z. Kisiel, B. H. Pate, *Chem. Phys. Lett.* **2013**, *571*, 1-15; c) G. B. Park, R. W. Field, *J. Chem. Phys.* **2016**, *144*, 200901/1-10.

[7] a) L. Martinache, W. Kresa, M. Wegener, U. Vonmont, A. Bauder, *Chem. Phys.* **1990**, *148*, 129-140; b) A. M. Daly, K. O. Douglass, L. C. Sarkozy, J. L. Neill, M. T. Muckle, D. P. Zaleski, B. H. Pate, S. G. Kukolich, *J. Chem. Phys*. **2011**, *135*, 154304/1-12; c) L. Evangelisti, P. Pcija, E. J. Cocinero, F. CastaÇo, A. Lesarri, W. Caminati, R. Meyer, *J. Phys. Chem. Lett.* **2012**, *3*, 3770-3775; d) G. Feng, Q. Gou, L. Evangelisti, W. Caminati, *Angew. Chem.* **2014**, *126*, 540-544; *Angew. Chem. Int. Ed.* **2014**, *53*, 530-534; e) J. Thomas, M. J. Carrillo, A. Serrato III, F. Xie, W. Jäger, Y. Xu, W. Lin, *Mol. Phys.* **2019**, *117*,1193-1199; f) A. Macario, S. Blanco, J.

Thomas, Y. Xu, J. C. López, *J. Phys. Chem. A* **2019**, *123*, 6772-6780; g) W. Li, L. Evangelisti, Q. Gou, W. Caminati, R. Meyer, *Angew. Chem.* **2019**, *131*, 869-875; *Angew. Chem. Int. Ed.* **2019**, *58*, 859-865; h) A. Macario, S. Blanco, J. Thomas, Y. Xu, J. C. López, *Chem. Eur. J.* **2019**, *25*, 12325-12331.

[8] B. H. Pate, L. Evangelisti, W. Caminati, Y. Xu, J. Thomas, D. Patterson, C. Perez, M. Schnell, in *Chiral Analysis: Advances in Spectroscopy, Chromatography and Emerging Methods*, ed. P. L. Polavarapu, Elsevier, **2018**, 679-729.

[9] J. L. Neill, Y. Yang, M. T. Muckle, R. L. Reynolds, L. Evangelisti, R. E. Sonstrom, B. H. Pate, B. F. Gupton, *Org. Process Res. Dev.* **2019**, *23*, 1046-1051.

[10] a) C. Pérez, J. C. López, S. Blanco, M. Schnell, *J. Phys. Chem. Lett.* **2016**, *7*, 20, 4053-4058; b) J. Thomas, N. A. Seifert, W. Jäger, Y. Xu, *Angew. Chem.* **2017**, *129*, 6386-6390; *Angew. Chem. Int. Ed.* **2017**, *56*, 6289-6293; c) S. Oswald, N. A. Seifert, F. Bohle, M. Gawrilow, S. Grimme, W. Jäger, Y. Xu, M. A. Suhm, *Angew. Chem.* **2019**, *131*, 5134-5138; *Angew. Chem. Int. Ed.* **2019**, *58*, 5080-5084.

[11] S. Grimme, *J. Chem. Theory Comput.* **2019**, *15*, 2847-2863.

[12] a) S. Grimme, C. Bannwarth, P. Shushkov, *J. Chem. Theory Comput.* **2017**, *13*, 1989-2009; b) S. Grimme, C. Bannwarth, S. Dohm, A. Hansen, J. Pisarek, P. Pracht, J. Seibert, F. Neese, *Angew. Chem.* **2017**, *129*, 14958-14964; *Angew Chem. Int. Ed.* **2017**, *56*, 14763-14769.

[13] D. Bernhard, M. Fatima, A. Poblotzki, A. L. Steber, C. Pérez, M. A. Suhm, M. Schnell, M. Gerhards, *Phys. Chem. Chem. Phys.* **2019**, *21*, 16032-16046.

[14] M. J. Frisch, et al., Gaussian 16, Revision A.03, Gaussian, Inc., Wallingford, CT, **2016**. See Supporting Information for the full reference.

[15] S. Grimme, S. Ehrlich, L. Goerigk, *J. Comput. Chem.* **2011**, *32*, 1456-1465.

[16] A. D. Becke, E. R. Johnson, *J. Chem. Phys.* **2005**, *123*, 154101/1-9.

[17] S. F. Boys, F. Bernardi, *Mol. Phys.* **1970**, *19*, 553-566.

[18] a) C. D. Carlson, N. A. Seifert, M. Heger, F. Xie, J. Thomas, Y. Xu, *J. Mol. Spectrosc.* **2018**, *351*, 62-67; b) N. A. Seifert, J. Thomas, W. Jäger, Y. Xu, *Phys. Chem. Chem. Phys.* **2018**, *20*, 27630-27637.

[19] a) J. C. McGurk, T. G. Schmalz, and W. H. Flygare, *J. Chem. Phys*. **1974**, *60*, 4181-4188; b) D. Schmitz, V. A. Shubert, T. Betz, M. Schnell, *J. Mol. Spectrosc.* **2012**, *280*, 77-84.

[20] J. K. G. Watson, in *Vibrational Spectra and Structure*, Vol. 6 (Ed.: J. R. Durig), Elsevier, New York, **1977**, pp. 1- 89.

[21] C. M. Western, *J. Quant. Spectrosc. Radiat. Transf.* **2017**, *186*, 221-242.

[22] D. P. Zaleski, J. L. Neill, M. T. Muckle, N. A. Seifert, P. B. Carroll, S. L. Widicus Weaver, B. H. Pate, *J. Mol. Spectrosc.* **2012**, *280*, 68–76.

[23] K. A. E. Meyer, M. A. Suhm, *J. Chem. Phys.* **2018**, *149*, 104307/1-12.

[24] F. Xie, Y. Xu (unpublished result).

[25] T. Kuppens, W. Herrebout, B. van der Veken, P. Bultinck, *J. Phys. Chem. A* **2006**, *110*, 10191-10200.

[26] a) H. B. Schlegel, *J. Comput. Chem.* **1982**, *3*, 214-218; b) C. Feng, H. B. Schlegel, *Israel J. Chem.* **1993**, *33*, 449-454.

[27] R. S. Ruoff, T. D. Klots, T. Emilsson, H. S. Gutowsky, *J. Chem. Phys.* **1990**, *93*, 3142-3150.

[28] F. Xie, N. A. Seifert, M. Heger, J. Thomas, W. Jager, Y. Xu, *Phys. Chem. Chem. Phys.* **2019**, *21*, 15408-15416.

[29] A. A. Hancock, S. A. Buckner, L. M. Ireland, S. M. Knepper, J. F. Jr. Kerwin, *J. Recept. Signal Transduct. Res.* **1995**, *15*, 863-885.

[30] a) J. A. Dale, H. S. Mosher, *J. Am. Chem. Soc.* **1973**, *95*, 512-517; b) T. R. Hoye, C. S. Jeffrey, F. Shao, *Nat. Protoc.* **2007**, *10*, 2451-2458.

[31] W. Caminati (private communication).

Chapter 7

Discovering the Elusive Global Minimum in a Ternary Chiral Cluster: Rotational Spectra of Propylene Oxide Trimer [a]

[a] This study has been published. Fan Xie, Marco Fusè, Arsh S. Hazrah, Wolfgang Jäger, Vincenzo Barone and Yunjie Xu. Discovering the elusive global minimum in a ternary chiral cluster: rotational spectra of propylene oxide trimer. *Angew. Chem. Int. Ed.,* **2020**.

7.1. Introduction

Propylene oxide (PO), a simple rigid chiral molecule, is widely used in the plastics industry as a building block for the synthesis of polyurethane polymers.[1] PO has played an important role in the development of theoretical treatments of chiroptical spectroscopies, such as optical rotation dispersion and vibrational circular dichroism,[2] and more recently in understanding solvent effects.[3] PO is one of the earliest chiral molecules investigated in the microwave region,[4] the foundation for its recent exciting discovery as the first chiral molecule in space.[5] Effects of chirality recognition in several PO containing homo-/heterochiral dimers[6] were detected by using Fourier transform microwave (FTMW) spectroscopy where several conformers were identified experimentally. The advent of the chirped pulse (CP)-FTMW[7] technique and these early studies[6,8] led to the development of chiral tag rotational spectroscopy for determination of chirality and enantiomeric excess (ee),[9] a method which may potentially be applied to ee determination in space and contribute to our understanding of the origin of homochirality of life.[10]

So far, no high-resolution spectroscopic study of PO aggregates beyond the dimer has been undertaken, in part because of the considerable theoretical and experimental challenges involved. Here we report the detection of multiple homo-/heterochiral PO trimers using CP-FTMW spectroscopy and point out unsolved problems in capturing the structural diversity of $(PO)_3$ theoretically, even with advanced meta-dynamic conformational search algorithms.[11] We found that none of the structures generated in the theoretical conformational search can account for the experimental transitions of heterochiral $(PO)_3$. By utilizing the classical isotopic substitution approach, we were able to establish the experimental heavy atom backbone of the heterochiral $(PO)_3$, finally leading to the theoretical identification of its structure. Excellent agreement was achieved between experimental and predicted rotational constants using a general hybrid B2/B3[12] and the further improved rPP/B3[13] approach (vide infra) to account for vibrational contributions.

A pair of PO enantiomers, R and S, gives rise to two indistinguishable rotational spectra, whereas for PO aggregates, different homo-/heterochiral diastereomers can be formed, as shown in Scheme 7.1.

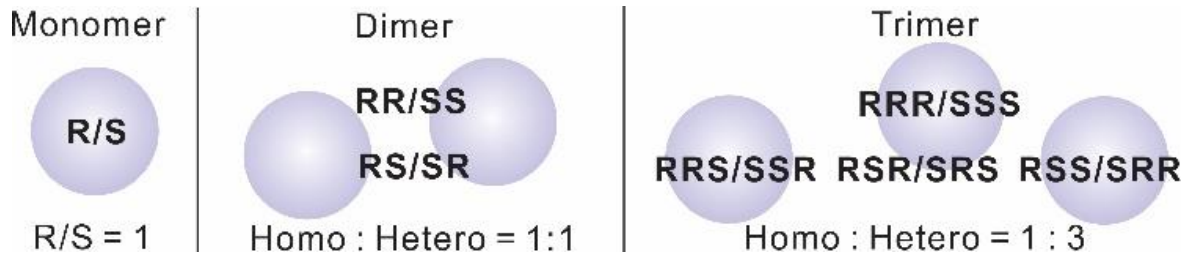

Scheme 7.1. The statistical distribution of homo-/heterochiral aggregates from monomer to trimer under racemic sample conditions, *without* consideration of thermodynamics, i.e. the energies of specific binding topologies.

For $(PO)_2$, specific binding topologies lead to 12 homo/ heterochiral conformers of which six were detected experimentally.[6a] The much larger structural diversity of $(PO)_3$ prompted us to employ the newly released CREST code,[14] which has been successfully used for sampling conformational landscapes of organic molecules and their clusters.[15] The details of the structural search are given in Point S1, Supporting Information (SI). The resulting $(PO)_3$ candidates were optimized at the B3LYP-D3BJ[16] /def2-TZVP level using Gaussian16.[17] The true minimum structures identified within a small energy window of 5 kJ mol^{-1}, which include 26 homochiral and 53 heterochiral $(PO)_3$, are summarized in Tables 7.S1 and S2, SI, respectively. The large number of possible conformers within such a small energy window highlights the difficulties in identifying them experimentally.

7.2. Results and Discussion

Broadband spectra of homo-/heterochiral $(PO)_3$ were collected using a 2-6 GHz CP-FTMW spectrometer.[18] Experimental and spectral fitting details are summarized in Point S1, SI. In the enantiopure PO spectrum, transitions belonging to two homochiral $(PO)_3$ conformers were assigned. A racemic PO spectrum is shown in Figure 7.1 where the two identified homochiral $(PO)_3$ are clearly visible, as well as a new set of strong transitions. This new set was tentatively assigned to a heterochiral $(PO)_3$ since the transitions are only visible with the racemic but not the enantiopure sample. The experimental rotational constants and relative magnitude of dipole moment components are compared with the DFT predictions in Table 7.1; the spectroscopic constants and the measured transition frequencies are listed in Tables 7.S3-S6, SI. The spectroscopic properties of the two homochiral $(PO)_3$ match those of the two most stable DFT homochiral $(PO)_3$, HOMO1 and HOMO2, quite well, confirming their identification. No reasonable match to a DFT structure, however, could be made for the experimental heterochiral $(PO)_3$ from the list of 53 heterochiral $(PO)_3$ candidates (Table 7.S2). For convenience, we name this experimental structure HETERO1.

The failure to produce a possible HETERO1 structure theoretically with the current conformational search strategy is a significant issue since conformational diversity is important in a wide range of chemistry and biochemistry subfields. While we could not capture the structural diversity of $(PO)_3$ in all details in our theoretical conformational search, the subtly different binding topologies can be easily discriminated by the CP-FTMW method with its very high spectral resolution. We therefore resorted to use isotopic substitution, a hallmark of rotational spectroscopy, to further explore the structural details of $(PO)_3$ experimentally.

To map out the heavy atom backbone of $(PO)_3$, it is ideal to have a single substitution at each heavy atom. Since the enriched ^{13}C and ^{18}O isotopologues of PO are prohibitively expensive, we optimized the experimental conditions and utilized the sensitivity achieved to measure and assign *all* 18 ^{13}C isotopologues of HOMO1 and HETERO1 in their natural

abundances. Figures 7.1b and c) showcase some transitions of ^{13}C isotopologues of HOMO1 and HETERO1; the experimental transition frequencies and spectroscopic constants are in Tables 7.S7-S10, SI. The ^{13}C isotopologues of HOMO2 were not detected because of the much lower abundance of this trimer (see Figure 7.1).

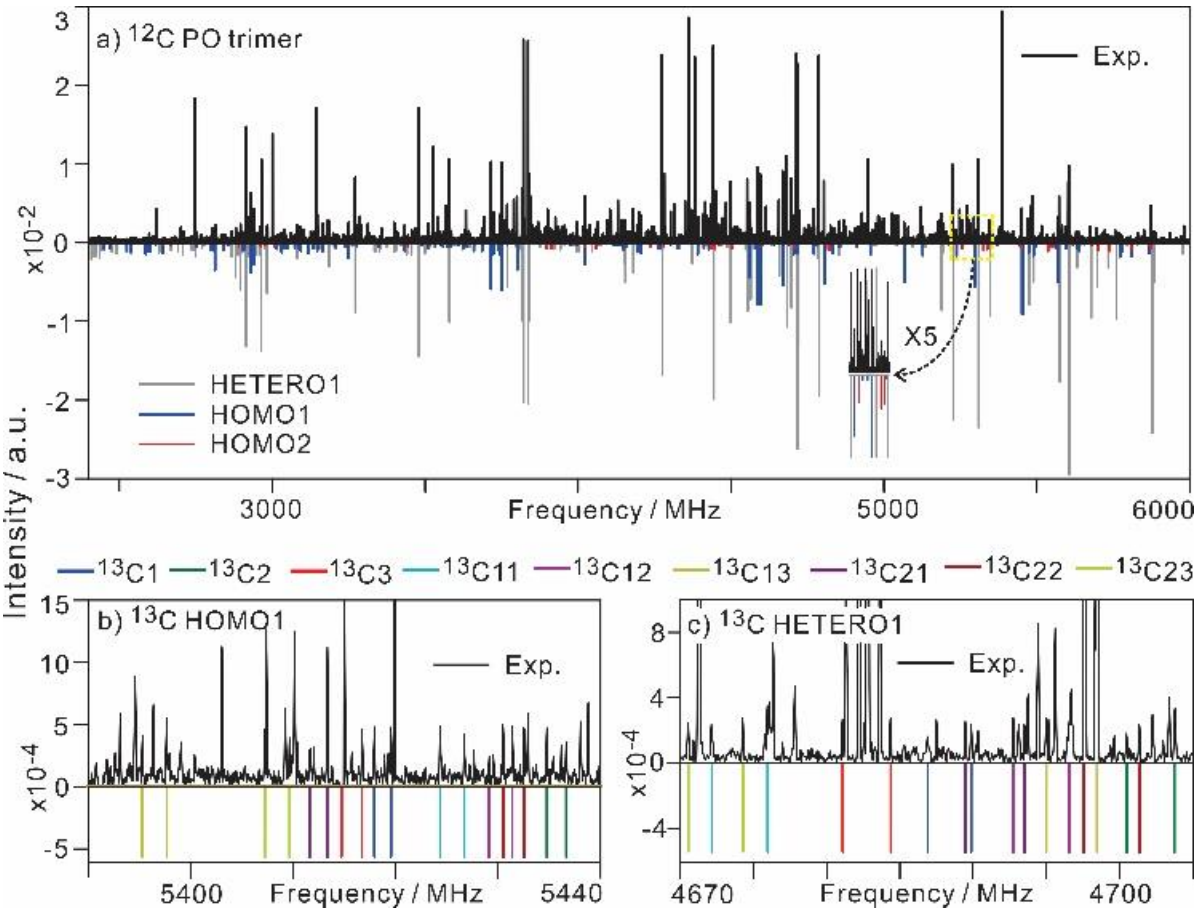

Figure 7.1. a) A broadband spectrum of $(PO)_3$ recorded with 10^6 FIDs using a racemic sample. Known lines of PO,[4] PO-Ne,[19] $(PO)_2$[6a] and PO-$(H_2O)_{1,2}$[3bc] were removed. The simulated spectra were generated with a rotational temperature of 1 K, experimental spectroscopic constants, calculated dipole moment components, and experimental relative abundance ratios of the three conformers. Bottom zoomed-in sections recorded with b) enantiopure PO and $5•10^6$ FIDs, showing the JK_aK_c = 606-515 and 616-505 transitions of

^{13}C isotopologues of HOMO1 and c) a racemic PO sample and 6•10^6 FIDs, showing the JK_aK_c = 515-414 and 505-404 transitions of ^{13}C isotopologues of HETERO1.

Table 7.1. Experimental and theoretical rotational constants (in MHz) and electric dipole moment components (in Debye) of the observed $(PO)_3$ conformers.

[a] B3LYP-D3BJ/def2-TZVP level. [b] Corrected for harmonic and anharmonic contributions. See the text for the abbreviations. [c] Experimentally estimated relative magnitudes. [d] N is the number of transitions included and σ is the standard deviation of the fit.

Const.	HOMO1				HOMO2				HETERO1			
	exp.	B3LYP[a]	B2/B3[b]	rPP/B3[b]	exp.	B3LYP[a]	B2/B3[b]	rPP/B3[b]	exp.	B3LYP[a]	B2/B3[b]	rPP/B3[b]
A	836.79876(67)	829	829	835	782.7474(26)	791	783	784	811.72688(42)	800	801	810
B	638.95770(89)	648	639	638	628.8592(13)	644	631	629	645.92417(27)	656	646	645
C	430.04824(37)	433	427	431	458.53594(94)	471	460	457	444.53303(24)	448	443	443
Dip. comp.	μ_b>μ_a≈μ_c[c]	0.7/1.6 /0.8	0.8/1.5 /0.8	0.8/1.5 /0.9	μ_a≈μ_c, no μ_b[c]	1.1/0.2 /1.3	1.1/0.3 /1.4	1.1/0.3 /1.4	μ_a>μ_b>μ_c[c]	1.5/1.1 /0.7	1.6/1.0 /0.8	1.6/0.9 /0.8
N[d], σ[d]	30, 4.0	-	-	-	18, 3.2	-	-	-	58, 2.9	-	-	-

The Kraitchman coordinates for singly substituted ^{13}C atoms are summarized in Tables 7.S11 and S12 of the SI for HOMO1 and HETERO1, respectively. Since Kraitchman's analyses provide only absolute values of the C atom coordinates, there are 8^9 possible C-backbone configurations without considering any chemical constraints because each of the nine carbon atoms has three Cartesian coordinates, leading to a total of $(2^3)^9 = 8^9$ possibilities. For HOMO1, we used the DFT geometry as a guide to determine the signs. The experimental substitution structure of the carbon backbone frame of HOMO1 is compared with the final DFT one (vide infra) in Figure 7.2a).

For HETERO1, a Python program was written to extract one unique structural candidate out of the 8^9 possibilities: by utilizing the known PO structure and setting limits for the intramolecular C-C distances, a few hundred possible C-backbone candidates were obtained initially. The O and H atoms were then put back in, based on the PO monomer geometry. After calculating the intermolecular bond lengths between the PO subunits, unphysical (i.e. too close) or unbound (i.e. too far) configurations were removed, leading to just one unique $(PO)_3$ structure. We successfully tested this procedure first with HOMO1, and then applied it to HETERO1. Details of the search are given in Point S2, SI. The derived HETERO1 C-backbone is shown in Figure 7.2b), together with the *ab initio* structure based on it. We note that the calculated rotational constants and electric dipole moment components of this DFT HETERO1 structure match the experiment results in Table 7.1. Interestingly, HOMO1 is made of RR6 and RR3 dimer subunits, HOMO2 utilizes the somewhat distorted binding topologies of RR2 and RR4, and HETERO1 contains RR6 and RS3,[6] whereas the third PO pair in these trimers utilizes mainly one CH···O contact for the interaction. (See Ref. 6 for notation of PO dimer units.)

The experimental relative abundance ratio of HETERO1:HOMO1:HOMO2 is estimated to be 3.3:1.0:0.2 for the racemic sample. If their stabilities were exactly the same, one would expect the HETERO1 versus HOMO1 ratio to be 3, based on statistical arguments (Scheme

1). The abundance ratio indicates that the experimental stability decreases from HETERO1 (most stable) to HOMO1 and then to the much less stable HOMO2. While the experimental intensities of HOMO1 and HOMO2 are consistent with the B3LYP energy ordering in Table 7.S1, HETERO1 is predicted to be ~0.1 kJmol^{-1} less stable than HOMO1 (Table 7.S2).

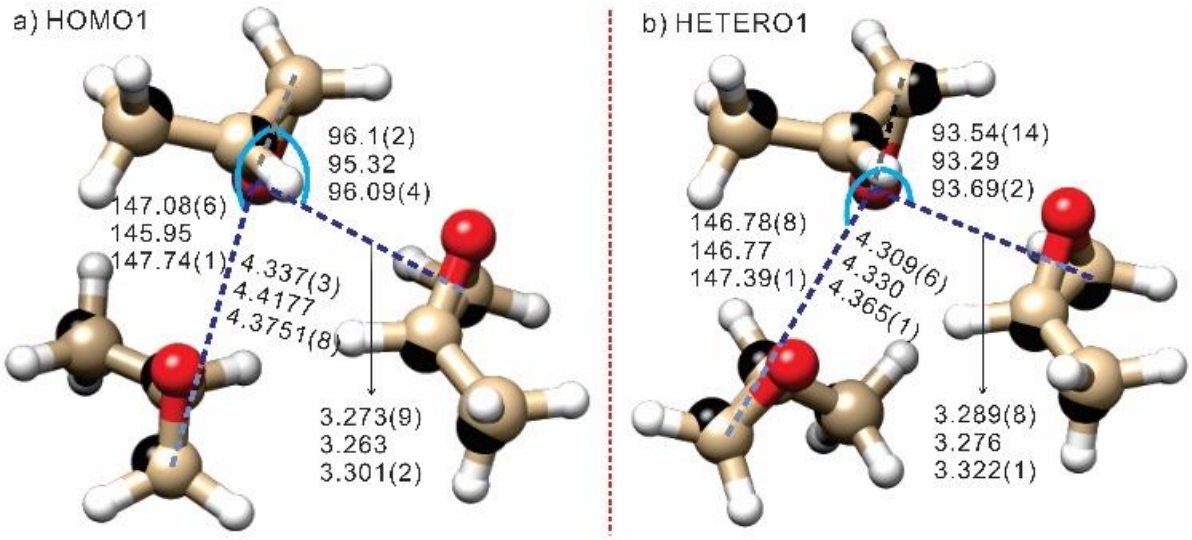

Figure 7.2. The rPP equilibrium structures of a) HOMO1 and b) HETERO1, together with the C-backbones (black balls) based on Kraitchman coordinates. Some key intermolecular structural parameters (bond lengths in Å and angles in °) are listed in order of semi-experimental equilibrium, rPP equilibrium, and experimental effective ones.

In the above discussion, experimental vibrational ground-state rotational constants (B_0) are compared with the equilibrium values (B_e). For fully quantitative purposes, the difference between them cannot be neglected. Here we applied a general hybrid approach, referred to as B2/B3, which is based on harmonic/anharmonic force fields computed with the B2PLYP/B3LYP-D3BJ functionals in conjunction with jun-cc-pVTZ and jun-cc-pVDZ basis sets, respectively. The B2/B3 approach has been validated for both covalent interactions and non-covalently bound complexes.[12] In addition, we replaced the B2PLYP-D3 functional by the revised version of the DSD-PBEP86-D3BJ functional (abbreviated as rPP),[13] which further improves results for non-covalent interactions over B2.

The six lowest homo-/heterochiral structures, including HETERO1, were re-optimized at the B2 and rPP levels and anharmonic vibrational corrections were computed at the B3 level. A full account of the computational details is given in Point S3, SI. The resulting B_e values, relative energies, dipole moment components at the B2 and rPP levels, and their vibrational corrections are summarized in Table 7.S13-S18. The results for all singly substituted ^{13}C isotopologues of HOMO1, HOMO2, and HETERO1 are in Tables 7.S19-S30, SI. It is noteworthy that at the rPP level, HETERO1 becomes the global minimum, thus restoring full agreement with the experimental energy ordering. As shown in Table 7.1, the maximum difference between experimental rotational constants and those from the B2/B3 hybrid scheme is *reduced* to 1.2% in comparison to 3.7% with just the equilibrium calculations, and the new hybrid rPP/B3 model further reduces the difference to below 0.3% for all $(PO)_3$ observed. This remarkable level of accuracy also allowed us to confidently identify the HOMO2 carrier. With the vibrational corrections, we obtained the 20 sets of semi-experimental equilibrium rotational constants (normal and ^{13}C isotopologues) of HOMO1 and HETERO1, which were used to refine their theoretical equilibrium structures while fixing the monomer geometries and some intermolecular structural parameters. The refined results are given in Table 7.S31-34, with some key parameters shown in Figure 7.2.

7.3. Conclusions

In conclusion, the conformational panorama of $(PO)_3$, a ternary chiral system of fundamental interest, was investigated in detail using CP-FTMW spectroscopy and a range of theoretical treatments including the CREST, B3LYP, B2/B3, and rPP/B3 calculations. The high sensitivity/resolution capability of the CP-FTMW instrument allowed us to uncover the elusive DFT HETERO1 structure based on the experimental ^{13}C isotopic data, aided by a Python program and subsequent DFT calculations. The study further reveals a slight chirality controlled conformational preference for the heterochiral trimer, continuing the same preference shown in $(PO)_2$. The highly sophisticated semiempirical conformational search program CREST was not able to find the most stable ternary heterochiral aggregate, and the current work may provide benchmark data for further improvements.

References

[1] N. Adam, G. Avar, H. Blankenheim, W. Friederichs, M. Giersig, E. Weigand, M. Halfmann, F.-W. Wittbecker, D.-R. Larimer, U. Maier, S. Meyer-Ahrens, K.-L. Noble, H.-G. Wussow, *Polyurethanes*, **2005**.

[2] a) R. K. Kondru, P. Wipf, D. N. Beratan, *Science* **1998**, *282*, 2247-2250; b) J. R. Cheeseman, M. J. Frisch, F. J. Devlin, P. J. Stephens, *J. Phys. Chem. A* **2000**, *104*, 1039-1046.

[3] a) S. M. Wilson, K. B. Wiberg, J. R. Cheeseman, M. J. Frisch, P. H. Vaccaro, *J. Phys. Chem. A* **2005**, *109*, 11752-11764; b) Z. Su, Q. Wen, Y. Xu, *J. Am. Chem. Soc.* **2006**, *128*, 6755-6760; c) Z. Su, Y. Xu, *Angew. Chem.* **2007**, *119*, 6275-6278; *Angew. Chem. Int. Ed.* **2007**, *46*, 6163-6166; d) M. Losada, P. Nguyen, Y. Xu, *J. Phys. Chem. A* **2008**, *112*, 5621-5627; e) F. Lipparini, F. Egidi, C. Cappelli, V. Barone, *J. Chem. Theory Comput.* **2013**, *9*, 1880-1884.

[4] a) J. D. Swalen, D. R. Herschbach, *J. Chem. Phys.* **1957**, *27*, 100-108; b) D. R. Herschbach, J. D. Swalen, *J. Chem. Phys.* **1958**, *29*, 761-776.

[5] B. A. McGuire, P. B. Carroll, R. A. Loomis, I. A. Finneran, P. R. Jewell, A. J. Remijan, G. A. Blake, *Science* **2016**, *352*, 1449-1452.

[6] a) Z. Su, N. Borho, Y. Xu, *J. Am. Chem. Soc.* **2006**, *128*, 17126-17131; b) N. Borho, Y. Xu, *Angew. Chem. Int. Ed.* **2007**, *46*, 2276-2279; c) N. Borho, Y. Xu, *J. Am. Chem. Soc.* **2008**, *130*, 5916-5921; d) J. Thomas, F. X. Sunahori, N. Borho, Y. Xu, *Chem. Eur. J.* **2011**, *17*, 4582-4587; e) J. Thomas, W. Jäger, Y. Xu, *Angew. Chem.* **2014**, *126*, 7405-7408; *Angew. Chem. Int. Ed.* **2014**, *53*, 7277-7280.

[7] a) G. G. Brown, B. C. Dian, K. O. Douglass, S. M. Geyer, B. H. Pate, *Rev. Sci. Instrum.* **2008**, *79*, 053103/1-13; b) C. Pérez, S. Lobsiger, N. A. Seifert, D. P. Zaleski, B. Temelso, G. C. Shields, Z. Kisiel, B. H. Pate, *Chem. Phys. Lett.* **2013**, *571*, 1-15.

[8] a) A. K. King, B. J. Howard, *Chem. Phys. Lett.* **2001**, *348*, 343-349; b) A. Maris, B. M. Giuliano, D. Bonazzi,W, Caminati, *J. Am. Chem. Soc.* **2008**, *130*, 13860-13861.

[9] a) B. H. Pate, L. Evangelisti, W. Caminati, Y. Xu, J. Thomas, D. Patterson, C. Perez, M. Schnell, in *Chiral Analysis (Second Edition)* (Ed.: P. L. Polavarapu), Elsevier, **2018**, pp. 679-729; b) F. Xie, N. A. Seifert, W. Jaeger, Y. Xu, *Angew. Chem. Int. Ed.* **2020**, DOI:10.1002 /anie.202005685 and /ange.202005685.

[10] D. P. Glavin, A. S. Burton, J. E. Elsila, J. C. Aponte, J. P. Dworkin, *Chem. Rev.* **2020**, *120*, 4660-4689.

[11] S. Grimme, C. Bannwarth, S. Dohm, A. Hansen, J. Pisarek, P. Pracht, J. Seibert, F. Neese, *Angew. Chem. Int. Ed.* **2017**, *56*, 14763-14769.

[12] a) E. Penocchio, M. Piccardo, V. Barone, *J. Chem. Theory Comput.* **2015**, *11*, 4689-4707; b) C. Puzzarini, J. Bloino, N. Tasinato and V. Barone, *Chem. Rev.* **2019**, *119*, 8131-8191.

[13] G. Santra, N. Sylvetsky, J. M. L. Martin, *J. Chem. Theory Comput.* **2019**, *123*, 5129-5143.

[14] S. Grimme, C. Bannwarth, P. Shushkov, *J. Chem. Theory Comput.* **2017**, *13*, 1989-2009.

[15] a) M. M. Quesada-Moreno, P. Pinacho, C. Pérez, M. Šekutor, P. R. Schreiner, M. Schnell, *Eur. J. Chem.* **2020**, DOI:10.1002/ chem.202001444; b) F. Xie, N. A. Seifert, M. Heger, J. Thomas, W. Jäger, Y. Xu, *Phys. Chem. Chem. Phys.* **2019**, *21*, 15408-15416.

[16] a) S. Grimme, S. Ehrlich, L. Goerigk, *J. Comput. Chem.* **2011**, *32*, 1456-1465; b) A. D. Becke, E. R. Johnson, *J. Chem. Phys.* **2005**, *123*, 154101/1-9.

[17] M. J. Frisch, et al., Gaussian 16, Revision A.03, Gaussian, Inc., Wallingford, CT, **2016**. Full reference in SI.

[18] a) C. D. Carlson, N. A. Seifert, M. Heger, F. Xie, J. Thomas, Y. Xu, *J. Mol. Spectrosc.* **2018**, *351*, 62-67; b) N. A. Seifert, J. Thomas, W. Jäger, Y. Xu, *Phys. Chem. Chem. Phys.* **2018**, *20*, 27630-27637.

[19] a) S. Blanco, A. Maris, S. Melandri, W. Caminati, *Mol. Phys.* **2002**, *100*, 3245-3249; b) Z. Su, Y. Xu, *J. Mol. Spectrosc*. **2005**, *232*, 112-114.

Chapter 8

Conclusions

During my Ph.D. career, I studied several chiral molecular systems, including perillyl alcohol, tetrahydro-2-furoic acid, its complexes with itself and propylene oxide, and trimers of propylene oxide using molecular rotational resonance (MRR) spectroscopy. These chiral molecular systems exhibit complex conformational landscapes, which I have probed in substantial detail. My work has been accomplished by using mainly a chirped pulsed Fourier transfer microwave spectrometer and a cavity-based Fourier transform spectrometer experimentally and by utilizing a considerable amount of theoretical modeling. From the spectroscopic observations, some exciting chirality-controlled structural preferences have been uncovered. These results have been discussed in my thesis chapters, and some highlights are listed below. These studies further extend our understanding of chiral recognition mechanisms from a fundamental perspective. My thesis work is among some of the earliest rotational spectroscopic studies that implement comprehensive conformational searches[1-3] for interpreting extremely dense and informative broadband chirped pulse rotational MW spectra of chiral species. In the thesis work, I have demonstrated that it is essential to have a comprehensive conformational search to interpret the experimental intensities to abundances of various species in a jet expansion.

During my Ph.D. study, I have developed several Python and Linux scripts[4] for automatic spectroscopic data processing. These scripts have significantly improved efficiency and reduced human errors in data handling, assigning broadband rotational spectra, and

extracting crucial experimental information such as rotational temperatures, abundances of species, and structural properties. These include scripts for automatic enantiomer excess(ee) analysis, facilitating conformational search job flows, extracting rotational temperature and species abundances, and so on. In relation to MRR spectroscopy application in the industry, these programs show the potential to automate several main spectroscopic analysis steps. They may push its commercialization one step forward.

In chapter 3, the perillyl alcohol monomer's conformational landscape was studied using a chirped pulse Fourier transform microwave spectrometer and a cavity-based Fourier transform microwave spectrometer. To aid the dense chirped pulse spectrum assignment, extensive theoretical conformational searches were carried out. By carefully considering possible conformational conversions, 12 out of 54 conformers were ultimately identified as observable candidates in a molecular jet expansion. Rotational spectra of eight out of the 12 candidates were observed experimentally and analyzed. The non-observation of the remaining four conformers may be attributed to their low abundance. The study points out the importance of identifying all conformers of relevant abundance, even those which could not be detected experimentally. To properly benchmark the relative theoretical stabilities with the experimental ones, a comprehensive study of the conformational distribution of perillyl alcohol contributes to our understanding of its structural properties, which may influence its functions. This study's central message is that detailed knowledge about the overall conformational landscape and theoretical abundances of *all* relevant conformers is crucial to relate experimental conformational abundances to relative stabilities and use them subsequently to benchmark the theoretical methods. The study showcases the power of CP-FTMW spectroscopy in distinguishing many conformers with only minor structural differences and the importance of identifying these conformers in detail to benchmark relative theoretical stabilities with the experimental ones properly.

From chapters 4 to 6, tetrahydro-2-furoic monomers, the binary complex between tetrahydro-2-furoic and propylene oxide and tetrahydro-2-furoic dimers were investigated.

For the tetrahydro-2-furoic monomers, manual scanning along three flexible structural coordinates was carried out to identify possible conformers related to the relative orientations of the carbonyl and hydroxyl groups in the COOH functional group, the COOH rotation, and the ring puckering motions in the system. Simultaneously, Grimme's conformational search code CREST[1-3] was used for the same purpose. Eight same conformers were identified from both search approaches, building our confidence in the aforementioned conformational code, especially its ability in identifying subtly different conformers. The three most stable conformers predicted, i.e., **I**, **II**, and **III**, were observed experimentally and conclusively assigned, although the experimental relative abundances differ drastically from the theoretically predicted abundances. Further extensive theoretical searches were done to identify the conformation conversion paths and the associated barriers. These details of the tetrahydro-2-furoic conformational landscape were used successfully to explain the experimental conformational abundances in some shallow conformational conversion barriers leading to the nearly total population transfer of several higher energy conformers.

The acid monomers study provides a solid foundation to explain the interesting conformational distribution of the complex consisting of tetrahydro-2-furoic and propylene oxide. The acid exists dominantly as **I**, **II**, and **III** in the jet expansion, with the first two taking on the *trans*-COOH configuration, whereas the last having the *cis*-COOH configuration. Six conformers of the mixed binary complex were detected by analyzing the broadband rotational spectrum recorded with a trace amount of tetrahydro-2-furoic + propylene oxide in neon in a supersonic jet expansion. Among the observed binary conformers, the kinetic binary conformers containing *trans*-COOH **I** are the dominant species, whereas the thermodynamically more stable adducts were also detected but with less abundance. Detailed analyses of the observed structures show interesting chirality dependent preference.

For the acid dimer, the conformational landscape shows further complication because both binding partners are flexible. A total of 84 possible homo- and heterochiral dimers which belong to the three types of structures were predicted. In Type 1 and 2 structures, further detailed potential energy scans and zero-point energy correction reveal only seven conformers survive the conformational cooling in the jet expansion. Six were detected out of these seven, while one has zero dipole moment and could not be detected. The *trans* versus *cis*-COOH competitions and chirality-controlled structural preferences were observed among six THFA dimers as well. By applying the recently proposed chiral self-tag approach, the ee value of a nearly enantiopure tetrahydro-2-furoic sample was determined accurately. Of particular significance, it was proved experimentally, even with the very complex conformational distribution, one can still obtain consistent ee results using rotational transitions of multiple conformers. High resolution, conformer-specific studies such as this one are essential for current research activities in benchmarking theoretical energetic predictions and exploring practical chiral tag spectroscopy applications.

The study discussed in chapter 7 highlights a challenging issue. In this study, the propylene oxide trimer's conformational panorama, a chiral ternary system of fundamental interest, was investigated in detail. Two sets of homochiral trimer transitions were assigned, and the associated conformers were identified with theoretical support. One set of heterochiral trimer transitions was assigned, but *no* structures generated by one of the latest, advanced conformational search codes could account for the set of transitions observed. As shown in the previous chapters, the theoretical input is essential for the assignment and the interpretation of all these interesting chiral molecular systems' rotational spectra. What can one do when theory fails to provide a structural candidate? This challenge was overcome by pushing the chirped pulse Fourier transform instrument's sensitivity to detect 18 ^{13}C isotopologues of both homochiral and heterochiral propylene oxide trimers in their natural abundances. With the aid of a Python program, the trimer's carbon atom backbone and then the whole trimer structure was generated using the ^{13}C isotopic data. This procedure was

tested with the homochiral trimer first and successfully applied to the heterochiral trimer. The study further reveals a slight chirality controlled conformational preference for the heterochiral trimer, continuing the same preference shown in the propylene oxide dimers. It appears that the highly sophisticated semiempirical conformational search program CREST[1-3], which has been utilized extensively in this thesis work, was not able to produce the most stable ternary heterochiral aggregate identified experimentally. The current work may provide benchmark data for further improvements.

References

[1] C. Bannwarth, S. Ehlert, S. Grimme, *J. Chem. Theory Comput.* **2019**, *15*, 1652-1671.

[2] S. Grimme, *J. Chem. Theory Comput.* **2019**, *15*, 2847-2862.

[3] P. Pracht, F. Bohle, S. Grimme, *Phys. Chem. Chem. Phys.* **2020**, *22*, 7169-7192.

[4] F. Xie, *https://github.com/FanXie001/MW-spectroscopy* **2016-2020**.

Bibliography

[1] L. C. R. Pasteur, *Acad. Sci.* **1858**, *46*, 615-818.

[2] L. Pasteur, *Ann. Chim. Phys.* **1848**, *28*, 56-99.

[3] L. Pasteur, *Compt. Rend. Acad. Sci.* **1853**, *36*, 19-26.

[4] D. G. Blackmond, *Cold Spring Harbor perspectives in biology* **2010**, *2*, 002147.

[5] G. Tranter, *J. Theor. Biol.* **1986**, *119*, 467-479.

[6] N. Fujii, T. Saito, *The Chemical Record* **2004**, *4*, 267-278.

[7] J. Gal, in *Chirality in Drug Research*, **2006**, pp. 1-26.

[8] W. Lenz, in *Problems of Birth Defects*, Springer, **1962**, pp. 199-199.

[9] A. Berthod, *Analytical Chemistry* **2006**, *78*, 2093-2099.

[10] J. Cronin, J. Reisse, in *Lectures in Astrobiology, Vol. 1*, **2005**, p. 473.

[11] W. A. Bonner, *Origins of Life and Evolution of the Biosphere* **1995**, *25*, 175-190.

[12] K. Michaeli, N. Kantor-Uriel, R. Naaman, D. H. Waldeck, *Chem. Soc. Rev.* **2016**, *45*, 6478-6487.

[13] L. Caglioti, K. Micskei, G. Pályi, *Chirality* **2011**, *23*, 65-68.

[14] T. H. Webb, C. S. Wilcox, *Chem. Soc. Rev.* **1993**, *22*, 383-395.

[15] S. C. Stinson, *Chem. Eng. News* **2001**, *79*, 45-57.

[16] T. Hirao, *J. Organomet. Chem.* **2009**, *694*, 806-811.

[17] B. Zheng, Y. Liu, J. Liu, S. Yin, J. Xu, *Int. J. Mech. Sci.* **2019**, *161-162*, 105025.

[18] M. Tsukamoto, H. B. Kagan, *Advanced Synthesis & Catalysis* **2002**, *344*, 453-463.

[19] A. Voituriez, A. Panossian, N. Fleury-Brégeot, P. Retailleau, A. Marinetti, *J. Am. Chem. Soc.* **2008**, *130*, 14030-14031.

[20] G. K. E. Scriba, *J. Chromatogr. A* **2016**, *1467*, 56-78.

[21] J. R. Sanchez-Valencia, T. Dienel, O. Gröning, I. Shorubalko, A. Mueller, M. Jansen, K. Amsharov, P. Ruffieux, R. Fasel, *Nature* **2014**, *512*, 61-64.

[22] B. L. Feringa, R. A. van Delden, *Angew. Chem. Int. Ed.* **1999**, *38*, 3418-3438.

[23] O. Riant, O. Samuel, H. B. Kagan, *J. Am. Chem. Soc.* **1993**, *115*, 5835-5836.

[24] G. J. Palenik, W. P. Jensen, I.-H. Suh, *J. Chem. Educ.* **2003**, *80*, 753.

[25] K. C. Engman, P. Sandin, S. Osborne, T. Brown, M. Billeter, P. Lincoln, B. Nordén, B. Albinsson, L. M. Wilhelmsson, *Nucleic Acids Research* **2004**, *32*, 5087-5095.

[26] M. T. Zanni, N.-H. Ge, Y. S. Kim, R. M. Hochstrasser, *Proceedings of the National Academy of Sciences* **2001**, *98*, 11265.

[27] D. Van Hemelrijk, L. Van den Enden, H. J. Geise, H. L. Sellers, L. Schaefer, *J. Am. Chem. Soc.* **1980**, *102*, 2189-2195.

[28] J. M. Steed, T. A. Dixon, W. Klemperer, *J. Chem. Phys.* **1979**, *70*, 4095-4100.

[29] K. Wuthrich, *Science* **1989**, *243*, 45.

[30] S. J. Opella, F. M. Marassi, *Chem. Rev.* **2004**, *104*, 3587-3606.

[31] S. Woutersen, P. Hamm, *J. Phys. Chem. B* **2000**, *104*, 11316-11320.

[32] G. B. Park, R. W. Field, *J. Chem. Phys.* **2016**, *144*, 200901.

[33] C. Abeysekera, L. N. Zack, G. B. Park, B. Joalland, J. M. Oldham, K. Prozument, N. M. Ariyasingha, I. R. Sims, R. W. Field, A. G. Suits, *J. Chem. Phys.* **2014**, *141*, 214203.

[34] S. M. Fritz, P. Mishra, J. Wullenkord, P. G. Fugazzi, K. Kohse-Höinghaus, T. S. Zwier, N. Hansen, *Proceedings of the Combustion Institute* **2020**.

[35] B. H. Pate, L. Evangelisti, W. Caminati, Y. Xu, J. Thomas, D. Patterson, C. Perez, M. Schnell, in *Chiral Analysis (Second Edition)* (Ed.: P. L. Polavarapu), Elsevier, **2018**, pp. 679-729.

[36] J. L. Neill, A. V. Mikhonin, T. Chen, R. E. Sonstrom, B. H. Pate, *J. Pharm. Biomed. Anal.* **2020**, *189*, 113474.

[37] L. A. Joyce, Danielle M. Schultz, E. C. Sherer, J. L. Neill, R. E. Sonstrom, B. H. Pate, *Chem. Sci.* **2020**, *11*, 6332-6338.

[38] M. Lämmerhofer, *J. Chromatogr. A* **2010**, *1217*, 814-856.

[39] T. R. Hoye, C. S. Jeffrey, F. Shao, *Nat. Protoc.* **2007**, *2*, 2451-2458.

[40] M. Hu, Y.-X. Yuan, W. Wang, D.-M. Li, H.-C. Zhang, B.-X. Wu, M. Liu, Y.-S. Zheng, *Nat. Commun.* **2020**, *11*, 161.

[41] A. Bauder, *Handbook of High-resolution Spectroscopy* **2011**.

[42] J. M. Brown, J. M. Brown, A. Carrington, *Rotational spectroscopy of diatomic molecules*, Cambridge University Press, **2003**.

[43] W. Gordy, R. L. Cook, *Microwave molecular spectra*, Wiley, **1984**.

[44] C. H. Townes, A. L. Schawlow, *Microwave spectroscopy*, Courier Corporation, **2013**.

[45] W. Tait, *Phys. Rev. B* **1972**, *5*, 648.

[46] J. Weiner, P.-T. Ho, *Light-matter interaction: fundamentals and applications, Vol. 1*, John Wiley & Sons, **2008**.

[47] G. B. Park, R. W. Field, *J. Chem. Phys.* **2016**, *144*, 200901.

[48] D. Schmitz, V. Alvin Shubert, T. Betz, M. Schnell, *J. Mol. Spectrosc.* **2012**, *280*, 77-84.

[49] W. Gordy, *Rev. Mod. Phys.* **1948**, *20*, 668.

[50] G. G. Brown, B. C. Dian, K. O. Douglass, S. M. Geyer, S. T. Shipman, B. H. Pate, *Rev. Sci. Instrum.* **2008**, *79*, 053103.

[51] N. A. Seifert, I. A. Finneran, C. Perez, D. P. Zaleski, J. L. Neill, A. L. Steber, R. D. Suenram, A. Lesarri, S. T. Shipman, B. H. Pate, *J. Mol. Spectrosc.* **2015**, *312*, 13-21.

[52] B. A. McGuire, P. B. Carroll, R. A. Loomis, I. A. Finneran, P. R. Jewell, A. J. Remijan, G. A. Blake, *Science* **2016**, *352*, 1449-1452.

[53] S. R. Domingos, C. Pérez, M. D. Marshall, H. O. Leung, M. Schnell, *Chem. Sci.* **2020**.

[54] B. H. Pate, L. Evangelisti, W. Caminati, Y. Xu, J. Thomas, D. Patterson, C. Perez, M. Schnell, in *Chiral Analysis (Second Edition)* (Ed.: P. L. Polavarapu), Elsevier, **2018**, pp. 679-729.

[55] P. Pracht, F. Bohle, S. Grimme, *Phys. Chem. Chem. Phys.* **2020**, *22*, 7169-7192.

[56] C. Bannwarth, S. Ehlert, S. Grimme, *J. Chem. Theory Comput.* **2019**, *15*, 1652-1671.

[57] S. Grimme, *J. Chem. Theory Comput.* **2019**, *15*, 2847-2862.

[58] C. F. Fischer, **1977**.

[59] in *Ideas of Quantum Chemistry* (Ed.: L. Piela), Elsevier, Amsterdam, **2007**, pp. 498-566.

[60] in *Ideas of Quantum Chemistry* (Ed.: L. Piela), Elsevier, Amsterdam, **2007**, pp. 567-614.

[61] S. Grimme, J. Antony, S. Ehrlich, H. Krieg, *J. Chem. Phys.* **2010**, *132*, 154104.

[62] S. Grimme, R. Huenerbein, S. Ehrlich, *ChemPhysChem* **2011**, *12*, 1258-1261.

[63] S. Grimme, S. Ehrlich, L. Goerigk, *J. Comput. Chem* **2011**, *32*, 1456-1465.

[64] C. M. Western, *J. Quant. Spectrosc. Radiat. Transf.* **2017**, *186*, 221-242.

[65] D. F. Plusquellic, R. D. Suenram, B. Maté, J. O. Jensen, A. C. Samuels, *J. Chem. Phys.* **2001**, *115*, 3057-3067.

[66] J. K. G. Watson, *J. Chem. Phys.* **1967**, *46*, 1935-1949.

[67] J. K. G. Watson, *Mol. Phys.* **1968**, *15*, 479-490.

[68] H. Hartwig, H. Dreizler, *Zeitschrift für Naturforschung A* **1996**, *51*, 923-932.

[69] T. C. Chen, C. O. Da Fonseca, A. H. Schönthal, *Am. J. Cancer. Res.*, **2015**, 5, 1580-1593.

[70] P. J. M. Boon, D. van der Boon, and G. J. Mulder, *Toxicol. Appl. Pharmacol.*, 2000, **167**, 55-62.

[71] T. C. Chen, C. O. Da Fonseca, A. H. Schönthal, *Int. J. Mol. Sci.*, 2018, **19**, 3905/1-21.

[72] J. G. Hill, A. C. Legon, D. P. Tew and N. R. Walker, *Top. Curr. Chem.*, 2015, **358**, 43-78.

[73] M. Becucci and S. Melandri, *Chem. Rev.*, 2016, **116**, 5014-5037.

[74] C. B. Park and R. W. Field, *J. Chem. Phys.*, 2016, **144**, 200901.

[75] G. T. Fraser, R. D. Suenram, and C. L. Lugez, *J. Phys. Chem. A*, 2001, **105**, 9859-9864.

[76] G. G. Brown, B. C. Dian, K. O. Douglass, S. M. Geyer, S. T. Shipman, B. H. Pate, *Rev. Sci. Instrum.*, 2008, **79**, 053103.

[77] N. A. Seifert, I. A. Finneran, C. Perez, D. P. Zaleski, J. L. Neill, A. L. Steber, R. D. Suenram, A. Lesarri, S. T. Shipman, B. H. Pate, *J. Mol. Spectrosc*., 2015, **312**, 13-21.

[78] S. R. Domingos, C. Pérez, C. Medcraft, P. Pinacho, M. Schnell, *Phys. Chem. Chem. Phys.* 2016, **18**, 16682-16689.

[79] D. Loru, M. M. Quesada-Moreno, J. R. Avilés-Moreno, N. Jarman, T. R. Huet, J. J. López-González, M. E. Sanz, *ChemPhysChem,* 2017, **18**, 274-280.

[80] F. Xie, X. Ng, N. A. Seifert, J. Thomas, W. Jäger, Y. Xu, *J. Chem. Phys*., 2018, **149**, 224306/1-10.

[81] N. A. Seifert, J. Thomas, W. Jäger, Y. Xu, *Phys. Chem. Chem. Phys.,* 2018, **20**, 27630-27637.

[82] J. Thomas, N. A. Seifert, W. Jager, Y. Xu, *Angew. Chem. Int. Ed.,* 2017, **56**, 6289-6293.

[83] S. Oswald, N. A. Seifert, F. Bohle, M. Gawrilow, S. Grimme, W. Jäger, Y. Xu and M. A. Suhm, *Angew. Chem. Int. Ed.,* 2019, **58**, 5080-5084.

[84] A. Poblotzki, H. C. Gottschalk and M. A. Suhm, *J. Phys. Chem. Lett.*, 2017, **8**, 5656-5665.

[85] F. R. Jensen and C. H. Bushweller, *J. Am. Chem. Soc.*, 1969, **91**, 5774–5782.

[86] K. Fukui, *Acc. Chem. Res.,* 1981, **14**, 363-368.

[87] R. S. Ruoff, T. D. Klots, T. Emilsson and H. S. Gutowsky, *J. Chem. Phys*., 1990, **93**, 3142-3150.

[88] C. M. Western, *J. Quant. Spectrosc. Radiat. Transfer*, 2017, **186**, 221-242.

[89] J. R. A. Moreno, F. P. Ureña, J. J. L. González and T. R. Huet, C*hem. Phys. Lett.*, 2009, **473**, 17-20.

[90] H. Hartwig and H. Dreizler, *Z. Naturforsch. A* 1996, **51**, 923-932.

[91] N. Hansen, H. Mäder and T. Bruhn, *Mol. Phys.*, 1999, **97**, 587-595.

[92] J. K. G. Watson, in Vibrational Spectra and Structure, ed. J. R. Durig, Elsevier, New York, 1977, vol. 6, p. 1.

[93] C. D. Carlson, N. A. Seifert, M. Heger, F. Xie, J. Thomas and Y. Xu, *J. Mol. Spec.,* 2018, **351**, 62-67.

[94] C. Pérez, S. Lobsiger, N. A. Seifert, D. P. Zaleski, B. Temelso, G. C. Shields, Z. Kisiel and B. H. Pate, *Chem. Phys. Lett.*, 2013, **571**, 1-15.

[95] T. J. Balle and W. H. Flygare, *Rev. Sci. Instrum.*, 1981, **52**, 33-45.

[96] Y. Xu, J. Van Wijngaarden and W. Jäger, *Int. Rev. Phys. Chem.*, 2005, **24**, 301-338.

[97] Y. Xu and W. Jäger, *J. Chem. Phys.*, 1997, **106**, 7968–7980.

[98] Gaussian 16, Revision B.01, M. J. Frisch, G. W. Trucks, H. B. Schlegel, G. E. Scuseria, M. A. Robb, J. R. Cheeseman, G. Scalmani, V. Barone, G. A. Petersson, H. Nakatsuji, X.; Li, M. Caricato, A. V. Marenich, J. Bloino, B. G. Janesko, R. Gomperts, B. Mennucci, H. P.. Hratchian, J. V. Ortiz, A. F. Izmaylov, J. L. Sonnenberg, D. Williams-Young, F. Ding, F. Lipparini, F. Egidi, J. Goings, B. Peng, A. Petrone, T. Henderson, D. Ranasinghe, V. G. Zakrzewski, J. Gao, N. Rega, G. Zheng, W. Liang, M. Hada, M. Ehara, K. Toyota, R. Fukuda, J. Hasegawa, M. Ishida, T. Nakajima, Y. Honda, O. Kitao, H. Nakai, T. Vreven, K. Throssell, J. A. Montgomery Jr., J. E. Peralta, F. Ogliaro, M. J. Bearpark, J. J. Heyd, E. N. Brothers, K. N. Kudin, V. N. Staroverov, T. A. Keith, R. Kobayashi, J. Normand, K. Raghavachari, A. P. Rendell, J. C. Burant, S. S. Iyengar, J. Tomasi, M. Cossi, J. M. Millam, M. Klene, C. Adamo, R. Cammi, J. W. Ochterski, R. L. Martin, K. Morokuma, O. Farkas, J. B. Foresman, D. J. Fox, Gaussian, Inc., Wallingford CT, 2016.

[99] MOLPRO, version 2015.1, a package of ab initio programs, H.-J. Werner, P. J. Knowles, G. Knizia, F. R. Manby, M. Schütz, P. Celani, W. Györffy, D. Kats, T. Korona, R. Lindh, A. Mitrushenkov, G. Rauhut, K. R. Shamasundar, T. B. Adler, R. D. Amos, A. Bernhardsson, A. Berning, D. L. Cooper, M. J. O. Deegan, A. J. Dobbyn, F. Eckert, E. Goll, C. Hampel, A. Hesselmann, G. Hetzer, T. Hrenar, G. Jansen, C. Köppl, Y. Liu, A. W. Lloyd, R. A. Mata, A. J. May, S. J. McNicholas, W. Meyer, M. E. Mura, A. Nicklass, D. P. O'Neill, P. Palmieri, D. Peng, K. Pflüger,

R. Pitzer, M. Reiher, T. Shiozaki, H. Stoll, A. J. Stone, R. Tarroni, T. Thorsteinsson, and M. Wang. see http://www.molpro.net.

[100] S. Grimme, S. Ehrlich and L. Goerigk, *J. Comput. Chem.*, 2011, **32**, 1456–1465.

[101] S. Grimme, J. Antony, S. Ehrlich and H. Krieg, *J. Chem. Phys.*, 2010, **132**, 154104.

[102] A. D. Becke and E. R. Johnson, *J. Chem. Phys.,* 2005, **123**, 154101.

[103] F. Weigend and R. Ahlrichs, *Phys. Chem. Chem. Phys.*, 2005, **7**, 3297-3305.

[104] A. Schäfer, C. Huber and R. Ahlrichs, *J. Chem. Phys.*, 1994, **100**, 5829–5835.

[105] T. Korona, D. Kats, M. Schütz, T. B. Adler, Y. Liu and H.-J. Werner, in *Linear-Scaling Techniques in Computational Chemistry and Physics* (Springer Netherlands, 2011), pp. 345–407.

[106] M. J. Frisch, M. Head-Gordon and J. A. Pople, *Chem. Phys. Lett.*, 1990, **166**, 275-280.

[107] J. Kaminsky, R. A. Mata, H.-J. Werner and F. Jensen, *Mol. Phys.*, 2008, **106**, 1899-1906.

[108] C. Peng and H. B. Schlegel, *Isr. J. Chem.*, 1993, **33**, 449-454.

[109] X. Li and M. J. Frisch, *J. Chem. Theory Comp.*, 2006, **2**, 835-839.

[110] S. Grimme, C. Bannwarth and P. Shushkov, *J. Chem. Theory Comput.*, 2017, **13**, 1989-2009.

[111] S. Grimme, *J. Chem. Theory Comput.*, 2019, **15**, 2847-2862. Article ASAP DOI: 10.1021/acs.jctc.9b00143.

[112] E. R. Johnson, S. Keinan, P. Mori-Snchez, J. Contreras-García, A. J. Cohen and W. Yang, *J. Am. Chem. Soc.*, 2010, **132**, 6498–6506.

[113] G. G. Engerholm, A. C. Luntz, W. D. Gwinn, and D. O. Harris, *J. Chem. Phys.* **50**, 2446 (1969).

[114] V. M. Rayón and J. A. Sordo, *J. Chem. Phys.* **122**, 204303 (2005).

[115] R. Meyer, J. C. López, J. L. Alonso, S. Melandri, P. G. Favero, and W. Caminati, *J. Chem. Phys.* **111**, 7871 (1999).

[116] A. H. Mamleev, L. N. Gunderova, and R. V. Gallev, *J. Struct. Chem.* **42**, 365 (2001).

[117] D. G. Melnik, S. Gopalakrishnan, T. A. Miller, and F. C. De Lucia, *J. Chem. Phys.* **118**, 3589 (2003).

[118] A. Wu, D. Cremer, *Int. J. Mol. Sci.* **4**, 158-192 (2003).

[119] G. Vallancien, M. Emberton, A. Alcaraz, H. Matzkin, R. J. A. van Moorselaar, R. Hartung, N. Harving, M. Elhilali, *BJU Int.* **101**, 847–852 (2008).

[120] I. Elia, D. Broekaert, S. Christen, R. Boon, E. Radaelli, M. F. Orth, C. Verfaillie, T. G. P. Grünewald, S.-M. Fendt, *Nat. Commun.* **8**, 15267 doi: 10.1038/ncomms15267 (2017).

[121] M. Zhang, T. A. White, J. P. Schuermann, B. A. Baban, D. F. Becker, J. J. Tanner, *Biochem.* **43**, 12539–12548 (2004).

[122] J. Bellet, A. Deldalle, C. Samson, G. Steenbeckeliers, R. Wertheimer, J. Mol. Struct. **9**, 65 (1971).

[123] F. W. Lichtenthaler, In *Ullmann's Encyclopedia of Industrial Chemistry*; Wiley-VCH Verlag GmbH & Co. KGaA: Weinheim, Germany, 2003.

[124] C. M. Western, B. E. Billinghurst, *Phys. Chem. Chem. Phys.* **19**, 10222–10226 (2017).

[125] J. K. G. Watson, in *Vibrational Spectra and Structure*, Vol. 6 (Ed.: J. R. Durig), Elsevier, New York, pp. 1- 89, (1977).

[126] a) N. Borho, Y. Xu, *Phys. Chem. Chem. Phys.* **9**, 4514–4520 (2007); b) N. Borho, Y. Xu, *Angew. Chem. Int. Ed.* **46**, 2276–2279 (2007); *Angew. Chem.* **119**, 2326–2329 (2007).

[127] R. S. Ruoff, T. D. Klots, T. Emilsson, H. S. Gutowsky, *J. Chem. Phys*. **93**, 3142-3150 (1990).

[128] M. Heger, K. E. Otto, R. A. Mata, M. A. Suhm, *Phys. Chem. Chem. Phys.* **17**, 9899-9909 (2015).

[129] J. L. Alonso, C. Pérez, M. E. Sanz, J. C. López, S. Blanco, *Phys. Chem. Chem. Phys.* **11**, 617-627 (2009).

[130] S. R. Domingos, C. Pérez, C. Medcraft, P. Pinacho, M. Schnell *Phys. Chem. Chem. Phys.* **18**, 16682-16689 (2016).

[131] P. R. Schreiner, H. P. Reisenauer, F. C. Pickard IV, A. C. Simmonett, W. D. Allen, E. Mátyus, and A. G. Császár, Nature **453**, 906 (2008).

[132] J. Thomas, E. Mariona, Y. Xu, *J. Chem. Phys.* **146**, 104303 (2017).

[133] a) M. Petković and M. Etinski, *RSC Adv*. **4**, 38517-38526 (2014); b) O. O. Brovarets, R. O. Zhurakivsky and D. M. Hovorun, *J. Comput. Chem*. **35**, 451-466 (2014).

[134] a) E. Espinosa, E. Molins, C. Lecomte, *Chem. Phys. Lett*. **285**, 170-173 (1998); b) I. Mata, I. Alkorta, E. Espinosa, E. Molins, *Chem. Phys. Lett*. **507**, 185-189 (2011).

[135] J. Kraitchman, *Am. J. Phys.* **21**, 17−24 (1953).

[136] C. C. Costain, *J. Chem. Phys.* **29**, 864−874 (1958).

[137] T. J. Balle, E. J. Campbell, M. R. Keenan, W. H. Flygare, *J. Chem. Phys.* **72**, 922–932 (1980).

[138] Y. Xu, W. Jäger, *J. Chem. Phys.* **106**, 7968-7980 (1997).

[139] a) G. G. Brown, B. C. Dian, K. O. Douglass, S. M. Geyer and B. H. Pate, *J. Mol. Spectrosc.* **238**, 200-212 (2006); b) G. S. Grubbs II, C. T. Dewberry, K. C. Etchison, K. E. Kerr and S. A. Cooke, *Rev. Sci. Instrum.* **78**, 096106/1-3 (2007); c) C. Pérez, S. Lobsiger, N. A. Seifert, D. P. Zaleski, B. Temelso, G. C. Shields, Z. Kisiel, B. H. Pate, *Chem. Phys. Lett.* **571**, 1–15 (2013).

[140] a) C. D. Carlson, N. A. Seifert, M. Heger, F. Xie, J. Thomas and Y. Xu, *J. Mol. Spectrosc.* **351**, 62–67 (2018); b) N. A. Seifert, J. Thomas, W. Jäger and Y. Xu, *Phys. Chem. Chem. Phys.* (submitted).

[141] a) S. Dempster, O. Sukhrukov, Q. Y. Lei and W. Jäger, *J. Chem. Phys.* **137**, 174303/1-8 (2012); b) J. Thomas, J. Yiu, J. Rebling, W. Jäger and Y. Xu, *J. Phys. Chem. A*. **117**, 13249-13254 (2013).

[142] Gaussian 16, Revision B.01, M. J. Frisch, G. W. Trucks, H. B. Schlegel, G. E. Scuseria, M. A. Robb, J. R. Cheeseman, G. Scalmani, V. Barone, G. A. Petersson, H. Nakatsuji, X.; Li, M. Caricato, A. V. Marenich, J. Bloino, B. G. Janesko, R. Gomperts, B. Mennucci, H. P.. Hratchian, J. V. Ortiz, A. F. Izmaylov, J. L.

Sonnenberg, D. Williams-Young, F. Ding, F. Lipparini, F. Egidi, J. Goings, B. Peng, A. Petrone, T. Henderson, D. Ranasinghe, V. G. Zakrzewski, J. Gao, N. Rega, G. Zheng, W. Liang, M. Hada, M. Ehara, K. Toyota, R. Fukuda, J. Hasegawa, M. Ishida, T. Nakajima, Y. Honda, O. Kitao, H. Nakai, T. Vreven, K. Throssell, J. A. Montgomery Jr., J. E. Peralta, F. Ogliaro, M. J. Bearpark, J. J. Heyd, E. N. Brothers, K. N. Kudin, V. N. Staroverov, T. A. Keith, R. Kobayashi, J. Normand, K. Raghavachari, A. P. Rendell, J. C. Burant, S. S. Iyengar, J. Tomasi, M. Cossi, J. M. Millam, M. Klene, C. Adamo, R. Cammi, J. W. Ochterski, R. L. Martin, K. Morokuma, O. Farkas, J. B. Foresman, D. J. Fox, Gaussian, Inc., Wallingford CT, 2016.

[143] J. S. Binkley and J. A. Pople, *Int. J. Quantum Chem.* **9**, 229-236 (1975).

[144] S. Grimme, S. Ehrlich and L. Goerigk, *J. Comp. Chem.* **32**, 1456-1465 (2011).

[145] S. Grimme, S. Ehrlich and L. Goerigk, *J. Comput. Chem.* **32**, 1456–1465 (2011).

[146] A. D. Becke and E. R. Johnson, *J. Chem. Phys.* **123**, 154101 (2005).

[147] R. Krishnan, J. S. Binkley, R. Seeger, and J. A. Pople, *J. Chem. Phys.* **72**, 650-654 (1980).

[148] a) F. Weigend and R. Ahlrichs, *Phys. Chem. Chem. Phys.* **7**, 3297 (2005); b) A. Schäfer, H. Horn and R. Ahlrichs, *J. Chem. Phys.* **97**, 2571–5648 (1992); c) A. Schäfer, C. Huber and R. Ahlrichs, *J. Chem. Phys.* **100**, 5829–5835 (1994).

[149] a) H. B. Schlegel, *J. Comp. Chem.* **3**, 214-218 (1982); b) C. Peng and H. B. Schlegel, *Isr. J. Chem.* **33**, 449-454 (1993); c) C. Peng and H. B. Schlegel, *Isr. J. Chem.* **33**, 449-454 (1993); d) X. Li and M. J. Frisch, *J. Chem. Theory Comp.* **2**, 835-839 (2006).

[150] S. Grimme, C. Bannwarth, and P. Shushkov, *J. Chem. Theory Comput.* **13**, 1989-2009 (2017).

[151] S. Grimme and C. Bannwarth, *J. Chem. Phys.* **145**, 054103 (2016).

[152] S. Grimme, C. Bannwarth, S. Dohm, A. Hansen, J. Pisarek, P. Pracht, J. Seibert, and F. Neese, *Angew Chem. Int. Ed.* **56**, 14763-14769 (2017); *Angew. Chem.* **129**, 14958-14964 (2017).

[153] S. Kirkpatrick, C. D. Gelatt, Jr., and M. P. Vecchi. *Science* **220**, 671-680 (1983).

[154] R. F. W. Bader, *Chem. Rev.* **91**, 893-928 (1991).

[155] E. R. Johnson, S. Keinan, P. Mori-Sánchez, J. Contreras-García, A. J. Cohen, W. Yang, J. Am. Chem. Soc. **132**, 6498-6506 (2010).

[156] M. D. Hanwell, D. E. Curtis, D. C. Lonie, T. Vandermeersh, E. Zurek, G. R. Hutchinson, J. Cheminformatics, **4**, 1-17 (2012). Version 4.8.6.

[157] T. Lu, F. Chen, J. Comp. Chem. **33**, 580-592 (2012).

[158] E. F. Pettersen, T. D. Goddard, C. C. Huang, G. S. Couch, D. M. Greenblatt, E. C. Meng, T. E. Ferrin, J. Comp. Chem. **25**, 1605-1612 (2004). Version 1.12.

[159] A. K. King, B. J. Howard, *Chem. Phys. Lett* **2001**, *348*, 343-349.

[160] A. Maris, B. M. Giuliano, D. Bonazzi, W. Caminati, *J. Am. Chem. Soc.* **2008**, *130*, 13860-13861.

[161] J. Thomas, F. X. Sunahori, N. Borho, Y. Xu, *Chem. Eur. J.* **2011**, *17*, 4582-4587.

[162] S. R. Domingos, C. Pérez, M. Schnell, AIP Publishing LLC, **2016**.

[163] L. Evangelisti, W. Caminati, D. Patterson, J. Thomas, Y. Xu, C. West, B. Pate, *ISMS* **2017**, RG03.

[164] G. G. Brown, B. C. Dian, K. O. Douglass, S. M. Geyer, S. T. Shipman, B. H. Pate, *Rev. Sci. Instrum.* **2008**, *79*, 053103.

[165] F. Xie, N. A. Seifert, W. Jäger, Y. Xu, *Angew. Chem. Int. Ed.* **2020**, *59*, 15703-15710.

[166] B. H. Pate, L. Evangelisti, W. Caminati, Y. Xu, J. Thomas, D. Patterson, C. Perez, M. Schnell, in *Chiral Analysis*, Elsevier, **2018**, pp. 679-729.

[167] S. R. Domingos, C. Pérez, M. Marshall, H. Leung, M. Schnell, *Chem. Sci.* **2020**.

[168] F. Xie, X. Ng, N. A. Seifert, J. Thomas, W. Jäger, Y. Xu, *J. Chem. Phys.* **2018**, *149*, 224306.

[169] J. R. Cheeseman, M. J. Frisch, F. J. Devlin, P. J. Stephens, *J. Phys. Chem. A* **2000**, *104*, 1039-1046.

[170] R. K. Kondru, P. Wipf, D. N. Beratan, *Science* **1998**, *282*, 2247-2250.

[171] M. A. Lowe, J. S. Alper, *J. Phys. Chem.* **1988**, *92*, 4035-4040.

[172] P. Mukhopadhyay, G. Zuber, M.-R. Goldsmith, P. Wipf, D. N. Beratan, *ChemPhysChem* **2006**, *7*, 2483-2486.

[173] M. Losada, P. Nguyen, Y. Xu, *J. Phys. Chem. A* **2008**, *112*, 5621-5627.

[174] Z. Su, Y. Xu, *Angew. Chem. Int. Ed.* **2007**, *46*, 6163-6166.

[175] J. D. Swalen, D. R. Herschbach, *J. Chem. Phys.* **1957**, *27*, 100-108.

[176] D. R. Herschbach, J. D. Swalen, *J. Chem. Phys.* **1958**, *29*, 761-776.

[177] B. A. McGuire, P. B. Carroll, R. A. Loomis, I. A. Finneran, P. R. Jewell, A. J. Remijan, G. A. Blake, *Science* **2016**, *352*, 1449-1452.

[178] S. Blanco, A. Maris, S. Melandri, W. Caminati, *Mol. Phys.* **2002**, *100*, 3245-3249.

[179] S. Blanco, A. Maris, A. Millemaggi, W. Caminati, *J. Mol. Struct.* **2002**, *612*, 309-313.

[180] S. Blanco, S. Melandri, A. Maris, W. Caminati, B. Velino, Z. Kisiel, *Phys. Chem. Chem. Phys.* **2003**, *5*, 1359-1364.

[181] Z. Su, N. Borho, Y. Xu, *J. Am. Chem. Soc.* **2006**, *128*, 17126-17131.

[182] Y. Orita, Y. Kawashima, E. Hirota, *J. Mol. Spectrosc.* **2011**, *268*, 78-84.

[183] Z. Su, Q. Wen, Y. Xu, *J. Am. Chem. Soc.* **2006**, *128*, 6755-6760.

[184] Z. Su, Y. Xu, *Angew. Chem.* **2007**, *119*, 6275-6278.

[185] S. Blanco, A. Maris, A. Millemaggi, W. Caminati, *J. Mol. Struct.* **2002**, *612*, 309-313.

[186] Z. Su, N. Borho, Y. Xu, *J. Am. Chem. Soc.* **2006**, *128*, 17126-17131.

[187] N. Borho, Y. Xu, *J. Am. Chem. Soc.* **2008**, *130*, 5916-5921.

[188] N. Borho, Y. Xu, *Angew. Chem. Int. Ed.* **2007**, *46*, 2276-2279.

[189] F. X. Sunahori, Z. Su, C. Kang, Y. Xu, *Chem. Phys. Lett.* **2010**, *494*, 14-20.

[190] F. Xie, M. Fusè, A. S. Hazrah, W. Jaeger, V. Barone, Y. Xu, *Angew. Chem. Int. Ed.* **2020**.

[191] D. Bernhard, M. Fatima, A. Poblotzki, A. Steber, C. Pérez, M. Suhm, M. Schnell, M. Gerhards, *Phys. Chem. Chem. Phys.* **2019**, *21*, 16032-16046.

[192] F. Xie, N. A. Seifert, M. Heger, J. Thomas, W. Jäger, Y. Xu, *Phys. Chem. Chem. Phys.* **2019**, *21*, 15408-15416.

[193] S. Oswald, N. A. Seifert, F. Bohle, M. Gawrilow, S. Grimme, W. Jäger, Y. Xu, M. A. Suhm, *Angew. Chem. Int. Ed.* **2019**, *58*, 5080-5084.

[194] C. Bannwarth, S. Ehlert, S. Grimme, *J. Chem. Theory Comput.* **2019**, *15*, 1652-1671.

[195] S. Grimme, *J. Chem. Theory Comput.* **2019**, *15*, 2847-2862.

[196] P. Pracht, F. Bohle, S. Grimme, *Phys. Chem. Chem. Phys.* **2020**, *22*, 7169-7192.

[197] A. D. Becke, E. R. Johnson, *J. Chem. Phys.* **2005**, *123*, 154101.

[198] J. K. G. Watson, *Mol. Phys.* **1968**, *15*, 479-490.

[199] C. M. Western, *J. Quant. Spectrosc. Radiat. Transf.* **2017**, *186*, 221-242.

[200] K. J. Mayer, C. Embly, B. Pate, L. Evangelisti, *ISMS* **2018**, TC06.

[201] K. J. Mayer, B. Pate, C. West, R. E. Sonstrom, M. S. Holdren, T. Smart, L. Evangelisti, *ISMS* **2019**.

[202] R. E. Sonstrom, K. J. Mayer, C. West, B. Pate, L. Evangelisti, *ISMS* **2019**.

[203] C. West, L. Evangelisti, R. E. Sonstrom, B. Pate, *ISMS* **2019**.

[204] R. E. Sonstrom, K. J. Mayer, C. West, B. Pate, *ISMS* **2019**.

[205] J. A. Dale, H. S. Mosher, *J. Am. Chem. Soc.* **1973**, *95*, 512-519.

[206] T. R. Hoye, C. S. Jeffrey, F. Shao, *Nat. Protoc.* **2007**, *2*, 2451-2458.

[207] C. D. Carlson, N. A. Seifert, M. Heger, F. Xie, J. Thomas, Y. Xu, *J. Mol. Spectrosc.* **2018**, *351*, 62-67.

[208] N. A. Seifert, J. Thomas, W. Jäger, Y. Xu, *Phys. Chem. Chem. Phys.* **2018**, *20*, 27630-27637.

Appendix A

Supporting Information for Chapter 3

The Rich Conformational Landscape of Perillyl Alcohol Revealed by Broadband Rotational Spectroscopy and Theoretical Modelling

Contents:

Table 3.S1. The theoretical raw ΔD_e and *ZPE* corrected ΔD_0 relative dissociation energies (in kJ mol^{-1}), rotational constants (in MHz) and electric dipole moment components (in Debye) of the 54 half-chair conformers calculated at B3LYP-B3DJ/def2-TZVP and LMP2/Aug-cc-pVQZ levels of theory

B3LYP-B3DJ/Def2-TZVP										LMP2/Aug-cc-pVQZ								
Conformer[a]	ΔD_e	ΔD_0	ΔG[b]	A	B	C	$\lvert\mu_a\rvert$	$\lvert\mu_b\rvert$	$\lvert\mu_c\rvert$	Conformer[a]	ΔD_e	ΔD_0[c]	A	B	C	$\lvert\mu_a\rvert$	$\lvert\mu_b\rvert$	$\lvert\mu_c\rvert$
Eq-TG-G+	0.0	0.0	0.0	2790	520	502	1.1	0.7	0.8	**Eq-TG-G+**	0.0	0.0	2800	524	505	1.2	0.8	0.7
Eq-TG-T	1.1	1.0	1.0	2829	531	481	1.2	1.2	0.3	**Ax-G+G+G-**	0.1	0.6	2039	669	643	1.3	0.8	1.0
Eq-G+G+G+	1.2	1.1	0.5	2722	519	507	1.2	1.0	0.3	**Eq-TG-T**	0.7	0.7	2836	535	484	1.3	1.2	0.2
Eq-TG-G-	2.2	2.0	1.0	2794	529	483	1.2	0.6	0.3	**Eq-G+G+G+**	1.2	1.1	2716	523	512	1.3	1.0	0.4
Eq-TTG+	2.7	2.2	2.3	2774	519	491	1.0	0.6	0.6	**Ax-TG-G-**	0.7	1.4	1687	758	714	1.5	1.2	0.3
Eq-G+G+T	2.4	2.3	1.8	2702	531	490	1.2	1.3	0.1	**Eq-G+G+T**	2.0	1.9	2696	535	494	1.3	1.2	0.2
Ax-G+G+G-	1.9	2.4	3.1	2122	644	620	1.3	0.6	1.2	Eq-TG-G-	2.2	2.1	2803	534	485	1.2	0.7	0.3
Eq-G+G+G-	3.3	3.2	2.3	2642	539	489	1.1	0.6	0.5	**Eq-TTG+**	3.3	2.8	2777	523	494	1.1	0.7	0.7
Eq-TTT	3.8	3.2	3.5	2729	534	474	1.1	0.0	1.3	Eq-G+G+G-	3.3	3.2	2631	545	492	1.2	0.3	0.7
Ax-TG-G-	2.6	3.2	3.8	1741	725	687	1.5	1.2	0.3	**Ax-G+TG-**	3.4	3.4	1961	680	658	1.9	0.5	0.4
Eq-G+TG+	3.8	3.3	3.4	2784	518	490	0.9	0.8	1.3	**Eq-TTT**	4.0	3.5	2731	538	477	1.1	0.1	1.2
Eq-G+TT	4.7	4.1	4.1	2744	531	473	0.9	0.6	0.5	Eq-G-G-G+	4.5	3.5	2822	525	504	0.8	0.6	0.7
Eq-TTG-	5.1	4.5	4.1	2794	528	475	1.2	1.1	1.0	Eq-G+TG+	4.4	3.9	2788	522	494	1.0	0.9	1.3
Ax-G+TG-	4.6	4.6	5.3	2037	655	632	1.9	0.5	0.3	Ax-G-G+G-	4.6	4.2	2011	676	648	0.0	0.1	1.0
Eq-G-G-G+	5.6	4.6	3.8	2814	521	500	1.0	0.4	0.7	Eq-G-G+G+	5.3	4.3	2738	525	511	0.9	0.4	1.5
Eq-G+TG-	6.0	5.4	4.7	2822	527	472	1.0	0.8	0.9	Ax-TTG-	4.3	4.3	2023	668	649	1.1	1.5	1.0
Ax-TTG-	5.4	5.5	6.4	2109	643	624	1.1	1.5	1.2	Eq-G-G-T	5.4	4.4	2862	536	483	0.7	1.1	1.2
Eq-G-G+G+	6.6	5.6	4.7	2747	520	506	0.9	0.3	1.6	Eq-G+TT	4.9	4.4	2746	536	477	1.0	0.7	0.6
Eq-G-G-T	6.9	5.9	5.2	2856	531	480	0.8	1.0	1.3	Eq-G-TG+	6.5	5.0	2786	525	496	1.0	1.5	0.2
Eq-G+G-G+	7.1	6.0	4.2	2817	516	496	0.8	0.7	0.9	Eq-G-G+T	5.9	5.0	2724	537	494	0.9	0.3	1.0
Eq-TG+G+	6.8	6.1	5.1	2746	518	502	1.0	0.8	1.5	Eq-TTG-	5.6	5.0	2791	533	477	1.3	1.1	0.9
Eq-G-TG+	7.8	6.2	5.1	2785	521	492	1.1	1.5	0.4	Eq-G-TT	7.1	5.6	2740	541	479	1.0	1.1	0.5
Eq-G-G+T	7.5	6.6	5.9	2732	531	489	1.0	0.2	0.9	Ax-G-TG-	6.5	5.6	2004	676	655	0.2	1.5	0.9
Eq-G-G-G-	8.0	6.9	5.3	2808	530	482	0.8	0.4	1.5	Eq-G-G-G-	6.8	5.4	2815	535	485	0.7	0.2	1.5
Eq-TG+T	7.7	7.0	6.3	2730	528	486	0.9	0.8	0.5	Ax-G-G-G-	6.3	5.7	1733	744	701	0.9	0.8	0.9
Ax-G-G+G-	7.6	7.1	6.9	2093	649	625	0.0	0.0	0.9	Eq-G+G-G+	7.1	5.9	2825	520	500	1.0	0.6	1.0
Eq-G+G-T	8.2	7.1	5.6	2856	527	476	1.0	0.1	1.5	Eq-TG+G+	6.8	6.1	2737	521	507	1.1	0.8	1.5
Eq-G-TT	8.6	7.2	6.4	2741	536	475	1.2	1.0	0.5	Eq-G-G+G-	7.3	6.3	2655	547	491	0.9	0.8	0.3
Eq-G-G+G-	8.5	7.6	6.3	2667	540	488	1.0	0.1	0.8	Ax-TG+G-	7.1	6.4	2014	668	642	1.8	0.9	0.3
Eq-G+G-G-	9.3	8.2	5.9	2811	526	479	1.0	1.4	1.1	Ax-G+G-G-	7.0	6.8	1740	736	694	1.3	1.7	1.0
Eq-TG+G-	9.0	8.2	6.9	2667	537	484	0.9	0.8	1.2	Eq-G+G-T	7.9	6.8	2862	531	479	1.1	0.1	1.5
Ax-G+G-G-	8.6	8.3	8.1	1815	702	666	1.3	0.9	1.8	Eq-TG+T	7.4	6.8	2722	533	491	1.0	0.8	0.7
Ax-TG+G-	8.9	8.3	7.1	2093	643	620	1.7	1.0	0.2	Eq-G-TG-	8.9	7.3	2808	536	477	0.8	1.8	0.0
Eq-G-TG-	10.1	8.5	6.8	2813	530	475	1.0	1.7	0.1	Eq-G+G-G-	9.4	8.2	2820	530	481	1.2	1.3	1.1
Ax-G-TG-	9.5	8.6	8.5	2083	651	630	0.4	1.5	0.7	Eq-TG+G-	9.0	8.3	2655	542	488	1.1	1.2	0.7
Ax-G-G-G-	9.2	8.6	8.2	1815	706	670	0.8	0.9	0.9	Eq-G+TG-	9.4	8.8	2820	530	481	1.2	1.3	1.1

Ax-G+G+G+	8.4	9.2	10.1	2225	630	622	0.7	0.1	1.4	Ax-TG-T	8.3	9.0	1561	791	750	1.6	0.7	1.3
Ax-TG-G+	8.8	9.9	11.1	1843	724	670	0.8	0.8	1.1	**Ax-G+G+G+**	8.3	9.1	2160	650	641	0.9	0.4	1.4
Ax-TG-T	10.0	11.2	12.0	1608	752	716	1.6	1.3	0.6	Ax-G+G+T	8.4	9.7	1933	683	650	1.4	1.3	0.8
Ax-G+G+T	10.0	11.3	12.5	2000	660	623	1.3	1.4	0.9	**Ax-TG-G+**	9.1	10.2	1815	742	685	0.9	1.1	1.0
Ax-G+TG+	11.1	11.6	13.1	2053	661	632	1.1	0.0	0.5	Ax-G+TT	11.0	11.9	1675	733	687	1.7	0.3	0.1
Ax-TTG+	11.6	12.1	13.3	2108	649	628	0.3	1.5	0.4	Ax-G+TG+	11.5	12.0	2021	680	650	1.3	0.0	0.5
Ax-G+TT	12.1	13.0	14.6	1720	703	659	1.6	0.2	0.0	Ax-G-G-G+	11.9	12.1	1805	750	695	1.5	0.1	1.1
Ax-G-G-G+	13.6	13.7	14.4	1849	722	672	1.6	1.1	0.0	**Ax-TTG+**	12.0	12.5	2065	670	646	0.5	1.5	0.4
Ax-G-G+G+	13.9	13.8	14.1	2202	634	627	0.7	1.2	0.4	Ax-G-G+G+	12.7	12.6	2137	654	647	0.5	1.2	0.5
Ax-G+G-G+	13.8	14.1	14.8	1835	718	671	0.3	1.3	1.0	Ax-G-G+T	12.6	12.9	1909	690	659	0.1	0.5	1.1
Ax-TTT	13.3	14.2	15.7	1767	694	650	0.7	0.7	1.6	Ax-TTT	12.1	13.0	1714	723	679	0.7	1.0	1.4
Ax-G-TG+	15.6	15.2	15.4	2079	660	634	1.3	0.7	1.1	Ax-G-TG+	14.1	13.7	2040	681	653	1.0	0.7	1.1
Ax-TG+G+	15.3	15.3	15.1	2193	630	623	1.0	0.0	0.8	Ax-G+G-G+	13.6	13.9	1795	743	691	0.4	1.0	1.4
Ax-G-G+T	15.5	15.8	16.3	1976	665	630	0.1	0.4	1.1	Ax-G-G-T	14.5	13.9	1605	767	731	1.0	0.0	1.2
Ax-TG+T	16.3	16.7	16.7	1952	664	630	1.5	0.6	0.0	Ax-G-TT	14.4	14.3	1696	734	687	0.6	1.0	0.5
Ax-G-TT	17.5	17.4	17.7	1746	703	656	0.8	0.9	0.3	Ax-TG+T	14.6	15.0	1892	687	657	1.6	0.6	0.1
Ax-G+G-T	17.0	17.5	17.7	1638	728	697	0.8	0.8	1.6	Ax-TG+G+	15.1	15.1	2134	649	642	1.2	0.1	0.7
Ax-G-G-T	17.3	17.6	18.1	1657	730	696	1.0	1.2	0.3	Ax-G+G-T	15.4	16.0	1584	765	732	0.9	1.3	1.3

[a] The bolded conformers are the ones which survive the conformational conversion in a jet expansion. Those in red are the ones observed experimentally. See the main text for discussions.

[b] Calculated at the 298 K.

[c] The *ZPE* corrections were obtained at the B3LYP-D3(BJ)/def2-TZVP level.

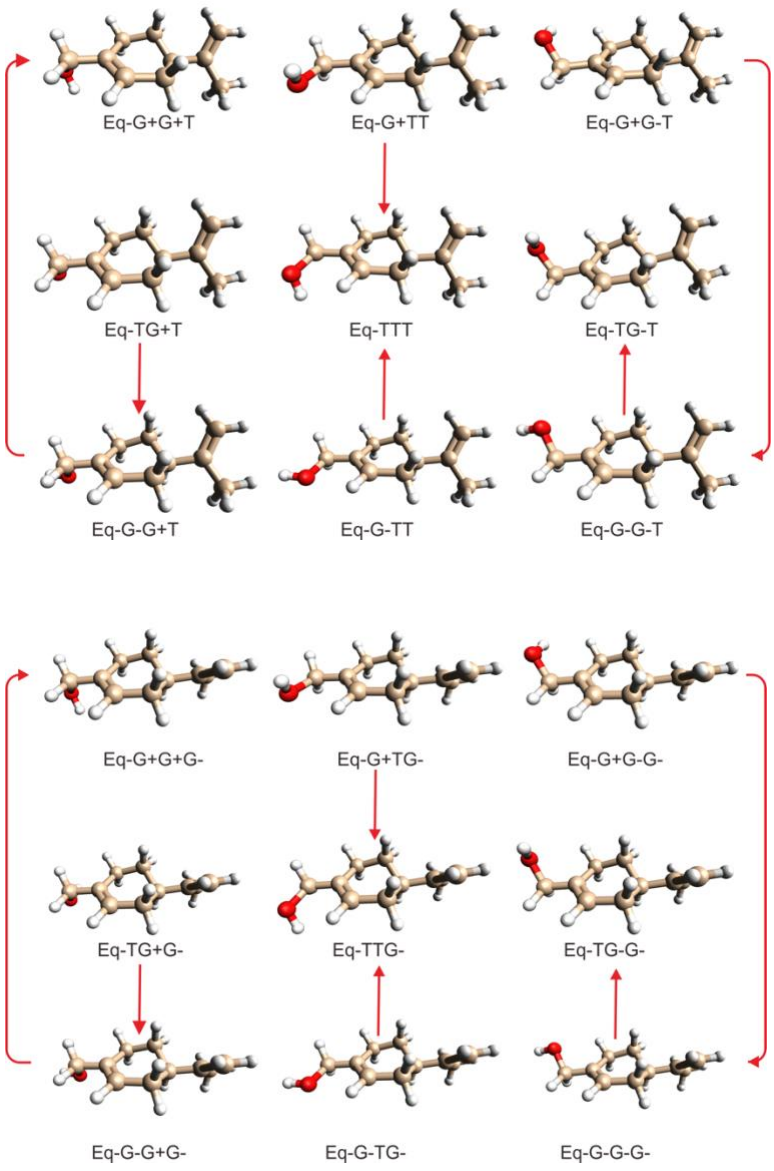

Figure 3.S1. Optimized geometries of the nine Eq-XXT (left) and nine Eq-XXG- (right) conformers where X can take on G+, T, and G-. The red arrows indicate that the corresponding conformational barriers are low enough to facilitate a nearly complete conformational cooling of the higher energy conformers in a jet expansion. See the main text for discussion.

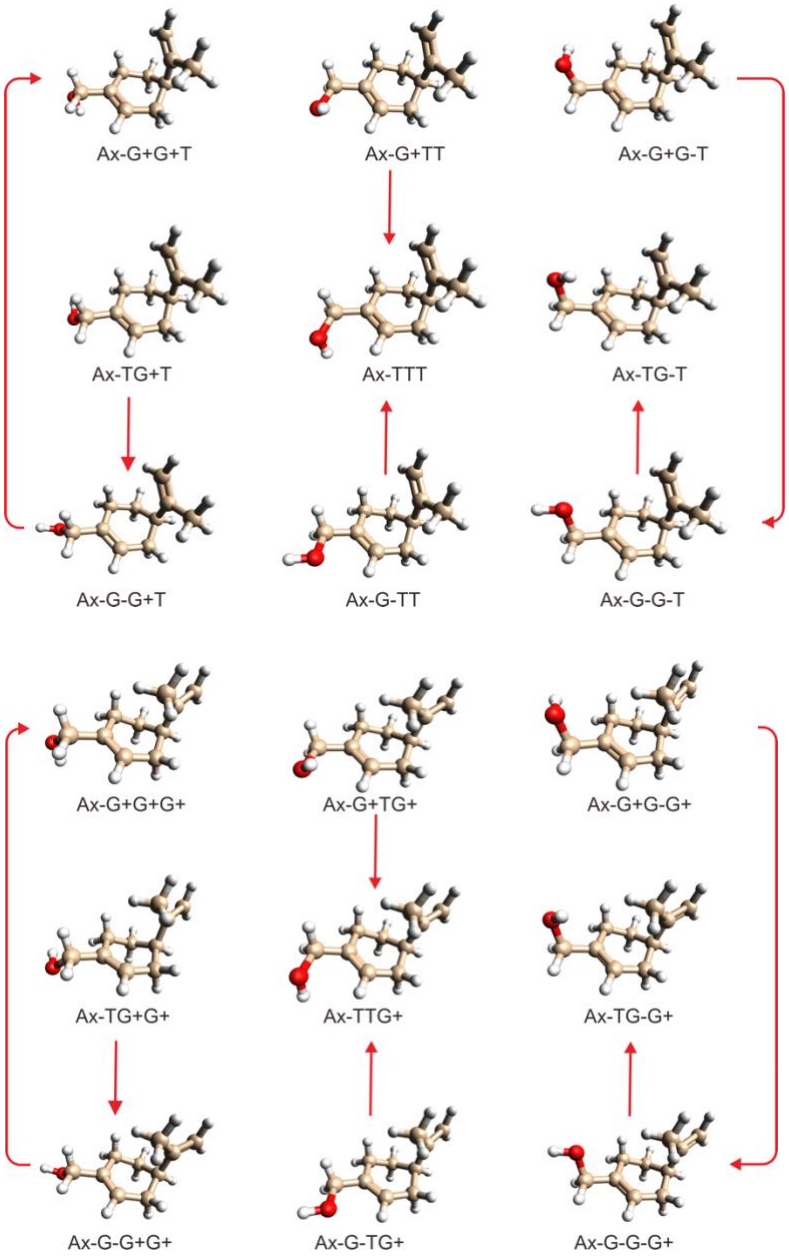

Figure 3.S2. Optimized geometries of the nine Ax-XXT (left) and nine Ax-XXG- (right) conformers where X can take on G+, T, and G-. The red arrows indicate that the corresponding conformational barriers are low enough to facilitate a nearly complete conformational cooling of the higher energy conformers in a jet expansion. See the main text for discussion.

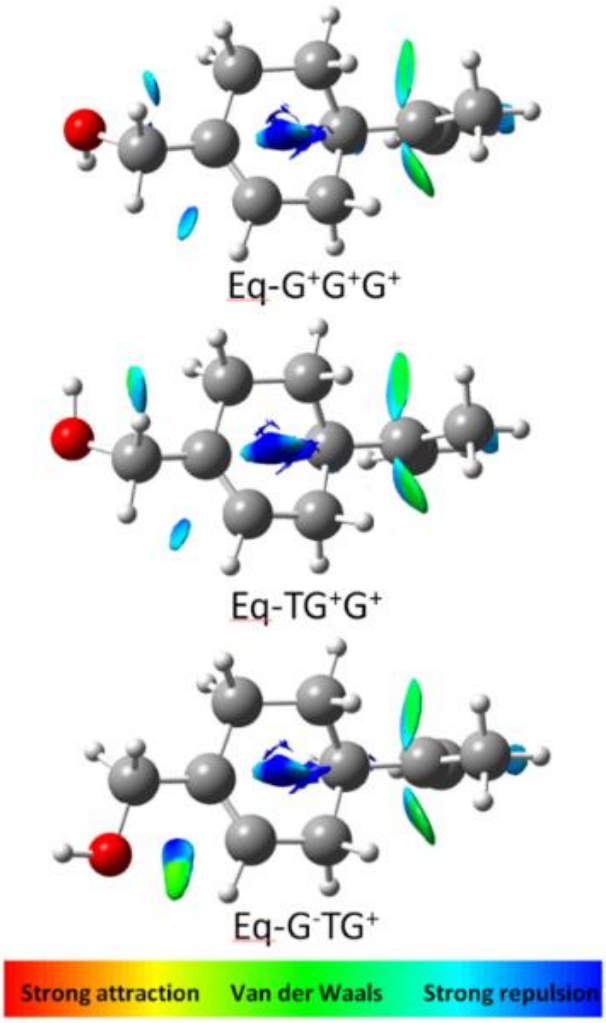

Figure 3.S3. The NCI analysis of Eq-G+G+G+, Eq-TG+G+, and Eq-G-TG+. The Eq-TG+G+ and Eq-G-TG+ conformers are less stable than Eq-G+G+G+ primarily because of the more severe steric repulsion, represented by the larger blue areas associated with the OH group.

Table 3.S2. Measured transition frequencies of Ax-G+G+G-

zJ'	K_a'	K_c'	J"	K_a"	K_c"	ν_{EXP} / MHz	$\Delta\nu^a$/ MHz
2	1	2	1	1	1	2539.0260	0.0002
2	0	2	1	0	1	2563.6280	0.0003
2	1	1	1	1	0	2588.8765	0.0002
3	1	3	2	1	2	3808.3308	0.0006
3	0	3	2	0	2	3844.6020	0.0007
3	1	2	2	1	1	3883.1100	0.0006
4	1	4	3	1	3	5077.3940	0.0009
4	0	4	3	0	3	5124.6011	0.0010
4	2	2	3	2	1	5130.9498	0.0006
4	2	3	3	2	2	5127.6503	0.0006
4	1	3	3	1	2	5177.0789	0.0009
3	1	3	2	0	2	5185.3261	0.0006
5	0	5	4	1	4	5109.8335	0.0004
4	0	4	3	1	3	3783.8946	0.0003
2	1	2	1	0	1	3940.6163	0.0004
1	1	0	0	0	0	2708.4915	0.0037
4	0	4	3	1	2	3634.3163	0.0015
2	1	1	1	0	1	4015.4012	0.0062
3	1	2	2	0	2	5334.9001	0.0066
5	0	5	4	1	3	4860.5237	0.0010
6	2	4	6	1	6	4529.2912	0.0001
3	2	2	3	1	3	4317.1483	0.0014
3	2	1	3	1	3	4318.8018	0.0017
3	2	1	3	1	2	4169.2372	0.0014
3	2	2	3	1	2	4167.5766	0.0017

[a] $\Delta\nu = \nu_{CALC.} - \nu_{EXP.}$

Table 3.S3. Measured transition frequencies of Ax-TG-G-

J'	K_a'	K_c'	J"	K_a"	K_c"	ν_{EXP} / MHz	$\Delta\nu^a$/ MHz
2	1	2	1	1	1	2819.8980	0.0003
2	0	2	1	0	1	2859.2250	0.0004
2	1	1	1	1	0	2901.0650	0.0003
3	1	3	2	1	2	4229.0510	0.0007
3	0	3	2	0	2	4285.7030	0.0008
3	1	2	2	1	1	4350.8010	0.0007
4	1	4	3	1	3	5637.3107	0.0010
4	0	4	3	0	3	5708.4827	0.0011
4	1	3	3	1	2	5799.5247	0.0010
2	1	2	1	0	1	3788.2200	0.0004
4	0	4	3	1	3	4836.1500	0.0004
3	1	3	2	0	2	5158.0280	0.0006
4	2	3	3	2	2	5719.9520	0.0007
4	2	2	3	2	1	5732.3820	0.0007
3	0	3	2	1	2	3356.7060	0.0042
2	2	1	1	1	0	5806.0470	0.0130

[a] $\Delta\nu = \nu_{CALC.} - \nu_{EXP.}$

Table 3.S4. Measured transition frequencies of Eq-TTT

J'	K_a'	K_c'	J"	K_a"	K_c"	ν_{EXP} / MHz	$\Delta\nu^a$ / MHz
5	1	5	4	1	4	4875.4010	0.0009
5	0	5	4	0	4	5006.0020	0.0010
4	1	4	3	1	3	3902.0756	0.0007
4	0	4	3	0	3	4012.0250	0.0008
4	1	3	3	1	2	4141.4000	0.0007
3	1	3	2	1	2	2927.5890	0.0004
3	0	3	2	0	2	3013.2514	0.0005
3	1	2	2	1	1	3107.1366	0.0004
2	1	1	1	0	1	4308.2950	0.0004
1	1	0	0	0	0	3242.3990	0.0002
6	0	6	5	1	4	3305.1500	0.0002
8	0	8	7	1	6	4790.4480	0.0001
3	1	2	2	0	2	5404.5735	0.0006
1	1	1	1	0	1	2176.4980	0.0002
7	0	7	6	1	5	4075.2006	0.0002
3	1	3	3	0	3	2032.2030	0.0018
2	1	2	2	0	2	2117.8710	0.0021

[a] $\Delta\nu = \nu_{CALC.} - \nu_{EXP.}$

Table 3.S5. Measured transition frequencies of Eq-TTG+

J'	K_a'	K_c'	J''	K_a''	K_c''	ν_{EXP} / MHz	$\Delta\nu^a$ / MHz
3	1	3	2	1	2	2981.9680	0.0004
3	0	3	2	0	2	3023.2270	0.0005
3	1	2	2	1	1	3066.2530	0.0004
4	1	4	3	1	3	3975.6495	0.0007
4	0	4	3	0	3	4029.7270	0.0008
4	1	3	3	1	2	4088.0260	0.0007
5	1	5	4	1	4	4969.0750	0.0009
5	0	5	4	0	4	5035.2015	0.0010
5	2	4	4	2	3	5039.8760	0.0005
5	1	4	4	1	3	5109.5260	0.0009
6	1	6	5	1	5	5962.1750	0.0010
2	1	1	1	0	1	4309.0001	0.0030
2	1	2	1	0	1	4224.7080	0.0030
3	1	3	2	0	2	5190.7500	0.0033
3	1	2	2	0	2	5359.3490	0.0034
1	1	1	0	0	0	3244.7180	0.0019
1	1	0	0	0	0	3272.8250	0.0019
2	0	2	1	0	1	2015.8932	0.0066

[a] $\Delta\nu = \nu_{CALC.} - \nu_{EXP.}$

Table 3.S6. Measured transition frequencies of Eq-G+G+G+

J'	K_a'	K_c'	J"	K_a"	K_c"	A/E	ν_{EXP} / MHz	$\Delta\nu^a$ / MHz
4	2	3	3	2	2	A	4098.8030	-0.0024
4	2	3	3	2	2	E	4098.9503	-0.0023
4	2	2	3	2	1	A	4099.3240	-0.0024
4	2	2	3	2	1	E	4099.1761	0.0015
5	2	4	4	2	3	A	5123.4390	-0.0026
5	2	4	4	2	3	E	5123.5751	0.0084
5	2	3	4	2	2	A	5124.4800	-0.0032
5	2	3	4	2	2	E	5124.3514	-0.0010
2	K	2	1	K	1	E	8615.4049	-0.0084
2	K	2	1	K	-1	E	8603.0752	0.0032
2	K	-2	1	K	-1	E	8604.1629	0.0092
3	2	2	2	1	1	A	9615.9813	-0.0051
3	2	2	2	1	1	E	9615.5557	0.0080
3	K	-2	2	K	-1	E	9616.6517	-0.0073
2	1	2	1	1	1	A	2037.0970	0.0026
2	1	2	1	1	1	E	2037.0970	-0.0002
2	0	2	1	0	1	A	2049.3690	-0.0018
2	0	2	1	0	1	E	2049.3690	-0.0007
2	1	1	1	1	0	A	2061.7460	-0.0055
2	1	1	1	1	0	E	2061.7460	-0.0005
2	1	1	2	0	2	A	2205.3250	-0.0021
2	1	1	2	0	2	E	2205.3250	-0.0010
3	1	2	3	0	3	A	2224.0000	0.0063
3	1	2	3	0	3	E	2224.0000	0.0084
3	0	3	2	0	2	A	3073.9240	-0.0020
3	0	3	2	0	2	E	3073.9240	-0.0002
3	1	3	2	1	2	A	3055.6130	0.0018
3	1	3	2	1	2	E	3055.6130	0.0026
3	1	2	2	1	1	A	3092.5990	0.0065
3	1	2	2	1	1	E	3092.5990	0.0091
4	0	4	3	0	3	A	4098.3230	-0.0019
4	0	4	3	0	3	E	4098.3230	0.0005
4	1	4	3	1	3	A	4074.0910	-0.0007
4	1	4	3	1	3	E	4074.0910	0.0012
4	1	3	3	1	2	A	4123.3880	-0.0037
4	1	3	3	1	2	E	4123.3880	-0.0010

[a] $\Delta\nu = \nu_{CALC.} - \nu_{EXP.}$

Table 3.S7. Measured transition frequencies of Eq-G+G+T

J'	K_a'	K_c'	J''	K_a''	K_c''	A/E	ν_{EXP} / MHz	$\Delta\nu^a$ / MHz
3	2	2	2	2	1	A	3058.6410	-0.0018
3	2	2	2	2	1	E	3058.9010	0.0076
3	2	1	2	2	0	A	3060.8830	-0.0015
3	2	1	2	2	0	E	3060.6283	-0.0032
2	2	1	1	1	0	A	8529.9847	-0.0073
2	2	1	1	1	0	E	8529.6037	-0.0018
2	2	0	1	1	1	A	8570.8341	0.0027
2	2	0	1	1	1	E	8571.1847	-0.0034
3	2	2	2	1	1	A	9509.2616	0.0014
3	2	2	2	1	1	E	9509.1339	0.0074
3	2	1	2	1	2	A	9632.9018	0.0030
3	2	1	2	1	2	E	9632.9993	-0.0028
2	0	2	1	0	1	A	2038.5330	-0.0022
2	0	2	1	0	1	E	2038.5330	-0.0014
2	1	1	1	1	0	A	2079.3740	-0.0006
2	1	1	1	1	0	E	2079.3740	0.0016
2	1	1	2	0	2	A	2231.3240	0.0000
2	1	1	2	0	2	E	2231.3240	0.0039
3	1	2	3	0	3	A	2293.6280	-0.0030
3	1	2	3	0	3	E	2293.6280	0.0011
3	0	3	2	0	2	A	3056.3990	-0.0021
3	0	3	2	0	2	E	3056.3990	-0.0009
3	1	3	2	1	2	A	2997.8760	-0.0007
3	1	3	2	1	2	E	2997.8760	0.0003
3	1	2	2	1	1	A	3118.7110	0.0029
3	1	2	2	1	1	E	3118.7110	0.0043
4	1	4	3	1	3	A	3996.5230	-0.0015
4	1	4	3	1	3	E	3996.5230	0.0002
4	1	3	3	1	2	A	4157.6080	-0.0023
4	1	3	3	1	2	E	4157.6080	-0.0008

[a] $\Delta\nu = \nu_{CALC.} - \nu_{EXP.}$

Table 3.S8. Measured transition frequencies of Eq-TG-G+

J'	K_a'	K_c'	J"	K_a"	K_c"	A/E	ν_{EXP} / MHz	$\Delta\nu$[a] / MHz
2	2	1	1	1	0	A	8840.1597	-0.0024
2	2	1	1	1	0	E	8839.8642	-0.0048
2	2	0	1	1	0	A	8840.2724	-0.0008
2	2	0	1	1	0	E	8840.5595	0.0039
2	2	1	1	1	1	A	8858.5021	-0.0033
2	2	1	1	1	1	E	8858.2218	0.0065
2	2	0	1	1	1	A	8858.6104	-0.0061
2	2	0	1	1	1	E	8858.9019	0.0000
3	2	2	2	1	1	A	9840.2581	-0.0009
3	2	2	2	1	1	E	9840.1025	0.0088
3	2	1	2	1	1	A	9840.8163	0.0016
3	2	1	2	1	1	E	9840.9728	0.0028
3	2	2	2	1	2	A	9895.2963	0.0061
3	2	2	2	1	2	E	9895.1193	-0.0062
3	2	1	2	1	2	A	9895.8433	-0.0025
3	2	1	2	1	2	E	9895.9990	-0.0028
2	1	2	1	1	1	A	2018.5260	-0.0086
2	1	2	1	1	1	E	2018.5260	-0.0082
7	1	7	7	0	7	A	2024.9890	0.0006
7	1	7	7	0	7	E	2024.9890	-0.0006
2	0	2	1	0	1	A	2036.7680	0.0007
2	0	2	1	0	1	E	2036.7680	0.0022
2	1	1	1	1	0	A	2055.2240	0.0016
2	1	1	1	1	0	E	2055.2240	0.0043
3	0	3	2	0	2	A	3054.8750	0.0002
3	0	3	2	0	2	E	3054.8750	0.0026
3	1	3	2	1	2	A	3027.7320	-0.0006
3	1	3	2	1	2	E	3027.7320	0.0012
3	1	2	2	1	1	A	3082.7690	0.0020
3	1	2	2	1	1	E	3082.7690	0.0047
4	0	4	3	0	3	A	4072.6480	-0.0028
4	0	4	3	0	3	E	4072.6480	0.0004
4	1	3	3	1	2	A	4110.2280	-0.0032
4	1	3	3	1	2	E	4110.2280	0.0003

[a] $\Delta\nu = \nu_{CALC.} - \nu_{EXP.}$

Table 3.S9. Measured transition frequencies of Eq-TG-T

J'	K_a'	K_c'	J''	K_a''	K_c''	A/E	ν_{EXP} / MHz	$\Delta\nu$[a] / MHz
3	2	2	2	2	1	A	3026.1240	-0.0032
3	2	2	2	2	1	E	3026.4264	-0.0037
3	2	1	2	2	0	A	3029.2830	-0.0033
3	2	1	2	2	0	E	3028.9751	-0.0048
3	2	1	4	1	4	A	3153.5810	0.0007
3	2	1	4	1	4	E	3153.7030	0.0017
2	2	1	1	1	0	A	8928.4036	0.0005
2	2	1	1	1	0	E	8927.9519	0.0032
2	2	0	1	1	1	A	8978.5433	-0.0032
2	2	0	1	1	1	E	8978.9696	0.0010
3	2	2	2	1	1	A	9887.7607	0.0007
3	2	2	2	1	1	E	9887.6077	-0.0032
3	2	1	2	1	1	A	9891.7095	0.0003
3	2	1	2	1	1	E	9891.8194	-0.0021
3	0	3	2	0	2	A	3022.9750	0.0068
3	0	3	2	0	2	E	3022.9750	0.0086
3	1	3	2	1	2	A	2951.6150	0.0061
3	1	3	2	1	2	E	2951.6150	0.0082
3	1	2	2	1	1	A	3099.6506	-0.0072
3	1	2	2	1	1	E	3099.6506	-0.0058
4	0	4	3	0	3	A	4026.9510	0.0010
4	0	4	3	0	3	E	4026.9510	0.0036
5	0	5	4	0	4	A	5027.8100	-0.0019
5	0	5	4	0	4	E	5027.8100	0.0015
1	1	0	1	0	1	A	2336.5540	-0.0052
1	1	0	1	0	1	E	2336.5540	-0.0032
3	1	2	3	0	3	A	2463.3940	0.0021
3	1	2	3	0	3	E	2463.3940	0.0050
4	1	3	4	0	4	A	2568.3780	-0.0010
4	1	3	4	0	4	E	2568.3780	0.0008
5	1	4	5	0	5	A	2703.9540	-0.0001
5	1	4	5	0	5	E	2703.9540	0.0001

[a] $\Delta\nu = \nu_{CALC.} - \nu_{EXP.}$

Table 3.S10. The percantage diffrerences between the experimental and theoretical rotational constants of the eight observed conformers

B3LYP	|ΔA|%[a]	|ΔB|%[a]	|ΔC|%[a]	ave%[b]	LMP2	|ΔA|%[a]	|ΔB|%[a]	|ΔC|%[a]	ave%[b]
Eq-G+G+G+	0.8	0.1	0.2	0.4	Eq-G+G+G+	0.6	0.9	1.1	0.9
Eq-G+G+T	0.8	0.2	0.1	0.4	Eq-G+G+T	0.6	1.0	0.9	0.8
Eq-TG-G+	0.4	0.3	0.4	0.4	Eq-TG-G+	0.7	1.1	1.0	0.9
Eq-TG-T	0.5	0.4	0.3	0.4	Eq-TG-T	0.7	1.1	0.9	0.9
Eq-TTG+	0.7	0.2	0.2	0.4	Eq-TTG+	0.8	0.9	0.8	0.9
Eq-TTT	0.7	0.2	0.2	0.4	Eq-TTT	0.8	0.9	0.8	0.9
ave for Eq[c]	0.6	0.2	0.2	0.4	ave for Eq[c]	0.7	1.0	0.9	0.9
Ax-G+G+G-	3.3	1.4	1.4	2.0	Ax-G+G+G-	0.8	2.4	2.3	1.8
Ax-TG-G-	2.2	1.4	1.1	1.6	Ax-TG-G-	1.0	3.1	2.8	2.3
ave for Ax[d]	2.7	1.4	1.2	1.8	ave for Ax[d]	0.9	2.7	2.5	2.0

[a] Percentage error in the A, B and C constants between the experimental and theoretical values.

[b] Average percentage error is A, B and C for each conformer.

[c] Average error for the six equatorial conformers observed.

[d] Average error for the two axial equatorial conformers observed

Table 3.S11. Comparison of the experimental and theoretical conformational abundances treating the axial and equatorial conformers *separately* and without/with conformational conversion

Levels of theory		B3LYP-D3BJ					LMP2				
Conformer[a]	Exp %	350K %	C_350K %	150K %	C_150K %	ΔD_0 kJ mol^{-1}	350K %	C_350K %	150K %	C_150K %	ΔD_0[b] kJ mol^{-1}
Eq-TG-G+	**30**	**14**	**19**	**36**	**37**	**0.0**	**14**	**19**	**34**	**36**	**0.0**
Eq-TG-T	**25**	**10**	**23**	**16**	**24**	**1.0**	**11**	**24**	**19**	**27**	**0.7**
Eq-G+G+G+	**22**	**10**	**14**	**15**	**16**	**1.1**	**9**	**14**	**14**	**15**	**1.1**
Eq-G+G+T	**10**	7	**16**	**6**	**9**	**2.3**	**7**	**18**	**7**	**11**	**1.9**
Eq-TG-G-	0	7	0	7	0	2.0	7	0	6	0	2.1
Eq-TTG+	**7**	**7**	**13**	**6**	**9**	**2.2**	**5**	**11**	**4**	**6**	**2.8**
Eq-G+G+G-	0	5	0	3	0	3.2	4	0	3	0	3.2
Eq-G-G-G+	0	3	0	1	0	4.6	4	0	2	0	3.5
Eq-TTT	**7**	**5**	**16**	**3**	**6**	**3.2**	**4**	**13**	**2**	**4**	**3.5**
Eq-G+TG+	0	5	0	3	0	3.3	3	0	1	0	3.9
Eq-G-G+G+	0	2	0	0	0	5.6	3	0	1	0	4.3
Eq-G+TT	0	4	0	1	0	4.1	3	0	1	0	4.4
Eq-G-G-T	0	2	0	0	0	5.9	3	0	1	0	4.4
Eq-G-G+T	0	2	0	0	0	6.6	2	0	1	0	5.0
Eq-G-TG+	0	2	0	0	0	6.2	2	0	1	0	5.0
Eq-TTG-	0	3	0	1	0	4.5	2	0	1	0	5.0
Eq-G-G-G-	0	1	0	0	0	6.9	2	0	0	0	5.4
Eq-G-TT	0	1	0	0	0	7.2	2	0	0	0	5.6
Eq-G+G-G+	0	2	0	0	0	6.0	2	0	0	0	5.9
Eq-TG+G+	0	2	0	0	0	6.1	2	0	0	0	6.1
Eq-G-G+G-	0	1	0	0	0	7.6	2	0	0	0	6.3
Eq-G+G-T	0	1	0	0	0	7.1	1	0	0	0	6.8
Eq-TG+T	0	1	0	0	0	7.0	1	0	0	0	6.8
Eq-G-TG-	0	1	0	0	0	8.5	1	0	0	0	7.3
Eq-G+G-G-	0	1	0	0	0	8.2	1	0	0	0	8.2
Eq-TG+G-	0	1	0	0	0	8.2	1	0	0	0	8.3
Eq-G+TG-	0	2	0	0	0	5.4	1	0	0	0	8.8
Sum	100	100	100	100	100	N/A	100	100	100	100	N/A
Ax-G+G+G-	**63**	**26**	**35**	**54**	**56**	**2.4**	**27**	**38**	**56**	**59**	**0.6**
Ax-TG-G-	**37**	**20**	**27**	**29**	**29**	**3.2**	**20**	**28**	**29**	**31**	**1.4**
Ax-G+TG-	**0**	**12**	**25**	**9**	**14**	**4.6**	**10**	**23**	**6**	**10**	**3.4**
Ax-G-G+G-	0	5	0	1.2	0	7.1	8	0	3	0	4.2
Ax-TTG-	0	9	0	4.5	0	5.5	8	0	3	0	4.3
Ax-G-TG-	0	3	0	0.4	0	8.6	5	0	1	0	5.6
Ax-G-G-G-	0	3	0	0.4	0	8.6	5	0	1	0	5.7
Ax-TG+G-	0	4	0	0.5	0	8.3	4	0	0	0	6.4
Ax-G+G-G-	0	4	0	0.5	0	8.3	3	0	0	0	6.8
Ax-TG-T	0	1	0	0	0	11.2	2	0	0	0	9.0
Ax-G+G+G+	**0**	**3**	**5**	**0**	**0**	**9.2**	**2**	**4**	**0**	**0**	**9.1**
Ax-G+G+T	0	1	0	0	0	11.3	1	0	0	0	9.7
Ax-TG-G+	**0**	**2**	**5**	**0**	**0**	**9.9**	**1**	**4**	**0**	**0**	**10.2**
Ax-G+TT	0	1	0	0	0	13	1	0	0	0	11.9

Ax-G+TG+	0	1	0	0	0	11.6	1	0	0	0	12.0
Ax-G-G-G+	0	0	0	0	0	13.7	1	0	0	0	12.1
Ax-TTG+	**0**	**1**	**3**	**0**	**0**	**12.1**	**1**	**3**	**0**	**0**	**12.5**
Ax-G-G+G+	0	0	0	0	0	13.8	0	0	0	0	12.6
Ax-G-G+T	0	0	0	0	0	15.8	0	0	0	0	12.9
Ax-TTT	0	0	0	0	0	14.2	0	0	0	0	13.0
Ax-G-TG+	0	0	0	0	0	15.2	0	0	0	0	13.7
Ax-G+G-G+	0	0	0	0	0	14.1	0	0	0	0	13.9
Ax-G-G-T	0	0	0	0	0	17.6	0	0	0	0	13.9
Ax-G-TT	0	0	0	0	0	17.4	0	0	0	0	14.3
Ax-TG+T	0	0	0	0	0	16.7	0	0	0	0	15.0
Ax-TG+G+	0	0	0	0	0	15.3	0	0	0	0	15.1
Sum	100	100	100	100	100	N/A	100	100	100	100	N/A

[a] The ordering is based on ΔD_0. The bolded conformers are the ones which survive the conformational conversion in a jet expansion. Those in red are the ones observed experimentally. See the main text for discussions.

[b] The *ZPE* corrections were taken from the B3LYP-D3(BJ) calculations.

Table 3.S12. Comparison of the experimental and theoretical conformational abundances treating the axial and equatorial conformers *together* and without/with conformational conversion

Levels of theory		B3LYP-D3BJ					LMP2				
Conformer[a]	Exp %	350K %	C_350K %	150K %	C_150K %	ΔD_0 kJ mol^{-1}	350K %	C_350K %	150K %	C_150K %	ΔD_0[b] kJ mol^{-1}
Eq-TG-G+	**27**	**12**	**15**	**33**	**34**	**0.0**	**10**	**14**	**25**	**26**	**0.0**
Eq-TG-T	**23**	**8**	**18**	**15**	**22**	**1.0**	**8**	**17**	**14**	**20**	**0.7**
Eq-G+G+G+	**20**	**8**	**11**	**14**	**14**	**1.1**	**7**	**10**	**10**	**11**	**1.1**
Eq-TG-G-	0	6	0	7	0	2.0	5	0	5	0	2.1
Eq-TTG+	**6**	**5**	**11**	**6**	**8**	**2.2**	**4**	**8**	**3**	**4**	**2.8**
Eq-G+G+T	**9**	**5**	**13**	**5**	**8**	**2.3**	**5**	**13**	**5**	**8**	**1.9**
Ax-G+G+G-	**6**	**5**	**7**	**5**	**5**	**2.4**	**8**	**11**	**15**	**16**	**0.6**
Ax-TG-G-	**3**	**4**	**5**	**3**	**3**	**3.2**	**6**	**8**	**8**	**8**	**1.4**
Eq-G+G+G-	0	4	0	3	0	3.2	3	0	2	0	3.2
Eq-TTT	**6**	**4**	**13**	**3**	**5**	**3.2**	**3**	**9**	**1**	**3**	**3.5**
Eq-G+TG+	0	4	0	2	0	3.3	3	0	1	0	3.9
Eq-G+TT	0	3	0	1	0	4.1	2	0	1	0	4.4
Eq-TTG-	0	2	0	1	0	4.5	2	0	0	0	5.0
Ax-G+TG-	**0**	**2**	**5**	**1**	**1**	**4.6**	**3**	**7**	**2**	**3**	**3.4**
Eq-G-G-G+	0	2	0	1	0	4.6	3	0	1	0	3.5
Eq-G+TG-	0	2	0	0	0	5.4	0	0	0	0	8.8
Ax-TTG-	0	2	0	0	0	5.5	0	0	1	0	4.3
Eq-G-G+G+	0	2	0	0	0	5.6	2	0	1	0	4.3
Eq-G-G-T	0	2	0	0	0	5.9	2	0	1	0	4.4
Eq-G+G-G+	0	1	0	0	0	6.0	1	0	0	0	5.9
Eq-TG+G+	0	1	0	0	0	6.1	1	0	0	0	6.1
Eq-G-TG+	0	1	0	0	0	6.2	2	0	0	0	5.0
Eq-G-G+T	0	1	0	0	0	6.6	2	0	0	0	5.0
Eq-G-G-G-	0	1	0	0	0	6.9	2	0	0	0	5.4
Eq-TG+T	0	1	0	0	0	7.0	1	0	0	0	6.8
Ax-G-G+G-	0	1	0	0	0	7.1	2	0	0	0	4.2
Eq-G+G-T	0	1	0	0	0	7.1	1	0	0	0	6.8
Eq-G-TT	0	1	0	0	0	7.2	1	0	0	0	5.6
Eq-G-G+G-	0	1	0	0	0	7.6	1	0	0	0	6.3
Eq-G+G-G-	0	1	0	0	0	8.2	1	0	0	0	8.2
Eq-TG+G-	0	1	0	0	0	8.2	1	0	0	0	8.3
Ax-TG+G-	0	1	0	0	0	8.3	1	0	0	0	6.4
Ax-G+G-G-	0	1	0	0	0	8.3	1	0	0	0	6.8
Eq-G-TG-	0	1	0	0	0	8.5	1	0	0	0	7.3
Ax-G-TG-	0	1	0	0	0	8.6	1	0	0	0	5.6
Ax-G-G-G-	0	1	0	0	0	8.6	1	0	0	0	5.7
Ax-G+G+G+	**0**	**0**	**1**	**0**	**0**	**9.2**	**0**	**1**	**0**	**0**	**9.1**
Ax-TG-G+	**0**	**0**	**1**	**0**	**0**	**9.9**	**0**	**1**	**0**	**0**	**10.2**
Ax-TG-T	0	0	0	0	0	11.2	0	0	0	0	9.0
Ax-G+G+T	0	0	0	0	0	11.3	0	0	0	0	9.7
Ax-G+TG+	0	0	0	0	0	11.6	0	0	0	0	12.0
Ax-TTG+	**0**	**0**	**1**	**0**	**0**	**12.1**	**0**	**1**	**0**	**0**	**12.5**

Ax-G+TT	0	0	0	0	0	13.0	0	0	0	0	11.9
Ax-G-G-G+	0	0	0	0	0	13.7	0	0	0	0	12.1
Ax-G-G+G+	0	0	0	0	0	13.8	0	0	0	0	12.6
Ax-G+G-G+	0	0	0	0	0	14.1	0	0	0	0	13.9
Ax-TTT	0	0	0	0	0	14.2	0	0	0	0	13
Ax-G-TG+	0	0	0	0	0	15.2	0	0	0	0	13.7
Ax-TG+G+	0	0	0	0	0	15.3	0	0	0	0	15.1
Ax-G-G+T	0	0	0	0	0	15.8	0	0	0	0	12.9
Ax-TG+T	0	0	0	0	0	16.7	0	0	0	0	15.0
Ax-G-TT	0	0	0	0	0	17.4	0	0	0	0	14.3
Ax-G+G-T	0	0	0	0	0	17.5	0	0	0	0	16.0
Ax-G-G-T	0	0	0	0	0	17.6	0	0	0	0	13.9
Sum	100	100	100	100	100	N/A	100	100	100	100	N/A

[a] The ordering is based on ΔD_0. The bolded conformers are the ones which survive the conformational conversion in a jet expansion. Those in red are the ones observed experimentally. See the main text for discussions.

[b] The *ZPE* corrections were taken from the B3LYP-D3(BJ) calculations.

Appendix B

Supporting Information for Chapter 4

Rotational Spectroscopy of Chiral Tetrahydro-2-Furoic Acid: Conformational Landscape, Conversion, and Abundances

Contents:

Table 4.S1. Relative energies and spectroscopic constants of the eight most stable conformers of THFA at the MP2/6-311++G(2d,p) level of theory.[a]

Conformer	ΔE_e	ΔE_0	A	B	C	$\lvert\mu_a\rvert$	$\lvert\mu_b\rvert$	$\lvert\mu_c\rvert$
I	0	0	3686	1753	1441	4.67	0.02	0.25
II	2.4	2.2	4179	1588	1273	5.10	0.20	0.17
III	5.9	4.8	3727	1680	1546	0.12	2.19	1.00
IV	7.7	6.8	4035	1592	1368	0.61	2.37	0.78
V	8.1	7.4	4158	1547	1388	1.63	0.12	1.76
VI	8.2	7.2	3685	1717	1557	1.95	0.23	1.90
VII	28.9	27.3	3719	1686	1549	1.58	3.86	0.73
VIII	31.3	29.6	4008	1593	1372	2.42	3.83	0.87

[a] ΔE_e, ΔE_0 are the raw, zero-point energy (*ZPE*) corrected relative dissociation energies in kJ mol^{-1}, respectively. A, B, and C are rotational constants in MHz, and $|\mu_{a,b,c}|$ are the magnitudes of the electric dipole moment components in Debye.

Table 4.S2. Relative energies and spectroscopic constants of the eight most stable conformers of THFA at the B3LYP-D3(BJ)/6-311++G(2d,p) level of theory.[a]

Conformer	ΔE_e	ΔE_0	A	B	C	$\lvert\mu_a\rvert$	$\lvert\mu_b\rvert$	$\lvert\mu_c\rvert$
I	0	0	3714	1720	1412	4.76	0.25	0.32
II	2.06	1.74	4157	1582	1264	5.11	0.41	0.09
III	7.21	6.05	3791	1637	1512	0.27	2.36	0.77
IV	8.34	7.41	4023	1578	1366	0.63	2.45	0.66
V	8.65	7.52	3761	1655	1524	1.93	0.02	1.79
VI	8.7	7.83	4127	1541	1377	2.09	0.06	1.87
VII	29.5	27.5	3781	1635	1515	1.62	3.97	0.92
VIII	31	29.2	3983	1585	1370	2.29	3.95	0.93

[a] ΔE_e, ΔE_0 are the raw, zero-point energy (*ZPE*) corrected relative dissociation energies in kJ mol^{-1}, respectively. A, B, and C are rotational constants in MHz, and $|\mu_{a,b,c}|$ are the magnitudes of the electric dipole moment components in Debye.

(a) *Z*-COOH (b) *E*-COOH

Figure 4.S1. The two observed conformations of formic acid, showing the nomenclature adopted. (a) is the *Z*-conformer, also named as *synperiplanar* where the dihedral angle H-C-O-H is 0°. (b) is the *E*-conformer, also named as *antiperiplanar* where the dihedral angle H-C-O-H is 180°.

Table 4.S3. Observed transition frequencies of the THFA **I** conformer.

J'	Ka'	Kc'	J''	Ka''	Kc''	ν_{EXP} / MHz	$\Delta\nu^a$ / MHz
4	1	3	4	1	4	3102.3905	-0.0079
1	0	1	0	0	0	3164.7192	0.0002
7	2	5	7	2	6	3219.1750	-0.0014
4	0	4	3	2	1	3535.9484	-0.0026
2	0	2	1	1	0	4023.1998	-0.0026
4	1	3	4	0	4	4066.3751	0.0071
5	2	4	5	1	4	4181.0000	-0.0020
5	1	4	5	1	5	4613.0705	-0.0079
8	2	6	8	2	7	4770.1237	0.0012
4	2	3	4	1	3	4860.6495	-0.0029
5	2	3	5	1	4	5258.6020	-0.0081
4	2	2	4	1	3	5350.4900	-0.0071
6	2	4	6	1	5	5417.0340	0.0031
3	2	2	3	1	2	5434.8881	-0.0059
1	1	0	0	0	0	5436.6005	0.0038
3	2	1	3	1	2	5603.9251	0.0028
5	0	5	4	2	2	5817.5570	-0.0041
2	2	1	2	1	1	5879.9206	0.0019
2	1	2	1	1	1	6017.5321	-0.0004
2	0	2	1	0	1	6295.0796	-0.0005
2	1	1	1	1	0	6641.3284	-0.0011
2	1	2	1	0	1	7977.5037	-0.0061
7	1	6	7	1	7	8273.5163	-0.0004
2	2	1	2	0	2	8498.0495	0.0037
3	2	2	3	0	3	8632.7889	0.0039
2	1	1	1	0	1	8913.1975	-0.0097
4	2	3	4	0	4	8927.0229	0.0024
3	1	3	2	1	2	9005.8657	-0.0001
3	0	3	2	0	2	9359.4077	0.0004
5	2	4	5	0	5	9439.7327	-0.0018
5	2	4	5	0	5	9439.7375	0.0030
3	2	2	2	2	1	9494.1504	0.0038
3	2	1	2	2	0	9628.8323	-0.0006
3	1	2	2	1	1	9939.1719	0.0006
6	2	5	6	0	6	10196.8659	0.0003
3	1	3	2	0	2	10688.2938	-0.0017
4	0	4	3	1	3	11008.8899	0.0136
4	1	4	3	1	3	11972.8453	-0.0006
4	0	4	3	0	3	12337.7643	-0.0001
4	2	3	3	2	2	12632.0002	0.0004
4	3	2	3	3	1	12720.9844	0.0008
4	3	1	3	3	0	12735.1534	0.0014
4	2	2	3	2	1	12952.8160	-0.0001
4	1	3	3	1	2	13206.2416	0.0003
5	1	5	4	1	4	14916.1099	-0.0007

5	0	5	4	0	4	15234.4262	0.0000
5	2	4	4	2	3	15747.1420	0.0018
5	2	3	4	2	2	16334.9036	-0.0001
5	1	4	4	1	3	16426.7924	0.0018
6	1	6	5	1	5	17836.2292	-0.0027

[a] $\Delta\nu = \nu_{CALC} - \nu_{EXP}$.

Table 4.S4. Observed transition frequencies of the THFA **II** conformer.

J'	Ka'	Kc'	J''	Ka''	Kc''	ν_{EXP} / MHz	$\Delta\nu^a$ / MHz
3	1	2	3	1	3	1915.7647	-0.0013
1	0	1	0	0	0	2855.0829	-0.0001
4	1	3	4	1	4	3184.8024	0.0000
2	1	1	2	0	2	3243.8513	-0.0008
3	1	2	3	0	3	3815.1727	0.0009
8	2	6	8	2	7	4320.1758	0.0000
5	1	4	5	1	5	4750.8479	0.0005
2	1	2	1	1	1	5390.6118	-0.0003
2	0	2	1	0	1	5682.2431	-0.0006
2	1	1	1	1	0	6029.7133	-0.0001
3	1	3	2	1	2	8069.1579	0.0004
3	0	3	2	0	2	8454.9500	-0.0003
3	2	2	2	2	1	8565.2481	0.0006
3	2	1	2	2	0	8675.5109	-0.0001
4	1	4	3	1	3	10729.6529	0.0003
4	2	3	3	2	2	11398.5417	-0.0005
4	2	2	3	2	1	11665.6407	0.0003
4	1	3	3	1	2	11998.6906	0.0016
5	0	5	4	0	4	13771.5440	-0.0008
5	2	3	4	2	2	14716.4604	-0.0006
5	1	4	4	1	3	14935.3112	-0.0008
6	1	6	5	1	5	15987.3344	0.0005
6	0	6	5	0	5	16325.1465	0.0003

[a] $\Delta\nu = \nu_{CALC} - \nu_{EXP}$.

Table 4.S5. Observed transition frequencies of the THFA **III** conformer.

J'	Ka'	Kc'	J''	Ka''	Kc''	ν_{EXP} / MHz	$\Delta\nu^a$ / MHz
1	1	1	1	0	1	2078.2720	0.0001
1	1	0	1	0	1	2227.0185	0.0011
2	1	1	2	0	2	2383.4730	0.0034
3	1	2	3	0	3	2632.3170	0.0050
4	1	3	4	0	4	2989.4090	0.0021
5	1	4	5	0	5	3472.9757	-0.0011
9	2	8	9	1	8	3473.6760	-0.0027
3	1	2	2	2	1	3560.4150	0.0011
8	2	7	8	1	7	4000.0180	0.0067
6	1	5	6	0	6	4099.6960	0.0003
2	0	2	1	1	0	4149.9940	0.0034
6	3	3	5	4	2	4162.3780	-0.0031
2	0	2	1	1	1	4298.7320	-0.0041
7	2	6	7	1	6	4502.2350	-0.0015
7	1	6	7	0	7	4879.7030	0.0006
6	2	5	6	1	5	4965.1100	0.0065
5	2	4	4	3	1	5154.2760	0.0032
1	1	1	0	0	0	5270.6350	0.0012
5	2	4	5	1	4	5376.9770	0.0008
7	2	5	7	1	6	5389.1550	-0.0074
8	2	6	8	1	7	5408.1100	0.0010
5	2	3	4	3	2	5418.2010	0.0058
1	1	0	0	0	0	5419.3840	0.0047
6	2	4	6	1	5	5476.3000	-0.0077
4	1	4	3	2	1	5509.9500	-0.0055
4	1	4	3	2	2	5548.3180	-0.0008
9	2	7	9	1	8	5558.4117	0.0052
5	2	3	5	1	4	5639.1527	-0.0024
4	2	3	4	1	3	5729.4390	0.0006
8	1	7	8	0	8	5812.3230	-0.0004
4	2	2	4	1	3	5843.5735	0.0001
4	2	3	4	1	4	7215.0645	0.0017
5	2	4	5	1	5	7600.9958	-0.0067
3	0	3	2	1	2	7609.1182	-0.0036
2	1	2	1	0	1	8314.2454	-0.0014
4	0	4	3	1	3	10953.3963	0.0000
3	1	3	2	0	2	11286.4778	-0.0002
2	2	1	1	1	0	12768.2499	0.0006
2	2	0	1	1	1	12924.6958	0.0006
3	2	2	2	1	1	15811.8707	0.0023
3	2	1	2	1	2	16296.4611	-0.0013

[a] $\Delta\nu = \nu_{CALC} - \nu_{EXP}$.

Table 4.S6. Observed transition frequencies of the $^{13}C3$ isotopologue of THFA **I**.

J'	Ka'	Kc'	J''	Ka''	Kc''	ν_{EXP} / MHz	$\Delta\nu^a$ / MHz
4	1	3	4	1	4	3068.4620	0.0008

1	0	1	0	0	0	3146.9763	-0.0009
2	1	2	1	1	1	5985.5119	0.0013
2	0	2	1	0	1	6260.5004	0.0030
2	1	1	1	1	0	6602.3771	-0.0069
3	0	3	2	0	2	9309.6373	-0.0014
3	2	2	2	2	1	9440.9250	0.0039
3	2	1	2	2	0	9572.1500	-0.0004

[a] $\Delta\nu = \nu_{CALC} - \nu_{EXP}$.

Table 4.S7. Observed transition frequencies of the ^{13}C6 isotopologue of THFA **I**

J'	Ka'	Kc'	J''	Ka''	Kc''	ν_{EXP} / MHz	$\Delta\nu^a$ / MHz
1	0	1	0	0	0	3161.3579	-0.0012
2	1	2	1	1	1	6014.1741	0.0003
2	0	2	1	0	1	6288.8500	0.0000
2	1	1	1	1	0	6631.2486	0.0003

[a] $\Delta\nu = \nu_{CALC} - \nu_{EXP}$.

Table 4.S8. Observed transition frequencies of the ^{13}C7 isotopologue of THFA **I**

J'	Ka'	Kc'	J''	Ka''	Kc''	ν_{EXP} / MHz	$\Delta\nu^a$ / MHz
1	0	1	0	0	0	3124.2263	0.0008
2	1	2	1	1	1	5942.5424	0.0037
2	0	2	1	0	1	6215.5380	0.0066
2	1	1	1	1	0	6554.3545	0.0036
3	0	3	2	0	2	9243.4500	-0.0056
3	2	1	2	2	0	9501.8250	-0.0039

[a] $\Delta\nu = \nu_{CALC} - \nu_{EXP}$.

Table 4.S9. Observed transition frequencies of the ^{13}C8 isotopologue of THFA **I**

J'	Ka'	Kc'	J''	Ka''	Kc''	ν_{EXP} / MHz	$\Delta\nu^a$ / MHz
1	0	1	0	0	0	3131.6044	0.0006

5	1	4	5	1	5	4502.2370	0.0001
2	1	2	1	1	1	5958.9520	0.0006
2	0	2	1	0	1	6230.3100	-0.0003
2	1	1	1	1	0	6567.4490	-0.0006

[a] $\Delta\nu = \nu_{CALC} - \nu_{EXP}$.

Table 4.S10. Observed transition frequencies of the ^{13}C9 isotopologue of THFA **I**

J'	Ka'	Kc'	J''	Ka''	Kc''	ν_{EXP} / MHz	$\Delta\nu^a$ / MHz
1	0	1	0	0	0	3151.1004	-0.0012
2	1	2	1	1	1	5984.4072	-0.0025
2	0	2	1	0	1	6265.7899	-0.0015
2	1	1	1	1	0	6619.9781	-0.0046
3	1	3	2	1	2	8955.0007	-0.0014
3	0	3	2	0	2	9310.7279	0.0041
3	2	1	2	2	0	9595.8154	0.0035

[a] $\Delta\nu = \nu_{CALC} - \nu_{EXP}$.

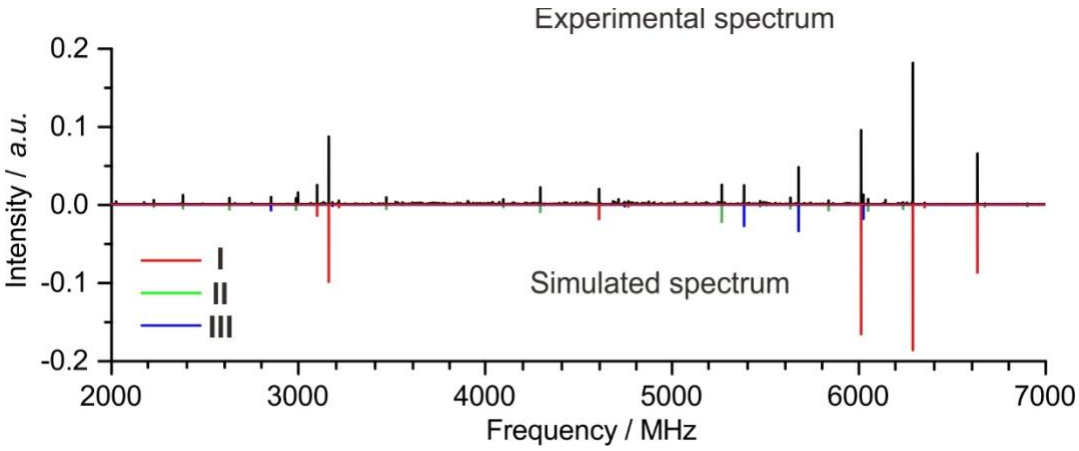

Figure 4.S2. A 2.0-7.0 GHz experimental chirped pulse spectrum and the simulated rotational spectra of **I**, **II**, and **III** using the experimental spectroscopic constants, the permanent electric dipole moment components calculated at the B3LYP-D3(BJ)/def2-TZVP level, an estimated rotational temperature of 1.5 K, and the estimated relative abundances of **I** : **II** : **III**, i.e. 10 : 1 : 1.6.

Table 4.S11. Ab initio coordinates in the principal inertial axis systems of the eight optimized conformers of THFA at the MP2 and B3LYP-D3BJ/6-311++G(2d,p) levels of theory.

Atom no.	Atom	THFA **I**					
		MP2/6-311++G(2d,p)			B3LYP-D3(BJ)/def2-TZVP		
		a	b	c	a	b	c
1	O	0.804928	-0.979323	0.630567	0.787786	-0.981441	0.610433
2	O	-1.494805	-1.225753	-0.507661	-1.524866	-1.211599	-0.508111
3	O	-2.161705	0.874529	-0.075988	-2.173808	0.879370	-0.067827
4	C	0.787747	1.362987	0.218380	0.795871	1.362350	0.198493
5	C	-0.018619	0.195210	0.778714	-0.023023	0.195876	0.758103
6	C	1.625037	0.665958	-0.855269	1.694418	0.662115	-0.824664
7	C	1.972929	-0.639984	-0.159502	1.983151	-0.663177	-0.132681
8	C	-1.334956	0.000259	0.023187	-1.353968	0.008443	0.019347
9	H	1.434387	1.775592	0.996257	1.395553	1.808809	0.992800
10	H	0.138178	2.152267	-0.157927	0.154765	2.132083	-0.224031
11	H	-0.264733	0.318139	1.835907	-0.262890	0.327693	1.815036
12	H	1.020712	0.476323	-1.746390	1.152946	0.496262	-1.758245
13	H	2.509884	1.231739	-1.148713	2.601126	1.221070	-1.051604
14	H	2.169400	-1.471725	-0.836539	2.183907	-1.486890	-0.817052
15	H	2.824476	-0.517612	0.516548	2.818226	-0.576967	0.568899
16	H	-0.678781	-1.713517	-0.269388	-0.714634	-1.714564	-0.294718
		THFA **II**					
Atom no.	Atom	MP2/6-311++G(2d,p)			B3LYP-D3(BJ)/def2-TZVP		
1	O	0.710154	-0.990274	0.515854	0.707069	-0.992723	0.502403
2	O	-1.683974	-1.168707	-0.455499	-1.701185	-1.166324	-0.431947
3	O	-2.257062	0.939925	0.066229	-2.245537	0.948813	0.038755
4	C	0.770395	1.247348	-0.297568	0.785010	1.265616	-0.254442
5	C	-0.017901	0.253587	0.559768	-0.019339	0.246117	0.565097
6	C	2.193139	0.704850	-0.169160	2.201611	0.692111	-0.183943
7	C	1.944362	-0.793456	-0.213771	1.936569	-0.806279	-0.224682
8	C	-1.435569	0.055750	0.046380	-1.439338	0.061224	0.040089
9	H	0.646228	2.271325	0.051744	0.693566	2.270581	0.149719

10	H	0.435375	1.195656	-1.337291	0.428352	1.286015	-1.285787
11	H	-0.079720	0.587318	1.599208	-0.095042	0.551716	1.611692
12	H	2.856897	1.044185	-0.965509	2.838000	1.026994	-1.002302
13	H	2.625358	0.986980	0.794038	2.680940	0.965563	0.758060
14	H	1.816185	-1.141138	-1.244825	1.808727	-1.159680	-1.253492
15	H	2.711280	-1.393437	0.275430	2.703850	-1.407640	0.261056
16	H	-0.866413	-1.683762	-0.296475	-0.894115	-1.695797	-0.283022

THFA **III**

Atom no.	Atom	MP2/6-311++G(2d,p)			B3LYP-D3(BJ)/def2-TZVP		
1	O	0.924791	-0.593133	1.059544	0.903549	-0.645048	1.019561
2	O	1.872842	-0.695779	-0.027757	1.920083	-0.685849	0.001227
3	O	1.564966	0.453862	-0.996767	1.631235	0.473332	-0.960937
4	C	0.699623	1.395133	-0.151666	0.711693	1.384622	-0.140000
5	C	2.869853	-0.614868	0.410412	2.887051	-0.580005	0.498689
6	C	1.762839	-1.672361	-0.501168	1.882836	-1.654687	-0.497749
7	C	2.470487	0.936589	-1.365125	2.539612	0.979891	-1.284328
8	C	0.997958	0.086550	-1.853153	1.110779	0.110033	-1.846584
9	H	1.318293	2.034038	0.481954	1.288359	2.041653	0.512142
10	H	0.028943	2.023524	-0.739234	0.049256	1.999596	-0.747387
11	H	-1.204026	-0.208795	-0.016035	-1.230984	-0.200268	-0.030887
12	H	-1.167050	-1.215617	-0.684260	-1.219965	-1.170282	-0.738662
13	H	-2.312796	0.567983	0.109173	-2.329427	0.570554	0.150945
14	H	-3.000729	0.148633	-0.435799	-3.038802	0.190733	-0.391262
15	H	-0.035484	0.392487	0.742230	-0.036707	0.361801	0.730364
16	H	-0.402109	0.831411	1.671418	-0.392395	0.788900	1.668306

THFA **IV**

Atom no.	Atom	MP2/6-311++G(2d,p)			B3LYP-D3(BJ)/def2-TZVP		
1	O	0.840093	-0.798746	0.871267	0.834917	-0.793813	0.869572
2	O	1.789202	-0.825685	-0.202726	1.809005	-0.831080	-0.174662
3	O	2.107342	0.642750	-0.438518	2.110946	0.636201	-0.455682
4	C	0.722153	1.289135	-0.296876	0.732184	1.295179	-0.291065
5	C	2.636306	-1.423762	0.131016	2.661582	-1.398961	0.194136
6	C	1.340686	-1.287014	-1.089944	1.396626	-1.332956	-1.056277
7	C	2.780623	1.000800	0.342662	2.810117	1.020078	0.288361
8	C	2.561677	0.834144	-1.411806	2.536973	0.800654	-1.445044
9	H	0.754592	2.293440	0.123702	0.785127	2.287895	0.150203
10	H	0.225680	1.345933	-1.268109	0.227970	1.387334	-1.253277
11	H	-1.307662	-0.154082	-0.023776	-1.314936	-0.151600	-0.031968
12	H	-1.453266	-1.155457	-0.683156	-1.455958	-1.136016	-0.703795
13	H	-2.290785	0.765770	0.172186	-2.307017	0.744719	0.186753
14	H	-3.064263	0.445231	-0.322722	-3.085497	0.434793	-0.302416
15	H	-0.025424	0.299586	0.640418	-0.027078	0.299503	0.636762
16	H	-0.268576	0.748705	1.604813	-0.275532	0.747576	1.599280

THFA **V**

Atom no.	Atom	MP2/6-311++G(2d,p)			B3LYP-D3(BJ)/def2-TZVP		
1	O	0.875746	-0.588331	1.059672	0.857572	-0.656511	1.004064
2	O	1.846939	-0.718922	-0.003009	1.906968	-0.698010	0.021092
3	O	1.568665	0.410728	-1.001714	1.630601	0.438518	-0.967752
4	C	0.737885	1.397408	-0.175612	0.743778	1.386674	-0.154587
5	C	2.836437	-0.634210	0.451852	2.859015	-0.566118	0.541792

6	C	1.742386	-1.706695	-0.455020	1.901678	-1.678459	-0.457014
7	C	2.486899	0.854653	-1.387259	2.545384	0.915281	-1.317349
8	C	0.986073	0.039674	-1.845940	1.089419	0.064997	-1.837208
9	H	1.382096	2.024068	0.444899	1.347074	2.031814	0.485442
10	H	0.089172	2.040140	-0.771850	0.095554	2.016000	-0.761695
11	H	-1.292932	-0.048851	0.043188	-1.317766	-0.043058	0.039603
12	H	-2.340925	0.558753	0.038293	-2.345730	0.581822	0.081560
13	H	-1.107292	-1.218549	-0.614775	-1.178487	-1.184219	-0.665446
14	H	-1.960765	-1.420506	-1.036823	-2.036670	-1.360073	-1.083078
15	H	-0.036472	0.445429	0.739489	-0.035443	0.402656	0.732801
16	H	-0.361205	0.920515	1.666403	-0.344692	0.853502	1.676050

THFA **VI**

Atom no.	Atom	MP2/6-311++G(2d,p)			B3LYP-D3(BJ)/def2-TZVP		
1	O	0.756873	-0.739567	0.915140	0.765373	-0.765390	0.882086
2	O	1.806566	-0.851105	-0.056030	1.824758	-0.850378	-0.072703
3	O	2.149990	0.589592	-0.395308	2.150769	0.598294	-0.409121
4	C	0.755862	1.222018	-0.457385	0.758948	1.242589	-0.417884
5	C	2.616815	-1.411294	0.409895	2.643851	-1.395178	0.394644
6	C	1.447992	-1.392759	-0.939117	1.490530	-1.400370	-0.959881
7	C	2.738405	1.029244	0.412923	2.771545	1.032849	0.376090
8	C	2.700692	0.692180	-1.331604	2.669961	0.709156	-1.360777
9	H	0.744075	2.286391	-0.225055	0.763129	2.291236	-0.129424
10	H	0.326634	1.082710	-1.452157	0.312457	1.170443	-1.410296
11	H	-1.390118	0.018075	0.038771	-1.396218	0.017997	0.039960
12	H	-2.415490	0.621930	0.264675	-2.393110	0.661441	0.241507
13	H	-1.320335	-1.046700	-0.796990	-1.368199	-1.067192	-0.761261
14	H	-2.226038	-1.189102	-1.121601	-2.270144	-1.192082	-1.095906
15	H	-0.034882	0.400169	0.589840	-0.031176	0.374195	0.599526
16	H	-0.213175	0.964968	1.506248	-0.210509	0.907268	1.533490

THFA **VII**

Atom no.	Atom	MP2/6-311++G(2d,p)			B3LYP-D3(BJ)/def2-TZVP		
1	O	0.923521	-0.559455	1.080815	0.906849	-0.628549	1.030022
2	O	-2.380652	0.480041	0.033813	-2.386674	0.502803	0.071047
3	O	-1.124874	-1.223486	-0.679671	-1.189174	-1.186274	-0.729230
4	C	0.691117	1.395198	-0.180420	0.698387	1.386540	-0.150525
5	C	-0.041753	0.407362	0.734634	-0.041043	0.363019	0.729247
6	C	1.564538	0.438186	-0.999690	1.622633	0.473069	-0.963983
7	C	1.871018	-0.689737	-0.005398	1.922469	-0.673524	0.009424
8	C	-1.209380	-0.220389	-0.020804	-1.236701	-0.215370	-0.034824
9	H	1.303744	2.054641	0.438050	1.272172	2.055747	0.491997
10	H	0.023931	2.003493	-0.794171	0.033870	1.988687	-0.769827
11	H	-0.396409	0.864423	1.664106	-0.384856	0.794308	1.674652
12	H	1.003262	0.051567	-1.850733	1.101933	0.097244	-1.843699
13	H	2.469986	0.918380	-1.371244	2.526191	0.983916	-1.293585
14	H	1.755458	-1.675684	-0.456453	1.888090	-1.647476	-0.478656
15	H	2.867532	-0.602049	0.432017	2.888986	-0.556277	0.504716
16	H	-2.287773	1.219729	0.651525	-2.280054	1.226037	0.702713

THFA **VIII**

Atom no.	Atom	MP2/6-311++G(2d,p)			B3LYP-D3(BJ)/def2-TZVP		
1	O	0.841508	-0.780196	0.889017	0.840397	-0.786479	0.876856

2	O	-2.371281	0.691410	0.102624	-2.369133	0.692140	0.104280
3	O	-1.412511	-1.163701	-0.689084	-1.430863	-1.155976	-0.690872
4	C	0.714774	1.290211	-0.307435	0.721101	1.299411	-0.285509
5	C	-0.029679	0.306025	0.641085	-0.030258	0.294992	0.642172
6	C	2.100862	0.644322	-0.446942	2.100274	0.643905	-0.464117
7	C	1.788181	-0.821349	-0.188184	1.806914	-0.823835	-0.176100
8	C	-1.313662	-0.164309	-0.028923	-1.321303	-0.164923	-0.034417
9	H	0.755270	2.299755	0.102096	0.783141	2.291035	0.159274
10	H	0.214907	1.335987	-1.277556	0.208996	1.394874	-1.243244
11	H	-0.261001	0.761301	1.609797	-0.268321	0.737267	1.614723
12	H	2.547771	0.823115	-1.425847	2.512806	0.807575	-1.459073
13	H	-0.044655	-1.328395	-1.537371	2.806730	1.032844	0.270153
14	H	-0.004305	1.238620	1.530169	1.387892	-1.330962	-1.050612
15	H	-1.184509	2.077305	0.542850	2.664592	-1.385871	0.189111
16	H	1.803763	0.000000	1.319538	-2.140291	1.418464	0.698996

Appendix C

Supporting Information for Chapter 5

Conformational Landscape, Chirality Recognition and Chiral Analyses: Broadband Rotational Spectra of the Tetrahydro-2-Furoic Acid···Propylene Oxide Conformers

Contents:

Table 5.S1. Relative raw (ΔD_e) and ZPE corrected (ΔD_0) energies (in kJ mol^{-1}), rotational constants (in MHz), and electric dipole moment components (in Debye) of the homochiral and heterochiral THFA···PO conformers, calculated at the B3LYP-D3(BJ)/def2-TZVP level of theory.

SS conformer	ΔD_e[a]	ΔD_0[a]	*A*	*B*	*C*	$\lvert\mu_a\rvert$	$\lvert\mu_b\rvert$	$\lvert\mu_c\rvert$
Type 1								
III(v_a)	0.0	0.0	2286	373	366	1.2	0.0	1.8
III(v_b)	1.5	1.1	1934	430	415	1.5	2.5	0.8
IV(v_a)	1.8	1.4	2490	356	346	1.0	0.3	1.6
V(v_a)	2.2	2.1	2139	381	378	1.6	1.4	1.3
IV(v_b)	3.2	2.5	2037	405	396	1.2	2.6	0.4
V(v_b)	3.2	2.6	2041	411	410	1.2	1.0	0.6
VI(v_a)	3.0	2.7	2353	358	355	1.2	1.6	1.0
VI(v_b)	3.9	3.2	2191	392	386	0.9	0.7	0.8
Type 2								
I(v_c)	8.7	9.0	1329	607	505	2.8	4.1	0.7
I(v_d)	9.5	10.1	1469	529	432	2.4	4.4	0.9
II(v_c)	10.3	10.9	1242	619	479	2.6	4.7	0.1
II(v_d)	11.2	11.9	1365	537	420	2.3	4.9	0.4
Type 3								
I(v_e)	12.8	12.9	1373	594	512	0.7	2.9	0.5
II(v_e)	13.7	13.8	1198	673	571	0.4	3.3	0.2
RS conformer	ΔD_e[a]	ΔD_0[a]	*A*	*B*	*C*	$\lvert\mu_a\rvert$	$\lvert\mu_b\rvert$	$\lvert\mu_c\rvert$
Type 1								
III(v_a)	0.2	0.1	2071	384	375	1.5	1.8	1.0
III(v_b)	1.1	0.6	2087	408	398	1.3	0.7	1.1
IV(v_a)	1.9	1.6	2207	362	359	1.2	1.5	1.3
IV(v_b)	2.8	2.0	2245	390	376	1.0	0.7	1.0
V(v_a)	2.9	2.6	2503	356	347	1.0	0.9	1.2
V(v_b)	3.7	3.1	1903	431	425	1.5	2.6	0.1
VI(v_b)	4.4	3.7	2054	404	394	1.2	2.3	1.1
VI(v_a)	8.7	9.3	2043	407	389	2.6	2.0	3.0
Type 2								
I(v_d)	8.9	9.4	1367	589	467	3.5	3.9	0.4
I(v_c)	9.6	10.2	1368	600	460	2.2	4.5	0.9
II(v_d)	10.4	11.1	1256	614	455	3.4	4.4	0.0
II(v_c)	11.3	12.0	1279	614	448	1.9	5.2	0.5
Type 3								

I(v_e)	12.8	12.9	1378	580	525	0.9	2.8	0.2
II(v_e)	13.5	13.1	1254	633	555	0.2	3.0	0.2

[a] All energies are referenced to the global minimum structure SS-**III**(v_a).

Table 5.S2. Measured transition frequencies of SS-**III**(v_a).

J'	K_a'	K_c'	J''	K_a''	K_c''	ν_{EXP} / MHz	$\Delta\nu$[a] / MHz
6	0	6	5	0	5	4448.8350	-0.0009
6	2	5	5	2	4	4449.4315	0.0002
6	2	4	5	2	3	4450.1030	-0.0020
5	0	5	4	0	4	3707.5416	-0.0018
5	2	4	4	2	3	3707.8881	-0.0057
5	2	3	4	2	2	3708.2729	-0.0060
5	1	5	4	1	4	3690.3960	0.0041
5	1	4	4	1	3	3725.2923	-0.0067
6	1	6	5	1	5	4428.4227	0.0096
6	1	5	5	1	4	4470.2972	-0.0022
7	1	7	6	1	6	5166.4119	0.0084
7	0	7	6	0	6	5190.0169	0.0063
7	2	6	6	2	5	5190.9500	0.0038
7	2	5	6	2	4	5192.0298	0.0058
7	1	6	6	1	5	5215.2720	0.0050
8	1	8	7	1	7	5904.3638	0.0057
8	0	8	7	0	7	5931.0405	-0.0076
4	1	4	3	1	3	2952.3412	-0.0036
4	0	4	3	0	3	2966.1470	-0.0057
5	2	3	5	1	5	5777.5440	0.0068
6	2	4	6	1	6	5799.2330	0.0038
7	2	5	7	1	7	5824.8433	-0.0064
8	2	6	8	1	8	5854.5375	-0.0051
9	2	7	9	1	9	5888.4748	0.0034
5	2	4	5	1	4	5672.1430	0.0053
5	1	4	4	0	4	5668.6016	-0.0037
4	2	3	4	1	3	5689.5410	-0.0019
4	1	3	3	0	3	4909.4596	0.0006
9	0	9	8	1	7	4635.0002	0.0007
3	1	2	2	0	2	4153.8732	0.0024
8	0	8	7	1	6	3923.2657	-0.0007
2	1	1	1	0	1	3401.7996	-0.0038
7	0	7	6	1	5	3207.4857	0.0004

10	0	10	9	1	8	5342.5484	-0.0050
6	2	5	6	1	5	5651.2636	-0.0059
8	1	7	7	1	6	5960.1913	-0.0049

[a] $\Delta\nu = \nu_{exp} - \nu_{cacl}$.

Table 5.S3. Measured transition frequencies of SS-**I**(v_c).

J'	K_a'	K_c'	J''	K_a''	K_c''	ν_{EXP} / MHz	$\Delta\nu$[a] / MHz
5	0	5	4	0	4	5300.7127	-0.0022
5	2	4	4	2	3	5433.6909	-0.0026
5	3	3	4	3	2	5476.7765	0.002
5	3	2	4	3	1	5486.4782	-0.0069
5	2	3	4	2	2	5585.2427	0.0084
5	1	4	4	1	3	5647.918	-0.0021
5	1	5	4	1	4	5182.6215	0.0037
4	1	3	3	1	2	4533.6191	-0.0023
4	2	2	3	2	1	4435.9615	-0.0022
4	2	3	3	2	2	4355.3875	0.0035
4	0	4	3	0	3	4281.3639	0.0019
6	1	6	5	1	5	6202.3692	0.0009
6	0	6	5	0	5	6300.9042	-0.0016
6	2	5	5	2	4	6505.1347	0.0038
2	2	1	1	1	0	4535.6507	-0.0009
2	2	0	1	1	1	4639.0909	-0.0008
4	1	4	3	0	3	4708.7793	-0.0018
5	0	5	4	1	4	4873.2935	-0.0022
5	4	1	5	3	2	5572.5272	0.0011
7	4	4	7	3	5	5576.3365	0.0021
6	4	3	6	3	4	5579.3723	0.0018
8	4	5	8	3	6	5581.2728	0.0008
4	4	0	4	3	1	5587.723	-0.0022
4	4	1	4	3	2	5590.9769	-0.0018
9	4	6	9	3	7	5600.9017	-0.0031
5	1	5	4	0	4	5610.0354	-0.0016
5	2	3	5	1	4	2004.039	-0.0082
4	2	2	4	1	3	2066.7286	-0.0044
2	1	2	1	1	1	2085.9872	0.0001
3	2	1	3	1	2	2164.3869	-0.0038
6	1	5	6	0	6	2167.496	-0.0004
2	0	2	1	0	1	2172.5633	0.0005

2	2	1	2	1	2	2544.672	-0.0002
3	0	3	2	1	2	2571.5473	0.0017
3	2	2	3	1	3	2692.2355	0.0037
7	1	6	7	0	7	2703.1951	-0.0043
2	1	2	1	0	1	2839.2036	-0.0014
4	2	3	4	1	4	2891.2167	0.0091
3	1	3	2	1	2	3123.9185	-0.0001
5	2	4	5	1	5	3142.2853	0.002
9	3	6	9	2	7	3148.1806	0.0072
3	0	3	2	0	2	3238.1879	0.0001
3	2	2	2	2	1	3271.4815	0.0033
3	2	1	2	2	0	3304.7751	0.0003
8	3	5	8	2	6	3307.804	-0.0002
8	1	7	8	0	8	3307.3351	0.0006
6	2	4	5	3	3	2946.3433	-0.0023
10	2	8	10	1	9	2979.6463	-0.0018
11	3	8	11	2	9	3036.1357	-0.0052
10	3	7	10	2	8	3047.7243	-0.0033
3	1	2	2	1	1	3408.467	0.0002
13	3	10	13	2	11	3362.1424	0.0043
7	2	6	6	3	3	3384.3351	0.0004
6	2	5	6	1	6	3445.0467	0.0009
7	3	4	7	2	5	3492.4677	0.0002
11	2	9	11	1	10	3502.7268	-0.001
6	3	3	6	2	4	3669.2088	0.0001
5	1	4	4	2	3	3703.4963	0.0004
4	0	4	3	1	3	3728.9892	0.0002
3	1	3	2	0	2	3790.5605	-0.0002
7	2	6	7	1	7	3797.5613	0.0012
5	3	2	5	2	3	3812.9683	-0.0001
6	1	5	5	1	4	6746.9944	0.0001

[a] $\Delta\nu = \nu_{exp} - \nu_{cacl}$.

Table 5.S4. Measured transition frequencies of SS-**I**(v_d).

J'	K_a'	K_c'	J''	K_a''	K_c''	ν_{EXP} / MHz	$\Delta\nu^{[a]}$ / MHz
6	1	6	5	1	5	5404.1504	0.0002
6	0	6	5	0	5	5529.0238	0.0001
6	2	5	5	2	4	5690.9249	-0.0005
6	3	4	5	3	3	5745.3635	0.0001
6	3	3	5	3	2	5759.6443	0.0005
6	2	4	5	2	3	5880.0443	0.0008
6	1	5	5	1	4	5933.8993	0.0001
5	1	5	4	1	4	4514.4623	-0.0015
5	0	5	4	0	4	4650.3218	0.0009
5	2	4	4	2	3	4751.7671	0.0011
5	3	3	4	3	2	4783.8815	0.0008
5	3	2	4	3	1	4789.3008	0.002
5	2	3	4	2	2	4866.7844	0.0006
5	1	4	4	1	3	4962.4132	-0.0004
2	2	1	1	1	0	4870.0017	-0.0009
5	3	2	5	2	3	4869.3377	-0.0006
4	3	1	4	2	2	4946.8235	0.0001
2	2	0	1	1	1	4966.8206	0.0025
3	3	0	3	2	1	4988.7277	0.0125
3	3	1	3	2	2	5018.9492	-0.0127
4	3	2	4	2	3	5035.2571	-0.0045
6	0	6	5	1	5	5040.1879	-0.0018
6	1	5	6	0	6	2246.5966	-0.0022
5	1	4	4	2	3	2394.3542	-0.0028
6	2	4	6	1	5	2508.8268	-0.0009
7	2	5	7	1	6	2518.4017	-0.0023
5	2	3	5	1	4	2562.6841	0.0006
8	2	6	8	1	7	2609.0764	-0.0026
4	2	2	4	1	3	2658.3148	0.0016
3	1	3	2	1	2	2719.5359	0.0014
7	1	6	7	0	7	2745.015	0.0023
3	2	1	3	1	2	2771.6117	0.0018
2	1	2	1	0	1	2773.2224	0.0019
9	2	7	9	1	8	2794.772	-0.0002
3	0	3	2	0	2	2834.897	0.0009
3	2	2	2	2	1	2859.2583	0.0007
2	2	0	2	1	1	2879.2868	0.0014
3	2	1	2	2	0	2883.6264	0.0002
3	1	2	2	1	1	2991.3016	-0.0002
4	0	4	3	1	3	2994.7662	-0.0008

9	2	8	8	3	5	3031.9672	0.0018
10	2	8	10	1	9	3085.8888	-0.0012
2	2	1	2	1	2	3145.1765	-0.0008
3	2	2	3	1	3	3284.8998	-0.0006
8	1	7	8	0	8	3327.8598	0.0075
8	2	6	7	3	5	3389.1976	-0.0036
4	2	3	4	1	4	3472.9804	-0.0158
11	2	9	11	1	10	3488.0199	0.0065
6	1	5	5	2	4	3576.4873	-0.0029
3	1	3	2	0	2	3592.7155	0.0023
4	1	4	3	1	3	3619.4593	0.0011
5	2	4	5	1	5	3710.2981	-0.0003
4	0	4	3	0	3	3752.585	0.0009
12	3	9	12	2	10	3805.0372	-0.0091
4	2	3	3	2	2	3807.5549	0.0009
4	3	1	3	3	0	3825.4011	-0.0104
4	3	2	3	3	1	3823.8572	0.0036
4	2	2	3	2	1	3867.3035	0.0001
11	3	8	11	2	9	3869.8367	0.0039
9	1	8	9	0	9	3977.424	0.0051
14	3	11	14	2	12	3976.9669	0.0004
4	1	3	3	1	2	3980.5995	-0.0005
6	2	5	6	1	6	3997.0739	0.0003
12	2	10	12	1	11	3999.402	0.0009
10	3	7	10	2	8	4007.7275	0.0001
5	0	5	4	1	4	4025.6284	-0.0013
9	3	6	9	2	7	4192.0948	0.0047
7	2	6	7	1	7	4332.6842	0.0016
4	1	4	3	0	3	4377.2764	0.0011
8	3	5	8	2	6	4394.088	0.0024
7	3	4	7	2	5	4586.6839	0.0022
9	2	7	8	3	6	4657.8004	0.0005
10	1	9	10	0	10	4671.0761	-0.005
8	2	7	8	1	8	4715.351	0.0049
5	3	3	5	2	4	5067.3756	-0.0006
6	3	4	6	2	5	5121.8137	-0.0006
5	1	5	4	0	4	5139.1557	0.0007
9	2	8	9	1	9	5142.0738	0.0026
7	3	5	7	2	6	5205.1941	-0.0006
8	3	6	8	2	7	5323.7693	-0.0004
11	1	10	11	0	11	5385.9378	0.0075
9	3	7	9	2	8	5483.0002	-0.0002
10	2	9	10	1	10	5608.7535	-0.0067

10	3	8	10	2	9	5687.2072	0.0004
3	2	2	2	1	1	5732.405	0.0004
6	5	1	5	5	0	5733.7591	0.0007
6	5	2	5	5	1	5733.7562	0.0007
6	1	6	5	0	5	5892.9847	0.0004
11	3	9	11	2	10	5939.3095	0.0007
7	0	7	6	1	6	6029.3267	-0.0004
3	2	1	2	1	2	6034.9418	-0.0002
11	2	10	11	1	11	6110.4792	-0.0006
12	4	8	12	3	9	6224.8792	0.0017
12	3	10	12	2	11	6240.6535	-0.0042
12	1	11	12	0	12	6103.0763	-0.0051
7	1	7	6	1	6	6288.5286	-0.0001
7	0	7	6	0	6	6393.2875	-0.0001
11	4	7	11	3	8	6459.4883	-0.0001
4	2	3	3	1	2	6548.6567	0.0001
7	2	6	6	2	5	6624.1376	-0.0001
7	1	7	6	0	6	6652.4891	-0.0001
7	5	2	6	5	1	6693.2515	-0.0002
7	5	3	6	5	2	6693.2355	-0.0002
7	4	4	6	4	3	6701.6083	0.0177
7	4	3	6	4	2	6702.6636	-0.0141
7	3	5	6	3	4	6707.5179	-0.0001
7	3	4	6	3	3	6739.0208	-0.0001
9	4	5	9	3	6	6786.1288	0.0001
8	4	4	8	3	5	6881.3952	0.0001
7	1	6	6	1	5	6891.7014	-0.0001
7	2	5	6	2	4	6901.2777	-0.0001
7	4	3	7	3	4	6942.3161	0.0001
6	4	2	6	3	3	6978.6593	0.0001
8	0	8	7	1	7	6990.1473	0.0001
8	4	5	8	3	6	6991.0151	0.0001
7	4	4	7	3	5	6993.8384	0.0001
9	4	6	9	3	7	6995.4946	0.0001

[a] $\Delta\nu = \nu_{exp} - \nu_{cacl}$.

Table 5.S5. Measured transition frequencies of SR-**III**(v_a).

J'	K_a'	K_c'	J''	K_a''	K_c''	ν_{EXP} / MHz	$\Delta\nu$[a] / MHz
7	0	7	6	0	6	5328.2258	-0.0007
7	2	6	6	2	5	5329.976	0.0024
7	2	5	6	2	4	5331.958	0.0005
6	0	6	5	0	5	4567.5273	-0.0007
6	2	5	5	2	4	4568.6406	-0.0009
6	2	4	5	2	3	4569.8883	0.0063
4	0	4	3	0	3	3045.5125	0.0044
5	1	5	4	1	4	3784.868	0.0021
5	1	4	4	1	3	3829.478	0.0026
6	1	5	5	1	4	4595.2576	-0.0003
6	1	6	5	1	5	4541.7284	-0.0008
7	1	7	6	1	6	5298.5372	0.0039
7	1	6	6	1	5	5360.9824	0.0042
5	0	5	4	0	4	3806.611	0.0013
5	2	4	4	2	3	3807.2664	-0.0002
5	2	3	4	2	2	3807.9734	-0.0023
4	1	4	3	1	3	3027.944	-0.0089
4	1	3	3	1	2	3063.6341	-0.0073
8	0	8	7	0	7	6088.6617	-0.0079
8	2	7	7	2	6	6091.2581	0.0024
8	2	6	7	2	5	6094.2281	-0.0016
8	1	8	7	1	7	6055.2687	-0.0003
6	2	4	6	1	5	4954.147	-0.0001
7	2	5	7	1	6	4925.1262	-0.0002
8	2	6	8	1	7	4892.7304	-0.0003
5	2	3	5	1	4	4979.523	0.0001
4	2	2	4	1	3	5001.0229	0.0001
5	2	4	5	1	5	5112.118	0.0046
7	2	6	7	1	7	5170.462	-0.0040
5	1	5	4	0	4	5422.385	0.0013
4	1	4	3	0	3	4683.027	0.0011
8	0	8	7	1	7	4528.3871	-0.0005
3	1	3	2	0	2	3939.3352	0.0026
7	0	7	6	1	6	3738.2508	-0.0005
6	1	6	5	0	5	6157.5012	-0.0020
10	0	10	9	1	9	6118.6629	0.0004
2	1	2	1	0	1	3191.2301	-0.0035

[a] $\Delta\nu = \nu_{exp} - \nu_{cacl}$.

Table S6. Measured transition frequencies of SR-**I**(v_d).

J'	K_a'	K_c'	J''	K_a''	K_c''	ν_{EXP} / MHz	$\Delta\nu^{[a]}$ / MHz
5	1	5	4	1	4	4874.8892	-0.0030
5	0	5	4	0	4	5004.5836	0.0004
5	2	4	4	2	3	5182.0392	-0.0011
5	4	1	4	4	0	5233.6812	-0.0047
5	4	2	4	4	1	5233.3797	-0.0039
5	3	3	4	3	2	5240.4263	0.0007
5	3	2	4	3	1	5255.4016	0.0003
5	2	3	4	2	2	5384.903	0.0001
5	1	4	4	1	3	5438.4112	0.0012
6	1	6	5	1	5	5827.8069	0.0027
6	0	6	5	0	5	5930.6201	0.0052
6	2	5	5	2	4	6197.5324	0.0033
6	4	3	5	4	2	6288.1235	0.0072
6	4	2	5	4	1	6289.467	0.0008
6	3	4	5	3	3	6294.5281	0.0055
6	3	3	5	3	2	6333.4187	0.0041
5	1	5	4	0	4	5299.3518	-0.0001
10	4	6	10	3	7	5305.526	-0.0017
9	2	8	9	1	9	5308.6375	0.0068
10	3	8	10	2	9	5448.5419	0.0038
10	1	9	10	0	10	5448.4051	-0.0028
3	2	2	2	1	1	5544.5822	-0.0012
9	4	5	9	3	6	5557.8763	-0.0005
6	0	6	5	1	5	5635.8477	0.0014
8	4	4	8	3	5	5750.7093	-0.0016
5	2	3	5	1	4	2151.963	-0.0158
6	2	4	6	1	5	2183.7254	0.0027
4	2	2	4	1	3	2205.4871	0.0012
3	2	1	3	1	2	2311.1122	0.0006
7	2	5	7	1	6	2326.4425	0.0006
3	0	3	2	1	2	2376.6166	-0.0025
6	1	5	6	0	6	2562.6913	-0.0076
8	2	6	8	1	7	2599.1496	0.0016
2	2	1	2	1	2	2767.0297	0.0073
2	1	2	1	0	1	2774.0605	0.0003
3	1	3	2	1	2	2944.2163	-0.003
3	2	2	3	1	3	2947.4716	-0.0019
9	2	7	9	1	8	3013.0087	0.0014
3	0	3	2	0	2	3079.1255	-0.0033
3	2	2	2	2	1	3124.667	-0.0034

3	2	1	2	2	0	3170.2209	0.0002
4	2	3	4	1	4	3190.9636	-0.0006
7	1	6	7	0	7	3215.6457	-0.0023
10	3	7	10	2	8	3265.1026	0.0015
3	1	2	2	1	1	3290.5937	-0.0036
9	3	6	9	2	7	3322.0007	0.0011
11	3	8	11	2	9	3335.0122	0.003
5	1	4	4	2	3	3399.3942	-0.0023
8	2	7	7	3	4	3392.7098	0.0044
8	3	5	8	2	6	3472.849	0.0011
4	0	4	3	1	3	3489.2331	-0.0031
5	2	4	5	1	5	3498.1114	-0.0009
12	3	9	12	2	10	3554.3889	-0.0008
10	2	8	10	1	9	3566.3569	0.0031
3	1	3	2	0	2	3646.7266	-0.0024
7	3	4	7	2	5	3676.0227	0.0012
7	2	5	6	3	4	3813.8857	0.0037
6	2	5	6	1	6	3867.8372	-0.0001
6	3	3	6	2	4	3887.158	0.0007
4	1	4	3	1	3	3913.6947	-0.0013
8	1	7	8	0	8	3937.206	-0.0006
4	0	4	3	0	3	4056.8351	-0.0013
5	3	2	5	2	3	4068.5636	0.0004
4	2	3	3	2	2	4157.1853	-0.0014
4	3	2	3	3	1	4187.3147	-0.0013
4	3	1	3	3	0	4191.6543	-0.0013
4	3	1	4	2	2	4198.065	0.0001
11	2	9	11	1	10	4240.5194	0.0025
4	2	2	3	2	1	4266.5319	-0.0016
3	3	0	3	2	1	4272.9427	-0.0001
7	2	6	7	1	7	4296.8434	0.0001
3	3	1	3	2	2	4329.3399	-0.0002
4	3	2	4	2	3	4359.4693	-0.0002
10	3	8	9	4	5	4358.9327	-0.0073
4	1	3	3	1	2	4372.1576	-0.0016
5	3	3	5	2	4	4417.8544	-0.0003
4	1	4	3	0	3	4481.2963	0.0001
6	3	4	6	2	5	4514.848	-0.0001
5	0	5	4	1	4	4580.1234	-0.0001
2	2	1	1	1	0	4618.7398	-0.0004
7	3	5	7	2	6	4659.9605	0.0001
9	1	8	9	0	9	4691.4168	-0.0001
6	1	5	5	2	4	4700.4325	-0.0003

12	4	8	12	3	9	4723.4581	0.0009
2	2	0	1	1	1	4746.0183	-0.0005
8	2	7	8	1	8	4779.5689	-0.0004
8	3	6	8	2	7	4860.9285	0.0004
11	4	7	11	3	8	5014.5735	0.0008
9	3	7	9	2	8	5123.0111	0.0009
3	2	1	2	1	2	5948.8176	-0.0006
6	4	2	6	3	3	5961.6944	0.0001
7	1	6	6	2	5	6002.288	-0.0002
5	4	1	5	3	2	6005.6425	-0.0002
6	1	6	5	0	5	6122.5731	0.0002
7	4	4	7	3	5	6018.1944	0.0004
6	4	3	6	3	4	6018.9397	0.0001
5	4	2	5	3	3	6025.3457	-0.0002
4	4	0	4	3	1	6027.3576	-0.0004
8	4	5	8	3	6	6030.6499	0.0007
4	4	1	4	3	2	6032.3874	-0.0004
9	4	6	9	3	7	6065.8462	0.0012
11	1	10	11	0	11	6190.5016	0.0034
11	4	8	11	3	9	6246.7397	0.0026
6	5	1	5	5	0	6278.2175	0.0007
6	5	2	5	5	1	6278.1996	0.0007
12	3	10	12	2	11	6283.902	-0.0076
4	2	3	3	1	2	6411.1726	-0.0002
12	4	9	12	3	10	6412.1568	-0.0081
11	2	10	11	1	11	6472.0524	-0.0001
6	1	5	5	1	4	6483.0766	0.0001
6	2	4	5	2	3	6514.8205	0.0001
7	0	7	6	1	6	6654.4775	0.0001
7	1	7	6	1	6	6773.2346	0.0001
7	0	7	6	0	6	6846.4355	0.0001
7	1	7	6	0	6	6965.1926	0.0001

[a] $\Delta\nu = \nu_{exp} - \nu_{cacl}$.

Table S7. Measured transition frequencies of SR-**I**(v_c).

J'	K_a'	K_c'	J''	K_a''	K_c''	ν_{EXP} / MHz	$\Delta\nu^{[a]}$ / MHz
5	1	5	4	1	4	4826.9616	-0.0050
5	0	5	4	0	4	4956.1927	0.0021
5	2	4	4	2	3	5175.251	-0.0024
5	4	1	4	4	0	5241.4711	0.0051
5	4	2	4	4	1	5240.9621	-0.0061
5	3	3	4	3	2	5248.8509	-0.0049
5	3	2	4	3	1	5270.473	-0.0012
5	2	3	4	2	2	5426.6858	0.0014
5	1	4	4	1	3	5458.2487	0.0019
6	1	6	5	1	5	5765.5253	0.0022
6	0	6	5	0	5	5862.0741	0.0007
6	2	5	5	2	4	6183.676	-0.0026
6	1	5	5	1	4	6493.2617	0.0001
6	2	4	5	2	3	6569.091	-0.0019
7	1	7	6	1	6	6695.6259	-0.0023
7	0	7	6	0	6	6760.2541	-0.0046
5	1	5	4	0	4	5209.2464	0.0007
9	3	7	9	2	8	5285.0477	0.0029
9	4	5	9	3	6	5380.2355	-0.0023
8	2	6	7	3	5	5462.9833	-0.0049
3	2	2	2	1	1	5509.0256	-0.0035
6	0	6	5	1	5	5609.0166	-0.0017
9	2	8	9	1	9	5633.6881	0.0002
10	3	8	10	2	9	5674.0779	-0.0031
7	4	3	7	3	4	5793.8617	0.0015
6	4	2	6	3	3	5900.6888	0.0032
5	2	3	5	1	4	2137.4245	0.0001
4	2	2	4	1	3	2168.987	0.0001
5	1	4	5	0	5	2182.8437	0.0015
6	2	4	6	1	5	2213.256	0.0002
2	1	1	1	1	0	2213.8724	0.0134
3	2	1	3	1	2	2270.9079	0.0002
3	0	3	2	1	2	2387.9598	0.0005
2	2	0	2	1	1	2398.9279	-0.0121
7	2	5	7	1	6	2424.1899	0.0005
2	1	2	1	0	1	2747.3961	0.0004
2	2	1	2	1	2	2775.9029	0.0068
8	2	6	8	1	7	2789.3355	0.0008
6	1	5	6	0	6	2814.0322	0.0018
3	1	3	2	1	2	2920.2378	0.001

3	2	2	3	1	3	2980.5565	0.0003
3	0	3	2	0	2	3066.8925	0.0013
3	2	2	2	2	1	3124.8983	0.0014
3	2	1	2	2	0	3182.9063	0.0016
9	3	6	9	2	7	3251.8001	0.0047
4	2	3	4	1	4	3256.8743	0.0038
10	3	7	10	2	8	3273.724	0.0018
3	1	2	2	1	1	3310.9389	0.0019
9	2	7	9	1	8	3315.0701	0.0015
8	3	5	8	2	6	3359.7062	-0.0025
11	3	8	11	2	9	3457.1289	-0.002
4	0	4	3	1	3	3496.37	0.0018
5	1	4	4	2	3	3499.886	0.0028
7	1	6	7	0	7	3545.1897	0.0034
7	3	4	7	2	5	3553.0582	-0.0024
3	1	3	2	0	2	3599.169	0.0003
5	2	4	5	1	5	3605.1583	0.001
6	3	3	6	2	4	3779.0851	0.0005
4	1	4	3	1	3	3878.6477	0.0005
5	3	2	5	2	3	3987.5542	-0.001
10	2	8	10	1	9	3987.8921	-0.0006
7	2	5	6	3	4	4007.9173	-0.0012
6	2	5	6	1	6	4023.3147	0.0018
4	0	4	3	0	3	4028.6463	0.0005
4	3	1	4	2	2	4143.7651	-0.0004
4	2	3	3	2	2	4154.9625	0.001
4	3	2	3	3	1	4193.212	0.001
9	3	6	8	4	5	4192.5467	0.0041
4	3	1	3	3	0	4199.5032	0.0011
3	3	0	3	2	1	4237.0327	0.0002
4	2	2	3	2	1	4292.7709	0.0017
3	3	1	3	2	2	4308.7912	0.0006
8	1	7	8	0	8	4334.304	-0.0111
4	3	2	4	2	3	4347.0407	0.0007
4	1	3	3	1	2	4394.6915	0.0015
4	1	4	3	0	3	4410.9242	-0.0005
5	3	3	5	2	4	4420.6431	0.0007
12	4	8	12	3	9	4494.0752	0.0023
7	2	6	7	1	7	4506.2924	-0.0001
6	3	4	6	2	5	4541.899	0.0007
5	0	5	4	1	4	4573.9118	0.0002
2	2	1	1	1	0	4597.9915	0.0004
7	3	5	7	2	6	4721.5764	-0.0021

2	2	0	1	1	1	4743.3884	0.0008
11	4	7	11	3	8	4768.6535	0.0003
11	2	9	11	1	10	4773.0716	-0.0047
6	1	5	5	2	4	4817.892	0.0006
8	3	6	8	2	7	4967.7658	0.0004
8	2	7	8	1	8	5046.3064	-0.0018
10	4	6	10	3	7	5082.5982	-0.0006
9	1	8	9	0	9	5140.6894	-0.0043
11	3	9	10	4	6	5142.7763	0.002
8	4	4	8	3	5	5622.3875	-0.0009
12	2	10	12	1	11	5623.0049	0.0053
10	1	9	10	0	10	5936.4759	0.0053
5	4	1	5	3	2	5959.7521	0.0001
3	2	1	2	1	2	5973.6087	0.0001
6	4	3	6	3	4	5982.5625	0.0001
7	4	4	7	3	5	5986.5031	0.0001
5	4	2	5	3	3	5988.1589	0.0001
4	4	0	4	3	1	5988.7603	0.0001
4	4	1	4	3	2	5996.0465	0.0002
8	4	5	8	3	6	6010.2597	0.0002
9	4	6	9	3	7	6066.1501	0.0001
7	1	6	6	2	5	6125.6273	0.0001
10	4	7	10	3	8	6167.0545	0.0001
11	3	9	11	2	10	6131.6279	0.0001
6	4	3	5	4	2	6299.3381	0.0001
6	4	2	5	4	1	6301.5559	0.0001
6	3	4	5	3	3	6304.9345	0.0001
11	4	8	11	3	9	6324.8087	0.0001
4	2	3	3	1	2	6353.0536	0.0001
6	3	3	5	3	2	6360.6222	0.0001
11	1	10	11	0	11	6709.9106	0.0001
7	1	7	6	0	6	6852.133	0.0001

[a] $\Delta\nu = \nu_{exp} - \nu_{cacl}$.

Appendix D

Supporting Information for Chapter 6

Conformational Panorama and Chirality Controlled Structure-Energy Relationship in a Chiral Carboxylic Acid Dimer

Contents:

Table 6.S1. Relative raw (ΔD_e) and ZPE corrected (ΔD_0) energies (in kJ mol^{-1}) to RR or RS **III**(Oc)-**III**(Oc), rotational constants (in MHz), and electric dipole moment components (in Debye) of the 10 most stable homochiral (RR) and10 most stable heterochiral (RS) **Type 1** $(THFA)_2$ conformers calculated at the B3LYP-D3(BJ)/def2-TZVP level of theory.

RR conformer	ΔD_e	ΔD_0	*A*	*B*	*C*	$\lvert\mu_a\rvert$	$\lvert\mu_b\rvert$	$\lvert\mu_c\rvert$
III(Oc)-**III**(Oc)	0.6	0.5	Relative to the global minimum RS **III**(Oc)-**III**(Oc)					
III(Oc)-**III**(Oc)[a]	**0.0**	**0.0**	**1437**	**189**	**186**	**0.0**	**0.0**	**3.7**
III(Oc)-**V**(Oc)	0.8	0.9	1357	193	185	0.1	0.0	0.0
III(Oc)-**IV**(Oc)	0.9	1.1	1499	182	179	0.3	1.1	3.5
III(Oc)-**VI**(Oc)	1.3	1.5	1429	185	177	0.4	0.1	0.1
IV(Oc)-**V**(Oc)	1.6	2.1	1437	185	177	0.2	0.1	0.1
IV(Oc)-**IV**(Oc)	1.8	2.3	1552	175	173	0.0	0.0	3.6
IV(Oc)-**VI**(Oc)	2.8	2.7	1517	177	170	0.1	0.0	0.0
V(Oc)-**V**(Oc)	2.7	2.9	1515	185	183	0.0	0.0	3.8
V(Oc)-**VI**(Oc)	3.1	3.6	1614	177	175	0.3	1.1	3.5
VI(Oc)-**VI**(Oc)	4.0	4.3	1710	170	168	0.0	0.0	3.7
RS conformer	ΔD_e	ΔD_0	*A*	*B*	*C*	$\lvert\mu_a\rvert$	$\lvert\mu_b\rvert$	$\lvert\mu_c\rvert$
III(Oc)-**III**(Oc)[b]	**0.0**	**0.0**	**1563**	**186**	**181**	**0.0**	**0.0**	**0.0**
III(Oc)-**IV**(Oc)	1.0	1.1	1641	179	175	0.3	0.1	0.1
III(Oc)-**V**(Oc)	2.1	2.1	1270	197	189	0.1	1.2	3.6
IV(Oc)-**IV**(Oc)	2.0	2.4	1728	173	168	0.0	0.0	0.0
III(Oc)-**VI**(Oc)	2.6	2.7	1340	187	181	0.4	0.9	3.6
V(Oc)-**V**(Oc)	3.0	2.9	1632	182	179	0.0	0.0	0.0
IV(Oc)-**V**(Oc)	3.1	3.2	1330	188	181	0.3	0.8	3.6
V(Oc)-**VI**(Oc)	3.4	3.6	1724	176	172	0.4	0.1	0.1
IV(Oc)-**VI**(Oc)	3.5	3.9	1405	179	174	0.1	0.5	3.6
VI(Oc)-**VI**(Oc)	3.8	4.3	1831	169	165	0.0	0.0	0.0

[a] All other homochiral, RR, conformers listed here are expected to cool to this one in a supersonic jet expansion. This conformer is observed experimentally.

[b] All other heterochiral, RS, conformers listed here are expected to cool to this lowest energy conformer in a supersonic jet expansion. It is not observed experimentally because it has an inversion symmetric center and its permanent dipole moment is zero.

Table 6.S2. Relative raw (ΔD_e) and ZPE corrected (ΔD_0) energies (in kJ mol^{-1}) to RR **I**+(Oe)-**III**(Oc), rotational constants (in MHz), and electric dipole moment components (in Debye) of the 30[a] most stable homochiral (RR) **Type 2** (THFA)2 conformers calculated at the B3LYP-D3(BJ)/def2-TZVP level of theory.

RR conformer[b]	ΔD_e	ΔD_0	A	B	C	$\lvert\mu_a\rvert$	$\lvert\mu_b\rvert$	$\lvert\mu_c\rvert$
I+(Oe)-**III**(Oc)	19.0	19.8 Relative to the global minimum RS **III**(Oc)-**III**(Oc)						
I+(Oe)-**III**(Oc)	**0**	**0.0**	**1115**	**242**	**217**	**1**	**4.7**	**0.3**[c]
I(Oc)-**III**(va)	**1.1**	**1.2**	**882**	**292**	**260**	**1.7**	**2.9**	**1.5**[c]
I+(Oe)-**IV**(Oc)	1.1	1.3	1155	231	209	1.4	4.9	0.1
I(Oc)-**III**(vb)	**1.8**	**1.8**	**956**	**250**	**221**	**1.7**	**4.6**	**2.2**[c]
II(Oc)-**III**(vb)	2.2	1.9	938	243	210	1.5	4	2.2
I(Oe)-**V**(Oc)	**2.0**	**2.1**	**1084**	**249**	**228**	**1.3**	**3.3**	**1.2**[d]
II+(Oe)-**III**(Oc)	1.9	2.1	1035	249	220	1.1	4.7	0.3
I(Oc)-**V**(vb)	2.2	2.4	1172	221	208	1.8	2	0
I(Oe)-**III**(Oc)	**2.6**	**2.5**	**1070**	**248**	**230**	**1.7**	**6.7**	**0.2**[d]
I(Oe)-**VI**(Oc)	2.3	2.6	1135	236	216	1.8	3.5	1.1
I(Oc)-**VI**(va)	2.3	2.7	906	275	246	1.3	2.8	1.5
I+(Oe)-**V**(Oc)	3.0	2.7	1054	244	219	2.8	4.8	2.6
I(Oc)-**VI**(vb)	2.4	3.0	1192	215	203	1.3	2.2	0.1
II(Oc)-**V**(vb)	2.5	3.0	1136	219	200	2.2	2	0.5
II(Oc)-**III**(va)	3.2	3.0	841	314	277	0.8	2.6	1.5
I(Oc)-**VI**(vb)	3.0	3.1	986	234	210	1.4	4.5	2.3
II(Oc)-**IV**(vb)	3.2	3.2	973	230	201	1.2	3.8	2.2
I+(Oe)-**VI**(Oc)	3.2	3.2	1101	231	209	3.1	4.8	2.9
II+(Oe)-**IV**(Oc)	3.0	3.5	1069	237	212	1.5	4.9	0.1
II(Oc)-**VI**(vb)	3.5	3.7	1166	211	195	1.6	2.1	0.2
I(Oe)-**IV**(Oc)	3.7	3.8	1114	238	219	2.1	6.6	0.3
II(Oc)-**IV**(va)	3.6	4.3	865	296	262	0.5	2.5	1.5
I(Oc)-**V**(va)	4.4	4.6	1186	238	223	2.1	3.1	1.1
II(Oe)-**V**(Oc)	4.5	4.6	1013	257	228	0.9	3.8	0.5
I(Oc)-**VI**(va)	5.2	5.2	1219	229	214	1.7	3.1	0.9

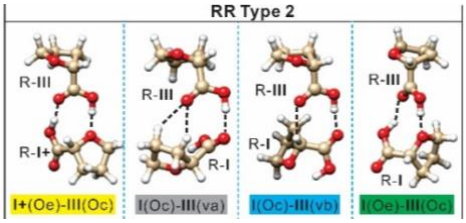

II+(Oe)-**V**(Oc)	4.9	5.2	975	254	223	3.1	5.2	2.6
II(Oe)-**VI**(Oc)	4.8	5.2	1053	245	217	1.5	3.9	0.4
II+(Oe)-**VI**(Oc)	5.5	5.8	1013	240	213	3.4	5.2	2.7
II(Oc)-**V**(va)	6.2	6.8	1077	256	237	1.4	3.3	1
II(Oc)-**VI**(va)	6.6	7.4	1107	245	227	1	3.3	0.8

[a] The homochiral **II**(Oe)-**III**(Oc) and **II**(Oe)-**III**(Oc) dimers identified by the CREST search are no longer true minima at the B3LYP-D3(BJ)/def2-TZVP level of theory. This reduces the number of expected conformers from 32 to 30.

[b] The four different H-bond binding categories shown for RR **Type 2** in Figure 2 (reproduced above) are identified in the table with four different color highlights. Conformers within each category can convert to the lowest energy ones completely or partially based on the reaction coordinate scans done.

[c] Red indicates the lowest energy conformers in the yellow, gray and blue categories. These three lowest energy conformers were observed experimentally.

[d] Bolded black indicates the two lowest energy conformers in the green category. **I**(Oe)-**V**(Oc) and **I**(Oe)-**III**(Oc) are quite close in energy and may switch their ordering if a different level of theory were used. Since the **V** monomer was not detected experimentally, it is unlikely that **I**(Oe)-**V**(Oc) has a higher abundance than **I**(Oe)-**III**(Oc). We therefore show **I**(Oe)-**III**(Oc) in Figure 2. Neither conformer was observed experimentally.

Table 6.S3. Relative raw (ΔD_e) and ZPE corrected (ΔD_0) energies (in kJ mol^{-1}) to RS **I**(Oc)-**III**(vb), rotational constants (in MHz), and electric dipole moment components (in Debye) of the 32 most stable heterochiral (RS) **Type 2** $(THFA)_2$ conformers calculated at the B3LYP-D3(BJ)/def2-TZVP level of theory.

RS conformer[a]	ΔD_e	ΔD_0	A	B	C	$\lvert\mu_a\rvert$	$\lvert\mu_b\rvert$	$\lvert\mu_c\rvert$
I(Oc)-**III**(vb)	18.8	19.8	Relative to the global minimum RS **III**(Oc)-**III**(Oc)					
I(Oc)-**III**(vb)	**0.0**	**0.0**	**1035**	**233**	**213**	**1.4**	**2.3**	**0**[b]
I(Oe)-**III**(Oc)	**0.1**	**0.0**	**1040**	**259**	**236**	**0.3**	**3.4**	**1.1**[b]
II(Oc)-**III**(vb)	0.8	0.5	967	237	210	1.5	2.5	0.5
I+(Oe)-**III**(Oc)	**1.6**	**1.2**	**1066**	**245**	**222**	**1.2**	**5.2**	**3.1**[b]
I(Oc)-**VI**(vb)	1.2	1.4	1081	224	203	1.2	2.3	0.1
I+(Oe)-**V**(Oc)	1.8	1.5	1088	242	216	2.6	4.2	0.2
I(Oc)-**III**(va)	**1.7**	**1.6**	**925**	**280**	**246**	**1.2**	**3.1**	**1.5**[b]
bI(Oe)-**IV**(Oc)	1.4	1.7	1076	245	226	0.7	3.5	1.3
II(Oc)-**IV**(vb)	2.0	1.9	1005	227	201	1.3	2.5	0.4
I+(Oe)-**VI**(Oc)	2.1	2.1	1135	231	206	2.9	4.3	0.4
I+(Oe)-**IV**(Oc)	2.7	2.5	1098	234	212	1.6	5.5	2.8
II(Oe)-**III**(Oc)	2.9	2.7	982	265	235	0.2	3.8	0.5
I(Oc)-**VI**(va)	2.8	3.0	959	266	234	0.9	3	1.4
II+(Oe)-**V**(Oc)	3.7	3.6	1006	250	219	2.6	4.2	0.1
II(Oc)-**III**(va)	3.4	3.7	855	308	266	0.4	3.1	1.4
I(Oc)-**V**(va)	3.9	3.8	1145	244	234	2.6	2.2	2.1
II+(Oe)-**III**(Oc)	3.8	3.8	981	253	225	1.4	5.8	2.8
I(Oc)-**V**(vb)	4.3	3.9	1107	227	210	2.4	4.4	2
I(Oe)-**V**(Oc)	4.2	3.9	1134	240	222	2.7	6.3	0.3
II(Oc)-**V**(vb)	4.4	4.2	1105	221	200	2.4	3.7	2.2
II+(Oe)-**VI**(Oc)	4.0	4.2	1044	239	209	3	4.3	0.2
II(Oe)-**IV**(Oc)	4.2	4.4	1014	251	225	0.6	3.8	0.7
I(Oe)-**VI**(Oc)	4.6	4.5	1182	228	213	2.9	6.4	0

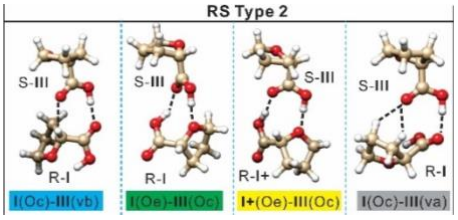

I(Oc)-**VI**(vb)	4.5	4.6	1155	216	199	2	4.4	2
I(Oc)-**VI**(va)	4.3	4.6	1175	233	224	2.1	2.5	1.8
II(Oc)-**VI**(vb)	4.8	4.7	1152	211	190	2	3.6	2
II(Oc)-**IV**(va)	4.8	5.0	886	290	252	0.1	3	1.4
II+(Oe)-**IV**(Oc)	4.4	5.0	1006	242	216	1.9	6	2.5
II(Oc)-**V**(va)	5.4	5.8	1082	259	246	1.8	2	2.1
II(Oc)-**VI**(va)	5.8	6.5	1102	247	237	1.4	2.2	1.9
II(Oe)-**V**(Oc)	7.7	7.4	1040	251	224	2.6	6.9	0.6
II(Oe)-**VI**(Oc)	8.1	7.9	1080	238	215	2.8	7	0.3

[a] The four different H-bond binding categories for RS **Type 2** in Figure 1 (reproduced above) are identified in the table with four different color highlights. Conformers within each category can convert to the lowest energy ones completely or partially based on the reaction coordinate scans done.

[b] Bold indicates the lowest energy conformer in each category. Red and Black indicate whether these lowest energy conformers were experimentally observed or not, respectively.

Table 6.S4. Relative raw (ΔD_e) and ZPE corrected (ΔD_0) energies (in kJ mol^{-1}), rotational constants (in MHz), and electric dipole components (in Debye) of the two most stable **Type 3** $(THFA)_2$ conformers calculated at the B3LYP-D3(BJ)/def2-TZVP level of theory.

conformer	ΔD_e	ΔD_0	*A*	*B*	*C*	$\lvert\mu_a\rvert$	$\lvert\mu_b\rvert$	$\lvert\mu_c\rvert$
RR I(Oc)-I(Oc)[a]	25.3	26.3	977	320	290	0.3	0.6	1.0
RS I(Oc)-I(Oc)[a]	24.2	24.8	963	343	314	0.0	0.0	0.0

[a] The ΔD_e and ΔD_0 values are relative to the global minimum RS I(Oc)-I(Oc).

Table 6.S5. Experimental spectroscopic constants[a] of the six THFA dimers observed.

	RR **III**(Oc)-**III**(Oc)	RR **I+**(Oe)-**III**(Oc)	RR **I**(Oc)-**III**(va)
A /MHz	1416.19705(26)	1113.38900(31)	884.99358(25)
B /MHz	190.25994(15)	241.82418(14)	291.83986(17)
C /MHz	187.57456(18)	217.36260(12)	260.04140(17)
D_K / kHz	1.844(25)	0.071(17)	0.6107(72)
D_{JK} / kHz	-0.1963(9)	0.013(2)	-0.366(3)
D_J / kHz	0.0109(2)	0.0106(4)	0.0908(8)
d_1 / kHz	-0.41(8)	-0.04(2)	0.21(4)
d_2 / kHz	-4.6E-4(3)	0.0013(2)	0.0108(4)
N	92	89	177
σ / kHz	2.8	4.4	6.3
	RR **I**(Oc)-**III**(vb)	RS **I**(Oc)-**III**(vb)	RS **I**(Oe)-**III**(Oc)
A /MHz	965.91323(35)	1039.13124(43)	1048.04605(41)
B /MHz	247.13957(19)	231.63946(19)	256.09287(26)
C /MHz	218.96286(18)	211.85513(16)	233.46374(19)
D_K / kHz	0.772(13)	0.329(23)	0.307(26)
D_{JK} / kHz	-0.3499(3)	0.014(3)	-0.059(4)
D_J / kHz	0.0859(8)	0.0122(5)	0.0312(8)
d_1 / kHz	0.24(3)	-0.17(4)	-0.032(5)
d_2 / kHz	0.0127(5)	9E-4(3)	0.0040(5)
N	64	102	52
σ / kHz	4	5.4	4.1

[a] A, B, C = rotational constants, N = number of transitions in the fit, and σ = standard deviation.

Table 6.S6. Measured transition frequencies of RR **III**(Oc)-**III**(Oc).

J'	K_a'	K_c'	J''	K_a''	K_c''	ν_{EXP} / MHz	$\Delta\nu$[a] / MHz
2	1	1	1	0	1	1986.9875	0.0092
2	2	1	1	1	1	4438.8301	0.0019
2	2	0	1	1	0	4436.1471	0.0015
3	1	2	2	0	2	2368.8495	0.0041
2	2	0	2	1	2	3685.8498	-0.0004
3	2	2	2	1	2	4819.3562	0.0033
2	2	1	2	1	1	3677.7830	-0.0017
3	2	1	2	1	1	4811.3165	0.0026
4	1	3	3	0	3	2752.0623	-0.0005
3	2	1	3	1	3	3689.9027	-0.0021
4	2	3	3	1	3	5201.2262	0.0055
3	2	2	3	1	2	3673.7595	-0.001
4	2	2	3	1	2	5185.1695	0.0047
5	1	4	4	0	4	3136.6394	0.0003
4	2	2	4	1	4	3695.3322	-0.001
5	2	4	4	1	4	5584.4366	0.0047
4	2	3	4	1	3	3668.3954	-0.0011
5	2	3	4	1	3	5557.7208	0.0048
6	1	5	5	0	5	3522.5864	0.0002
5	2	3	5	1	5	3702.1528	-0.0018
6	2	5	5	1	5	5968.9911	0.0041
6	2	4	5	1	4	5928.9951	0.0048
5	2	4	5	1	4	3661.6937	-0.0004
4	3	2	5	2	4	4247.1450	-0.0038
4	3	1	5	2	3	4246.9909	-0.0033
7	1	6	6	0	6	3909.9212	0.002
7	2	6	6	1	6	6354.8877	0.001
6	2	4	6	1	6	3710.3924	-0.0006
7	2	5	6	1	5	6299.0139	-0.0009
6	2	5	6	1	5	3653.6529	-0.0024
5	3	3	6	2	5	3869.3593	-0.0024
5	3	2	6	2	4	3869.0507	-0.0019
8	1	7	7	0	7	4298.6560	-0.0006
7	2	5	7	1	7	3720.0750	-0.002
7	2	6	7	1	6	3644.2798	-0.0023
6	3	4	7	2	6	3491.6006	-0.0012
6	3	3	7	2	5	3491.0453	-0.0002
7	3	5	7	2	5	6135.9333	0.0005
9	1	8	8	0	8	4688.8160	-0.004
8	2	6	8	1	8	3731.2388	-0.0012

8	2	7	8	1	7	3633.5753	-0.002
7	3	5	8	2	7	3113.8778	0.0002
8	3	5	8	2	7	6136.6138	0
7	3	4	8	2	6	3112.9530	0.0021
8	3	6	8	2	6	6135.6847	0.0006
10	1	9	9	0	9	5080.4307	-0.0036
9	2	7	9	1	9	3743.9193	-0.0009
9	2	8	9	1	8	3621.5425	-0.0013
10	0	10	9	1	8	2488.6996	-0.0022
9	3	6	9	2	8	6136.7863	0.0002
9	3	7	9	2	7	6135.3261	0.0018
11	1	10	10	0	10	5473.5247	-0.0029
10	2	8	10	1	10	3758.1580	-0.0022
10	2	9	10	1	9	3608.1828	-0.0023
11	0	11	10	1	9	2852.2837	-0.0055
10	3	7	10	2	9	6137.0196	0.0007
10	3	8	10	2	8	6134.8257	0.0007
12	1	11	11	0	11	5868.1258	-0.0051
11	2	9	11	1	11	3774.0054	-0.0021
11	2	10	11	1	10	3593.5033	-0.0018
12	0	12	11	1	10	3214.2949	-0.0049
11	3	8	11	2	10	6137.3256	-0.0001
11	3	9	11	2	9	6134.1558	0.0011
12	2	10	12	1	12	3791.5116	-0.0025
13	0	13	12	1	11	3574.6861	-0.0074
12	2	11	12	1	11	3577.5055	-0.0028
12	3	9	12	2	11	6137.7205	-0.0005
12	3	10	12	2	10	6133.2808	0.0018
13	2	11	13	1	13	3810.7339	-0.0023
13	2	12	13	1	12	3560.1978	-0.0016
14	0	14	13	1	12	3933.4233	-0.0037
13	3	10	13	2	12	6138.2205	-0.0006
13	3	11	13	2	11	6132.1621	0.0021
14	2	12	14	1	14	3831.7341	-0.0007
14	2	13	14	1	13	3541.5831	-0.001
14	3	12	14	2	12	6130.7590	0.0021
15	2	13	15	1	15	3854.5724	-0.0025
15	2	14	15	1	14	3521.6661	-0.0021
16	0	16	15	1	14	4645.7323	0.0049
15	3	12	15	2	14	6139.6053	-0.0022
15	3	13	15	2	13	6129.0288	0.0026
16	2	14	16	1	16	3879.3244	-0.0014
16	2	15	16	1	15	3500.4559	-0.0025

16	3	14	16	2	14	6126.9219	0.001
18	0	18	17	1	16	5350.8082	0.0065
17	2	16	17	1	16	3477.9625	0.0004
18	2	16	18	1	18	3934.8569	0.0009
18	2	17	18	1	17	3454.1860	-0.001
19	2	17	19	1	19	3965.7934	0.0005
19	2	18	19	1	18	3429.1420	0.0001
20	2	18	20	1	20	3998.9589	0.0039
20	2	19	20	1	19	3402.8379	0.0018

[a] $\Delta\nu = \nu_{CALC.} - \nu_{EXP.}$

Table 6.S7. Measured transition frequencies of RR **I+**(Oe)-**III**(Oc).

J'	K_a'	K_c'	J''	K_a''	K_c''	ν_{EXP} / MHz	$\Delta\nu$[a]/ MHz
2	2	0	1	1	1	3582.5969	-0.0046
2	2	1	1	1	0	3557.5233	-0.0046
3	2	1	2	1	2	4068.5012	0.0061
3	2	1	2	1	2	4068.4956	0.0005
3	2	2	2	1	1	3992.2521	0.0003
3	3	0	2	2	1	5796.9120	0.0071
3	3	1	2	2	0	5796.3880	0.0017
4	2	2	3	1	3	4569.6469	0.0004
4	2	3	3	1	2	4414.6195	0.0001
3	3	1	3	2	2	4419.0401	0.0008
4	3	1	3	2	2	6257.2341	0.0005
4	3	2	3	2	1	6254.6293	0.0005
3	3	0	3	2	1	4416.4887	0.0007
5	1	5	4	0	4	3000.1362	0.0021
5	2	3	4	1	4	5088.0959	0.0051
5	2	4	4	1	3	4824.6811	-0.0053
4	3	2	4	2	3	4420.4419	0.0007
5	3	3	4	2	2	6710.8957	0.0003
4	3	1	4	2	2	4412.8269	0.0028
6	1	6	5	0	5	3391.9915	-0.0006
6	2	4	5	1	5	5626.3117	-0.0057
6	2	5	5	1	4	5222.5756	0.003
5	3	3	5	2	4	4423.2694	0.0007
5	3	2	5	2	3	4405.6205	-0.0003
5	4	2	5	3	3	6184.7194	-0.0091
5	4	1	5	3	2	6184.5351	-0.0075
7	1	7	6	0	6	3776.6753	-0.0007
7	2	5	6	1	6	6187.1711	0.0009
6	2	5	6	1	6	2912.6897	-0.0049

7	2	6	6	1	5	5608.4767	0.0016
6	3	4	6	2	5	4428.1992	-0.0035
6	3	3	6	2	4	4393.2590	0.0043
6	4	3	6	3	4	6183.8290	-0.0065
6	4	2	6	3	3	6183.2790	-0.0003
8	1	8	7	0	7	4156.2504	-0.0008
8	2	6	7	1	7	6773.6995	0.0011
7	2	6	7	1	7	3000.9841	-0.0039
8	0	8	7	1	7	3043.3848	0.0071
8	2	7	7	1	6	5982.6862	-0.0011
7	3	5	7	2	6	4436.0250	0.0006
7	3	4	7	2	5	4373.9629	0.0039
7	4	4	7	3	5	6182.5380	0.0028
7	4	3	7	3	4	6181.1549	0.0046
9	1	9	8	0	8	4532.9496	-0.0021
9	0	9	8	1	8	3552.7534	-0.0001
9	2	8	8	1	7	6345.6192	-0.0015
8	3	6	8	2	7	4447.5973	-0.0005
8	3	5	8	2	6	4345.9790	0.0012
8	4	5	8	3	6	6180.7928	0.0006
8	4	4	8	3	5	6177.7628	0.0017
10	1	10	9	0	9	4909.0250	-0.0009
10	0	10	9	1	9	4059.0785	-0.0042
10	2	9	9	1	8	6697.8294	-0.002
9	3	7	9	2	8	4463.8415	-0.007
9	3	6	9	2	7	4307.7743	0.0089
9	4	6	9	3	7	6178.6241	0.0028
9	4	5	9	3	6	6172.5993	0.0019
11	1	11	10	0	10	5286.5567	-0.0033
11	0	11	10	1	10	4560.6139	0.002
10	3	8	10	2	9	4485.7360	-0.0064
10	3	7	10	2	8	4258.2008	-0.0088
10	4	7	10	3	8	6176.1008	-0.0027
10	4	6	10	3	7	6165.0003	-0.0038
12	1	12	11	0	11	5667.3164	0.0036
12	0	12	11	1	11	5056.0552	-0.0134
12	1	11	11	2	10	3731.4640	0.0011
11	3	9	11	2	10	4514.2644	0.0013
11	3	8	11	2	9	4196.8434	-0.0016
11	4	8	11	3	9	6173.4013	-0.001
11	4	7	11	3	8	6154.1760	0.0108
13	1	13	12	0	12	6052.5954	-0.0007
13	0	13	12	1	12	5544.7209	0.0147

12	3	10	12	2	11	4550.3977	0.0085
13	1	12	12	2	11	4317.4254	-0.0046
12	4	9	12	3	10	6170.7742	-0.0024
12	4	8	12	3	9	6139.0995	0.0088
14	1	14	13	0	13	6443.2245	-0.0004
13	2	12	13	1	13	3807.2530	-0.0019
14	0	14	13	1	13	6026.2742	-0.0001
13	3	11	13	2	12	4595.0747	0.0019
14	1	13	13	2	12	4906.1311	0.0014
13	3	10	13	2	11	4040.9538	-0.0023
13	4	10	13	3	11	6168.5958	0.0055
15	1	15	14	0	14	6839.5425	-0.0002
14	3	11	14	2	12	3949.7900	0.0006
14	4	11	14	3	12	6167.3163	-0.0021
15	4	12	15	3	13	6167.5428	-0.0044
16	3	14	16	2	15	4789.1660	0.0011
16	4	13	16	3	14	6169.9653	-0.0051

[a] $\Delta\nu = \nu_{CALC.} - \nu_{EXP.}$

Table 6.S9. Measured transition frequencies of RR **I**(Oc)-**III**(va).

J'	K_a'	K_c'	J''	K_a''	K_c''	ν_{EXP} / MHz	$\Delta\nu^{[a]}$/ MHz
2	2	1	1	1	1	2946.8050	-0.0111
2	2	0	1	1	1	2948.0515	-0.009
2	2	1	1	1	0	2915.0107	-0.0079
3	2	1	2	1	2	3536.6961	-0.008
3	2	2	2	1	2	3530.4856	-0.0095
3	2	1	2	1	1	3441.3044	-0.0076
3	2	2	2	1	1	3435.0946	-0.0084
3	3	0	2	2	1	4701.6825	-0.0007
3	3	1	2	2	0	4700.4057	-0.0027
4	1	3	3	0	3	2978.3770	-0.0019
4	2	3	3	1	3	4129.8544	-0.0084
4	2	2	3	1	3	4148.3936	-0.007
4	2	2	3	1	2	3957.6418	-0.0067
4	2	3	3	1	2	3939.1042	-0.0065
4	3	1	3	2	2	5256.1497	-0.0007
4	3	2	3	2	2	5255.9370	-0.0004
3	3	0	3	2	1	3039.8267	-0.0047
4	3	1	3	2	1	5249.9410	-0.0004
4	3	2	3	2	1	5249.7250	-0.0034
5	1	4	4	0	4	3616.2883	-0.0019
5	1	5	4	0	4	3140.1968	0.0007

5	2	4	4	1	4	4744.9550	-0.0069
5	2	3	4	1	4	4787.8140	-0.0082
5	1	5	4	1	4	2674.7486	0.0046
5	1	4	4	1	3	2833.0862	0.0026
5	2	3	4	1	3	4470.0602	-0.0076
4	3	2	4	2	3	3049.3861	-0.0055
5	3	3	4	2	3	5812.7492	-0.0018
5	3	2	4	2	3	5813.6020	0.0004
4	3	1	4	2	3	3049.5987	-0.006
5	3	2	4	2	2	5795.0626	-0.0012
5	3	3	4	2	2	5794.2113	-0.0019
4	4	1	4	3	2	4261.1337	0.0131
4	4	1	4	3	1	4260.9211	0.0135
6	1	6	5	0	5	3611.8641	0.0008
6	1	5	5	0	5	4277.0281	-0.0025
6	0	6	5	0	5	3269.6284	0.0053
6	1	6	5	1	5	3206.7041	0.0036
6	2	4	5	1	5	5460.2689	-0.0092
6	2	5	5	1	5	5375.8454	-0.0087
6	0	6	5	1	5	2864.4691	0.0087
6	2	5	5	1	4	4899.7520	-0.008
6	1	5	5	1	4	3395.7795	0.0058
6	2	4	5	1	4	4984.1771	-0.0069
5	3	3	5	2	4	3056.1322	-0.0067
6	3	4	5	2	4	6373.4034	-0.0033
6	2	5	5	2	4	3305.6405	0.0043
6	3	3	5	2	4	6375.9492	-0.0018
6	2	4	5	2	3	3347.2052	0.0053
6	3	3	5	2	3	6333.0906	-0.0001
5	3	2	5	2	3	3014.1227	-0.0065
6	3	4	5	2	3	6330.5436	-0.0027
5	4	2	5	3	3	4259.9561	0.0119
6	3	4	5	3	3	3317.2706	0.0029
5	4	2	5	3	2	4259.1067	0.0132
5	4	1	5	3	2	4259.1112	0.0121
6	3	3	5	3	2	3318.9646	0.0032
6	4	3	5	4	2	3315.5024	0.0005
6	4	2	5	4	1	3315.5253	0.0012
6	5	2	5	5	1	3314.4270	-0.0021
6	5	1	5	5	0	3314.4270	-0.0022
7	1	7	6	0	6	4079.5139	-0.0001
7	0	7	6	0	6	3798.8695	0.0053
7	0	7	6	1	6	3456.6319	0.0079

7	1	7	6	1	6	3737.2760	0.0022
7	2	6	6	1	5	5357.3990	-0.0053
7	1	6	6	1	5	3956.0472	0.0068
7	2	5	6	1	5	5505.9271	-0.0072
7	2	6	6	2	5	3853.4223	0.0043
7	3	4	6	2	5	6945.7001	-0.003
6	3	4	6	2	5	3067.7623	-0.0082
7	3	5	6	2	4	6854.9447	-0.0036
6	3	3	6	2	4	2985.8823	-0.0085
7	2	5	6	2	4	3917.5311	0.0071
6	4	2	6	3	4	4258.2169	0.0108
7	3	5	6	3	4	3871.6055	0.0037
6	4	3	6	3	4	4258.1889	0.0106
6	4	2	6	3	3	4255.6730	0.0112
6	4	3	6	3	3	4255.6459	0.0119
6	5	2	6	4	3	5477.7243	0.0118
6	5	2	6	4	2	5477.6959	0.0112
8	0	8	7	0	7	4323.3172	0.004
8	1	8	7	0	7	4547.0680	-0.0014
8	1	7	7	0	7	5677.8412	0.0018
8	1	8	7	1	7	4266.4240	0.0044
8	0	8	7	1	7	4042.6728	0.0094
8	1	7	7	1	6	4513.2587	0.0029
8	2	6	7	1	6	6041.0040	-0.0041
8	2	7	7	1	6	5801.1206	-0.0094
8	2	7	7	2	6	4399.7704	0.0043
7	3	5	7	2	6	3085.9451	-0.0092
8	2	6	7	2	5	4491.1169	0.0027
7	3	4	7	2	5	2943.7428	-0.0123
8	3	6	7	3	5	4426.2490	0.0026
7	4	4	7	3	5	4255.8761	0.0085
7	4	3	7	3	4	4249.6492	0.0108
8	3	5	7	3	4	4433.7468	0.0023
8	4	5	7	4	4	4423.6141	0.001
8	4	4	7	4	3	4423.8179	0.0021
8	5	4	7	5	3	4421.0960	-0.0003
8	5	3	7	5	2	4421.0996	0.0008
7	6	2	7	5	2	6695.5441	-0.01
7	6	1	7	5	2	6695.5460	-0.0081
8	6	3	7	6	2	4419.7642	-0.0023
8	6	2	7	6	1	4419.7642	-0.0023
8	7	2	7	7	1	4419.0118	-0.0053
8	7	1	7	7	0	4419.0118	-0.0053

9	1	9	8	0	8	5017.9150	0.0035
9	0	9	8	0	8	4844.0476	0.0056
9	0	9	8	1	8	4620.2963	0.0105
9	1	9	8	1	8	4794.1617	0.0064
9	2	8	8	1	7	6232.3691	-0.0084
9	1	8	8	1	7	5066.7214	0.004
9	2	8	8	2	7	4944.5080	0.0048
9	2	7	8	2	6	5066.6450	0.0017
8	4	4	8	3	6	4253.5464	0.0078
9	3	7	8	3	6	4981.0291	0.0042
8	4	5	8	3	6	4253.2418	0.0075
9	3	6	8	3	5	4994.5724	0.0021
8	4	4	8	3	5	4239.7180	0.0083
9	4	6	8	4	5	4978.5204	0.0036
9	4	5	8	4	4	4979.0025	0.0016
9	5	5	8	5	4	4975.0024	0.0005
8	6	3	8	5	4	6694.2124	-0.0126
8	6	2	8	5	3	6694.2089	-0.0129
9	5	4	8	5	3	4975.0102	0.0002
9	6	4	8	6	3	4973.0893	-0.0011
9	6	3	8	6	2	4973.0893	-0.0012
10	1	10	9	0	9	5494.4319	0.0104
10	0	10	9	1	9	5188.4848	0.0133
10	1	10	9	1	9	5320.5598	0.0078
10	2	9	9	1	8	6653.1229	-0.0088
10	1	9	9	1	8	5615.6852	0.0021
10	2	9	9	2	8	5487.4732	0.0016
10	2	8	9	2	7	5642.5386	0.0018
9	4	5	9	3	7	4251.5175	0.0028
9	4	6	9	3	7	4250.7309	0.0047
10	3	8	9	3	7	5535.7100	0.0027
9	4	5	9	3	6	4224.1520	0.0117
9	5	5	9	4	6	5469.9792	0.001
10	4	7	9	4	6	5534.0327	0.0018
9	5	4	9	4	5	5469.2031	0.002
10	4	6	9	4	5	5535.0740	0.0006
9	6	4	9	5	5	6692.3057	-0.0078
9	6	3	9	5	4	6692.2935	-0.0088
11	0	11	10	0	10	5879.3995	0.0038
11	1	11	10	0	10	5977.8061	0.0029
11	0	11	10	1	10	5747.3234	0.0082
11	1	11	10	1	10	5845.7263	0.0036
11	2	10	10	2	9	6028.5330	-0.0071

10	4	7	10	3	8	4249.0521	0.0023
11	3	9	10	3	8	6090.0170	-0.0066
10	4	6	10	3	8	4250.8827	0.002
10	4	6	10	3	7	4200.7765	0.0064
11	3	8	10	3	7	6125.9020	-0.0013
10	5	5	10	4	7	5465.3397	0.0041
11	4	8	10	4	7	6090.1500	-0.0074
10	5	6	10	4	7	5465.3036	0.0018
10	5	6	10	4	6	5463.4774	0.0066
11	4	7	10	4	6	6092.2180	-0.0071
10	5	5	10	4	6	5463.5117	0.0071
12	0	12	11	0	11	6396.0819	-0.0025
12	1	12	11	1	11	6369.8070	-0.0006
12	0	12	11	1	11	6297.6776	0.0007
11	4	8	11	3	9	4249.1816	-0.002
11	4	7	11	3	9	4253.0793	-0.003
11	4	7	11	3	8	4167.0977	0.0058
11	5	7	11	4	8	5459.3488	0.0032
13	0	13	12	0	12	6912.9280	-0.0103
13	1	13	12	0	12	6965.0805	-0.0103
12	4	8	12	3	9	4120.4714	0.0056
12	5	8	12	4	9	5452.0698	0.0015
12	5	7	12	4	8	5444.5554	0.0025
13	4	9	13	3	10	4058.5066	0.0022
13	5	9	13	4	10	5443.5410	0.0001
13	5	8	13	4	9	5429.5670	-0.0092
14	5	10	14	4	11	5433.9850	0.0004

[a] $\Delta\nu = \nu_{CALC.} - \nu_{EXP.}$

Table 6.S10. Measured transition frequencies of RR **I**(Oc)-**III**(vb).

J'	K_a'	K_c'	J''	K_a''	K_c''	ν_{EXP} / MHz	$\Delta\nu$[a]/ MHz
3	2	1	2	1	2	3643.2062	-0.0002
3	2	2	2	1	1	3554.6238	-0.0002
4	2	2	3	1	3	4159.5183	0.0018
4	2	3	3	1	2	3978.3433	-0.0009
4	3	1	3	2	2	5530.8724	-0.0049
4	3	2	3	2	1	5526.7216	0.0028
5	1	4	4	0	4	3280.8904	-0.0018
5	2	3	4	1	3	4416.1262	-0.0022
6	1	6	5	0	5	3250.1890	-0.0033
6	1	5	5	0	5	3840.6122	-0.0001
5	3	3	5	2	4	3671.4702	0.0012

5	3	2	5	2	3	3643.7038	0.0003
5	4	1	5	3	2	5127.2806	0.0024
7	1	7	6	0	6	3635.5958	-0.0013
7	1	6	6	0	6	4421.3840	0.0022
7	2	6	6	1	5	5165.8163	-0.0142
6	3	4	6	2	5	3679.2094	0.0031
6	3	3	6	2	4	3624.5648	0.0017
6	4	3	6	3	4	5126.4020	-0.0042
6	4	2	6	3	3	5125.1900	-0.0004
8	0	8	7	0	7	3665.4669	-0.0007
8	1	8	7	0	7	4017.9038	-0.0028
8	1	8	7	1	7	3601.4998	-0.0007
8	0	8	7	1	7	3249.0608	-0.0008
8	2	7	7	1	6	5535.0056	0.0071
8	1	7	7	1	6	3823.2120	-0.0005
8	2	7	7	2	6	3718.7750	-0.0008
7	3	5	7	2	6	3691.3921	0.0006
8	2	6	7	2	5	3781.8791	-0.0006
7	3	4	7	2	5	3595.2016	0.0049
8	3	6	7	3	5	3736.6730	-0.0011
8	3	5	7	3	4	3740.3143	-0.0011
9	0	9	8	0	8	4108.0113	0.0016
9	0	9	8	1	8	3755.5659	-0.0048
9	1	9	8	1	8	4047.6754	0.0018
9	1	8	8	1	7	4294.5571	0.0014
9	2	8	8	2	7	4180.1609	0.0003
9	2	7	8	2	6	4266.6513	0.0012
9	3	7	8	3	6	4205.0907	0.001
9	3	6	8	3	5	4211.7141	0.0009
9	4	6	8	4	5	4202.4970	0.0002
8	5	4	8	4	5	6590.4399	-0.0028
8	5	3	8	4	4	6590.3361	0.0005
9	4	5	8	4	4	4202.6691	0.0002
9	5	5	8	5	4	4200.1589	-0.0006
9	5	4	8	5	3	4200.1610	-0.0006
10	0	10	9	0	9	4547.4871	0.0193
10	1	10	9	1	9	4492.7636	-0.0019
10	2	9	9	2	8	4640.3550	0.0026
10	3	8	9	3	7	4673.6384	-0.0016
9	5	5	9	4	6	6588.1040	-0.0014
10	4	7	9	4	6	4671.0176	0.0039
9	5	4	9	4	5	6587.8336	0.0052
10	4	6	9	4	5	4671.3916	0.0063

10	5	6	9	5	5	4667.8510	-0.0006
10	5	5	9	5	4	4667.8570	-0.0005
10	6	5	9	6	4	4666.1514	-0.0014
10	6	4	9	6	3	4666.1514	-0.0015
11	1	11	10	0	10	5174.2119	0.0001
12	1	12	11	0	11	5569.4169	0.0014
11	3	8	11	2	10	3852.9684	0.0001
11	3	9	11	2	9	3307.5033	0.0007
11	4	8	11	3	8	5072.3983	-0.0039
13	0	13	12	1	12	5706.5320	-0.0101

[a] $\Delta\nu = \nu_{CALC.} - \nu_{EXP.}$

Table 6.S11. Measured transition frequencies of RS **I**(Oc)-**III**(vb).

J'	K_a'	K_c'	J''	K_a''	K_c''	ν_{EXP} / MHz	$\Delta\nu^{[a]}$/ MHz
3	2	1	2	1	2	3814.1009	-0.0004
3	2	2	2	1	1	3752.9493	-0.002
3	3	0	2	2	1	5417.6043	-0.0019
3	3	1	2	2	0	5417.2417	-0.0012
4	2	3	3	1	2	4166.7203	0.007
3	3	1	3	2	2	4087.1205	0.0005
4	3	1	3	2	2	5861.8291	0.0001
4	3	2	3	2	1	5860.0056	0.0001
3	3	0	3	2	1	4085.3294	0.0003
5	2	3	4	1	4	4780.9122	-0.0024
5	2	4	4	1	3	4570.5644	-0.0026
5	3	2	4	2	3	6306.8773	0.0001
4	3	1	4	2	2	4082.7552	0.0007
5	3	3	4	2	2	6301.3838	0.0001
4	4	1	4	3	2	5720.9806	0.002
4	4	0	4	3	1	5720.9521	0.002
6	1	6	5	0	5	3277.9002	-0.0061
6	2	4	5	1	5	5286.2166	-0.0024
6	2	5	5	1	4	4964.5918	-0.001
5	3	3	5	2	4	4090.0981	0.0026
5	3	2	5	2	3	4077.6840	0.0011
5	4	2	5	3	3	5720.5839	0.0001
5	4	1	5	3	2	5720.4724	0.0022
7	1	7	6	0	6	3660.1226	-0.0041
7	0	7	6	0	6	3084.7021	-0.0084
7	2	5	6	1	6	5808.7594	0.0001
7	2	6	6	1	5	5348.9221	-0.0002
7	1	6	6	1	5	3168.7121	-0.004

6	3	4	6	2	5	4093.5782	0.0044
6	3	3	6	2	4	4068.9505	0.0014
6	4	3	6	3	4	5719.9436	0.0024
6	4	2	6	3	3	5719.6034	0.0024
8	1	8	7	0	7	4037.5258	0.0004
8	0	8	7	0	7	3518.7083	-0.0013
8	1	8	7	1	7	3462.1095	0.0002
8	0	8	7	1	7	2943.2904	-0.003
8	2	7	7	1	6	5723.7495	-0.0003
8	1	7	7	1	6	3619.3672	0.004
7	3	5	7	2	6	4099.1055	0.0066
8	2	7	7	2	6	3543.5421	-0.0015
8	2	6	7	2	5	3572.7474	-0.0058
7	3	4	7	2	5	4055.2574	0.0015
7	4	4	7	3	5	5718.9958	0.0026
9	0	9	8	0	8	3950.4173	-0.0033
9	0	9	8	1	8	3431.6020	-0.0027
9	1	9	8	1	8	3892.9257	0.0023
9	2	8	8	1	7	6089.3452	0.0001
9	1	8	8	1	7	4069.1141	-0.0002
8	3	6	8	2	7	4107.2891	-0.0033
9	2	8	8	2	7	3984.9621	0.0035
8	3	5	8	2	6	4035.2635	0.0013
9	2	7	8	2	6	4025.9269	0.0035
8	4	5	8	3	6	5717.7033	0.0029
9	3	7	8	3	6	3996.4872	-0.0061
8	4	4	8	3	5	5715.8400	-0.003
9	3	6	8	3	5	3998.3627	0.001
9	5	5	8	5	4	3993.7773	0.0107
9	5	4	8	5	3	3993.7776	0.0107
10	1	10	9	0	9	4784.4699	-0.0013
10	1	9	9	1	8	4517.8045	-0.0004
10	2	9	9	2	8	4425.8448	0.0055
9	3	7	9	2	8	4118.8348	0.0077
9	3	6	9	2	7	4007.7015	0.001
9	4	6	9	3	7	5716.0750	0.0223
9	4	5	9	3	6	5712.3550	-0.0021
10	3	7	9	3	6	4444.6186	0.0043
10	4	7	9	4	6	4439.4553	0.0035
10	4	6	9	4	5	4439.5209	0.0034
11	0	11	10	1	10	4402.6307	-0.0019
11	1	11	10	1	10	4752.7846	0.0009
10	3	8	10	2	9	4134.3990	-0.0136

11	2	10	10	2	9	4866.1359	0.0052
11	2	9	10	2	8	4937.1496	0.0037
10	3	7	10	2	8	3971.5161	-0.002
10	4	7	10	3	8	5714.0770	-0.0028
11	3	8	10	3	7	4891.6562	0.004
10	4	6	10	3	7	5707.2391	-0.0212
12	0	12	11	0	11	5232.7611	0.003
12	1	12	11	0	11	5531.9670	-0.0004
12	1	12	11	1	11	5181.8184	0.0022
12	1	11	11	1	10	5411.2622	-0.0023
12	2	11	11	2	10	5305.7757	-0.0049
11	3	9	11	2	10	4154.7746	-0.0061
11	3	8	11	2	9	3926.0268	0.0024
12	2	10	11	2	9	5394.6229	-0.0054
11	4	8	11	3	9	5711.8509	-0.0116
11	4	7	11	3	8	5700.0148	-0.006
13	1	13	12	0	12	5909.4701	0.0001
13	0	13	12	0	12	5656.8004	-0.0089
13	2	12	12	2	11	5744.7397	0.0001
12	4	9	12	3	10	5709.5387	-0.0034
12	4	8	12	3	9	5689.9825	-0.008
14	1	14	13	0	13	6290.7995	0.0001
14	0	14	13	1	13	5827.1018	0.0001
14	1	13	13	1	12	6298.1273	0.0001
13	3	10	13	2	11	3806.8999	-0.0023
13	4	10	13	3	11	5707.3472	0.0183
13	4	9	13	3	10	5676.4002	0.0023
15	0	15	14	1	14	6290.9457	0.0001
14	3	11	14	2	12	3734.6909	0.0049
14	4	10	14	3	11	5658.3513	0.0037
15	4	11	15	3	12	5634.8254	-0.007

[a] $\Delta\nu = \nu_{CALC.} - \nu_{EXP.}$

Table 6.S12. Measured transition frequencies of RS **I**(Oe)-**III**(Oc).

J'	K_a'	K_c'	J''	K_a''	K_c''	ν_{EXP} / MHz	$\Delta\nu$[a]/ MHz
3	2	1	2	1	2	3914.7995	-0.0007
3	2	2	2	1	1	3844.5141	-0.0097
3	3	0	2	2	1	5485.2938	0.0016
3	3	1	2	2	0	5484.8094	0.0016
4	2	2	3	1	3	4442.9908	0.0023
4	2	3	3	1	2	4300.0648	0.0008
4	3	1	3	2	2	5975.8261	0.0038

4	3	2	3	2	1	5973.3883	-0.001
5	1	5	4	0	4	3085.2258	0.0079
5	2	3	4	1	4	4987.1700	0.002
5	2	4	4	1	3	4744.2704	0.0001
5	3	2	4	2	3	6467.4573	0.0004
5	3	3	4	2	2	6460.1242	0.0003
6	1	6	5	0	5	3512.7266	0.001
6	2	4	5	1	5	5549.6596	0.0003
6	2	5	5	1	4	5177.2534	-0.0013
5	3	3	5	2	4	4020.5743	0.0015
5	3	2	5	2	3	4004.0930	-0.004
7	1	7	6	0	6	3933.6880	0.0038
7	2	5	6	1	6	6133.1087	-0.005
7	2	6	6	1	5	5599.1970	0.007
6	3	4	6	2	5	4025.1892	-0.0058
6	3	3	6	2	4	3992.5563	-0.0044
6	4	3	6	3	4	5620.6261	0.0059
6	4	2	6	3	3	5620.1100	0.001
8	1	8	7	0	7	4350.0186	-0.0027
7	3	5	7	2	6	4032.4833	0.0007
7	3	4	7	2	5	3974.5724	0.0008
7	4	4	7	3	5	5619.4290	-0.0012
7	4	3	7	3	4	5618.1165	0.0005
9	1	9	8	0	8	4763.8017	-0.0052
9	0	9	8	1	8	3880.1430	-0.001
9	2	8	8	1	7	6411.1977	-0.0028
8	3	6	8	2	7	4043.2855	-0.0091
8	3	5	8	2	6	3948.4933	-0.0012
8	4	4	8	3	5	5614.9491	-0.0003
10	1	10	9	0	9	5177.1154	0.0054
9	3	7	9	2	8	4058.4368	-0.0011
9	4	5	9	3	6	5610.1240	0.0014
11	1	11	10	0	10	5591.8801	0.0037
10	3	8	10	2	9	4078.8703	0.0003
10	4	7	10	3	8	5613.5088	-0.0055
10	4	6	10	3	7	5603.0069	0.0024
12	1	12	11	0	11	6009.6974	0.0015
12	0	12	11	1	11	5462.1025	0.0138
11	3	9	11	2	10	4105.4581	-0.0025
11	3	8	11	2	9	3809.9510	-0.0061
11	4	8	11	3	9	5611.0358	0.0001
11	4	7	11	3	8	5592.8410	0.0035
13	1	13	12	0	12	6431.7616	0.0003

12	4	8	12	3	9	5578.7101	-0.0035
14	0	14	13	1	13	6486.9748	0.0006
13	4	10	13	3	11	5606.7284	-0.0007
13	4	9	13	3	10	5559.4972	-0.0097
14	4	11	14	3	12	5605.6802	0.0016

[a] $\Delta v = v_{CALC.} - v_{EXP.}$

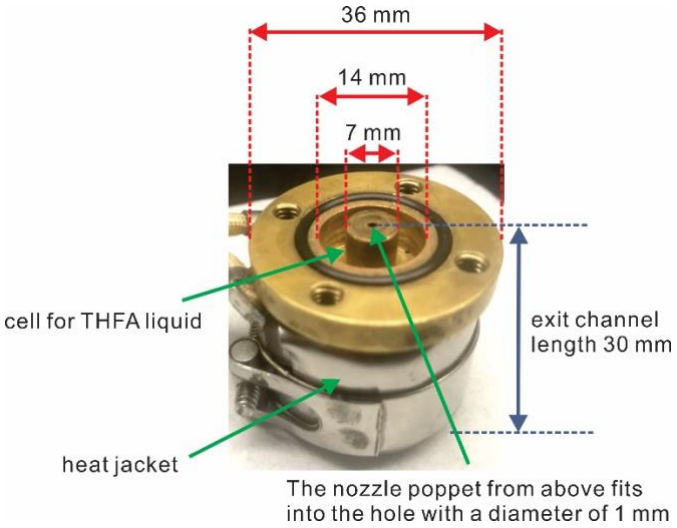

Figure 6.S1. The dimensions of the modified General Valve nozzle cap.

Point 6.S1. Experiments with different carrier gases and source temperatures

These experiments were carried out with three different carrier gasses, i.e. helium, neon, and a mixture of 10% argon with helium at 3 bar, and at four different nozzle temperatures: 26 °C, 56 °C, 86 °C, and 116 °C in neon at 3 bar. To ensure that the experimental conditions remained exactly the same except for the change of carrier gas or the nozzle temperature, these experiments were performed consecutively without additional filling of THFA.

The boiling temperature of THFA is ~135°C. It is very difficult for us to complete the large number of averaging cycles needed while maintaining stable experimental conditions if the nozzle temperature is raised much higher than 116 °C.

For the carrier gas and nozzle temperature experiments, 300 K and 150 K FIDs were collected, respectively.

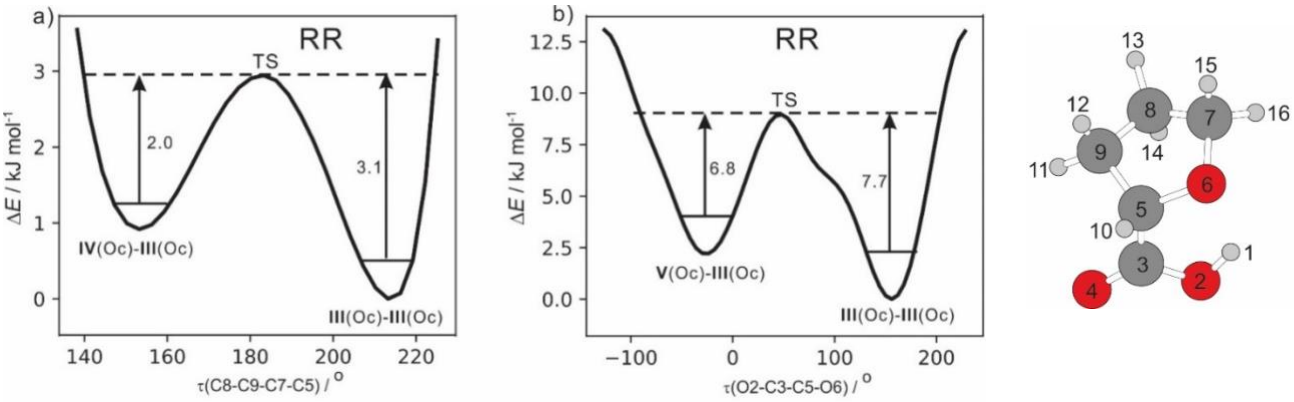

Figure 6.S2. Examples of several potential energy scans of possible relaxation pathways among some **Type 1** conformers of the THFA dimer: a) PES profile along the □(C8-C9-C7-C6) coordinate of the monomer **III** subunit between RR **IV**(Oc)-**III**(Oc) and RR **III**(Oc)-**III**(Oc) and b) PES profile along the □(O2-C3-C5-O6) coordinate of the monomer **III** subunit between RR **V**(Oc)-**III**(Oc) and RR **III**(Oc)-**III**(Oc). Atom numbering is shown on the right side.

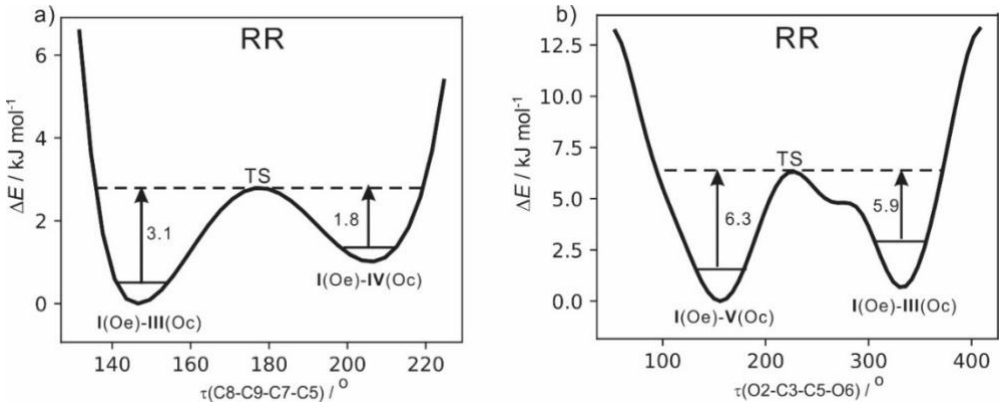

Figure 6.S3. Example potential energy scans of relaxation pathways among **Type 2** $(THFA)_2$ conformers belonging to the *same* subcategory: a) the PES profile from RR **I**(Oe)-**III**(Oc) to RR I(Oe)-**IV**(Oc) and b) the PES profile from RR **I**(Oe)-**V**(Oc) to RR **I**(Oe)-**III**(Oc). We note that RR **I**(Oe)-**V**(Oc) and RR **I**(Oe)-**III**(Oc) are quite close in energy. The energy ordering may easily switch if another level of theory were used. See Table S3, footnote d, for details. Atom numbering is shown in Figure S1.

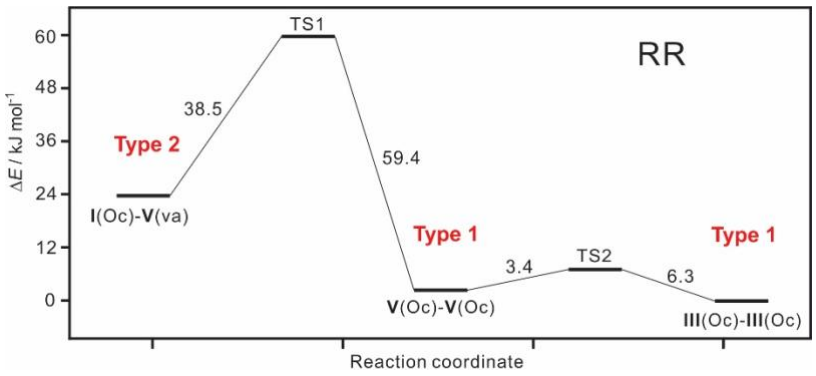

Figure 6.S4. Example transition state calculation along possible relaxation pathways among some **Type 1** and **Type 2** conformers of the THFA dimer. Generally, the conversion barriers between **Type 1** and **Type 2** conformers are very high (>> 30 kJ mol^{-1}) and no interconversion is expected between them in a supersonic jet expansion. All higher energy **Type 1** conformers are expected to cool to the lowest energy one, RR **III**(Oc)-**III**(Oc), since the conversion barriers are small as shown here and in Figure S1.

To search for a transition state for **Type 3** to **Type 2** or **Type 1** proved to be very difficult because **Type 3** which contains two *trans* subunits are quite loosely bound and the conversions to other types involve motions of many atoms. Based on the *trans* to *cis* conversion barriers in the THFA monomer (Ref. 4) and in the conversion of **Type 2** to **Type 1** where one subunit flips from *trans* to *cis*, we estimate that the conversion barriers from the *most stable* **Type 3 I-I** to a **Type 2** structure would be in the range of ~40 kJ mol^{-1}. A direct conversion of the most stable **Type 3 I-I** structure to a **Type 1** structure involves flipping both *trans* subunits to *cis*, not likely to happen in the current jet expansion.

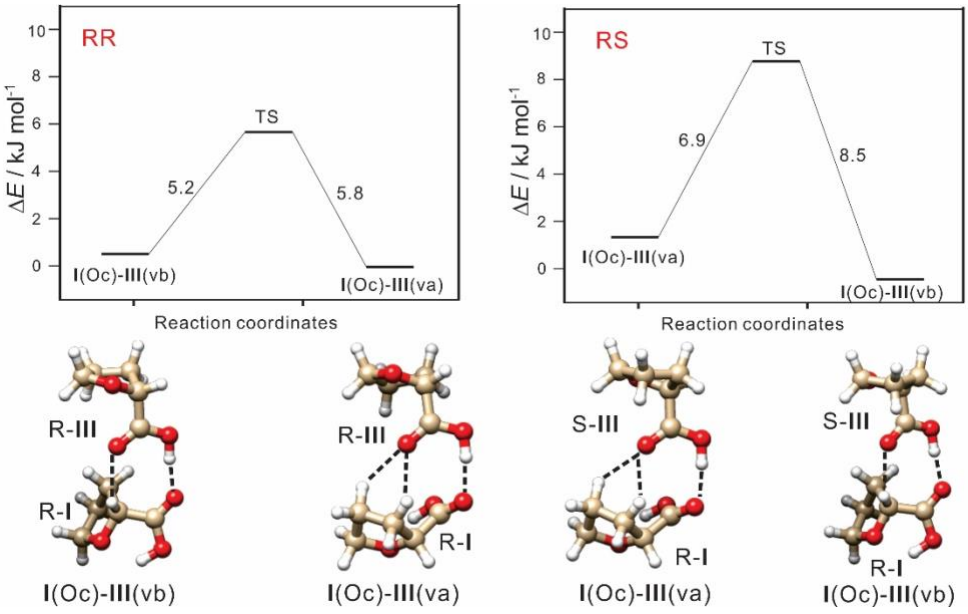

Figure 6.S5. Role of chirality in the conformational preferences in two homochiral $(THFA)_2$ in comparison to the corresponding heterochiral $(THFA)_2$. A transition state calculation along a possible relaxation pathway from RR **I**(Oc)-**III**(vb) to RR **I**(Oc)-**III**(va) (left) versus a related one from RS **I**(Oc)-**III**(va) to RS **I**(Oc)-**III**(vb) (right).

Point 6.S2. Chiral analyses

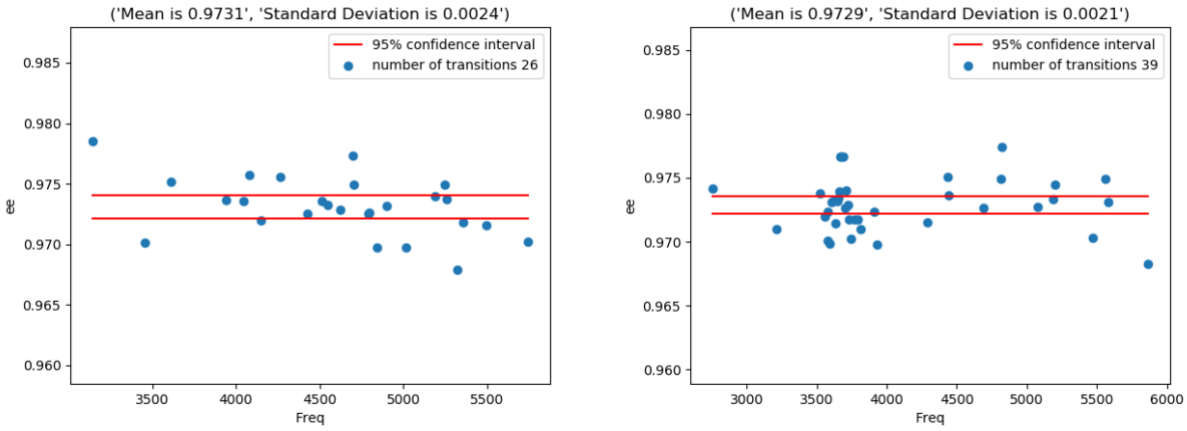

Two ee analyses using the chiral self-tag method for THFA are shown. Here, $ee_{sample} = ee_{tag} = [(1-R)/(1+R)]^{1/2}$ where R is the intensity ratio between a heterochiral and a homochiral ratio measured using R-THFA. The R value needs to be normalized by measuring the same pair of transitions using racemic THFA. In the left, a strong heterochiral transition, 7_{17}-6_{06} of RS **I**(Oc)-**III**(vb) at 3933.6842 MHz, was selected and a homochiral transition was selected from 26 lines of RR **I**(Oc)-**III**(va) with s/n ratio larger than 5. We obtained ee ≥ 0.9731(24). The same analysis with 39 lines of RR **III**(Oc)-**III**(Oc) with s/n ratio larger than 5, we obtained ee ≥ 0.9729(21). As indicated in the main text and in Figure 7, the ee of R-THFA is very high and we could not detect even the strongest heterochiral transition. Its intensity is set to the same as the noise level to obtain R. This is the reason for "≥" in the ee values obtained.

Appendix E

Supporting Information for Chapter 7

Discovering the Elusive Global Minimum in a Ternary Chiral Cluster: Rotational Spectra of Propylene Oxide Trimer

Contents:

8. Point 7.S3 Details of the hybrid approach for evaluating harmonic and anharmonic contributions

9. Table 7.S13-S30 Results of B2/B3 and rPP calculations for HOMO1 and HETERO1

10. Table 7.S31-S34 Equilibrium and semi-experimental equilibrium structural parameters of HOMO1 and HETERO1

11. Completion of reference 16

Table 7.S1. The theoretical raw (ΔD_e) and *ZPE* corrected (ΔD_0) relative dissociation energy (kJ mol^{-1}), rotational constants (MHz) and electric dipole moments (Debye) of homochiral PO trimers within a window of 5 kJ mol^{-1} at the B3LYP-D3BJ/def2-TZVP level of theory.

Conformer	ΔD_e	ΔD_0	*A*	*B*	*C*	$\lvert\mu_a\rvert$	$\lvert\mu_b\rvert$	$\lvert\mu_c\rvert$
HOMO1[a]	**0.8**	**0.0**	**829**	**648**	**434**	**0.7**	**1.6**	**0.8**
HOMO2[a]	**0.0**	**0.4**	**791**	**644**	**471**	**1.1**	**0.2**	**1.4**
HOMO3	1.2	1.1	784	654	422	0.9	1.1	1.0
HOMO4	1.9	1.2	763	655	445	1.0	0.2	1.5
HOMO5	1.9	1.2	795	618	449	0.1	1.2	0.1
HOMO6	2.0	1.2	758	669	394	1.5	0.1	1.0
HOMO7	2.4	2.1	926	553	422	1.1	0.1	1.5
HOMO8	3.4	2.6	861	538	400	0.9	0.1	0.8
HOMO9	3.6	2.8	812	551	384	2.1	0.6	0.3
HOMO10	3.2	2.9	939	562	420	1.0	0.1	1.2
HOMO11	4.1	2.9	680	680	448	0.0	0.0	0.7
HOMO12	4.2	3.0	761	587	368	2.3	0.7	0.4
HOMO13	4.1	3.5	1463	328	318	0.2	1.4	1.2
HOMO14	4.1	3.5	814	623	428	0.9	0.1	1.4
HOMO15	4.9	3.6	774	639	420	2.0	0.4	0.2
HOMO16	4.8	3.6	702	626	383	0.6	1.1	1.6
HOMO17	5.2	3.6	880	560	393	0.2	2.0	0.5
HOMO18	4.3	3.7	1382	335	302	0.1	1.7	0.8
HOMO19	4.5	3.7	1452	320	293	0.3	1.3	1.2
HOMO20	4.5	3.7	883	577	442	1.4	0.0	1.2
HOMO21	4.4	3.7	786	568	374	1.3	0.2	1.5
HOMO22	4.9	3.8	1549	330	299	0.5	1.2	1.6
HOMO23	5.8	4.3	926	548	407	0.1	1.6	0.3

HOMO24	5.8	4.4	916	550	407	0.1	1.6	0.4
HOMO25	6.1	4.4	905	500	378	0.5	1.2	0.9
HOMO26	5.9	5.0	1010	497	394	0.7	1.6	0.6

[a] The red color indicates the conformers detected experimentally.

Table 7.S2. The theoretical raw (ΔD_e) and *ZPE* corrected (ΔD_0) relative dissociation energy (kJ mol^{-1}), rotational constants (MHz) and electric dipole moments (Debye) of homochiral PO trimers within a window of 5 kJ mol^{-1} at the B3LYP-D3BJ/def2-TZVP level of theory.[a]

Conformer	ΔD_e	ΔD_0	*A*	*B*	*C*	$\lvert\mu_a\rvert$	$\lvert\mu_b\rvert$	$\lvert\mu_c\rvert$
HETERO1o[b]	0.0	0.0	726	687	439	0.2	1.8	0.8
HETERO1[a,c]	**0.8**	**0.1**	**800**	**656**	**448**	**1.5**	**1.1**	**0.7**
HETERO2	0.3	0.1	744	672	457	1.3	0.1	1.1
HETERO3	0.7	0.6	807	604	463	1.4	0.4	1.1
HETRTO4	0.2	0.8	888	580	441	1.1	0.4	1.1
HETERO5	1.2	0.8	768	679	427	1.0	0.5	1.1
HETERO6	1.4	1.0	875	621	448	0.7	1.6	0.3
HETERO7	0.8	1.2	801	621	438	1.1	0.5	1.5
HETERO8	1.6	1.2	845	572	421	0.2	1.1	0.1
HETERO9	1.6	1.3	752	621	444	1.2	0.4	0.3
HETERO10	1.5	1.5	866	607	424	1.4	0.1	1.0
HETERO11	1.5	1.6	763	651	471	1.1	0.4	0.9
HETERO12	1.6	1.7	864	592	426	0.9	0.5	1.2
HETERO13	2.0	1.8	851	613	413	1.1	0.6	0.9
HETERO14	2.3	1.8	751	633	457	1.2	0.4	0.2
HETERO15	2.3	1.9	748	651	411	0.1	1.3	1.0
HETERO16	2.7	2.0	790	655	438	1.2	0.6	0.7

HETERO17	2.2	2.1	794	620	465	0.7	0.6	0.6
HETERO18	2.3	2.2	872	580	431	0.9	0.3	0.7
HETERO19	2.1	2.2	1104	468	395	0.8	1.4	0.7
HETERO20	2.4	2.3	763	647	430	1.0	0.0	1.5
HETERO21	2.3	2.4	795	616	425	1.3	0.4	1.1
HETERO22	2.8	2.5	875	545	406	0.5	0.8	1.1
HETERO23	2.3	2.5	686	657	413	1.2	0.7	1.4
HETERO24	3.0	2.6	893	585	426	0.7	0.7	1.5
HETERO25	3.1	2.7	776	638	456	0.5	1.2	0.3
HETERO26	2.9	2.7	840	563	416	1.1	0.0	0.9
HETERO27	3.6	2.8	694	669	447	0.0	0.4	0.1
HETERO28	3.1	2.9	731	612	387	1.2	0.0	1.2
HETERO29	3.5	2.9	793	556	399	1.5	0.0	0.1
HETERO30	3.2	3.0	986	539	416	0.2	1.0	0.6
HETERO31	3.8	3.1	807	631	425	0.8	0.4	1.1
HETERO32	3.9	3.1	839	608	444	2.6	0.6	0.8
HETERO33	3.5	3.2	1487	346	318	0.5	1.1	1.5
HETERO34	3.6	3.3	936	547	425	0.9	0.2	1.3
HETERO35	3.3	3.4	1320	368	329	0.2	1.1	1.5
HETERO36	3.9	3.4	871	580	465	1.5	0.1	1.2
HETERO37	3.8	3.5	1260	381	322	0.5	0.6	1.9
HETERO38	3.7	3.5	1541	325	314	0.8	1.9	0.4
HETERO39	4.1	3.6	1051	479	376	0.6	0.2	1.4
HETERO40	4.0	3.7	1058	429	348	0.6	1.2	1.3
HETERO41	4.2	3.8	783	607	403	2.2	0.8	0.6
HETERO42	4.0	3.8	1474	346	317	0.8	1.2	1.3
HETERO43	4.1	3.9	1219	377	313	0.1	1.3	1.4
HETERO44	4.5	3.9	1326	379	317	0.8	1.1	1.4
HETERO45	4.6	4.0	1059	470	380	1.2	0.6	1.2
HETERO46	4.7	4.0	1540	330	298	0.8	1.2	1.4

HETERO47	5.0	4.1	844	600	437	0.4	2.4	0.0
HETERO48	4.7	4.2	778	666	443	2.4	1.8	0.7
HETERO49	5.0	4.3	1528	335	307	0.2	1.5	0.9
HETERO50	5.6	4.3	883	566	421	0.3	2.3	0.0
HETERO51	4.9	4.4	800	609	447	2.6	1.3	1.1
HETERO52	5.3	4.5	1312	385	353	0.4	1.6	0.9
HETERO53	5.1	4.8	759	670	434	2.1	1.3	0.6

[a] All conformers are sampled from the CREST search *except HETERO1* which was ONLY identified using the isotopic procedure described in the main text.

[b] ΔD_0 of HETERO1o is 0.1 kJ mol^{-1} **less** stable than HOMO1, inconsistent with the experimental observation. See main text for discussions.

[c] The red color indicates the conformer detected experimentally.

Point 7.S1. Structural searching and experimental and spectral fitting details

For the conformational structural search of the homo- and heterochiral PO trimers, we applied the most recent version of CREST (version 2.6) [S1]. Each CREST run contains multiple runs of META MD and then multiple runs of regular MD as designed by the code [S1]. As reported by the authors of this version of CREST, the search results do not depend on the starting structures. We have identified the homochiral species in agreement with the experimental observation as discussed in the main text. For the heterochiral PO trimer, we carried out multiple CREST runs with different starting structures, including the HETERO1 structure identified experimentally, but CREST did not produce the correct HETERO1 structure in all these runs. The HETERO1 structure was identified using isotopic substitution data as described in the main text.

For measurements of the broadband spectra of the PO sample, a modest MW power set at ~100 W, about ¼ of the full power available, was used. Enantiomeric pure (>99.0%) and racemic PO (99%) samples from Sigma Aldrich were used as is. The liquid PO samples were treated with the usual freeze-thaw cycles and a gas mixture of less than 1% PO in 9 bar helium and 1 bar neon was expanded through a home-made nozzle cap with an exit channel length of 25 mm and an exit hole diameter of 1 mm which was described in a recent publication [S2]. 1 million to 6 million free induction decays were collected for spectral analyses of the parents and the ^{13}C isotopologues.

Two sets of rotational transitions belonging to the homochiral $(PO)_3$ conformers were assigned in the spectrum recorded using an enantiomerically pure PO sample. One set of rotational transitions belonging to the heterochiral PO trimer were assigned in the spectrum recorded using a racemic PO sample and are not visible in the spectrum recorded using the enantiomerically pure PO sample.

The three sets of rotational transitions of $(PO)_3$, as well as 18 sets of ^{13}C isotopologues of $(PO)_3$ were fitted using Watson's A-reduction [S3] Hamiltonian in its I^r representation with the Pgopher program [S4].

[S1] S. Grimme, C. Bannwarth, P. Shushkov, *J. Chem. Theory Comput.* **2017**, *13*, 1989-2009; P. Pracht, F. Bohle, S. Grimme, *Phys. Chem. Chem. Phys*. **2020**, 22, 7169-7192.

[S2] F. Xie, N. A. Seifert, W. Jaeger, Y. Xu, *Angew. Chem. Int. Ed.* **2020**, DOI:10.1002/anie.202005685 and 10.1002 /ange.202005685.

[S3] J. K. G. Watson, in *Vibrational Spectra and Structure*, Vol. 6 (Ed.: J. R. Durig), Elsevier, New York, **1977**, pp. 1- 89.

[S3] C. M. Western, *J. Quant. Spectrosc. Radiat. Transf.* **2017**, *186*, 221-242.

Table 7.S3. Experimental spectroscopic constants of the three observed $(PO)_3$.

	HOMO1	HOMO2	HETERO1
A / MHz	836.79876(67)	782.7474(26)	811.72688(42)
B / MHz	638.95770(89)	628.8592(13)	645.92417(27)
C / MHz	430.04824(37)	458.53594(94)	444.53303(24)
Δ_K / kHz	-0.004(27)	0.41(21)	0.167(29)
Δ_{JK} / kHz	0.297(23)	0.252(90)	0.013(25)
Δ_J / kHz	0.1658(78)	0.152(28)	0.1884(58)
δ_K / kHz	0.285(17)	-0.062(58)	0.097(17)
δ_J / kHz	0.0497(42)	0.037(12)	0.0549(27)
N^a	30	18	58
σ^a / kHz	4.7	3.2	3.2

[a] N is the number of transitions included and σ is the standard deviation of the fit.

Table 7.S4. Experimental transition frequencies of HOMO1.

J'	K_a'	K_c'	J''	K_a''	K_c''	ν_{EXP} / MHz	$\Delta\nu^a$/ MHz
6	0	6	5	1	5	5451.4210	-0.0037
6	1	6	5	0	5	5453.5070	0.0001
5	1	5	4	0	4	4597.2300	0.0043
5	0	5	4	1	4	4588.1980	0.0044
4	0	4	3	1	3	3715.4270	-0.0014
4	1	4	3	0	3	3750.9360	0.0005
4	3	2	3	2	1	5570.2292	-0.0061
6	2	5	5	1	4	6080.5490	-0.0005
7	0	7	6	1	6	6312.1545	0.0095
7	1	7	6	0	6	6312.5879	-0.0085
5	4	2	5	3	3	2098.6262	0.0075
2	1	2	1	0	1	2126.9497	0.0098
5	3	3	5	2	4	2128.7940	-0.0010
9	6	3	9	5	4	2288.4823	-0.0016
6	4	3	6	3	4	2303.8516	-0.0025
6	2	4	6	1	5	2358.5762	-0.0022
5	5	1	5	4	2	2524.2660	0.0001
6	5	2	6	4	3	2524.4610	0.0022
5	1	4	5	0	5	2536.8257	-0.0016
6	3	4	6	2	5	2586.6402	0.0012
5	2	4	5	1	5	2594.6895	0.0004
7	5	3	7	4	4	2602.1685	0.0029
7	4	4	7	3	5	2641.1001	0.0011
8	6	2	8	5	3	2643.6583	-0.0031
8	5	4	8	4	5	2799.6630	0.0018
8	3	5	8	2	6	2805.4742	-0.0032
3	0	3	2	1	2	2812.6278	-0.0002
7	6	1	7	5	2	2909.7246	-0.0011
3	1	3	2	0	2	2929.7524	-0.0015
2	2	1	1	1	0	2940.4320	-0.0037

[a] $\nu_{obs.} - \nu_{cacl.}$

Table 7.S5. Experimental transition frequencies of HOMO2.

J'	K_a'	K_c'	J''	K_a''	K_c''	ν_{EXP} / MHz	$\Delta\nu^a$ / MHz
6	0	6	5	0	5	5738.1170	-0.0043
6	1	6	5	1	5	5737.2030	0.0010
5	1	5	4	1	4	4818.8700	0.0091
5	0	5	4	0	4	4822.8600	-0.0029
4	3	2	3	2	2	5701.1820	-0.0006
4	2	3	3	1	3	5552.5950	0.0006
5	3	3	4	3	2	5541.8635	-0.0003
4	3	1	3	2	1	5536.9507	0.0024
5	2	4	4	2	3	5254.9358	0.0013
4	2	2	3	1	2	5325.8739	0.0006
5	1	4	4	1	3	5337.8080	0.0009
4	1	3	3	0	3	5447.9720	0.0009
4	2	2	3	2	1	4709.3618	0.0013
4	3	1	3	3	0	4604.5873	-0.0020
4	1	3	3	1	2	4435.1041	-0.0070
3	3	0	2	2	0	4447.4231	-0.0028

[a] $\Delta\nu = \nu_{exp} - \nu_{cacl}$.

Table 7.S6. Experimental transition frequencies of HETERO1.

J'	K_a'	K_c'	J''	K_a''	K_c''	ν_{EXP} / MHz	$\Delta\nu^a$ / MHz
6	0	6	5	1	5	5606.0070	-0.0023
6	1	6	5	1	5	5606.2001	0.0010
6	0	6	5	0	5	5606.9710	-0.0009
6	1	6	5	0	5	5607.1631	0.0014
5	0	5	4	1	4	4715.0177	-0.0010
5	1	5	4	1	4	4715.9791	-0.0022
5	0	5	4	0	4	4719.5900	-0.0009
5	1	5	4	0	4	4720.5520	-0.0015
5	3	3	4	3	2	5575.3112	0.0015
5	4	2	4	4	1	5677.7210	0.0025
5	4	1	4	4	0	5760.1747	-0.0056
5	2	3	4	2	2	5876.8008	0.0004
5	3	2	4	3	1	5985.1505	0.0032
6	1	5	5	2	4	6131.4808	-0.0046
6	2	5	5	2	4	6141.4410	-0.0012
6	1	5	5	1	4	6169.4353	-0.0034
6	2	5	5	1	4	6179.4001	0.0047
4	4	1	3	3	0	6219.8824	-0.0015
5	3	3	4	2	2	6261.4125	-0.0035

4	4	0	3	3	1	6271.3755	0.0055
6	3	4	5	3	3	6590.6761	-0.0010
6	2	4	5	2	3	6812.6709	0.0040
6	4	3	5	4	2	6813.6440	0.0075
2	2	1	1	1	0	2879.7108	0.0054
3	0	3	2	1	2	2895.2364	-0.0061
3	1	3	2	1	2	2914.7710	-0.0009
7	3	5	7	2	6	2918.3626	-0.0066
7	3	5	7	1	6	2920.7135	0.0004
3	0	3	2	0	2	2963.6500	-0.0014
3	1	3	2	0	2	2983.1893	0.0084
2	2	0	1	1	1	3185.0864	-0.0042
3	2	2	2	2	1	3271.3515	0.0005
3	1	2	2	1	1	3479.6443	0.0016
3	2	1	2	2	0	3579.0494	-0.0011
3	2	2	2	1	1	3768.7588	-0.0003
4	0	4	3	1	3	3817.1616	0.0006
4	1	4	3	1	3	3821.7338	0.0006
4	0	4	3	0	3	3836.6910	0.0006
4	1	4	3	0	3	3841.2632	0.0006
4	1	3	3	2	2	4154.4052	0.0002
4	2	3	3	2	2	4275.3450	0.0001
4	1	3	3	1	2	4443.5217	0.0002
4	3	2	3	3	1	4499.0588	-0.0006
3	3	1	2	2	0	4554.3346	-0.0005
4	2	3	3	1	2	4564.4614	0.0001
4	3	1	3	3	0	4682.8047	-0.0008
3	3	0	2	2	1	4697.6184	-0.0009
3	2	1	2	1	2	4784.6248	0.0030
4	2	2	3	2	1	4788.2375	-0.0002
5	1	4	4	2	3	5188.7029	-0.0064
5	2	3	4	3	2	5190.6952	0.0012
3	3	0	2	1	1	5195.0276	0.0002
5	2	4	4	2	3	5226.6627	0.0002
5	1	4	4	1	3	5309.6493	0.0002
5	2	4	4	1	3	5347.6023	-0.0001
4	3	2	3	2	1	5474.3438	-0.0001
2	1	1	1	1	0	2382.2970	-0.0002
2	0	2	1	0	1	2076.9133	0.0001

[a] $\Delta v = v_{exp} - v_{cacl}$.

Table 7.S7. Experimental spectroscopic constants of the nine singly ^{13}C substituted HOMO1[a]

Sub. Species	*A* / MHz	*B* / MHz	*C* / MHz	*N*[b]	*σ* / kHz[b]
C1	826.39601(21)	638.82518(31)	427.32300(7)	12	1.7
C2	831.7216(12)	638.3885(15)	428.72152(4)	10	6.2
C3	829.28112(62)	634.6659(12)	427.21172(23)	11	4.1
C11	834.99631(82)	633.41164(98)	427.99785(31)	13	5.9
C12	836.2286(11)	635.3405(10)	428.26699(45)	11	7.2
C13	832.6839(10)	630.8293(19)	425.58523(39)	11	6.8
C21	827.0727(12)	637.4005(24)	426.81596(56)	9	7.6
C22	833.3091(15)	636.7990(15)	428.38573(45)	11	7.7
C23	833.93125(42)	631.39723(79)	426.60083(18)	11	2.9

[a] All quartic centrifugal distortion constants are fixed at the values of the parent species.

[b] *N* is the number of transitions included and *σ* is the standard deviation of the fit.

Table 7.S8. Experimental transition frequencies of all nine ^{13}C isotopologues of HOMO1.

J'	K_a'	K_c'	J''	K_a''	K_c''	ν_{EXP} / MHz	$\Delta\nu$[a] / MHz
C1							
5	0	5	4	1	4	4560.6962	-0.0030
5	1	5	4	0	4	4568.1030	0.0001
4	0	4	3	1	3	3695.0450	0.0040
4	1	4	3	0	3	3725.5659	-0.0003
3	3	1	2	2	0	4615.2740	0.0009
3	3	0	2	2	1	4757.9405	-0.0009
5	2	4	4	1	3	5251.9210	-0.0001
6	0	6	5	1	5	5417.9248	0.0001
6	1	6	5	0	5	5419.5525	0.0001
4	2	3	3	1	2	4516.1204	-0.0001
3	2	2	2	1	1	3761.1302	0.0001
4	1	3	3	2	2	4028.3505	0.0001
C2							
4	0	4	3	1	3	3705.0300	0.0012
4	1	4	3	0	3	3738.3800	-0.0014
5	0	5	4	1	4	4574.4354	0.0091
3	3	1	2	2	0	4643.9773	0.0008
3	2	2	2	1	1	3781.3005	-0.0022
4	1	3	3	2	2	4023.3769	-0.0001
4	2	3	3	1	2	4539.1907	0.0107

5	2	4	4	1	3	5274.8700	-0.0124
6	0	6	5	1	5	5434.7575	-0.0053
6	1	6	5	0	5	5436.6467	0.0018
C3							
4	0	4	3	1	3	3690.5497	0.0005
4	1	4	3	0	3	3724.9891	-0.0035
5	0	5	4	1	4	4557.2900	0.0083
5	1	5	4	0	4	4565.9746	-0.0092
6	0	6	5	1	5	5414.7263	-0.0007
6	1	6	5	0	5	5416.7230	0.0033
3	3	1	2	2	0	4630.1750	0.0018
3	3	0	2	2	1	4764.4597	-0.0014
5	1	4	4	2	3	5034.5086	-0.0001
5	2	4	4	1	3	5257.2943	0.0001
3	2	2	2	1	1	3769.4517	-0.0001
C11							
4	0	4	3	1	3	3695.4110	0.0156
4	1	4	3	0	3	3733.5090	-0.0095
5	0	5	4	1	4	4564.9081	-0.0001
4	2	3	3	1	2	4546.2748	0.0009
3	3	1	2	2	0	4660.2960	0.0064
3	3	0	2	2	1	4788.8568	-0.0031
5	1	4	4	2	3	5032.1240	-0.0022
6	0	6	5	1	5	5424.3484	0.0021
6	1	6	5	0	5	5426.6981	-0.0010
5	1	5	4	0	4	4574.8577	0.0010
5	2	4	4	1	3	5276.9099	-0.0077
3	2	2	2	1	1	3788.9557	0.0001
4	1	3	3	2	2	3986.5515	0.0001
C12							
5	0	5	4	1	4	4569.2500	0.0117
5	1	5	4	0	4	4578.9100	0.0030
4	0	4	3	1	3	3699.4277	-0.0042
4	1	4	3	0	3	3736.7751	-0.0133
3	3	1	2	2	0	4666.8511	0.0042
3	2	2	2	1	1	3793.4670	0.0069
3	3	0	2	2	1	4797.5771	-0.0029
3	1	3	2	0	2	2920.0757	0.0023
5	2	4	4	1	3	5282.0052	-0.0115
6	0	6	5	1	5	5429.1252	0.0038
5	1	4	4	2	3	5041.6906	0.0001
C13							

6	0	6	5	1	5	5395.3070	0.0035
6	1	6	5	0	5	5397.6770	0.0028
5	0	5	4	1	4	4540.6754	0.0051
4	0	4	3	1	3	3675.9396	0.0125
4	1	4	3	0	3	3714.2130	-0.0092
5	1	5	4	0	4	4550.6721	-0.0072
3	2	2	2	1	1	3774.7760	-0.0047
3	3	1	2	2	0	4646.3260	-0.0046
3	3	0	2	2	1	4774.5947	0.0090
5	2	4	4	1	3	5253.0293	-0.0012
5	1	4	4	2	3	5007.2165	-0.0066
C21							
5	0	5	4	1	4	4555.2755	0.0043
5	1	5	4	0	4	4563.0234	0.0024
4	0	4	3	1	3	3690.2660	-0.0047
6	0	6	5	1	5	5411.5930	-0.0082
3	2	2	2	1	1	3761.6260	-0.0133
3	3	1	2	2	0	4618.3740	0.0028
4	2	3	3	1	2	4515.7480	0.0143
3	3	0	2	2	1	4758.8244	-0.0030
5	1	4	4	2	3	5043.8310	0.0037
C22							
5	0	5	4	1	4	4570.6300	-0.0029
5	1	5	4	0	4	4579.5300	0.0116
4	0	4	3	1	3	3701.3488	-0.0008
4	1	4	3	0	3	3736.3762	-0.0144
6	0	6	5	1	5	5430.4820	-0.0070
6	1	6	5	0	5	5432.5370	0.0059
3	3	1	2	2	0	4651.8930	-0.0059
5	1	4	4	2	3	5049.5120	0.0061
5	2	4	4	1	3	5275.9740	-0.0014
3	2	2	2	1	1	3785.0690	0.0113
4	1	3	3	2	2	4010.5293	-0.0039
C23							
4	0	4	3	1	3	3683.6020	-0.0026
4	1	4	3	0	3	3722.3350	-0.0058
6	1	6	5	0	5	5409.6560	0.0008
3	3	1	2	2	0	4653.6170	-0.0009
3	3	0	2	2	1	4781.0580	-0.0022
5	0	5	4	1	4	4550.5246	0.0028
5	1	5	4	0	4	4560.6842	-0.0020
4	2	3	3	1	2	4536.2630	0.0055
3	2	2	2	1	1	3781.5704	0.0009

5	1	4	4	2	3	5015.3350	0.0018
5	2	4	4	1	3	5263.7410	-0.0001

[a] $\Delta\nu = \nu_{exp} - \nu_{cacl}$.

Table 7.S9. Experimental spectroscopic constants of the nine singly ^{13}C substituted HETERO1[a]

Sub. Species	*A* / MHz	*B* / MHz	*C* / MHz	*N*[b]	*σ* / kHz[b]
C1	802.1575(29)	645.57449(72)	441.68231(28)	11	4.8
C2	806.5321(43)	645.6251(10)	443.02460(48)	9	6.8
C3	803.3460(27)	642.61036(64)	441.21847(26)	10	4.3
C11	807.0302(41)	639.4832(18)	440.32721(34)	10	5.5
C12	810.0304(67)	641.9275(33)	442.32192(67)	7	8.7
C13	804.7948(54)	642.3326(12)	442.74105(53)	10	8.5
C21	810.4912(42)	640.1209(18)	442.08263(46)	8	5.4
C22	810.6288(32)	642.77522(51)	442.76789(23)	8	3.3
C23	805.6379(53)	639.22317(91)	440.22108(36)	8	5.6

[a] All quartic centrifugal distortion constants are fixed at the values of the parent species.

[b] *N* is the number of transitions included and *σ* is the standard deviation of the fit.

Table 7.S10. Experimental transition frequencies of all nine ^{13}C isotopologues of HETERO1.

J'	K_a'	K_c'	J''	K_a''	K_c''	ν_{EXP} / MHz	$\Delta\nu$[a] / MHz
C1							
4	1	4	3	1	3	3798.9760	0.0010
4	0	4	3	0	3	3811.9860	0.0004
5	0	5	4	0	4	4689.8725	0.0019
5	1	5	4	1	4	4686.9010	0.0021
4	2	3	3	2	2	4257.8600	-0.0001
4	1	3	3	1	2	4417.0605	-0.0071
4	2	2	3	2	1	4780.7918	0.0014
5	2	4	4	2	3	5200.0548	-0.0013
5	1	4	4	1	3	5273.8194	0.0064
6	1	6	5	1	5	5571.2106	0.0034
6	0	6	5	0	5	5571.8023	-0.0080
C2							
4	1	4	3	1	3	3809.5830	0.0040
4	2	3	3	2	2	4265.7464	0.0008
4	1	3	3	1	2	4429.2300	-0.0037

5	0	5	4	0	4	4703.7542	0.0110
5	1	5	4	1	4	4700.4761	-0.0026
4	2	2	3	2	1	4783.6706	-0.0008
5	2	4	4	2	3	5212.2542	0.0029
5	1	4	4	1	3	5290.3486	0.0011
6	1	6	5	1	5	5587.5570	-0.0105
C3							
4	0	4	3	0	3	3807.7537	-0.0031
4	2	3	3	2	2	4247.2430	-0.0011
4	1	3	3	1	2	4410.5309	0.0014
5	0	5	4	0	4	4684.3686	-0.0045
5	1	5	4	1	4	4681.0756	-0.0047
4	2	2	3	2	1	4761.8240	0.0008
5	2	4	4	2	3	5190.0683	-0.0015
5	1	4	4	1	3	5268.4184	0.0005
6	0	6	5	0	5	5565.2556	0.0013
6	1	6	5	1	5	5564.5745	0.0085
C11							
4	0	4	3	0	3	3801.6276	-0.0140
4	1	4	3	1	3	3786.1460	0.0007
4	2	3	3	2	2	4234.8055	-0.0009
4	1	3	3	1	2	4404.4990	0.0003
5	0	5	4	0	4	4675.9540	0.0016
5	1	5	4	1	4	4672.1503	0.0018
5	2	4	4	2	3	5178.3173	0.0002
5	1	4	4	1	3	5263.6895	0.0021
6	0	6	5	0	5	5554.8475	0.0023
6	1	6	5	1	5	5554.0196	0.0022
C12							
4	0	4	3	0	3	3818.3050	-0.0090
4	1	4	3	1	3	3802.7491	0.0016
4	2	3	3	2	2	4252.4258	0.0004
4	1	3	3	1	2	4422.6660	-0.0007
5	1	5	4	1	4	4692.7540	-0.0095
5	1	4	4	1	3	5285.8608	0.0023
6	0	6	5	0	5	5579.4724	0.0111
C13							
3	1	2	2	1	1	3460.8106	-0.0005
4	0	4	3	0	3	3818.9607	-0.0007
4	1	4	3	1	3	3804.4798	-0.0186
4	1	3	3	1	2	4418.8968	-0.0046
5	1	5	4	1	4	4695.0010	0.0004

4	2	2	3	2	1	4762.9440	0.0023
5	2	4	4	2	3	5200.5043	-0.0009
5	1	4	4	1	3	5281.0487	0.0052
6	1	6	5	1	5	5581.5959	0.0104
6	0	6	5	0	5	5582.3200	0.0004
C21							
4	1	4	3	1	3	3799.7430	-0.0080
4	0	4	3	0	3	3815.9220	0.0075
4	2	3	3	2	2	4245.9680	0.0006
4	1	3	3	1	2	4418.1870	-0.0030
5	0	5	4	0	4	4693.5090	-0.0023
5	1	5	4	1	4	4689.4750	0.0014
5	2	4	4	2	3	5193.9803	0.0026
5	1	4	4	1	3	5282.3575	0.0005
C22							
4	1	4	3	1	3	3806.6761	-0.0071
4	0	4	3	0	3	3822.1650	0.0005
4	2	3	3	2	2	4257.2540	0.0004
4	1	3	3	1	2	4427.2879	0.0001
5	0	5	4	0	4	4701.3590	0.0012
4	2	2	3	2	1	4765.5340	0.0002
6	0	6	5	0	5	5585.1370	0.0015
6	1	6	5	1	5	5584.3130	0.0014
C23							
4	1	4	3	1	3	3784.8012	-0.0116
4	0	4	3	0	3	3800.0990	0.0005
4	1	3	3	1	2	4401.7270	0.0004
5	0	5	4	0	4	4674.2700	-0.0009
5	1	5	4	1	4	4670.5380	0.0015
4	2	2	3	2	1	4739.0360	0.0006
6	0	6	5	0	5	5552.9827	0.0031
6	1	6	5	1	5	5552.1737	0.0031

[a] $\Delta\nu = \nu_{exp} - \nu_{cacl}$.

Table 7.S11. Kraitchman's coordinates (in Å) and the corresponding *ab initio* values (in Å) at the B3LYP-D3BJ/def2-TZVP level of the nine C atoms in HOMO1 in its principal inertial axis system.

Constants/	*a*		*B*		*c*	
Species	cal	|kra|	cal	|kra|	cal	|kra|
C1	0.323074	0.1644(94)	2.787510	2.73548(57)	0.364990	0.3728(42)
C2	0.728302	0.5677(20)	1.779970	1.82196(90)	-0.612940	0.6181(26)
C3	2.055187	1.93800(83)	1.812868	2.00988(80)	-1.310283	1.2409(13)
C11	-2.270239	2.37198(68)	0.216516	0.065(25)	1.133463	1.1470(14)
C12	-2.190082	2.11910(77)	-0.518842	0.6393(26)	-0.129270	0.117(13)
C13	-3.292510	3.10606(54)	-1.421769	1.6418(11)	-0.600161	0.6613(26)
C21	1.136971	1.3412(13)	-2.781570	2.66845(67)	-0.275588	0.2628(68)
C22	1.375400	1.5274(11)	-1.617869	1.4952(11)	0.577678	0.5734(29)
C23	2.745546	2.8988(54)	-1.217819	1.0481(15)	1.035986	1.0227(16)

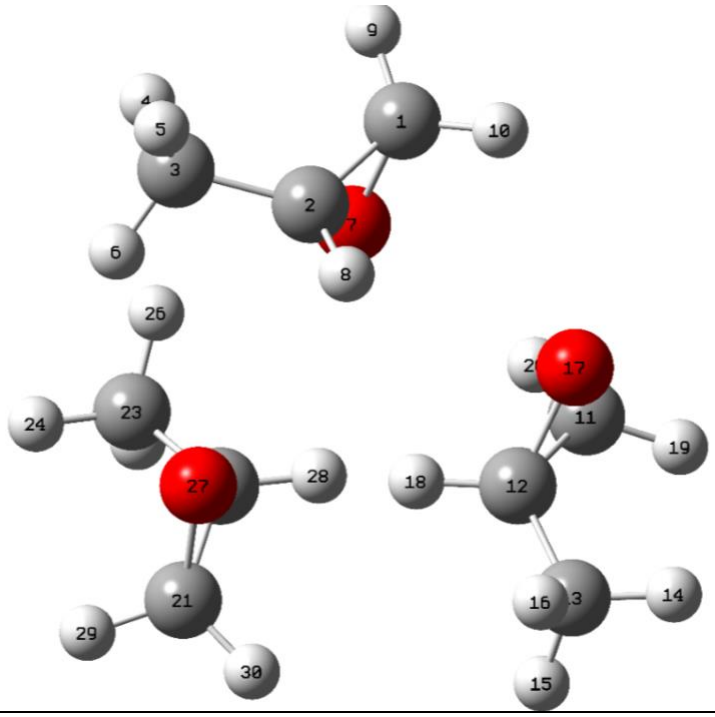

Table 7.S12. Kraitchman's coordinates (in Å) and the corresponding *ab initio* values (in Å) at the B3LYP-D3BJ/def2-TZVP level of the nine C atoms in HETERO1 in its principal inertial axis system.

Constants/	*a*		*B*		*c*	
Species	cal	|kra|	cal	|kra|	cal	|kra|
C1	-0.169189	0.3996(41)	2.771075	2.68146(61)	0.504970	0.5125(32)
C2	0.462181	0.3302(54)	1.928137	1.94124(92)	-0.508248	0.5042(35)
C3	1.809693	1.71364(94)	2.234212	2.36706(69)	-1.089946	1.0093(16)
C11	2.567216	2.72305(66)	-2.059416	1.86069(99)	-0.552845	0.5754(32)
C12	2.065940	2.1455(11)	-1.174212	1.0442(22)	0.498459	0.4997(46)
C13	1.232522	1.3306(14)	-1.670314	1.6771(11)	1.641632	1.6136(12)
C21	-2.436594	2.49481(73)	-0.126588	0.2861(65)	0.947152	0.9399(20)
C22	-2.000285	1.93679(85)	-0.827134	0.8896(19)	-0.259738	0.2701(61)
C23	-2.820445	2.67317(69)	-1.910294	1.99854(95)	-0.896489	0.9542(20)

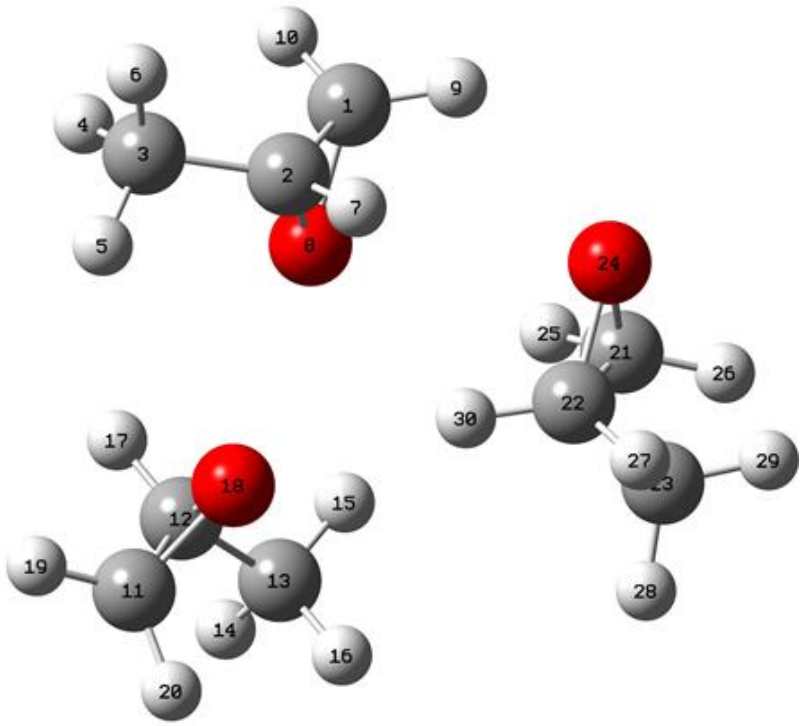

Point 7.S2. The Python program for extracting the heavy atom frame using the ^{13}C isotopic data.

A python program was written to aid the extraction of the heavy atom frame using the absolute Cartesian coordinates obtained using the ^{13}C isotopic data. It is available upon requested from the authors. It consists of three main steps.

Step 1. Group the C atoms to form three PO subunits

Each x, y and z coordinates from the Kraitchman's substitution procedure can take on "+" or "-" signs. From these combinations, possible C-C distances are calculated. Suitable C atoms to make up a PO subunit should have one ring C-C distance and one side chain C-C distance in the range of 1.45-1.47 and 1.49-1.54, respectively., In addition, the third C-C distance should be in the range of 2.55-2.63 Å.

These criteria were first tested on HOMO1 and then used for the HETERO1 search. It is important to test these thresholds. As mentioned in the main text, each C atom has three Cartesian coordinates, i.e. x, y, and z, and for each x, y or z, we have two possible signs, leading to 2 x 2 x 2 = 8 possible positions. Since the starting C atom of each PO unit can take on any one of the eight possible Cartesian coordinates, one would expect eight possible sets of Cartesian coordinates for each PO unit, keeping in mind that the two further C atoms have to choose their Cartesian coordinates based on the first C atom. In total, we have 3 PO subunits and would expect 24 sets of the "three-carbon-atom" groups. If the threshold is set too tight, this would result in fewer possible sets of the "three-carbon-atom" groups. For example, one may obtain only 8 sets which correspond to only one PO subunit. If the threshold is set too loose, one may obtain some "extra" sets which contain fake (or improper) PO subunit(s). We found that a good approach is to use the related HOMO1 distances and then slowly expanded the thresholds until we got the expected 24 sets of the "three-carbon-atom" groups.

Step 2. Add O and H atoms to each PO subunit and assemble a reasonable PO trimer structure

First, we put the O and H atoms back into the carbon frames identified in Step 1 to complete the PO subunits. As mentioned in Step 1, the 24 sets of Cartesian coordinates obtained for the "three-carbon-atom" groups actually correspond to 3 PO subunits where each subunit has 8 possible sets of Cartesian coordinates. For the PO trimer, we have 8x8x8 (i.e. 512) Cartesian coordinate combinations in total.

Second, since overlapping/overcrowding of the PO subunits is not physically sensible in the trimer, we utilized this requirement to further reduce the number of possible trimer combinations. To do this, one needs to set a minimum acceptable separation for all *intermolecular* distances. Generally, we found that this criterion is not as strict as those thresholds set in Step 1. As along as this threshold is set to any value between 2 to 3 Å, the possible combination is reduced from 512 to 8. On the other hand, if the threshold is set to a value between 0 to 2 Å, all 512 combinations remain. This basically means that we did not control the overlapping/overcrowding of the PO subunits. If the threshold is set to a value larger than 3 Å, no combination was obtained. This is because the substitution coordinates place a constraint on the 512 Cartesian combinations and do not allow PO subunits to be so far away from each other.

The eight sets of possible Cartesian coordinates identified for the PO trimer correspond actually to just one PO trimer structure if we count the mirror-image structures as the same.

Step 3. DFT geometry optimization

The HETERO1 geometry obtained above was used as the starting point for a DFT geometry optimization to obtain the HETERO1 structure that corresponds to the experimental spectrum observed. See the main text for further discussion on the vibrational corrections to the equilibrium structure.

Point 7.S3. Computational details on vibrational corrections

In many rotational spectroscopic research papers, the experimental rotational constants in the ground vibrational state, also called effective rotational constants, are directly compared to the equilibrium rotational constants obtained from ab initio calculations. For fully quantitative purposes, the difference between the two quantities, issuing from the vibration-rotation interaction constants ruled by semi-diagonal cubic force constants [S1,S2], however, cannot be neglected. The availability of effective codes for the computation of analytical harmonic frequencies for double-hybrid functionals [S3] and of effective numerical evaluations of third- and fourth-energy derivatives [S2] allows, in principle, the computation of accurate ground state rotational constants including vibrational corrections, providing full reconciliation between accuracy and interpretability in the challenging field of large non-covalent complexes.

All calculations on vibrational corrections were performed with Gaussian16 suite of programs [S4]. The six lower energy structures from the conformational search were further refined by employing the B2PLYP [S5] (B2) and the DSD-PBEP86 [S6] (rPP) double hybrid functionals in conjunction with the jun-cc-pVTZ [S7,S8]. In all calculation the empirical dispersion (D3BJ) [S9] were included. Geometry optimizations were performed with tight convergence criteria (i.e., 1×10^{-5} hartree/bohr and 4×10^{-5} bohr on RMS force and displacements, respectively, with maximum values being 1.5 times larger).

Harmonic and anharmonic calculations were carried out at B3LYP-D3BJ [S9,S10] / jun-cc-pVDZ [S7,S8] level of theory. Harmonic force fields were obtained using analytic derivatives of energy and transition moments, whereas higher-order derivatives were computed through numerical differentiation using a step of 0.01 amu$^{1/2}$ Å for the displacements along the mass-weighted normal coordinates. Equilibrium rotational constants (B_x^e, x=a,b,c) were derived from the B2 and rPP optimized geometries, while, in order to obtain rotational constants of the vibrational ground-state (B_x^0), the vibrational

corrections were computed from the vibration-rotation interaction constants (α_k^x) obtained within the vibrational perturbation theory (VPT2) at B3 level according to the following equation:

$$B_x^0 = B_x^e - \frac{1}{2}\sum_{k=1}^{3N-6} \alpha_k^x$$

Within the same composite scheme, the equilibrium and vibrational ground-state dipole moments were also computed.

The electronic contribution to the corrections has been neglected, since it contributes less than 0.05% with respect to the vibrational corrections [S10].

Bibliography

[S1] I. M. Mills in Molecular Spectroscopy: Modern Research, ed. K.N. Rao and C.W. Mathews, Academic Press, **1972**.

[S2] V. Barone, *J. Chem. Phys.* **2005**, *122*, 014108/1-10.

[S3] M. Biczysko, G. Scalmani, J. Bloino, V. Barone, *J. Chem. Theory Comput.* **2010**, *6*, 2115-2125.

[S4] Gaussian 16, Revision C.01, M. J. Frisch, *et al.* Gaussian, Inc., Wallingford CT, **2016**. See page S27 for the full reference

[S5] a) S. Grimme, J. Chem. Phys. **2006**, *124*, 034108/1-16; b) A. D. Becke, *J. Chem. Phys.* **1993**, *98*, 5648-5652.

[S6] G. Santra, N. Sylvetsky, J. M. L. Martin, *J. Chem. Theory Comput.* **2019**, *123*, 5129-5143.

[S7] T. H. Dunning Jr., *J. Chem. Phys.* **1989**, *90*, 1007.

[S8] E. Papajak, H. R. Leverentz, J. Zheng, D. G. Truhlar, *J. Chem. Theory Comput.* **2009**, *5*, 1197-1202.

[S9] S. Grimme, S. Ehrlich, L. Goerigk, *J. Comput. Chem.* **2011**, *32*, 1456-1465.

[S10] M. Piccardo, E. Penocchio, C. Puzzarini, M. Biczysko, V. Barone, *J. Phys. Chem. A* **2015**, *119*, 10, 2058-2082.

Table 7.S13. Rotational constants (MHz) of HOMO and HETERO complexes. Equilibrium geometries, at B2PLYPD3/jun-cc-pVTZ (B2) level of theory; vibrational correction at B3LYP/jun-cc-pVDZ + empirical dispersion D3BJ (B3) level of theory.

	Ae	*Be*	*Ce*	*vibA0*	*vibB0*	*vibC0*	*A0*	*B0*	*C0*
HOMO1	*842.195*	*649.778*	*434.669*	*-13.333*	*-10.377*	*-7.601*	828.862	639.401	427.068
HOMO2	*795.369*	*642.248*	*471.165*	*-12.060*	*-11.182*	*-11.499*	783.309	631.066	459.666
HOMO3	*790.169*	*656.189*	*424.418*	*-8.819*	*-11.417*	*-7.139*	781.350	644.772	417.279
HOMO4	*767.152*	*655.671*	*444.383*	*-13.441*	*-10.033*	*-9.133*	753.711	645.638	435.250
HOMO5	*801.240*	*618.221*	*448.915*	*-13.809*	*-11.672*	*-10.774*	787.431	606.549	438.141
HOMO6	*762.179*	*672.498*	*396.359*	*-11.225*	*-9.468*	*-5.600*	750.954	663.030	390.759
HETERO1	*816.209*	*656.550*	*452.306*	*-14.744*	*-10.511*	*-9.373*	801.465	646.039	442.933
HETERO1o	*733.845*	*685.917*	*441.625*	*-11.483*	*-11.057*	*-8.259*	722.362	674.860	433.366
HETERO2	*748.796*	*677.420*	*455.350*	*-10.766*	*-13.236*	*-10.321*	738.030	664.184	445.029
HETERO3	*813.402*	*602.213*	*463.960*	*-10.630*	*-8.221*	*-8.191*	802.772	593.992	455.769
HETERO4	*887.267*	*579.747*	*441.027*	*-16.523*	*-9.744*	*-9.471*	870.744	570.003	431.556
HETERO5	*791.026*	*675.544*	*437.733*	*-7.426*	*-11.389*	*-6.381*	783.600	664.155	431.352

Table 7.S14. Rotational constants (MHz) of HOMO and HETERO complexes. Equilibrium geometries, at DSD-PBEP86-D3BJ/jun-cc-pVTZ (rPP) level of theory; vibrational correction at B3LYP/jun-cc-pVDZ + empirical dispersion D3BJ (B3) level of theory.

	Ae	*Be*	*Ce*	*vibA0*	*vibB0*	*vibC0*	*A0*	*B0*	*C0*
HOMO1	*848.642*	*648.445*	*438.418*	*-13.333*	*-10.377*	*-7.601*	835.309	638.068	430.817
HOMO2	*795.778*	*639.697*	*468.845*	*-12.060*	*-11.182*	*-11.499*	783.718	628.515	457.346
HOMO3	*796.206*	*656.791*	*424.845*	*-8.819*	*-11.417*	*-7.139*	787.387	645.374	417.706
HOMO4	*763.303*	*653.939*	*441.867*	*-13.441*	*-10.033*	*-9.133*	749.862	643.906	432.734
HOMO5	*802.173*	*616.057*	*447.774*	*-13.809*	*-11.672*	*-10.774*	788.364	604.385	437.000
HOMO6	*761.905*	*673.655*	*397.195*	*-11.225*	*-9.468*	*-5.600*	750.680	664.187	391.595
HETERO1	*824.591*	*655.451*	*452.751*	*-14.744*	*-10.511*	*-9.373*	809.847	644.940	443.378
HETERO1o	*742.342*	*679.443*	*443.092*	*-11.483*	*-11.057*	*-8.259*	730.859	668.386	434.833
HETERO2	*747.707*	*675.017*	*452.402*	*-10.766*	*-13.236*	*-10.321*	736.941	661.781	442.081
HETERO3	*823.651*	*599.809*	*462.276*	*-10.630*	*-8.221*	*-8.191*	813.021	591.588	454.085
HETERO4	*886.032*	*576.825*	*438.744*	*-16.523*	*-9.744*	*-9.471*	869.509	567.081	429.273
HETERO5	*801.509*	*670.080*	*443.173*	*-7.426*	*-11.389*	*-6.381*	794.083	658.691	436.792

Table 7.S15. Results: dipole moments of HOMO and HETERO complexes (Debye) in Principal Axis frame. dipole moments at B2PLYPD3/jun-cc-pVTZ (B2) level of theory; vibrational correction at B3LYP/jun-cc-pVDZ + empirical dispersion D3BJ (B3) level of theory.

	$\mu_a e$	$\mu_b e$	$\mu_c e$	$\Delta\mu_a 0$	$\Delta\mu_b 0$	$\Delta\mu_c 0$
HOMO1	*0.7527*	*-1.5136*	*0.8259*	*-0.0164*	*0.0361*	*-0.0270*
HOMO2	*-1.1450*	*-0.2357*	*-1.4072*	*0.0081*	*0.0230*	*-0.0076*
HOMO3	*0.9717*	*-1.1374*	*-1.0459*	*-0.0260*	*0.0260*	*0.0107*
HOMO4	*-0.9640*	*0.1983*	*1.4650*	*-0.0188*	*-0.0675*	*-0.0557*
HOMO5	*0.1994*	*-1.2975*	*-0.1122*	*0.0568*	*-0.0565*	*-0.0374*
HOMO6	*-1.4628*	*0.0076*	*1.0764*	*0.0178*	*-0.0072*	*-0.0591*
HETERO1	*1.6342*	*-0.9718*	*0.7500*	*-0.0534*	*0.0451*	*0.0093*
HETERO1o	*-0.1267*	*1.8539*	*0.7944*	*0.0075*	*-0.0227*	*-0.0265*
HETERO2	*1.2274*	*-0.0333*	*1.1976*	*-0.0582*	*0.0239*	*0.0311*
HETERO3	*1.4732*	*-0.4987*	*0.9978*	*-0.0273*	*0.0100*	*-0.0098*
HETERO4	*-1.1362*	*-0.4189*	*-1.1145*	*-0.0318*	*0.0409*	*0.0372*
HETERO5	*-1.1400*	*-0.5574*	*-1.1858*	*-0.0142*	*-0.0877*	*0.0300*

Table 7.S16. Results: dipole moments of HOMO and HETERO complexes (Debye) in Principal Axis frame. dipole moments at DSD-PBEP86-D3BJ/jun-cc-pVTZ (rPP) level of theory; vibrational correction at B3LYP/jun-cc-pVDZ + empirical dispersion D3BJ (B3) level of theory.

	$\mu_a e$	$\mu_b e$	$\mu_c e$	$\Delta\mu_a 0$	$\Delta\mu_b 0$	$\Delta\mu_c 0$
HOMO1	*0.7837*	*-1.4584*	*0.8518*	*-0.0164*	*0.0361*	*-0.0270*
HOMO2	*1.1341*	*-0.2502*	*1.4118*	*0.0081*	*0.0230*	*-0.0076*
HOMO3	*-1.0319*	*-1.1153*	*1.0783*	*-0.0260*	*0.0260*	*0.0107*
HOMO4	*0.8990*	*0.2360*	*-1.4407*	*-0.0188*	*-0.0675*	*-0.0557*
HOMO5	*-0.2130*	*-1.3258*	*0.1105*	*0.0568*	*-0.0565*	*-0.0374*
HOMO6	*-1.4366*	*0.0317*	*1.0835*	*0.0178*	*-0.0072*	*-0.0591*

HETERO1	*1.6256*	*-0.9096*	*0.7876*	*-0.0534*	*0.0451*	*0.0093*
HETERO1o	*0.0181*	*1.9177*	*0.7665*	*0.0075*	*-0.0227*	*-0.0265*
HETERO2	*1.1720*	*-0.0995*	*1.2393*	*-0.0582*	*0.0239*	*0.0311*
HETERO3	*1.4435*	*-0.5495*	*0.9540*	*-0.0273*	*0.0100*	*-0.0098*
HETERO4	*-1.1263*	*-0.4513*	*-1.0959*	*-0.0318*	*0.0409*	*0.0372*
HETERO5	*-1.2230*	*-0.5149*	*-1.1837*	*-0.0142*	*-0.0877*	*0.0300*

Table 7.S17. Absolute Energies of HOMO and HETERO most stable conformers and relative stabilities of the HOMO and HETERO complexes (kJ mol^{-1}). Within parenthesis, the relative stabilities between the HOMO and HETERO most stable conformers are given. Energies, at B2PLYPD3/jun-cc-pVTZ (B2), harmonic zero point vibrational energy at B3LYP/jun-cc-pVDZ + empirical dispersion D3BJ (B3) level of theory.

	E	*ΔE*	*E +ZPVE(Harm)*	*ΔE +ZPVE(Harm)*
HOMO1	*-1520408.700*	*0.000 (0.000)*	*-1519734.828*	*0.000 (0.000)*
HOMO2		*0.196*		*1.512*
HOMO3		*0.872*		*1.696*
HOMO4		*1.528*		*1.862*
HOMO5		*0.995*		*1.077*
HOMO6		*1.583*		*1.585*
HETERO1	*-1520408.590*	*0.000 (0.111)*	*-1519734.791*	*0.000 (0.037)*
HETERO1o		*0.017*		*0.650*
HETERO2		*0.191*		*0.503*
HETERO3		*1.002*		*1.145*
HETERO4		*0.689*		*1.606*
HETERO5		*1.014*		*1.412*

Table 7.S18. Absolute Energies of HOMO and HETERO most stable conformers and relative stabilities of the HOMO and HETERO complexes (kJ mol^{-1}). Within parenthesis, the relative stabilities between the HOMO and HETERO most stable conformers are given.

Energies, at DSD-PBEP86-D3BJ/jun-cc-pVTZ (rPP), harmonic zero point vibrational energy at B3LYP-D3BJ/jun-cc-pVDZ (B3) level of theory.

	E	*ΔE*	*E +ZPVE(Harm)*	*ΔE +ZPVE(Harm)*
HOMO1	*-1518879.746*	*0.000 (0.006)*	*-1518205.874*	*0.000 (0.079)*
HOMO2		*0.779*		*2.095*
HOMO3		*1.071*		*1.895*
HOMO4		*2.306*		*2.640*
HOMO5		*1.362*		*1.444*
HOMO6		*1.821*		*1.823*
HETERO1	*-1518879.752*	*0.000 (0.000)*	*-1518205.953*	*0.000 (0.000)*
HETERO1o		*0.931*		*1.564*
HETERO2		*1.047*		*1.360*
HETERO3		*1.849*		*1.992*
HETERO4		*1.542*		*2.460*
HETERO5		*1.588*		*1.987*

Table 7.S19. HOMO1 ^{13}C isotolologues: equi. B2, vib. B3 level of theory (MHz)

	Ae	*Be*	*Ce*	*vibA0*	*vibB0*	*vibC0*	*A0*	*B0*	*C0*
HOMO1	*842.195*	*649.778*	*434.669*	*-13.333*	*-10.377*	*-7.601*	*828.862*	*639.401*	*427.068*
C1	*840.353*	*644.221*	*435.495*	*-12.646*	*-10.260*	*-7.434*	*827.707*	*633.961*	*428.061*
C2	*837.174*	*649.120*	*436.169*	*-13.483*	*-10.181*	*-7.517*	*823.691*	*638.939*	*428.652*
C3	*834.927*	*645.154*	*434.669*	*-14.116*	*-9.876*	*-7.680*	*820.811*	*635.278*	*426.989*
C11	*840.353*	*644.221*	*435.495*	*-14.373*	*-10.377*	*-7.737*	*825.980*	*633.844*	*427.758*
C12	*841.685*	*645.969*	*435.680*	*-13.394*	*-10.259*	*-7.537*	*828.291*	*635.710*	*428.143*
C13	*838.433*	*641.085*	*432.885*	*-14.505*	*-9.680*	*-7.303*	*823.928*	*631.405*	*425.582*
C21	*832.030*	*648.350*	*434.188*	*-13.421*	*-10.299*	*-7.635*	*818.609*	*638.051*	*426.553*
C22	*838.490*	*647.689*	*435.840*	*-13.150*	*-9.892*	*-7.338*	*825.340*	*637.797*	*428.502*
C23	*839.137*	*642.276*	*434.075*	*-13.981*	*-10.027*	*-7.537*	*825.156*	*632.249*	*426.538*

Table 7.S20. Electric Dipole Moment HOMO1 ^{13}C isotolologues: equi. B2, vib. B3 level of theory (Debye) in Principal Axis frame

	$\mu_a e$	$\mu_b e$	$\mu_c e$	$\Delta\mu_a 0$	$\Delta\mu_b 0$	$\Delta\mu_c 0$
HOMO1	*0.7527*	*-1.5136*	*0.8259*	*-0.0164*	*0.0361*	*-0.0270*
C1	*0.7492*	*-1.5132*	*0.8298*	*-0.0187*	*0.0361*	*-0.0280*
C2	*0.7422*	*-1.5209*	*0.8219*	*-0.0171*	*0.0250*	*-0.0333*
C3	*0.7163*	*-1.5346*	*0.8195*	*-0.0129*	*0.0283*	*-0.0282*
C11	*0.7508*	*-1.5123*	*0.8299*	*-0.0189*	*0.0324*	*-0.0358*
C12	*0.7424*	*-1.5188*	*0.8258*	*-0.0135*	*0.0334*	*-0.0323*
C13	*0.7154*	*-1.5310*	*0.8271*	*-0.0178*	*0.0312*	*-0.0350*
C21	*0.7819*	*-1.4970*	*0.8291*	*-0.0202*	*0.0551*	*-0.0137*
C22	*0.7730*	*-1.5059*	*0.8212*	*-0.0140*	*0.0459*	*-0.0192*
C23	*0.7823*	*-1.5031*	*0.8175*	*-0.0228*	*0.0380*	*-0.0212*

Table 7.S21. HOMO1 ^{13}C isotolologues: equi. rPP, vib. B3 level of theory (MHz)

	Ae	*Be*	*Ce*	*vibA0*	*vibB0*	*vibC0*	*A0*	*B0*	*C0*
HOMO1	*848.642*	*648.445*	*438.418*	*-13.333*	*-10.377*	*-7.601*	*835.309*	*638.068*	*430.817*
C1	*837.952*	*648.334*	*435.596*	*-12.646*	*-10.260*	*-7.434*	*825.306*	*638.074*	*428.162*
C2	*843.492*	*647.832*	*437.057*	*-13.483*	*-10.181*	*-7.517*	*830.009*	*637.651*	*429.540*
C3	*841.057*	*644.008*	*435.514*	*-14.116*	*-9.876*	*-7.680*	*826.941*	*634.132*	*427.834*
C11	*846.774*	*642.755*	*436.300*	*-14.373*	*-10.377*	*-7.737*	*832.401*	*632.378*	*428.563*
C12	*848.057*	*644.740*	*436.576*	*-13.394*	*-10.259*	*-7.537*	*834.663*	*634.481*	*429.039*
C13	*844.440*	*640.140*	*433.826*	*-14.505*	*-9.680*	*-7.303*	*829.935*	*630.460*	*426.523*
C21	*838.618*	*646.843*	*435.057*	*-13.421*	*-10.299*	*-7.635*	*825.197*	*636.544*	*427.422*
C22	*845.052*	*646.253*	*436.711*	*-13.150*	*-9.892*	*-7.338*	*831.902*	*636.361*	*429.373*
C23	*845.701*	*640.799*	*434.925*	*-13.981*	*-10.027*	*-7.537*	*831.720*	*630.772*	*427.388*

Table 7.S22. Electric Dipole Moment HOMO1 ^{13}C isotolologues: equi. rPP, vib. B3 level of theory (Debye) in Principal Axis frame

	$\mu_a e$	$\mu_b e$	$\mu_c e$	$\Delta\mu_a 0$	$\Delta\mu_b 0$	$\Delta\mu_c 0$
HOMO1	*0.7837*	*-1.4584*	*0.8518*	*-0.0164*	*0.0361*	*-0.0270*
C1	*0.7826*	*1.4567*	*-0.8555*	*-0.0187*	*0.0361*	*-0.0280*
C2	*0.7747*	*1.4654*	*-0.8479*	*-0.0171*	*0.0250*	*-0.0333*
C3	*0.7493*	*1.4799*	*-0.8456*	*-0.0129*	*0.0283*	*-0.0282*
C11	*0.7807*	*1.4576*	*-0.8558*	*-0.0189*	*0.0324*	*-0.0358*
C12	*0.7736*	*1.4638*	*-0.8517*	*-0.0135*	*0.0334*	*-0.0323*
C13	*0.7481*	*1.4762*	*-0.8531*	*-0.0178*	*0.0312*	*-0.0350*
C21	*0.8121*	*1.4408*	*-0.8550*	*-0.0202*	*0.0551*	*-0.0137*
C22	*0.8029*	*1.4506*	*-0.8472*	*-0.0140*	*0.0459*	*-0.0192*
C23	*0.8106*	*1.4484*	*-0.8435*	*-0.0228*	*0.0380*	*-0.0212*

Table 7.S23. HOMO2 ^{13}C isotolologues: equi. B2, vib. B3 level of theory (MHz)

	Ae	*Be*	*Ce*	*vibA0*	*vibB0*	*vibC0*	*A0*	*B0*	*C0*
HOMO2	*795.369*	*642.248*	*471.165*	*-12.060*	*-11.182*	*-11.499*	*783.309*	*631.066*	*459.666*
C1	*785.530*	*644.831*	*471.717*	*-11.175*	*-13.300*	*-10.952*	*774.355*	*631.531*	*460.765*
C2	*790.919*	*645.825*	*473.242*	*-11.437*	*-13.296*	*-11.115*	*779.482*	*632.529*	*462.127*
C3	*786.877*	*644.250*	*472.314*	*-11.291*	*-13.210*	*-10.848*	*775.586*	*631.040*	*461.466*
C11	*792.258*	*642.886*	*473.220*	*-12.262*	*-13.469*	*-11.426*	*779.996*	*629.417*	*461.794*
C12	*793.734*	*640.523*	*471.359*	*-12.428*	*-12.711*	*-11.240*	*781.306*	*627.812*	*460.119*
C13	*792.506*	*640.278*	*472.408*	*-11.815*	*-13.000*	*-10.989*	*780.691*	*627.278*	*461.419*
C21	*795.802*	*639.144*	*471.367*	*-11.737*	*-12.780*	*-10.899*	*784.065*	*626.364*	*460.468*
C22	*792.747*	*641.107*	*471.333*	*-11.151*	*-12.975*	*-10.577*	*781.596*	*628.132*	*460.756*
C23	*789.528*	*642.840*	*472.457*	*-12.085*	*-13.059*	*-11.130*	*777.443*	*629.781*	*461.327*

Table 7.S24. Electric Dipole Moment HOMO2 ^{13}C isotolologues: equi. B2, vib. B3 level of theory (Debye) in Principal Axis frame

	$\mu_a e$	$\mu_b e$	$\mu_c e$	$\Delta\mu_a 0$	$\Delta\mu_b 0$	$\Delta\mu_c 0$
HOMO2	*-1.1450*	*-0.2357*	*-1.4072*	*0.0081*	*0.0230*	*-0.0076*
C1	*-1.1519*	*-0.1906*	*-1.4084*	*0.0159*	*0.0106*	*-0.0070*
C2	*-1.1528*	*-0.2101*	*-1.4048*	*0.0108*	*0.0180*	*-0.0107*
C3	*-1.1465*	*-0.2408*	*-1.4051*	*0.0014*	*0.0198*	*-0.0059*
C11	*-1.1545*	*-0.2217*	*-1.4016*	*0.0137*	*0.0153*	*-0.0088*
C12	*-1.1471*	*-0.2389*	*-1.4049*	*0.0088*	*0.0202*	*-0.0144*
C13	*-1.1386*	*-0.2360*	*-1.4123*	*0.0111*	*0.0229*	*-0.0122*
C21	*-1.1511*	*-0.2072*	*-1.4067*	*0.0094*	*0.0215*	*-0.0070*
C22	*-1.1577*	*-0.1840*	*-1.4045*	*0.0065*	*0.0261*	*-0.0082*
C23	*-1.1618*	*-0.2024*	*-1.3985*	*0.0103*	*0.0275*	*-0.0121*

Table 7.S25. HOMO2 ^{13}C isotolologues: equi. rPP, vib. B3 level of theory (MHz)

	Ae	*Be*	*Ce*	*vibA0*	*vibB0*	*vibC0*	*A0*	*B0*	*C0*
HOMO2	*795.778*	*639.697*	*468.845*	*-12.060*	*-11.182*	*-11.499*	*783.718*	*628.515*	*457.346*
C1	*785.136*	*638.705*	*465.585*	*-11.175*	*-13.300*	*-10.952*	*773.961*	*625.405*	*454.633*
C2	*790.720*	*639.639*	*467.083*	*-11.437*	*-13.296*	*-11.115*	*779.283*	*626.343*	*455.968*
C3	*786.799*	*637.936*	*466.088*	*-11.291*	*-13.210*	*-10.848*	*775.508*	*624.726*	*455.240*
C11	*792.300*	*636.605*	*467.038*	*-12.262*	*-13.469*	*-11.426*	*780.038*	*623.136*	*455.612*
C12	*793.795*	*634.142*	*465.177*	*-12.428*	*-12.711*	*-11.240*	*781.367*	*621.431*	*453.937*
C13	*792.578*	*633.931*	*466.191*	*-11.815*	*-13.000*	*-10.989*	*780.763*	*620.931*	*455.202*
C21	*795.568*	*632.994*	*465.188*	*-11.737*	*-12.780*	*-10.899*	*783.831*	*620.214*	*454.289*
C22	*792.239*	*635.189*	*465.209*	*-11.151*	*-12.975*	*-10.577*	*781.088*	*622.214*	*454.632*
C23	*789.203*	*636.865*	*466.340*	*-12.085*	*-13.059*	*-11.130*	*777.118*	*623.806*	*455.210*

Table 7.S26. Electric Dipole Moment HOMO2 ^{13}C isotolologues: equi. rPP, vib. B3 level of theory (Debye) in Principal Axis frame

	$\mu_a e$	$\mu_b e$	$\mu_c e$	$\Delta\mu_a 0$	$\Delta\mu_b 0$	$\Delta\mu_c 0$
HOMO2	*1.1341*	*-0.2502*	*1.4118*	*0.0081*	*0.0230*	*-0.0076*
C1	*1.1344*	*-0.2301*	*1.4150*	*0.0159*	*0.0106*	*-0.0070*
C2	*1.1349*	*-0.2491*	*1.4114*	*0.0108*	*0.0180*	*-0.0107*
C3	*1.1276*	*-0.2789*	*1.4116*	*0.0014*	*0.0198*	*-0.0059*
C11	*1.1365*	*-0.2581*	*1.4084*	*0.0137*	*0.0153*	*-0.0088*
C12	*1.1291*	*-0.2736*	*1.4115*	*0.0088*	*0.0202*	*-0.0144*
C13	*1.1209*	*-0.2704*	*1.4186*	*0.0111*	*0.0229*	*-0.0122*
C21	*1.1342*	*-0.2422*	*1.4131*	*0.0094*	*0.0215*	*-0.0070*
C22	*1.1409*	*-0.2220*	*1.4110*	*0.0065*	*0.0261*	*-0.0082*
C23	*1.1441*	*-0.2414*	*1.4053*	*0.0103*	*0.0275*	*-0.0121*

Table 7.S27. HETERO1 ^{13}C isotolologues: equi. B2, vib. B3 level of theory (MHz)

	Ae	*Be*	*Ce*	*vibA0*	*vibB0*	*vibC0*	*A0*	*B0*	*C0*
HETERO1	*816.209*	*656.550*	*452.306*	*-14.744*	*-10.511*	*-9.373*	*801.465*	*646.039*	*442.933*
C1	*806.369*	*656.237*	*449.318*	*-14.445*	*-10.610*	*-9.277*	*791.924*	*645.627*	*440.041*
C2	*811.001*	*656.211*	*450.746*	*-14.469*	*-10.623*	*-9.295*	*796.532*	*645.588*	*441.451*
C3	*807.885*	*653.072*	*448.940*	*-14.135*	*-10.637*	*-9.271*	*793.750*	*642.435*	*439.669*
C11	*811.280*	*650.088*	*447.964*	*-13.511*	*-11.190*	*-9.066*	*797.769*	*638.898*	*438.898*
C12	*814.430*	*652.513*	*450.039*	*-14.678*	*-11.420*	*-9.636*	*799.752*	*641.093*	*440.403*
C13	*809.312*	*652.825*	*450.522*	*-14.590*	*-10.967*	*-9.490*	*794.722*	*641.858*	*441.032*
C21	*814.952*	*650.656*	*449.830*	*-14.989*	*-10.363*	*-9.188*	*799.963*	*640.293*	*440.642*
C22	*815.119*	*653.285*	*450.468*	*-13.662*	*-11.220*	*-9.419*	*801.457*	*642.065*	*441.049*
C23	*810.095*	*649.630*	*447.842*	*-14.188*	*-10.530*	*-9.192*	*795.907*	*639.100*	*438.650*

Table 7.S28. Electric Dipole Moment HETERO1 ^{13}C isotolologues: equi. B2, vib. B3 level of theory (Debye) in Principal Axis frame

	$\mu_a e$	$\mu_b e$	$\mu_c e$	$\Delta\mu_a 0$	$\Delta\mu_b 0$	$\Delta\mu_c 0$
HETERO1	*1.6342*	*-0.9718*	*0.7500*	*-0.0534*	*0.0451*	*0.0093*

C1	*1.6400*	*-0.9586*	*0.7543*	*-0.0567*	*0.0597*	*0.0136*
C2	*1.6292*	*-0.9818*	*0.7478*	*-0.0513*	*0.0535*	*0.0096*
C3	*1.6047*	*-1.0205*	*0.7490*	*-0.0425*	*0.0603*	*0.0075*
C11	*1.6632*	*-0.9150*	*0.7576*	*-0.0507*	*0.0400*	*0.0039*
C12	*1.6499*	*-0.9489*	*0.7450*	*-0.0464*	*0.0437*	*0.0033*
C13	*1.6513*	*-0.9538*	*0.7355*	*-0.0398*	*0.0435*	*-0.0018*
C21	*1.6269*	*-0.9787*	*0.7569*	*-0.0473*	*0.0492*	*0.0026*
C22	*1.6240*	*-0.9895*	*0.7490*	*-0.0510*	*0.0560*	*0.0094*
C23	*1.6034*	*-1.0240*	*0.7470*	*-0.0540*	*0.0486*	*0.0050*

Table 7.S29. HETERO1 ^{13}C isotolologues: equi. rPP, vib. B3 level of theory (MHz)

	Ae	*Be*	*Ce*	*vibA0*	*vibB0*	*vibC0*	*A0*	*B0*	*C0*
HETERO1	*824.629*	*655.418*	*452.741*	*-14.744*	*-10.511*	*-9.373*	*809.885*	*644.907*	*443.368*
C1	*814.780*	*655.073*	*449.798*	*-14.445*	*-10.610*	*-9.277*	*800.335*	*644.463*	*440.521*
C2	*819.332*	*655.092*	*451.191*	*-14.469*	*-10.623*	*-9.295*	*804.863*	*644.469*	*441.896*
C3	*816.065*	*652.049*	*449.335*	*-14.135*	*-10.637*	*-9.271*	*801.930*	*641.412*	*440.064*
C11	*819.896*	*648.772*	*448.380*	*-13.511*	*-11.190*	*-9.066*	*806.385*	*637.582*	*439.314*
C12	*822.873*	*651.371*	*450.489*	*-14.678*	*-11.420*	*-9.636*	*808.195*	*639.951*	*440.853*
C13	*817.577*	*651.765*	*450.936*	*-14.590*	*-10.967*	*-9.490*	*802.987*	*640.798*	*441.446*
C21	*823.357*	*649.441*	*450.204*	*-14.989*	*-10.363*	*-9.188*	*808.368*	*639.078*	*441.016*
C22	*823.502*	*652.213*	*450.923*	*-13.662*	*-11.220*	*-9.419*	*809.840*	*640.993*	*441.504*
C23	*818.220*	*648.729*	*448.346*	*-14.188*	*-10.530*	*-9.192*	*804.032*	*638.199*	*439.154*

Table 7.S30. Electric Dipole Moment HETERO1 ^{13}C isotolologues: equi. rPP, vib. B3 level of theory (Debye) in Principal Axis frame

	$\mu_a e$	$\mu_b e$	$\mu_c e$	$\Delta\mu_a 0$	$\Delta\mu_b 0$	$\Delta\mu_c 0$
HETERO1	*1.6256*	*-0.9096*	*0.7876*	*-0.0534*	*0.0451*	*0.0093*
C1	*1.6314*	*-0.8955*	*0.7917*	*-0.0567*	*0.0597*	*0.0136*
C2	*1.6214*	*-0.9188*	*0.7856*	*-0.0513*	*0.0535*	*0.0096*
C3	*1.5990*	*-0.9563*	*0.7868*	*-0.0425*	*0.0603*	*0.0075*
C11	*1.6507*	*-0.8565*	*0.7948*	*-0.0507*	*0.0400*	*0.0039*
C12	*1.6396*	*-0.8884*	*0.7827*	*-0.0464*	*0.0437*	*0.0033*
C13	*1.6414*	*-0.8929*	*0.7738*	*-0.0398*	*0.0435*	*-0.0018*
C21	*1.6183*	*-0.9167*	*0.7944*	*-0.0473*	*0.0492*	*0.0026*
C22	*1.6167*	*-0.9262*	*0.7866*	*-0.0510*	*0.0560*	*0.0094*
C23	*1.5990*	*-0.9581*	*0.7846*	*-0.0540*	*0.0486*	*0.0050*

Table 7.S32. The structural fitting results of HOMO1 based on B_0 and B_{semi}.

Parameters[a]	B_0 fit	B_{semi} fit	rPP cal. equil.
R(11, 7) /Å	3.3008 +/- 0.0021	3.2733 +/- 0.0094	3.2634
A(11, 7, 1) /°	96.088 +/- 0.045	96.10 +/- 0.23	95.318
R(21,7) /Å	4.37514 +/- 0.00076	4.3370 +/- 0.0031	4.4177
A(21,7,1) /°	147.736 +/- 0.014	147.080 +/- 0.065	145.949
Chi-squared	0.1513	3.0977	N/A
Deviation of fit	0.0763	0.3452	N/A

[a] All other structural parameters are fixed at the rPP values listed in Table S31 as well as atom numbers.

Table 7.S33. The rPP equilibrium z-matrix coordinates and atom numbering of HETERO1.

NO	NA	NB	NC	Distance / Å	Angle / °	Dihedral Angle / °	Mass / amu
1	0	0	0	0.000000	0.000000	0.000000	12.0000000
2	1	0	0	1.462779	0.000000	0.000000	12.0000000
3	2	1	0	1.500538	122.127959	0.000000	12.0000000
4	3	2	1	1.091773	110.528249	27.093855	1.0078250
5	3	2	1	1.091711	110.052150	147.820236	1.0078250
6	3	2	1	1.093200	110.159230	-93.035716	1.0078250
7	2	1	3	1.085491	116.678665	-154.562317	1.0078250
8	1	2	3	1.440694	59.503452	-103.530859	15.9949100
9	1	8	2	1.084415	114.479452	110.621912	1.0078250
10	1	8	2	1.086052	114.359542	-110.740596	1.0078250

11	8	1	2	4.330035	146.774637	0.732136	12.0000000
12	11	8	1	1.464064	27.544373	166.753877	12.0000000
13	12	11	8	1.500345	122.064067	127.795203	12.0000000
14	13	12	11	1.093152	110.148467	93.629698	1.0078250
15	13	12	11	1.090741	109.891491	-146.928496	1.0078250
16	13	12	11	1.091874	110.439607	-26.499578	1.0078250
17	12	11	8	1.086424	117.636471	-77.422551	1.0078250
18	11	8	1	1.437588	35.496831	-50.464128	15.9949100
19	11	8	1	1.085469	111.475784	52.403375	1.0078250
20	11	8	1	1.085926	132.505664	-122.413554	1.0078250
21	8	1	2	3.276247	93.293655	-103.823231	12.0000000
22	21	8	1	1.463457	82.518018	111.276420	12.0000000
23	22	21	8	1.501269	121.774151	177.145897	12.0000000
24	21	8	1	1.438624	77.246917	50.925009	15.9949100
25	21	8	1	1.084758	43.055981	-98.794520	1.0078250
26	21	8	1	1.086284	158.321094	-74.422037	1.0078250
27	23	22	21	1.092218	110.480762	145.300586	1.0078250
28	23	22	21	1.093188	110.235438	-95.395109	1.0078250
29	23	22	21	1.091392	110.588069	25.068309	1.0078250
30	22	21	8	1.086056	117.278196	22.610211	1.0078250

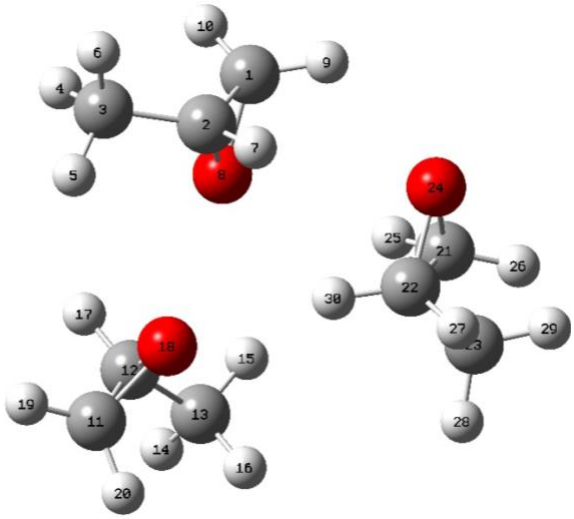

Table 7.S34. The structural fitting results of HETERO1 based on B_0 and B_{semi}.

Parameters[a]	B_0 fit	B_{semi} fit	rPP cal. equil.
R(11, 8) /Å	4.3652 +/- 0.0011	4.3092 +/- 0.0065	4.3300
A(11, 8, 1) /°	147.392 +/- 0.014	146.781 +/- 0.080	146.775
R(21,8) /Å	3.3219 +/- 0.0014	3.2888 +- 0.0082	3.2762
A(21,8,1) /°	93.687 +- 0.022	93.54 +- 0.14	93.294
Chi-squared	0.1003	3.3869	N/A
Deviation of fit	0.0621	0.3609	N/A

[a] All other structural parameters are fixed at the rPP values listed in Table S33 as well as atom numbers.

Completion of reference 14.

Gaussian 16, Revision C.01. M. J. Frisch, G. W. Trucks, H. B. Schlegel, G. E. Scuseria, M. A. Robb, J. R. Cheeseman, G. Scalmani, V. Barone, G. A. Petersson, H. Nakatsuji, X. Li, M. Caricato, A. V. Marenich, J. Bloino, B. G. Janesko, R. Gomperts, B. Mennucci, H. P. Hratchian, J. V. Ortiz, A. F. Izmaylov, J. L. Sonnenberg, D. Williams-Young, F. Ding, F. Lipparini, F. Egidi, J. Goings, B. Peng, A. Petrone, T. Henderson, D. Ranasinghe, V. G. Zakrzewski, J. Gao, N. Rega, G. Zheng, W. Liang, M. Hada, M. Ehara, K. Toyota, R. Fukuda, J. Hasegawa, M. Ishida, T. Nakajima, Y. Honda, O. Kitao, H. Nakai, T. Vreven, K. Throssell, J. A. Montgomery, Jr., J. E. Peralta, F. Ogliaro, M. J. Bearpark, J. J. Heyd, E. N. Brothers, K. N. Kudin, V. N. Staroverov, T. A. Keith, R. Kobayashi, J. Normand, K. Raghavachari, A. P. Rendell, J. C. Burant, S. S. Iyengar, J. Tomasi, M. Cossi, J. M.

Millam, M. Klene, C. Adamo, R. Cammi, J. W. Ochterski, R. L. Martin, K. Morokuma, O. Farkas, J. B. Foresman, and D. J. Fox, Gaussian, Inc., Wallingford CT, **2016**.